8-2019

Chemical Transformations of Hydrated Uranyl Fluoride

Marie Kirkegaard
University of Tennessee, mkirkega@vols.utk.edu

Chemical Transformations of Hydrated Uranyl Fluoride

A Dissertation Presented for the

Doctor of Philosophy

Degree

The University of Tennessee, Knoxville

Marie Claire Kirkegaard

August 2019

In loving memory of J. Chance Crompton.

Thank you for sharing your passion.

Acknowledgments

This work has been supported by a number of people who deserve my whole-hearted thanks:

- Brian Anderson, my advisor and the Nuclear Security Advanced Technologies (NSAT) Group Leader at Oak Ridge National Laboratory (ORNL);
- Andrew Miskowiec, Michael Ambrogio, Ashley Shields, Jennifer Niedziela, Tyler Spano, and Roger Kapsimalis, colleagues and mentors on the NSAT Materials and Chemistry Team;
- Lee Trowbridge, Darrell Simmons, and Hal Jennings of the Process Engineering Group at ORNL, who provided uranyl fluoride source material;
- David Harris and the rest of the radiation control technicians; and
- Lee Riedinger, Wanda Davis, and the rest of the Bredesen Center team at the University of Tennessee.

The following facilities and resources have supported this work:

- Spallation Neutron Source (SNS) at ORNL, which is a US Department of Energy Office of Science User Facility;
- Center for Nanophase Materials Sciences (CNMS) at ORNL; and
- Compute and Data Environment for Science (CADES) at ORNL, which is supported by the Office of Science under contract no. DE-AC05-00OR22725.

This material is based upon work supported by the US Department of Homeland Security (DHS) under grant award no. 2012-DN-130-NF0001. The views and conclusions contained

in this document are those of the author and should not be interpreted as representing the official policies, either expressed or implied, of the DHS.

Abstract

The chemical behavior of uranyl fluoride (UO_2F_2), a byproduct of the nuclear fuel cycle, is of significant interest for nuclear security applications. Two phases of uranyl fluoride (UO_2F_2 and $[(UO_2F_2)(H_2O)]_7 \cdot 4\,H_2O$) have been previously identified; these structures and the phase transition between them are further characterized in this work. In addition, the stability of uranyl fluoride is assessed under varying environmental conditions. While previous studies have suggested that uranyl fluoride may degrade upon exposure to high humidity, the chemical pathway of degradation was not well understood. This work demonstrates that uranyl fluoride undergoes a chemical reaction with water vapor to form a novel uranyl hydroxide hydration product. This species, shown to be structurally similar to the uranyl hydroxide mineral schoepite, can be further hydrated to form a uranyl peroxide species.

The unexpected and novel nonphotochemical formation of uranyl peroxide from multiple uranyl hydroxide species is explained by unusually high uranyl ion reactivity in these reactant species. While the uranyl ion is typically fairly inert, strong σ-donating equatorial ligands and strong interactions between uranyl oxygens and interlayer water molecules weaken the uranyl ion in these species such that an increase in the water vapor pressure can induce a redox reaction that is normally dependent on the photoexcitation of the uranyl ion.

Table of Contents

Chapter 1

Introduction

1.1 Motivation

The chemistry of uranium is exceedingly complex. Uranium supports a wide number of coordination environments in the solid state, leading to a large number of potential structures, many of which have highly complex or noncrystalline structural arrangements. It is likely that only a small fraction of possible solid-state uranium compounds have been identified, and of those that have been identified, an even smaller number have been rigorously characterized. Characterization of solid-state inorganic uranium compounds has been generally limited to the study of uranium oxides for nuclear fuel development or naturally occurring uranium-containing minerals of interest to geochemists. Detailed structural and chemical information is often lacking for other compounds, including nuclear fuel cycle byproducts. However, characterization of these byproducts is important to support nuclear forensics and environmental monitoring for nonproliferation treaty compliance, as well as environmental remediation and waste management.

One nuclear fuel cycle byproduct of particular interest is uranyl fluoride (UO_2F_2), which is the hydrolysis product of uranium hexafluoride (UF_6) via Reaction 1.1. Solid-state uranyl fluoride is produced when traces of UF_6 interact with moisture in the environment, and is thus an important material in the context of nuclear forensics and environmental monitoring analyses. Understanding the chemical behavior of uranyl fluoride under various environmental conditions is crucial for identifying unknown species and connecting

laboratory measurements to material history. However, the degradation pathways of uranyl fluoride in environmentally relevant conditions are not well understood. While earlier work has suggested that uranyl fluoride undergoes chemical reactions upon exposure to a humid environment, including a loss of fluorine, potential hydration products have not been well characterized. This has left significant uncertainty about the fate of uranyl fluoride in different conditions, motivating a rigorous analysis of degradation pathways and thorough characterization of all relevant species.

$$UF_6 + 2\,H_2O \longrightarrow UO_2F_2 + 4\,HF \tag{1.1}$$

One of the main themes of this dissertation is the correlation of the structural and vibrational properties of uranyl fluoride and its degradation products. Vibrational spectroscopic techniques such as Raman and infrared (IR) spectroscopy are nondestructive, rapid, and relatively low-cost methods that are commonly used to identify uranium compounds. However, clear connections between the structure, vibrational spectra, and chemical properties of the material are often lacking. This essentially limits the utility of vibrational characterization to spectral matching, which becomes problematic when the vibrational spectrum of a sample of interest does not match any known, well-characterized materials. Performing complementary structural and vibrational studies on the material of interest in this study not only improves the ability to identify and characterize these materials in the future, but also provides insight into the structure–spectroscopy relationship of other related materials.

In addition to having direct applications in nuclear forensics and environmental monitoring, the study of uranyl fluoride and its degradation products is also motivated by a desire to advance the current understanding of uranyl chemistry. Despite the maturity of the nuclear fuel industry, uranium chemistry remains in its infancy in many regards. Work in this field consistently uncovers new findings, some of which may cause reexamination of previously held beliefs. For example, one of the fundamental tenets of uranium chemistry has been the stability and inertness of the linear uranyl ion, UO_2^{2+} [83, 109, 16, 122, 95]. The uranyl ion lacks the complex redox chemistry of transition metal oxides due to the formation of

hybrid *5f-6p* orbitals, which participate in a strong σ bond. However, recent studies have demonstrated that the uranyl ion can be functionalized under specific conditions after all [8, 21, 9, 57, 10].

Findings like these challenge old assumptions about the chemical behavior of uranium and may have revolutionary impacts on fields such as advanced fuel development, waste management, and environmental remediation. Developing a better understanding of uranium chemistry is possible through rigorous study of different compounds under a variety of conditions. In addition to clarifying the conditions in which uranyl fluoride is unstable and characterizing the hydration products, elucidating the mechanistic details of these hydration reactions will contribute to a more complete understanding of the chemical behavior of the uranyl ion. In this manner, the present work has impact beyond the study of uranyl fluoride, as it will provide insight into the types of reactions that other uranyl compounds may undergo in similar environments.

1.2 Scope

This dissertation presents a rigorous characterization of the structural forms of species in the uranyl fluoride degradation pathway, as well as their chemical response to environmentally relevant perturbations. Complementary experimental and computational techniques are employed to more fully interpret structural information and to correlate structural and vibrational properties. In addition, both bulk and microanalytic tools are used to examine chemical behavior on different scales. The remaining section of this chapter provides more details of the methodology of this study.

Chapters 2–5 each focus on a specific aspect of the degradation pathway of uranyl fluoride. Each chapter begins with a discussion of relevant prior research that motivates or informs the present study. Chapter 2 clarifies the relationship between the two known uranyl fluoride structures (i.e., anhydrous and hydrated) and presents a thorough analysis of the structure and spectroscopic properties of hydrated uranyl fluoride. Chapter 3 describes findings that uranyl fluoride is not stable at elevated water vapor pressure, but rather undergoes a chemical transformation to form a uranyl hydroxide hydration product, which can be further hydrated

to form a uranyl peroxide hydrate. Chapter 4 further characterizes the novel layered uranyl hydroxide hydrate produced from the hydration of uranyl fluoride via comparison to synthetic metaschoepite ($[(UO_2)_4O(OH)_6] \cdot 5\,H_2O$), a known uranyl hydroxide hydrate. Chapter 5 elucidates the novel nonphotochemical formation reaction of a uranyl peroxide hydrate from hydrated uranyl hydroxide. Chapter 6 offers conclusions and avenues for further research.

A number of articles presenting components of this dissertation have been published or are in preparation, including:

A. Miskowiec, **M. C. Kirkegaard**, A. Huq, E. Mamontov, K. W. Herwig, L. Trowbridge, A. Rondinone, and B. B. Anderson. "Structural phase transitions and water dynamics in uranyl fluoride hydrates." *J. Phys. Chem. A* 2015, 119, 11900-11910.

M. C. Kirkegaard, A. Miskowiec, M. W. Ambrogio, and B. B. Anderson. "Evidence of a nonphotochemical mechanism for the solid-state formation of uranyl peroxide." *Inorg. Chem.*, 2018, 57, 5711-5715.

M. C. Kirkegaard, A. Miskowiec, M. W. Ambrogio, J. Langford, A. E. Shields, J. L. Niedziela, R. Kapsimalis, and B. B. Anderson. "Characterizing the chemical behavior of uranium compounds for nuclear forensics." Proceedings of the Institute for Nuclear Materials Management, 2018.

M. C. Kirkegaard, J. L. Niedziela, A. Miskowiec, A. E. Shields, and B. B. Anderson. "Elucidation of the structure and vibrational spectroscopy of synthetic metaschoepite and its dehydration product." Accepted to *Inorg. Chem.*

M. C. Kirkegaard, M. W. Ambrogio, T. L. Spano, J. L. Niedziela, A. Miskowiec, A. E. Shields and B. B. Anderson. "Formation of a uranyl hydroxide hydrate via hydration of $[(UO_2F_2)(H_2O)]_7 \cdot 4\,H_2O$." Submitted to *Dalton Trans.*

M. C. Kirkegaard, M. W. Ambrogio, A. Miskowiec, J. L. Niedziela, T. L. Spano, A. E. Shields and B. B. Anderson. "Characterization of the degradation of $[(UO_2F_2)(H_2O)]_7 \cdot 4\,H_2O$ under humid conditions." In preparation.

M. C. Kirkegaard, T. L. Spano, A. Miskowiec, J. L. Niedziela, A. E. Shields and B. B. Anderson. "Evidence of unusual uranyl ion reactivity in uranyl hydroxide hydrates." In preparation.

1.3 Methodology

1.3.1 Experimental techniques

The experimental techniques used in this study focus on structural and spectroscopic characterization of uranyl fluorides, hydroxides, and peroxides. The diffraction techniques utilized in this study (x-ray and neutron diffraction) allow for the identification of these species. These techniques are reliant on the presence of long-range order, however, and do not provide useful information about amorphous materials, alterations in local ordering, or particle samples with a mass below the limit of detection of these methods. Vibrational characterization via Raman and infrared (IR) spectroscopy can provide indirect structural information in these cases. Where appropriate, structural and vibrational techniques are also complemented by additional analytical techniques such as scanning electron microscopy–energy dispersive x-ray spectroscopy (SEM-EDS) that provide additional information about the morphology and elemental composition of a material. Each of these methods is discussed in further detail below.

X-ray and neutron diffraction

Structural analysis of materials in this study was performed using both x-ray and neutron diffraction techniques. x-ray and neutron diffraction are complementary structural characterization techniques as they probe distinct atomic constituents. The x-ray and neutron scattering cross sections of the atoms in materials relevant to this study are shown in Table 1.1. Since x-ray cross sections are equal to Z number, x-ray diffraction (XRD) is the most sensitive to the position of uranium atoms. The location of the lighter atoms, especially hydrogen/deuterium, must be determined instead via neutron diffraction.

Table 1.1: X-ray and neutron scattering cross sections of relevant atoms.

Atom	x-ray (e)	Neutron (b)
U-238	92	13.78
U-235	92	8.87
F	9	4.0
O	8	4.2
D	1	7.64
H	1	82

The XRD experimental parameters used in this dissertation are summarized in Table 1.2. Samples were produced by dispersing material on zero-background silicon plates. Samples were prepared in the absence of any solvent to prevent dehydration or other unintended alteration. A small amount of either Si or LaB_6 powder was frequently mixed with samples to serve as an in situ standard for lineshape and diffractometer calibration.

Time-of-flight neutron diffraction data was collected using the POWGEN instrument [73] at the Spallation Neutron Source (SNS). Sample material was loaded into 6 mm vanadium sample cans, which were backfilled with argon prior to sealing. Other relevant experimental parameters are shown in Table 1.3. Reduction of neutron diffraction data was performed using the Mantid framework [7]. Where possible, Rietveld refinement was performed on x-ray and neutron diffraction patterns using GSAS-II [157]. This technique uses an iterative approach to refine metrics such as the lattice parameters and crystallite size to derive a calculated diffraction pattern that best fits the experimental data.

Raman and IR spectroscopy

Raman and IR spectroscopy are vibrational spectroscopic techniques that are useful for characterizing the local structure of materials. These techniques complement diffraction data by providing insight into how atoms are organized in a structure, clarifying things like the functional groups present, the equatorial coordination of the uranyl ion, and the water structure in crystal hydrates. Vibrational spectroscopy can also be used to characterize materials that cannot be studied via diffraction, such as amorphous species or very small samples.

While Raman and IR spectroscopy are both optical spectroscopy techniques that provide similar chemical information, they are fundamentally different processes. IR spectroscopy is an absorption technique that measures the energy required to bring a system to an excited vibrational state (Figure 1.1). In comparison, Raman spectroscopy is a scattering technique; the system is excited to a virtual energy state (not quantized) and then relaxes. Rayleigh scattering occurs when the system relaxes to the initial ground-state energy state, while Stokes Raman scattering occurs when the system relaxes to an excited vibrational state.

Table 1.2: XRD experimental parameters.

Instrument	Proto AXRD
x-ray source	Cu K_α
Slit width	0.5 mm
Range	2θ = [10,50] degrees
Step size	$\delta 2\theta$ = 0.02 deg
Scan time	1-14 hours

Table 1.3: Neutron diffraction parameters.

Instrument	POWGEN [73]
Sample container	6 mm vanadium cans
Center wavelength	1.5 Å
Range	d = 0.5 to 12 Å

The recorded Raman shift is the difference between the excitation and emission energy (Figure 1.1).

IR and Raman spectroscopy are often used together as complementary techniques because distinct selection rules make some vibrational modes Raman active and others IR active. Vibrational modes that involve a change in dipole moment are IR active, and vibrational modes that involve a change of polarizability are Raman-active. If a vibrational mode is both IR and Raman active, the measured IR absorption frequency will be equal to the Raman shift, as demonstrated in Figure 1.1.

Raman and IR spectroscopy are particularly useful for characterizing the coordination environment of the uranyl ion. Because of the different selection rules associated with Raman and IR spectroscopy, the symmetric uranyl stretching mode is a dominant peak in the Raman spectra, while the asymmetric uranyl stretching mode is a dominant peak in the IR spectra. Both of these modes are highly sensitive to the environment of the uranyl ion, such as the number and type of equatorial ligands [27, 122, 47, 100]. Therefore, shifts in the band frequency are often indicative of structural or chemical changes [107, 82].

Vibrational spectroscopy can also complement XRD measurements by providing information about the water structure within crystal hydrates. As shown in Table 1.1, x-rays are not sensitive to light elements such as hydrogen, and the Raman scattering cross-section of water is very low. In contrast, IR spectroscopy is very sensitive to water and hydrogen-bonding interactions, [101, 59] and can thus be used to characterize the water structure in crystal hydrates.

Vibrational spectroscopy is also useful for studying reaction mechanisms, particularly through isotopic labeling studies. Because the frequency of vibrational modes is dependent on element masses, isotopic substitution causes observable shifts of the modes related to the movement of the substituted atoms. Labeling a subset of the atoms in a system can thus help elucidate how those atoms are or are not involved in chemical reactions [110].

The experimental parameters for the Raman and IR spectroscopy experiments described in this dissertation are summarized in Tables 1.4 and 1.5. Since IR spectroscopy is very sensitive to water, a diamond attenuated total reflectance (ATR) attachment was used to obtain all IR spectra to prevent oversaturation of the detectors when studying hydrated

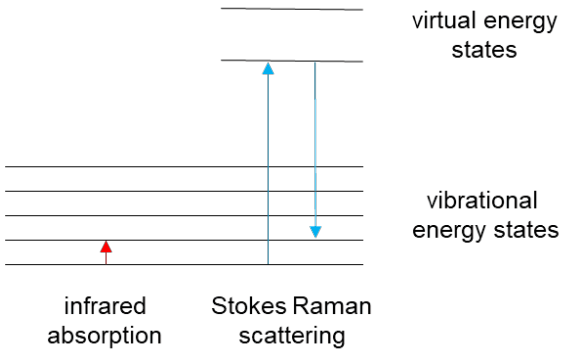

Figure 1.1: Schematic of infrared absorption and Stokes Raman scattering.

Table 1.4: Raman spectroscopy experimental parameters.

Instrument	inVia^{TM} Raman spectrometer (Renishaw)
Excitation wavelength	typically 785 nm (532 nm where noted)
Laser power density	typically $\leq$100 W/cm^2
Grating	1200 l/mm (2400 l/mm when 532 nm laser used)
Microscope objective	typically 50x (8.2 mm working distance)
Scan settings	3-second exposure time, 25+ accumulations
Range	typically 0–1200 cm^{-1}

Table 1.5: IR spectroscopy experimental parameters.

Instrument	Nicolet iS50 FTIR (Thermo Scientific) with ATR attachment
ATR crystal	Diamond
Scan settings	2-second exposure time, 32 accumulations
Range	650–4000 cm^{-1}

materials. For most of the Raman spectroscopy experiments, a 785 nm excitation laser and low laser power density (∼100 W/cm^2) were used throughout to avoid alteration of the studied material via laser heating, which was observed to occur for some samples at higher laser powers [90]. Samples were examined through a microscope objective, providing spatial resolution unlike bulk diffraction techniques. The Raman spectrometer used in this study is also capable of performing in situ studies with temperature and/or relative humidity control.

Where possible, Raman and IR spectra were fit to pseudo-Voigt functions with both Gaussian and Lorentzian components using the *LmFit* curve-fitting package in Python [121]. Prior to fitting, spectra were baseline corrected using the asymmetric least squares (ALS) approach [51, 52]. Due to significant peak overlap and a more complex background component, IR peak locations were more often identified by examining the first and second derivatives of the spectra than by peak fitting.

Multivariate curve analysis (MCR) was also used to analyze Raman datasets collected over time. MCR decomposes a set of time-resolved spectra into "pure" spectral components and the concentration profiles of each component. The MCR equation,

$$\mathbf{D} = \mathbf{C}\mathbf{S}^T + \mathbf{E}, \tag{1.2}$$

where $\mathbf{D}$ is the matrix of collected spectra, $\mathbf{S}$ is the matrix of component, "pure" spectra, $\mathbf{C}$ is the matrix of concentration profiles for each component, and $\mathbf{E}$ is the residual matrix, is solved iteratively using the alternating least squares (ALS) method. Calculations were performed with the MCR-ALS GUI 2.0 implemented in MATLAB [79, 78].

SEM-EDX

SEM-EDS was employed to provide elemental information. The principle of SEM is that an incident electron beam interacts with the sample and produces secondary and backscattered electrons that produce high resolution images of the sample and can provide morphological information. Detection of secondary electrons provides topographical information, while detection of backscattered electrons provides qualitative compositional information, since heavier elements backscatter electrons more strongly than light elements.

The incident electron beam also leads to the production of characteristic x-rays for the different elements in the sample, which are detected in EDS spectroscopy. These x-rays are produced because the electron beam excites electrons in the inner shells of atoms, creating electron holes that are then filled by electrons from higher energy outer shells. The excess energy of these electrons is released in the form of x-rays. This mechanism is shown in Figure 1.2. Because the electrons of different elements reside in different discrete energy levels, the energy of the released x-ray is characteristic of the atom it comes from. The EDS spectrum thus provides information about elements present in the sample. Table 1.6 shows experimental parameters for the SEM-EDS experiments described in this dissertation.

1.3.2 Computational techniques

Computational modeling was carried out to complement experimental studies. In particular, computational geometry optimization provides additional structural insight, such as the location of water atoms in crystal hydrates, which can be difficult to assess experimentally. Ab initio molecular dynamics simulations provide additional dynamic information about these water molecules and also allow for the prediction of vibrational spectra. These predicted spectra can be broken down by atomic components and the direction of movement, assisting in the interpretation of experimental spectra by comparison and allowing for the correlation of structural and vibrational properties. [90]

Density Functional Theory

While more accurate methods of calculating electronic structure and ground-state energies are feasible on smaller and less complex systems, the large number of electrons in solid-state uranium compounds limits the applicable computational method to Density Functional Theory (DFT). DFT can be applied to larger systems because it reduces the $4N$ variables ($3N$ spatial + N spin) required to calculate the electronic wavefunctions of an N atom system into just three variables that define the electron density (ρ) of the system. Since the external potential of a many-electron system is a unique functional of the electron density, the electron density uniquely determines the Hamiltonian and associated properties including the

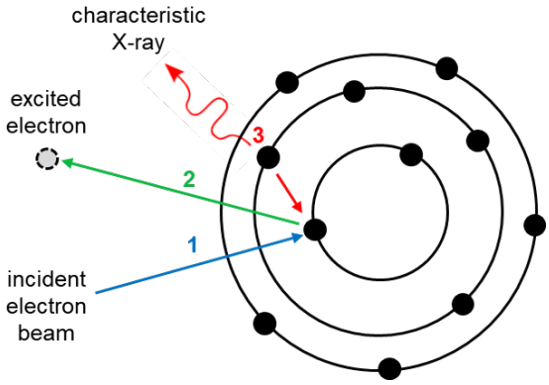

Figure 1.2: Schematic of energy dispersive x-ray spectroscopy. The incident electron beam excites an electron in a lower energy level, leaving a hole that is quickly replaced by a higher energy electron. The residual energy is released in the form of an x-ray, with an energy that is characteristic of the initial energy levels of the two electrons.

Table 1.6: SEM-EDS experimental parameters.

Instrument	Carl Zeiss MERLIN VP-SEM (Carl Zeiss)
Detector	XFlash detector 5030 (Bruker Nano GmbH)
Accelerating voltage	10 kV
Beam current	1.1 nA
Magnification	∼2000–8000x

ground-state energy. The energy functional, E_{KS}, contains three terms: the kinetic potential (T), classical Coulombic potential (J), and the electron–electron interaction (E), as shown below.

$$E_{KS}[\rho] = T[\rho] + J[\rho] + E[\rho] \tag{1.3}$$

The classical external potential of the system is well defined, as is the kinetic energy of the system assuming noninteracting electrons (T_s.) However, the residual of the true kinetic energy and the electron–electron functional are unknown. For simplicity, the energy functional can be rewritten to combine these unknown components into one term, the exchange-correlation energy, E_{xc}, as shown below.

$$E_{KS}[\rho] = T_s[\rho] + J[\rho] + E_{xc}[\rho] \tag{1.4}$$

This equation can be expanded as

$$E_{KS}[\rho] = \sum_i -\frac{1}{2} < \psi_i|\nabla^2|\psi_i > + \int \rho(\mathbf{r}) v_{ext}(\mathbf{r}) + \frac{1}{2}\int\int \frac{\rho(\mathbf{r})\rho(\mathbf{r'})}{|\mathbf{r}-\mathbf{r'}|} + E_{xc}[\rho], \tag{1.5}$$

where $\psi_i(\mathbf{r})$ are Kohn-Sham "orbitals". The electron density, $\rho(\mathbf{r})$, can be rewritten in terms of these "orbitals" as

$$\rho(\mathbf{r}) = \sum_i^N |\psi_i(\mathbf{r})|^2. \tag{1.6}$$

In a periodic system, the Kohn-Sham orbitals are typically expanded using a basis set of orthogonal plane waves,

$$\psi_i(\mathbf{r}) = \sum_{\mathbf{G}} c_i(\mathbf{G}) e^{i\mathbf{G}\cdot\mathbf{r}}, \tag{1.7}$$

where $\mathbf{G}$ is the reciprocal lattice vector.

From Equation 1.5, the Kohn-Sham orbitals satisfy the Kohn-Sham equation,

$$\left\{-\frac{1}{2}\nabla^2 + V_{KS}(\mathbf{r})\right\}\psi_i(\mathbf{r}) = \epsilon_i \psi_i(\mathbf{r}), \tag{1.8}$$

where V_{KS} is the ground-state Kohn-Sham potential.

Since the Kohn-Sham potential depends on the unknown electron density, $\rho(\mathbf{r})$, Equation 1.8 must be solved iteratively, beginning with an initial estimate of the electron density:

$$\rho^{initial} \rightarrow V_{KS}^{initial} \rightarrow \psi_{KS}^{initial} \rightarrow \rho^1 \rightarrow V_{KS}^1 \rightarrow \psi_{KS}^1 \rightarrow \rho^2 ... \tag{1.9}$$

This process is further complicated by the fact that E_{xc} is still unknown. However, it is at least constrained by the variational principle, which requires that the correct energy density is that which produces the lowest ground-state energy. Various approximations exist to describe E_{xc}, which can be expressed in terms of the exchange-correlation energy density as

$$E_{xc} = \int \epsilon_{xc}(\mathbf{r}). \tag{1.10}$$

The simplest approximation is the Local Density Approximation (LDA), which states that ϵ_{xc} at point $\mathbf{r}$ depends only on the density at that point. A more accurate description is the Generalized Gradient Approximation (GGA), which takes into account the derivatives of the density at point $\mathbf{r}$ as well. The GGA-type Perdew-Burke-Ernzerhof (PBE) functional [128] is used in this work. A second functional optimized to best account for dispersion forces, op!86b-vdW [91, 92], is used where appropriate to more accurately describe van der Waals interactions in crystal hydrates and layered structures.

DFT is used in this work to calculate optimized crystal structures as well as absorption energies of water molecules in crystal hydrates. Structural optimization was typically conducted using the conjugate-gradient algorithm. Following the first calculation, the ion positions (and/or cell parameters, if allowed) are moved in the direction of the calculated stress tensor. The energy and forces are then recalculated, and the minimum of the total energy is approximated via interpolation from the change in both total energy and forces. A corrector step to the approximate minimum is performed, and the forces are recalculated. This process is repeated until the minimization is sufficiently accurate, defined in this study as producing atomic forces <5 meV/atom. A more precise minimization, to <1 meV/atom, was utilized for Density Functional Perturbation Theory (DFPT) calculations, discussed in the next section. In instances where the starting atomic positions were unknown, i.e. the location of hydrogen atoms in crystal hydrates, damped molecular dynamics was used to

perform a preliminary optimization before beginning a more precise optimization via the conjugate-gradient algorithm.

DFT parameters were optimized for each calculation to produce convergent values. Typical parameters are summarized in Table 1.7. Uranyl hydrates are particularly complicated systems to study computationally due to the large unit cells, f electrons, mobile hydrogen-bonded water molecules, and van der Waals forces between polyhedra layers. These characteristics present challenges and can require correction factors. For example, accurate treatment of actinide compounds can sometimes require using the DFT+U method, which includes an extra intra-atomic interaction term in the energy functional to better account for localized d and f electrons, such that the new energy can be written as [5]

$$E_{DFT+U}[\rho(\mathbf{r})] = E_{DFT}[\rho(\mathbf{r})] + \sum_a \frac{\bar{U} - \bar{J}}{2} Tr(\rho_a - \rho_a^2), \tag{1.11}$$

where ρ_a is the orbital occupation matrix and $\bar{U}$ and $\bar{J}$ are semi-empirical parameters to describe the additional Coulomb and exchange interactions, respectively. For simplicity, these terms can be combined into a single effective +U parameter, $U_{eff} = \bar{U} - \bar{J}$ [49]. The +U correction was used where appropriate in this work, with U_{eff} set to 5.5 eV, which was shown to best reproduce the experimental parameters of anhydrous uranyl fluoride [88].

Density Functional Perturbation Theory

To complement experimental vibrational spectroscopy studies, Density Functional Perturbation Theory (DFPT) was used to calculate the predicted vibrational modes of systems of interest. This technique has been used in several recent studies of uranyl materials [20, 89, 40, 39, 38, 41] and is most appropriate for highly symmetric, static systems. For more complex, mobile systems, vibrational information was calculated from ab initio molecular dynamics (AIMD) simulations, described in the following section.

In the equilibrium geometry of the system, the forces acting on individual atoms equal zero:

$$F_i = -\frac{\partial E(R)}{\partial R_i} = 0. \tag{1.12}$$

Table 1.7: DFT parameters.

DFT implementation	VASP 5.4.4
Functional	PBE [128]/optB86b-vdW [91, 92]
Cut-off energy	typically 600 eV
Ionic optimization	conjugate-gradient algorithm damped molecular dynamics
Structural convergence	all forces <5 meV/atom (<1 meV for DFPT)

The vibrational frequencies of interest, ω, are determined by the eigenvalues of the Hessian matrix of the ground-state energy, also called the interatomic force constant matrix:

$$\det \left| \frac{1}{\sqrt{M_i M_j}} \frac{\partial^2 E(R)}{\partial R_i \partial R_j} - \omega^2 \right| = 0. \tag{1.13}$$

The Hessian can be rewritten in terms of the forces and then expanded by way of the Hellmann-Feynman theorem, which relates the derivative of the total energy with respect to a parameter to the expectation value of the derivative of the Hamiltonian with respect to that same parameter,

$$\frac{\partial^2 E(R)}{\partial R_i \partial R_j} = -\frac{\partial F_i}{\partial R_j} = \int \frac{\partial \rho(r)}{\partial R_j} \frac{\partial V(r)}{\partial R_i} dr + \int \rho(r) \frac{\partial^2 V(r)}{\partial R_i \partial R_j} dr + \frac{\partial^2 E_N(r)}{\partial R_i \partial R_j}. \tag{1.14}$$

Expanded in this manner, the above equation states that determination of the Hessian requires the calculation of the electron density, $\rho(r)$, as well as the linear response of the electron density to a geometric distortion, $\frac{\partial \rho(r)}{\partial R_j}$. For this reason, DFPT is also known as linear response theory. The electron density is solved via DFT as previously described. The linear response is solved using first-order perturbation theory [15].

Ab Initio Molecular Dynamics

Ab initio molecular dynamics (AIMD) simulations were used to both characterize dynamic information and calculate the vibrational properties of systems that cannot be adequately described using DFPT. Like classical molecular dynamics simulations, AIMD simulations involve the propagation of atoms over time based on a force field. In classical molecular dynamics, this force field is static and described by predefined interatomic potentials, which are generally empirically derived or determined from an electronic structure calculation. This method fails when interatomic interactions are particularly complex or change during the course of the simulation. In AIMD, the electronic variables are treated as active degrees of freedom. Instead of using predefined pair potentials, the full many-body potential is derived via DFT or other quantum mechanical methods. This study uses Born-Oppenheimer AIMD,

in which the electronic and ionic dynamics are decoupled due to a difference in timescale, and the static electronic structure is solved self-consistently at each time step.

All AIMD simulations were conducted in the canonical (NVT) ensemble using a Nosé-Hoover thermostat [125, 124, 72]. A slightly elevated temperature of 400 K was used in some cases to improve system convergence, while other calculations were run at room temperature (298.5 K). A 1 fs time step was used in order to capture the dynamics of crystallographic water molecules. These parameters and others are summarized in Table 1.8. The software package TRAVIS [22] was used to calculate radial distribution functions (RDFs), mean squared displacements (MSDs), and mass-weighted power spectra.

RDFs describe the probability of finding an observed particle a certain distance from a reference particle, relative to the uniform density of the observed particle:

$$g_{ab}(r) = \frac{V}{N_a \cdot N_b} \sum_{i=1}^{N_a} \sum_{j=i+1}^{N_b} \left\langle \delta \left(r - |\vec{r}_i(t) - \vec{r}_j(t)| \right) \right\rangle_t . \tag{1.15}$$

MSDs describe the average distance that a particle has moved away from its starting point within the time interval τ:

$$M(\tau) = \left\langle |\vec{r}_i(t+\tau) - \vec{r}_i(t)|^2 \right\rangle_{t,i} . \tag{1.16}$$

Power spectra contain the frequencies of all of the normal mode vectors and are calculated by Fourier transforming the sum of all velocity autocorrelation functions in the system or subsystem of interest:

$$P(\omega) = m \int \langle \dot{r}(\tau)\dot{r}(t+\tau) \rangle_\tau \, e^{-i\omega t} dt. \tag{1.17}$$

Prediction of vibrational spectra for molecules via AIMD has proved useful for demonstrating the effect of solvent influence, especially when hydrogen bonds form between the solvent and analyte [154]. Similarly, AIMD is a promising method for calculating the vibrational properties of solid-state uranyl hydroxide hydrates, which are characterized by strong hydrogen bonding interactions between the uranyl layers and interlayer water molecules that fluctuate over time [90].

Table 1.8: Ab initio molecular dynamics (AIMD) parameters.

DFT/AIMD implementation	VASP 5.4.4
Functional	PBE [128]/optB86b-vdW [91, 92]
Cut-off energy	typically 600 eV
Ensemble	canonical (NVT)
Temperature	298.5K / 400K
Time step	1 fs
Simulation length	15-20 ps

Chapter 2

Characterization of uranyl fluoride

This chapter presents a computational analysis of the structure and spectroscopic properties of the uranyl fluoride hydrate and clarifies the relationship between the hydrous and anhydrous phases of uranyl fluoride. Components of this chapter come from the following papers:

> A. Miskowiec, **M. C. Kirkegaard**, A. Huq, E. Mamontov, K. W. Herwig, L. Trowbridge, A. Rondinone, and B. B. Anderson. "Structural phase transitions and water dynamics in uranyl fluoride hydrates." *J. Phys. Chem. A* 2015, 119, 11900-11910.
>
> **M. C. Kirkegaard**, A. Miskowiec, M. W. Ambrogio, J. Langford, A. E. Shields, J. L. Niedziela, R. Kapsimalis, and B. B. Anderson. "Characterizing the chemical behavior of uranium compounds for nuclear forensics." Proceedings of the Institute for Nuclear Materials Management, 2018.

2.1 Previous studies of uranyl fluoride

Uranyl fluoride exists in the form of an anhydrous crystal and one or more crystal hydrates. Anhydrous uranyl fluoride (UO_2F_2) has a hexagonal layered structure, as shown in Figure 2.1, with $a = 4.206$ Å and $c = 15.69$ Å ($R\bar{3}m$) [174, 11]. The structure can alternatively be described by a rhombohedral unit cell with $a = 5.755$ Å and $\alpha = 42.5°$. Significant line

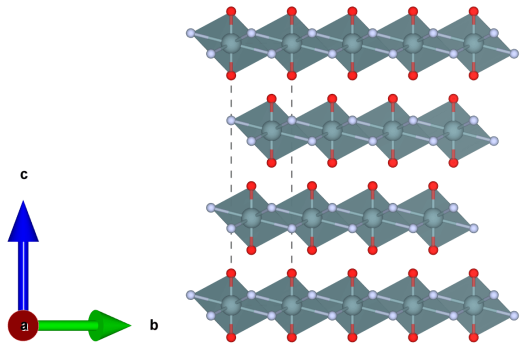

Figure 2.1: The structure of anhydrous uranyl fluoride, UO_2F_2, as solved by Zachariasen, shown in the hexagonal representation [174].

broadening in the XRD pattern of UO_2F_2 observed by both Zachariasen [174] and Atoji [11] is suggestive of stacking faults in the c direction.

Anhydrous uranyl fluoride is hygroscopic and has been observed to absorb some amount of water between the layers of uranyl polyhedra without inducing a significant change in the crystal structure [115, 102]. Measurements by Lychev et al. [102] showed a continuous mass increase in a sample of anhydrous uranyl fluoride exposed to increasing water vapor pressure up to 0.68 kPa, above which a discrete phase transition occurs. The mass increase before this phase transition corresponded to the absorption of 0.5 H_2O per uranium atom. The presence of water molecules in the anhydrous crystal structure was further explored by Miskowiec et al. [112], who used quasi-elastic neutron scattering (QENS) to probe the water dynamics in the species. The water content of a commercial sample of anhydrous uranyl fluoride was first assessed by dehydrating the material at 130°C. The observed mass loss corresponded to the loss of 0.46 H_2O/U, consistent with the previous findings of Lychev et al. Neutron diffraction showed that the initial partially hydrated material was isostructural with the dehydrated material, with both matching the Zachariasen structure for anhydrous uranyl fluoride (with significant line broadening as observed previously). The presence of water in the initial material was supported by the observation of a significant background contribution in the diffraction pattern due to the large incoherent cross section of hydrogen. This background contribution was significantly reduced for the dehydrated sample. The QENS data of partially hydrated sample could be modeled by spherically restricted diffusion, suggesting that water molecules reside in pockets between the uranyl polymerization units in the anhydrous structure. The presence of these water molecules was proposed to be at least partially responsible for the stacking disorder in the c direction [112].

While the precise amount of water that can be absorbed between the layers of anhydrous uranyl fluoride remains in question, multiple studies have found that above a threshold water vapor pressure (0.68 kPa, according to Lychev et al. [102]), a discrete phase transition occurs to produce a crystal hydrate [23, 102, 115]. The chemical formula of this hydrate has been reported to be between $UO_2F_2 \cdot 1.5\,H_2O$ and $UO_2F_2 \cdot 2\,H_2O$ [23, 102, 115]. Variation in the reported water content could indicate the formation of a hydrate capable of absorbing nonstructural water molecules. Alternatively, the existence of multiple distinct uranyl

fluoride hydrate species has also been proposed [104]. A lack of thorough characterization of the hydrate specie(s) leaves significant uncertainty as to the number of structures that can be formed from the hydration of uranyl fluoride as well as their attributes.

In 2001, the structure of a uranyl fluoride hydrate with the form $[(UO_2F_2)(H_2O)]_7 \cdot 4\,H_2O$ was solved by Mikhailov. This hydrate, shown in Figure 2.2, is monoclinic and belongs to the $C2/c$ space-group. The uranyl ion is pentagonally coordinated to four fluorine equatorial ligands and one water ligand. This hydrate was produced from the reaction of uranyl acetate dihydrate in excess n-perfluoropropoxy-1-perfluoropropionic acid [111]. Because this structure was not produced from anhydrous uranyl fluoride, it is not clear how this structure relates to the previously proposed uranyl fluoride hydrate structures. The water content of this structure, 1.57 H_2O/U, as well as the observed stability at ambient conditions, are both consistent with the previously proposed hydrates. As shown in Figure 2.3, the x-ray diffraction (XRD) pattern of the Mikhailov structure matches the reflections observed by Lychev et al. on a material believed to be uranyl fluoride dihydrate [102, 111].

Miskowiec et al. [114] sought to clarify the relationship between these species by collecting neutron diffraction data on a sample of anhydrous uranyl fluoride initially, after hydration at 40% relative humidity (RH) at ambient temperature, and after subsequent desiccation (Figure 2.4). The initial sample was consistent with anhydrous uranyl fluoride, UO_2F_2. Upon hydration and subsequent desiccation, anhydrous uranyl fluoride was observed to undergo a phase transition to form the Mikhailov hydrate structure, $[(UO_2F_2)(H_2O)]_7 \cdot 4\,H_2O$. A liquid-like intermediate with little long-range order was observed upon hydration prior to desiccation. Pair distribution function measurements showed that the uranyl ion is pentagonally coordinated in this intermediate, as in the hydrated structure, indicating that a change in coordination number from six to five occurs between the anhydrous and liquid-like intermediate [114].

Miskowiec et al. [114] also investigated the water content and thermal properties of the resulting uranyl fluoride hydrate via thermogravimetric analysis (TGA). The observed thermogram is shown in Figure 2.5 . The initial reduction in mass below 65°C was presumed to be due to the loss of surface-bound water. Between about 70 and 90°C another mass loss occurs, hypothesized to be due to the loss of the four hydrogen bonded water molecules per

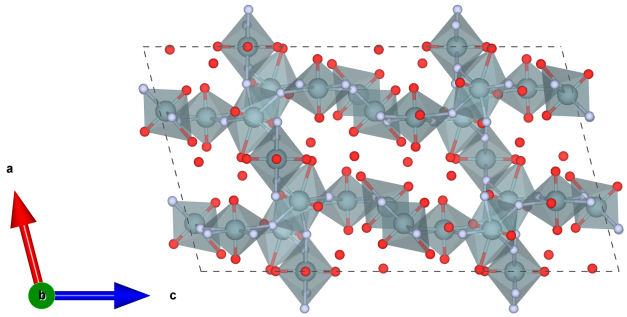

Figure 2.2: The structure of hydrated uranyl fluoride, $[(UO_2F_2)(H_2O)]_7 \cdot 4\,H_2O$, as solved by Mikhailov [111]. The four oxygen atoms in each pore correspond to water molecules. Additional water molecules are coordinated to the uranium atoms; hydrogen atoms have been omitted as their locations have not been determined experimentally.

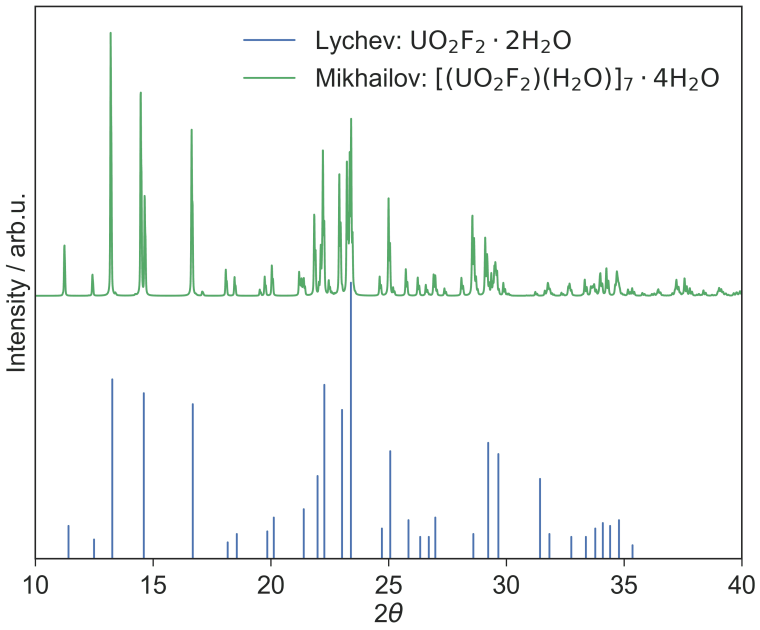

Figure 2.3: Comparison of the reflections reported for $UO_2F_2 \cdot 2\,H_2O$ by Lychev et al [102]. and of the XRD pattern of $[(UO_2F_2)(H_2O)]_7 \cdot 4\,H_2O$ as solved by Mikhailov [111]. In both cases, a Cu K_α sourced was used.

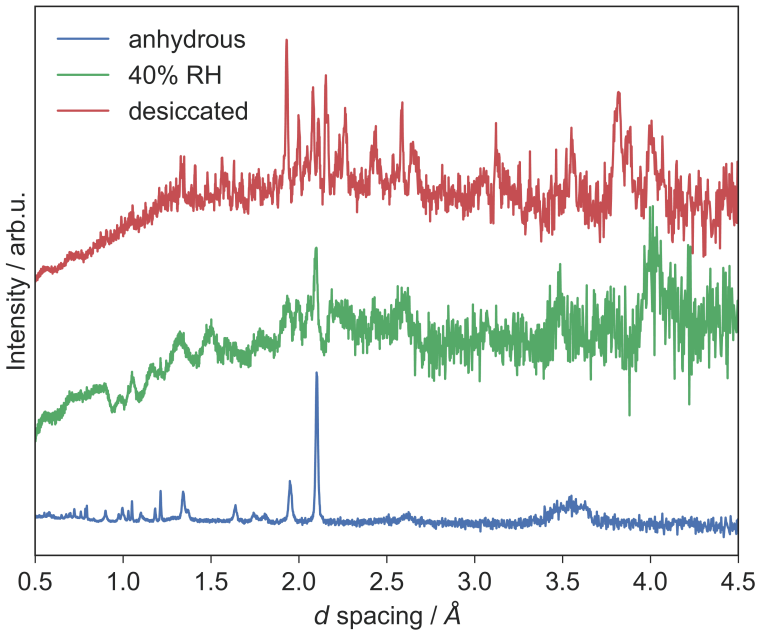

Figure 2.4: Neutron diffraction patterns of anhydrous uranyl fluoride initially, after exposure to 40% RH, and after subsequent dessication. The diffraction pattern after dessication matches that expected for $[(UO_2F_2)(H_2O)]_7 \cdot 4\,H_2O$, as solved by Mikhailov [111]. Data reproduced from Miskowiec et al. [114].

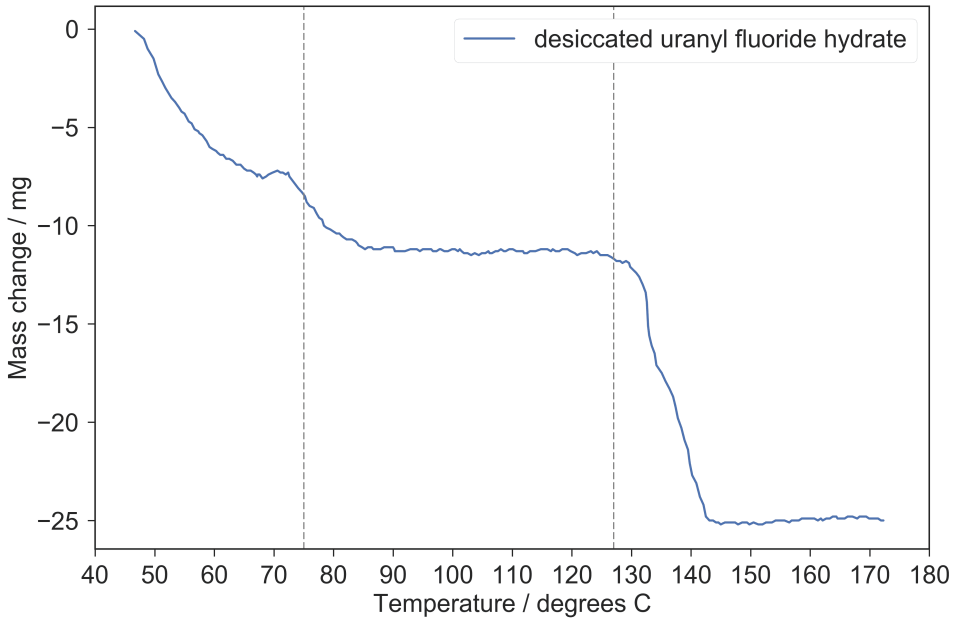

Figure 2.5: Thermogram of a 262.1 mg sample of uranyl fluoride that was hydrated at 40% RH and subsequently desiccated such that the diffraction pattern of the material matches that of the Mikhailov hydrate, $[(UO_2F_2)(H_2O)]_7 \cdot 4\,H_2O$. The temperature was ramped at 0.48°C against an Al_2O_3 standard under 100 mL/min Ar flow. Dashed lines at T = 70°C and 127°C indicate dehydration temperatures. Data reproduced from Miskowiec et al. [114].

unit cell that are present in the pores of the $[(UO_2F_2)(H_2O)]_7 \cdot 4\,H_2O$ structure as solved by Mikhailov. Finally, beginning at 127°C, a large mass loss occurs as the material is dehydrated to form anhydrous uranyl fluoride. No further mass loss was noted up to 170°C. Based on the mass loss over these transitions, the water content of the hydrate was calculated to be 1.65 H_2O/U, between the value of 1.57 H_2O/U as determined by Mikhailov [111] and 1.98 H_2O/U as determined by Lychev et al. [102] This discrepancy could indicate that the uranyl fluoride hydrate can absorb a variable number of water molecules. This theory is supported by additional QENS measurements by Miskowiec et al. that show that the water enters the uranyl fluoride crystal structure at a rate proportional to the water vapor pressure over at least an 80 hour timescale [113]. While the initial material in this study was anhydrous uranyl fluoride, subsequent dynamic rehydration experiments (described below) indicate that a transition to the hydrate structure likely occurred in the first hours of of the QENS hydration experiment, and that at least a portion of the increase in water intensity upon hydration can thus be assigned to absorption in the hydrate structure.

Observation of a two-step dehydration process for the uranyl fluoride hydrate was consistent with prior thermogravimetric analysis of uranyl fluoride hydrates. Both Lychev et al. [102] and Morato et al. [115] observed a small initial mass loss between 70 and 90°C prior to a large mass loss at 95-100°C corresponding to the formation of anhydrous uranyl fluoride. The lower dehydration temperature in these studies suggests that the uranyl fluoride hydrate analyzed may differ slightly in structure from the species characterized by Miskowiec et al. [114]. Additionally, Morato et al. found the dehydration reaction to be sensitive to the environmental water vapor pressure. While dehydration was observed to occur around 95°C in ambient air (40-80% RH), it was found to start at 80°C under vacuum and as low as 70°C under nitrogen. Additional shifting of some of the XRD peaks under vacuum and nitrogen that was not observed at ambient conditions, suggesting that water vapor pressure not only affects transition temperature, but also the mechanism of the phase transition [115].

2.2 Computational analysis of hydrated uranyl fluoride

2.2.1 Water structure and dynamics in hydrated uranyl fluoride

The structure and dynamics of water molecules that exist between the uranyl layers of anhydrous uranyl fluoride have been recently characterized in multiple publications by Miskowiec et al. [112, 113] Crystallographic water molecules are also present in the uranyl fluoride hydrate. The structure as solved by Mikhailov [111] includes four water molecules per unit cell that exist within the pores of the uranyl polyhedra framework, such that the H_2O/U ratio is 1.57. The location of hydrogen atoms of these water molecules has not been solved experimentally. Hydrogen atoms cannot be effectively analyzed via XRD, which is not sensitive to lighter elements. While neutron diffraction can often be used to identify hydrogen locations, the inability to do so for this structure [114] suggests that the water molecules may be disordered or dynamic.

Computational studies can help clarify the structure of the water molecules in the hydrate structure in the absence of an experimental determination. The unit cell of $[(UO_2F_2)(H_2O)]_7 \cdot 4\,H_2O$ was structurally optimized via Density Funcational Theory (DFT) using both the Perdew-Burke-Ernzerhof (PBE) [128] and op86b-vdW (vdW) [91, 92]) functionals (see Chapter 1 for more detail). The structure as solved experimentally by Mikhailov was used as the initial input for the structural optimization. Hydrogen atoms were added manually in reasonable locations. Both calculations were carried out in three steps. First, the location of the manually added hydrogen atoms was optimized while the other atoms were frozen in place. Then, the location of all atoms was optimized. Finally, the lattice parameters were relaxed along with the atomic positions. The final computationally optimized structures are shown in Figure 2.6.

A comparison of experimentally and computationally determined structural parameters is shown in Table 2.1. All of the lattice parameters as well as the average uranyl bond length are slightly overestimated relative to the experimental structure using the PBE functional (0.8–1.6%), leading to a 2.7% overestimation of the unit cell volume. Overestimation of bond lengths and lattice parameters is common for generalized gradient approximation (GGA) functionals like PBE [61]. The same overestimation of the uranyl bond length is observed

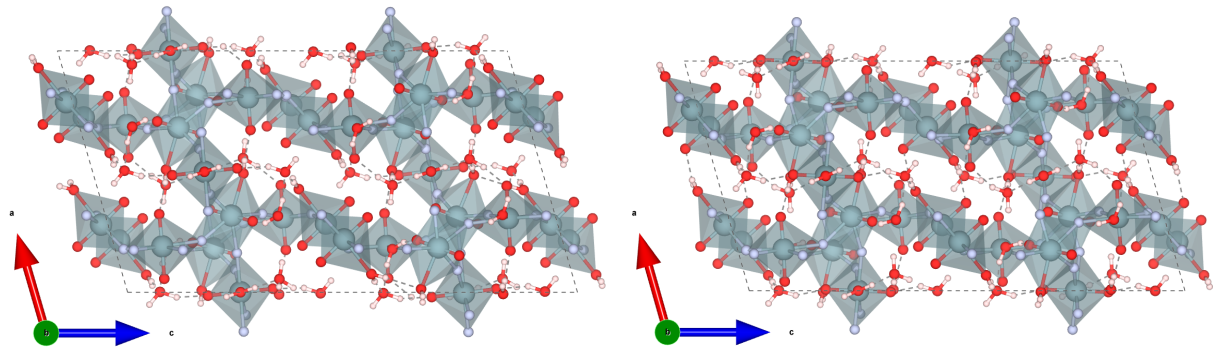

(a) **(b)**

Figure 2.6: (a) Unit cell of $[(UO_2F_2)(H_2O)]_7 \cdot 4\,H_2O$ with all atoms and cell parameters computationally optimized via DFT with the PBE functional. (b) Unit cell of $[(UO_2F_2)(H_2O)]_7 \cdot 4\,H_2O$ with all atoms and cell parameters computationally optimized via DFT with the vdW functional. Slight differences exist in the lattice parameters as well of the tilt of some uranyl polyhedra and the hydrogen bonding network formed by the water molecules.

Table 2.1: Comparison of experimentally determined and computationally optimized structural parameters of $[(UO_2F_2)(H_2O)]_7 \cdot 4\,H_2O$. Symmetry was not forced on the computationally optimized structures, leading to slight deviations in the α and γ angles. However, these deviations were $<0.008°$ from 90° and thus not reported.

	Exp [111]	DFT-PBE	DFT-vdW
a	13.843	14.068 (+1.6%)	13.373 (−3.4%)
b	9.801	9.910 (+1.1%)	9.823 (+0.2%)
c	24.970	25.160 (+0.8%)	24.448 (−2.1%)
β	104.470	106.206 (+1.7%)	105.818 (+1.3%)
V	3280.3	3368.1 (+2.7%)	3089.9 (−5.8%)
avg U=O	1.771	1.811 (+2.3%)	1.815 (+2.5%)
avg U−F	2.309	2.321 (+0.5%)	2.307 (−0.1%)
avg U−O_w	2.447	2.443 (−0.2%)	2.396 (−2.1%)

for the vdW functional as well, but the a and c lattice parameters are underestimated by 3.4 and 2.1%, respectively, leading to a more significant 5.8% underestimation of the volume. This is expected, as the vdW functional increases the strength of vdW interactions like hydrogen bonding, which leads to a contraction of the uranyl polyhedra towards the pore water molecules.

Despite these small differences, both DFT-optimized structures are relatively consistent with the experimental structure, as demonstrated by comparison of the predicted XRD pattern of each structure (Figure 2.7). Optimizing the location of the hydrogen atoms in the hydrate structure reveals an intricate hydrogen bonding network. Hydrogen bonds are formed between uranyl oxygens and pore water molecules, between pore water molecules and equatorially bound water molecules, and between equatorially bound water molecules and uranyl oxygens. These three different types of hydrogen bonds are illustrated in Figure 2.8.

Aspects of the hydrogen bonding network cannot be understood from examining the static structure of $[(UO_2F_2)(H_2O)]_7 \cdot 4\,H_2O$ since the water molecules have at least some limited rotational dynamics that cause fluctuations in the hydrogen bonding network. To better characterize the water dynamics and hydrogen bonding network, an ab initio molecular dynamics (AIMD) simulation was performed. The unit cell optimized with the vdW functional was used as the starting structure for this calculation. The optimized structure was evolved in 1 ps timesteps at 400K to accelerate equilibration. Following 5 ps of equilibration, an additional 20 ps of data was collected for analysis.

Calculation of the AIMD trajectory allows for additional characterization of the hydrogen bonding network. The average length of each of the three types of hydrogen bonding outlined in Figure 2.8 was determined by calculating the radial distribution function (RDF) between all hydrogen bond donors and acceptors. Figure 2.9 shows the average RDF for each type of hydrogen bond. Hydrogen bonds between uranyl oxygens and the hydrogens of pore water molecules are the shortest, normally distributed about 1.59 Å with a large variation. Hydrogen bonds of this type as short as 1.20 Å exist over the course of the simulation, suggesting that strong hydrogen interactions with uranyl oxygens could have a significant effect on the vibrational properties or reactivity of the uranyl ion in this system. Hydrogen bonds between uranyl oxygens and the hydrogens of equatorial bound water molecules

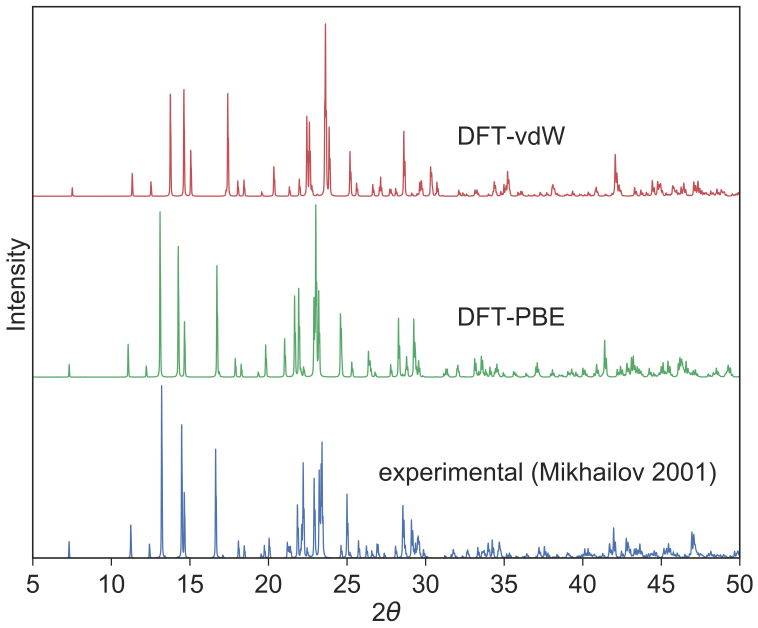

Figure 2.7: XRD patterns of the experimentally determined unit cell of $[(UO_2F_2)(H_2O)]_7 \cdot 4\,H_2O$ [111] and the DFT-optimized unit cell of $[(UO_2F_2)(H_2O)]_7 \cdot 4\,H_2O$, calculated with the PBE and vdW functionals.

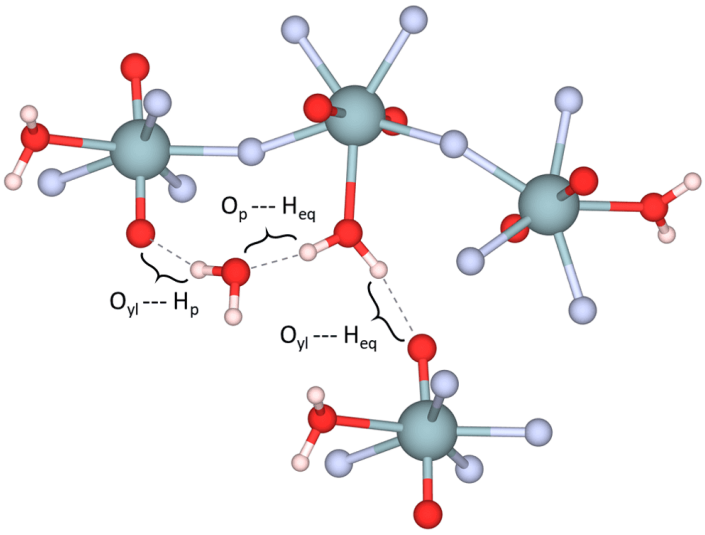

Figure 2.8: Subset of $[(UO_2F_2)(H_2O)]_7 \cdot 4\,H_2O$ structure demonstrating the three different types of hydrogen bonds formed in the hydrate.

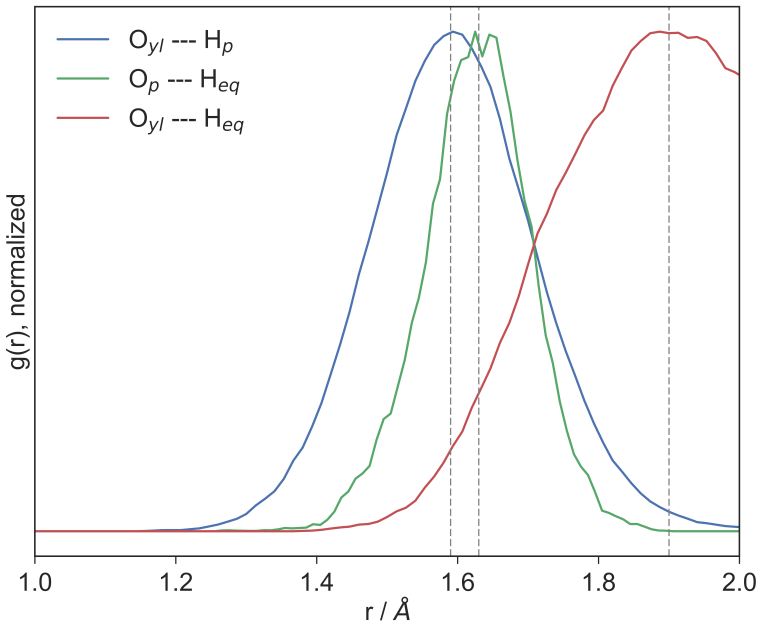

Figure 2.9: Average RDFs over the AIMD simulation depicting O–H lengths for each of the three different types of hydrogen bonds in the $[(UO_2F_2)(H_2O)]_7 \cdot 4\,H_2O$ structure. Each RDF is normalized to 1.0 to better compare the bond lengths. Dashed lines at x = 1.59, 1.63, and 1.90 Å show the most likely O_{yl}–H_p, O_p–H_{eq}, and O_{yl}–H_{eq} distance, respectively.

are slightly longer on average (1.63 Å), but more consistent in length. Hydrogen bonds between the oxygens of the pore water molecules and hydrogens of equatorial bound water molecules are significantly longer on average (1.90 Å). These hydrogen bonds can still be characterized as medium strength, however: hydrogen bonds between 1.2 and 1.5 Å are typically characterized as strong hydrogen bonds, 1.5–2.2 Å as medium hydrogen bonds, and 2.2+ Å as weak hydrogen bonds [147].

2.2.2 Vibrational characterization of hydrated uranyl fluoride

The calculation of the AIMD trajectory of hydrated uranyl fluoride also provides information about the vibrational properties of the structure. The vibrational properties of anhydrous uranyl fluoride were previously assessed using Density Functional Perturbation Theory (DFPT) [89], a static technique that works well for calculating the vibrational modes of rigid symmetric structures but does not adequately describe more mobile systems like uranyl hydrates [90]. Instead, the predicted power spectrum of $[(UO_2F_2)(H_2O)]_7 \cdot 4\,H_2O$ was calculated by Fourier transforming the velocity autocorrelation function obtained from the AIMD trajectory (see Chapter 1 for more details). This method has the benefit of better characterizing the influence of fluctuating hydrogen bonding interactions on the vibrational modes [90].

Calculation of the predicted power spectrum can provide insight into the vibrational spectrum of $[(UO_2F_2)(H_2O)]_7 \cdot 4\,H_2O$. The Raman spectrum of $[(UO_2F_2)(H_2O)]_7 \cdot 4\,H_2O$ has been well determined experimentally and is dominated by the symmetric uranyl stretching mode at 868 cm^{-1} which has a low-energy shoulder centered near 862 cm^{-1} (Figure 2.10) [89]. The presence of multiple uranyl stretching modes is not unexpected given the complexity of the crystal structure and multiple slightly variant uranyl ion environments. However, it is difficult to assign each peak component to specific uranyl ions from the experimental spectrum alone, motivating a computational comparison study.

Figure 2.11 shows the computationally determined power spectrum broken into atomic components. The symmetric uranyl stretching modes appear between 810 and 870 cm^{-1}. These modes can be distinguished from the infrared (IR) active asymmetric uranyl stretching

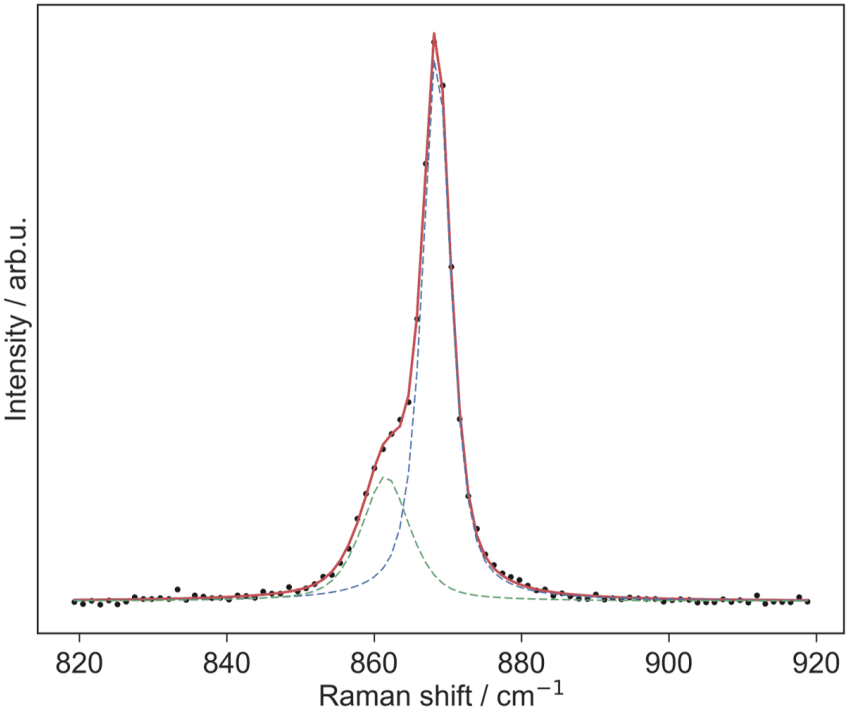

Figure 2.10: Uranyl stretching region of the Raman spectrum of $[(UO_2F_2)(H_2O)]_7 \cdot 4\,H_2O$ fit to two pseudo-Voigt curves centered at 868.5 and 861.6 cm^{-1}. The full-width-half-maximum of the curves are 4.3 and 7.2 cm^{-1}, respectively.

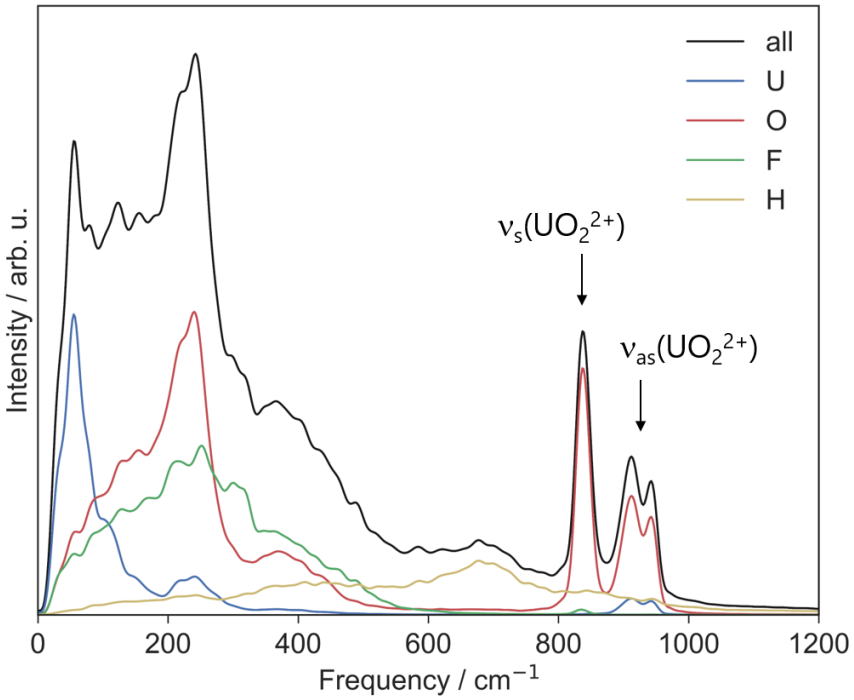

Figure 2.11: Power spectrum of $[(UO_2F_2)(H_2O)]_7 \cdot 4\,H_2O$, decomposed into atomic contributions and compared to the experimental Raman spectrum.

modes that exist at slightly higher energy because the latter involve the movement of the uranium atoms in addition to the uranyl oxygens.

The structure of $[(UO_2F_2)(H_2O)]_7 \cdot 4\,H_2O$ as determined by Mikhailov contains four symmetrically distinct uranyl ions (Figure 2.12) with slightly differing coordination environments. The most significant difference is that U1 uranyl ions are connected via double fluorine bridges (Figure 2.13a), while the rest of the uranyl ions are solely coordinated to single fluorine bridges (Figure 2.13b). The distinct environments of these uranyl ions leads to splitting of the uranyl stretching modes. As shown in Figure 2.14, the symmetric and asymmetric stretching modes of the U1 uranyl ions are higher in energy than the other uranyl ions.

The U2–4 uranyl ions have nearly identical equatorial planes, but the orientation of the uranyl ions results in distinct hydrogen bonding interactions with both equatorial and pore water molecules that further split the vibrational frequencies of the symmetric uranyl stretch. Differences in hydrogen bonding interactions to each type of uranyl ion are illustrated in Figure 2.15, where the $O_{yl}\cdots H_{water}$ RDF is shown for both pore and equatorially bound waters. U3 and U4 uranyl ions are characterized by strong hydrogen bonding to pore water molecules. U3 uranyl ions also form moderate hydrogen bonds with equatorially bound water molecules, while U4 uranyl ions do not. U1 and U2 uranyl ions have weak hydrogen bonding interactions with equatorially bound water molecules and even weaker interactions with the pore waters. The overall extent of hydrogen bonding can be characterized as U3>U4>U1$\simeq$U2. This explains the split in symmetric uranyl stretching frequency between U2, U3, and U4 uranyl ions.

While the four symmetrically distinct uranyl ions are predicted to have slightly different uranyl symmetric stretching frequencies, only two distinct peaks appear in the Raman spectrum: a dominant peak at 868 cm^{-1} with a weaker shoulder near 862 cm^{-1}. The computational analysis leaves some uncertainty as to whether these peaks can be attributed to U1 uranyl ions vs. U2+U3+U4 uranyl ions (separation based on equatorial environment) or U1+U2+U4 uranyl ions vs. U3 uranyl ions (separation based on hydrogen bonding). The stronger intensity of the higher energy peak seems to favor the latter, but a rigorous determination cannot be made. Slight variations in the location and intensity of the 862 cm^{-1}

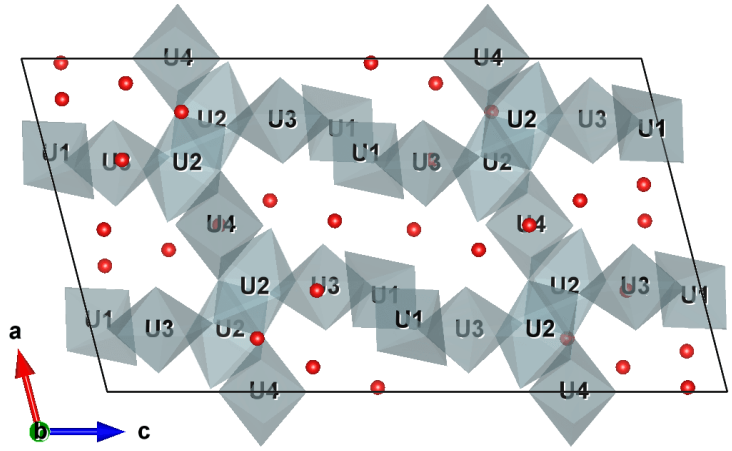

Figure 2.12: Symmetrically distinct uranyl ions labeled in $[(UO_2F_2)(H_2O)]_7 \cdot 4\,H_2O$. Atoms within the uranyl polyhedra have been omitted for clarity.

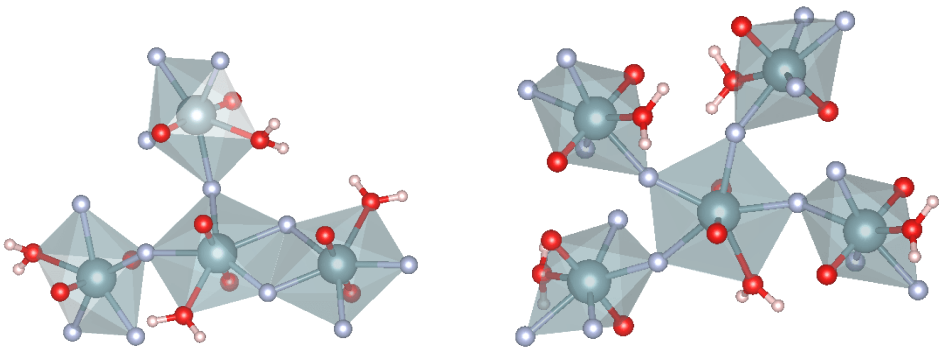

(a) **(b)**

Figure 2.13: (a) Equatorial bonding environment of U1 uranyl ions in the $[(UO_2F_2)(H_2O)]_7 \cdot 4\,H_2O$ structure. (b) Equatorial bonding environment of the U2–4 uranyl ions in the $[(UO_2F_2)(H_2O)]_7 \cdot 4\,H_2O$ structure.

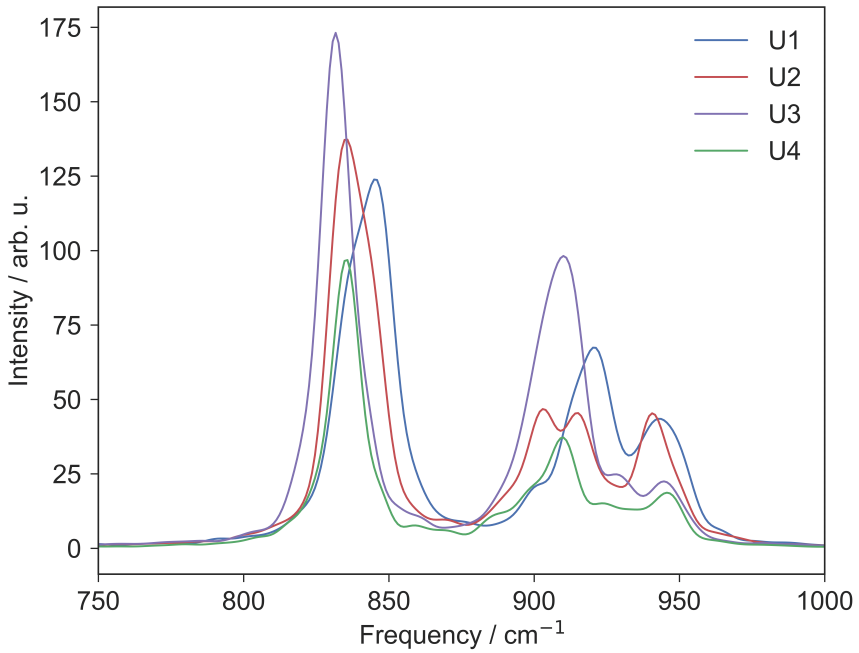

Figure 2.14: Uranyl stretching region of the power spectrum of $[(UO_2F_2)(H_2O)]_7 \cdot 4\,H_2O$, decomposed into contributions from each symmetrically distinct uranyl ion. Symmetric uranyl stretching modes (Raman-active) appear between 810 and 870 cm^{-1} while the asymmetric modes appear at slightly higher energy. The splitting of the asymmetric peaks for each uranyl ion occurs as a result of the slight bend in the uranyl ion in this structure. The U4 peaks are smaller, as there are half as many U4 uranyl ions in the $[(UO_2F_2)(H_2O)]_7 \cdot 4\,H_2O$ unit cell compared to the other types.

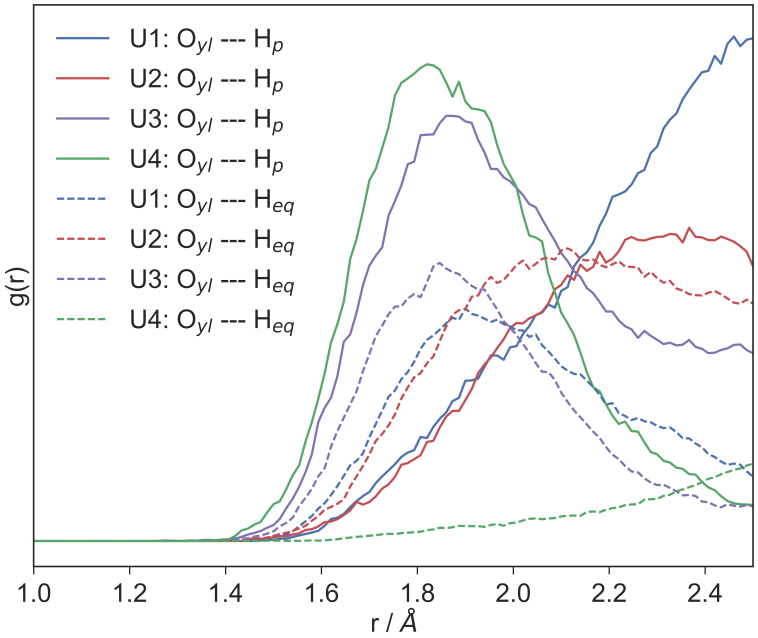

Figure 2.15: $O_{yl}\cdots H_{water}$ RDFs for pore and equatorially bound water molecules with respect to each symmetrically distinct uranyl ion in $[(UO_2F_2)(H_2O)]_7 \cdot 4\,H_2O$.

shoulder between batches of $[(UO_2F_2)(H_2O)]_7 \cdot 4\,H_2O$ (Figure 2.16) is also more consistent with observed splitting being due to hydrogen bonding interactions, which are more likely to vary if, as suggested by previous studies, the amount of crystallographic water in the uranyl fluoride hydrate is dependent on the synthesis and environmental conditions [112]. Further characterization work on this point is required.

2.3 Relationship between anhydrous and hydrated uranyl fluoride

The relationship between anhydrous and hydrated uranyl fluoride was clarified first by performing dynamic XRD and Raman spectroscopy experiments to characterize both the hydration of anhydrous uranyl fluoride and the dehydration of hydrated uranyl fluoride. Uranyl fluoride was prepared as previously published [113] through the hydrolysis of UF_6 ($UF_6 + 2\,H_2O \longrightarrow UO_2F_2 + 4\,HF$) in a reaction chamber containing approximately 20% RH at 23°C. Uranyl fluoride particulates were collected on silicon plates at the bottom of the chamber, and the harvested material was then baked under a steady flow of N_2 (10 ml/s) at 150°C for 18 hours. This methodology has been shown to produce anhydrous uranyl fluoride [113]. This material was then allowed to hydrate at ambient temperature and humidity (20–22°C, 20–50% RH) for several weeks. After this time, the material was confirmed to be $[(UO_2F_2)(H_2O)]_7 \cdot 4\,H_2O$ via powder XRD.

Samples of this material were prepared for dynamic XRD and Raman experiments. For the XRD experiment, a small amount of $[(UO_2F_2)(H_2O)]_7 \cdot 4\,H_2O$ powder was mixed with Si standard and deposited on a silicon XRD plate without the use of solvent. For the Raman experiment, a small amount of $[(UO_2F_2)(H_2O)]_7 \cdot 4\,H_2O$ powder was placed in an aluminum crucible. Both samples were analyzed using temperature stages with humidity control via RH generators.

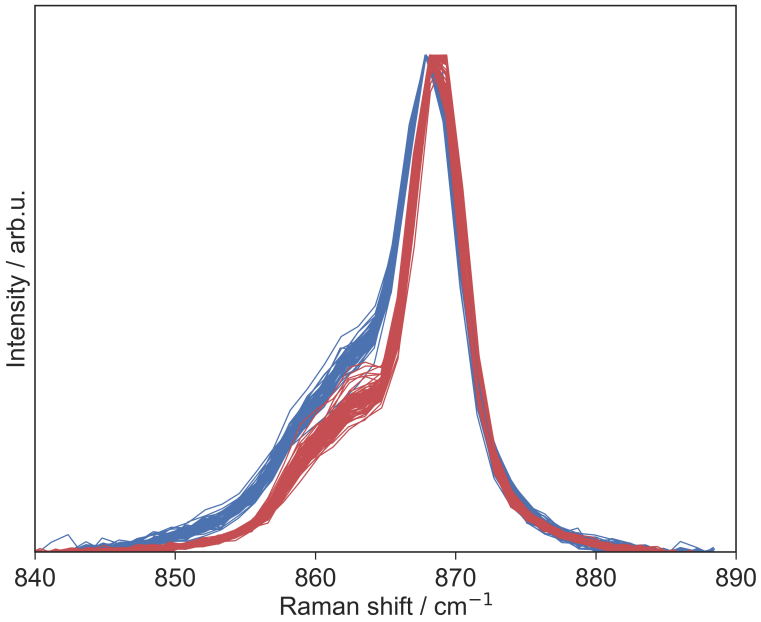

Figure 2.16: Comparison of the Raman spectra of different batches of $[(UO_2F_2)(H_2O)]_7 \cdot 4\,H_2O$ prepared by the same synthesis method.

2.3.1 In situ X-ray diffraction

Dehydration of hydrated uranyl fluoride

Figure 2.17 shows the XRD pattern of uranyl fluoride as $[(UO_2F_2)(H_2O)]_7 \cdot 4\,H_2O$ was heated from 30 to 130°C in 10°C increments while under a steady flow of dry air (<5% RH). Each XRD pattern was collected over approximately 2 hours after the sample had equilibrated for 30 minutes at each temperature. The temperature was ramped at 1°C/min between set points. The initial material has an XRD pattern consistent with that of $[(UO_2F_2)(H_2O)]_7 \cdot 4\,H_2O$, with the exception of an extraneous peak at $2\theta = 12.7°$ that cannot be assigned and is presumably a contaminant or other instrumental artifact. This peak does not move as the sample was heated and does not obscure the phase transition to anhydrous uranyl fluoride (UO_2F_2) that occurs between 100 and 110°C. This transition temperature was found to be slightly lower than previously determined via TGA [112] and dynamic Raman spectroscopy [89], which could be due to slight structural differences in the starting material. Previous Raman measurements were also conducted under ambient humidity, and a significant effect of humidity on the phase transition has been previously characterized [115, 112].

The anhydrous UO_2F_2 produced by heating $[(UO_2F_2)(H_2O)]_7 \cdot 4\,H_2O$ has very broad XRD peaks, consistent with prior observations of this material [174, 11, 115, 112]. The broadness of the peaks has been interpreted as indicative of stacking disorder in the c direction, due in part to the presence of strongly hydrogen-bonded water molecules between the layers of the anhydrous structure [114]. The anhydrous UO_2F_2 produced in this experiment has an expanded interlayer spacing compared to the structure solved by Zachariasen [174], as indicated by the location of the (003) reflection. This reflection appears at $2\theta = 16.70°$ rather than $2\theta = 16.94°$, as observed by Zachariasen, corresponding to an interlayer spacing of 5.3 Årather than 5.23 Å. It is plausible that the presence of interlayer water molecules expands the layer spacing, and that the layer spacing would have been observed to shrink slightly upon heating to a higher temperature.

Prior to the phase transition, minor changes are noted in the XRD pattern between 60 and 100°C. These minor shifts are better visible by overlaying the XRD patterns, as

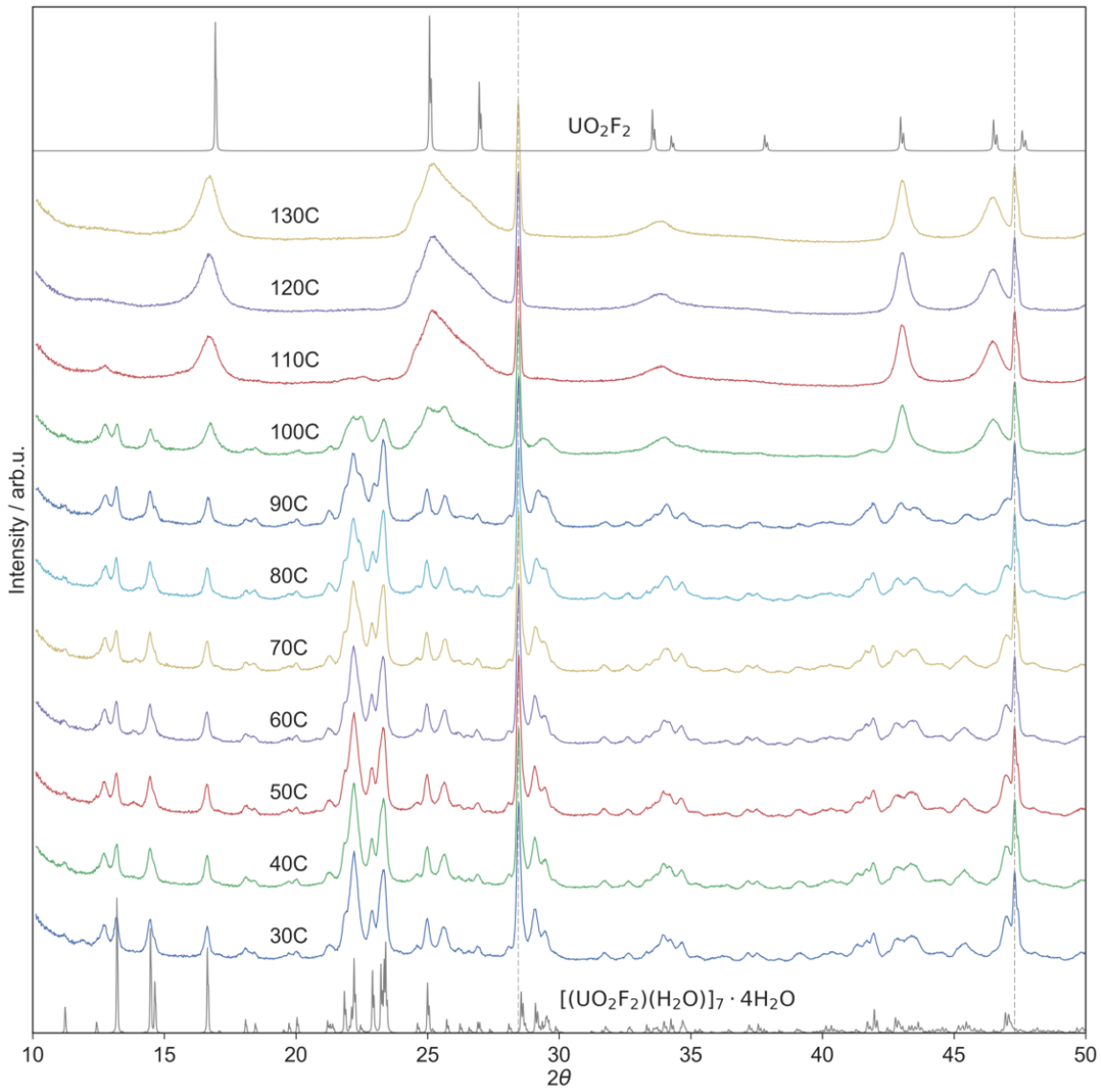

Figure 2.17: XRD pattern of a sample of uranyl fluoride hydrate at increasing temperature. The expected patterns of $[(UO_2F_2)(H_2O)]_7 \cdot 4\,H_2O$ [111] and anhydrous UO_2F_2 [174] are shown for comparison. Dashed lines at $2\theta = 28.443°$ and $47.303°$ correspond to the Si standard added to the sample.

shown in Figure 2.18. The slight changes in the XRD pattern above 60°C are consistent with previously collected TGA data (Figure 2.5), which showed a small mass reduction between 70 and 90°C, corresponding to the loss of the hydrogen-bonded water molecules in the pores of the structure. Because these water molecules are not directly bound to the $[(UO_2F_2)(H_2O)]_7$ backbone, their removal is not expected to have a significant effect on the structure.

The structural effect of losing these water molecules can be further analyzed by examining the resulting diffraction maxima shift or change in intensity. The most notable changes in the XRD pattern occur near $2\theta = 22°$ and near $2\theta = 29°$. Figure 2.19 further examines these regions. As shown in Figure 2.19a, the $(22\bar{1})$ reflection is observed to decrease in intensity, while the (220) reflection shifts slightly. The (115) is also observed to shift, although not until 80°C. The shift in the (314) reflection, shown in Figure 2.19b, is more similar to that of the (220) reflection, starting at 70°C. These shifts are consistent with a buckling of the fluorine ligands in the $[(UO_2F_2)(H_2O)]_7 \cdot 4\,H_2O$ structure, suggesting that removal of the pore water molecules allows for a slight rearrangement of the fluorine ligands as they start to move into the staggered orientation observed in the anhydrous structure (Figure 2.1).

Hydration of anhydrous uranyl fluoride

After ramping the temperature to 130°C, the temperature was reduced back to 30°C at 1°C/min while continuing to expose the sample to a flow of dry air to prevent rehydration. Once the sample had cooled, rehydration of the anhydrous product was examined by increasing the water vapor pressure. Due to a malfunction of the RH generator, the precise water vapor pressure during this rehydration experiment is unknown. However, the rate of rehydration was observed to be consistent with rehydration experiments at 40–50% RH relative to 30°C, or a water vapor pressure of 1.70–2.13 kPa. Changes in the XRD pattern upon rehydration are shown in Figure 2.20. The rehydrated structure is nominally consistent with the Mikhailov hydrate, $[(UO_2F_2)(H_2O)]_7 \cdot 4\,H_2O$. However, slight differences are noticed between the pattern of the initial sample prior to dehydration and the pattern of the hydrated material, which are illustrated more clearly in Figure 2.21. The most significant differences are the disappearance of the peak at $2\theta = 12.7°$ attributed to a contaminant, and the growth

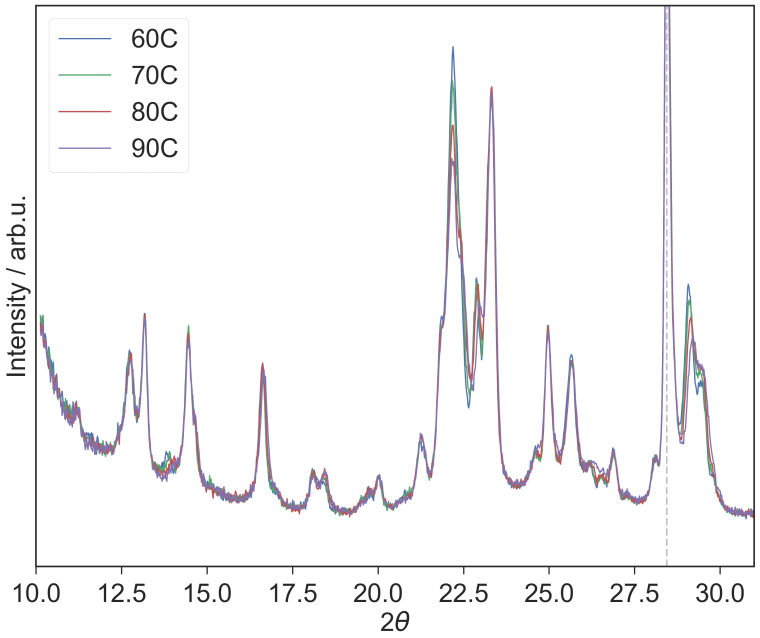

Figure 2.18: XRD pattern of a sample of uranyl fluoride hydrate at increasing temperature. The dashed line at $2\theta = 28.443°$ corresponds to the Si standard added to the sample.

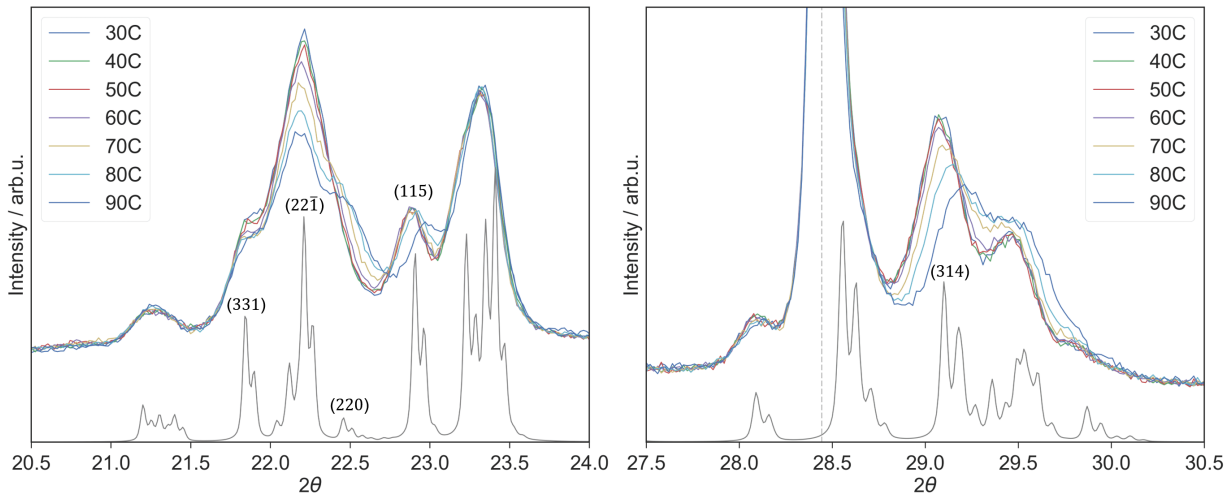

Figure 2.19: Two regions of the XRD pattern of a sample of uranyl fluoride hydrate at increasing temperature. The dashed line at $2\theta = 28.443°$ corresponds to the Si standard added to the sample.

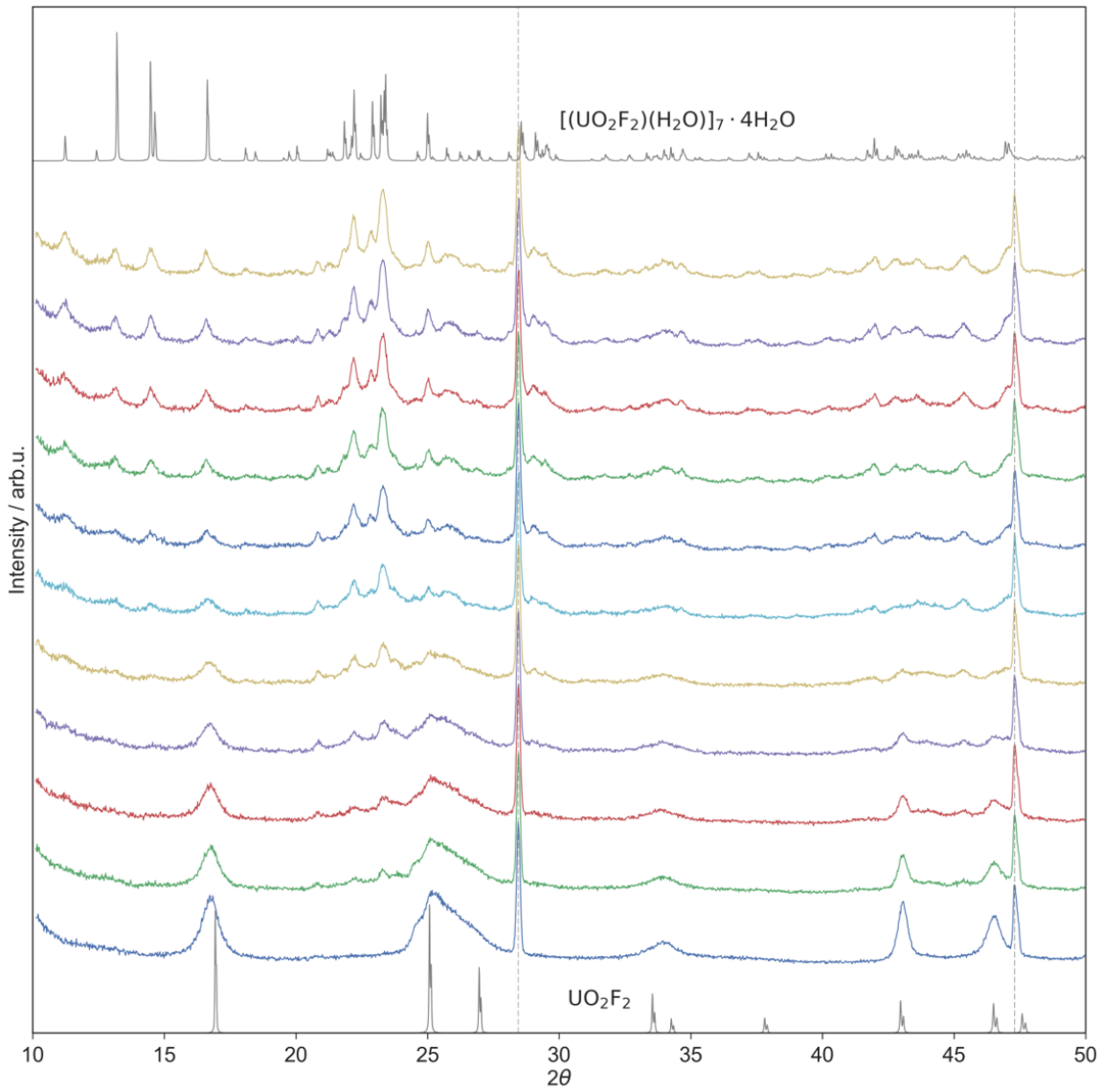

Figure 2.20: XRD pattern of a sample of anhydrous uranyl fluoride exposed to increasing RH at 30°C. The sample of anhydrous uranyl fluoride was produced by heating $[(UO_2F_2)(H_2O)]_7 \cdot 4\,H_2O$ to 30°C and cooling under dry air. The expected patterns of $[(UO_2F_2)(H_2O)]_7 \cdot 4\,H_2O$ [111] and anhydrous UO_2F_2 [174] are shown for comparison.

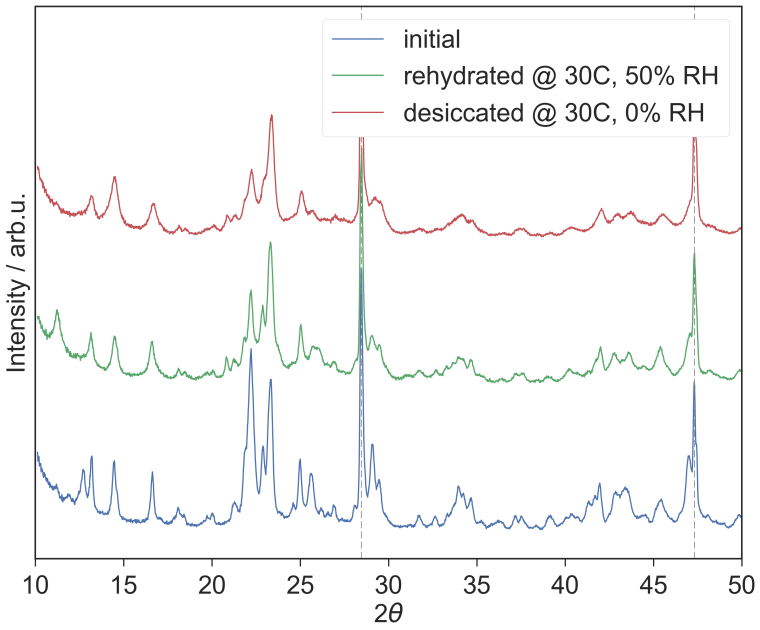

Figure 2.21: Comparison of the XRD pattern of a sample of $[(UO_2F_2)(H_2O)]_7 \cdot 4\,H_2O$ initially, after dehydration at 150°C and rehydration for 70 hours at 50% RH/30°C, and after an additional 22 hours of desiccation at 0% RH/30°C.

of a peak at 2θ=11.2°, which may correspond to either the same contaminant or the (110) reflection of $[(UO_2F_2)(H_2O)]_7 \cdot 4\,H_2O$. Replication of this experiment is required to elucidate this.

Miskowiec et al. [114] observed a liquid-like intermediate upon hydration of anhydrous uranyl fluoride at 40% RH at ambient temperature. Subsequent desiccation was required to convert this intermediate into $[(UO_2F_2)(H_2O)]_7 \cdot 4\,H_2O$. It is therefore plausible that the rehydrated material in this study is similarly an intermediate structure, although the diffraction data suggests that it is much more crystalline than the previously observed intermediate. To assess this possibility, after hydrating for 70 hours, the sample was desiccated under a steady flow of dry air while continuing to collect XRD data. As shown in Figure 2.21, slight changes in the XRD pattern were observed, including the disappearance of the peak at $2\theta = 11.2°$. Thus, it remains unclear how the previous observance of a liquid-like intermediate connects with these results.

2.3.2 In situ Raman spectroscopy

Dehydration of hydrated uranyl fluoride

In situ Raman spectroscopy also proved useful for studying these dehydration and rehydration transitions, since anhydrous and hydrated uranyl fluoride can be easily distinguished via Raman spectroscopy. The Raman-active uranyl symmetric stretching mode is highly sensitive to the environment of the uranyl ion (i.e., number and type of equatorial ligands) [27, 122, 47, 100] and thus appears at a distinct frequency in anhydrous and hydrated uranyl fluoride. Raman spectra collected on samples of anhydrous and hydrated uranyl fluoride were in agreement with past studies [6, 87, 132], with the Raman-active uranyl stretching mode appearing at 915 and 868 cm^{-1}, respectively (Figure 2.22).

Raman data were collected on a sample of $[(UO_2F_2)(H_2O)]_7 \cdot 4\,H_2O$ as the sample was heated from 30°C to 130°C under a steady flow of dry air (<5% RH). The temperature was ramped at 1°C/min while spectra were collected continuously in 1 min increments. The microscope was refocused every 10°C without causing a significant gap in the data collection. Data were collected using the 532 nm laser because a large fluorescence background

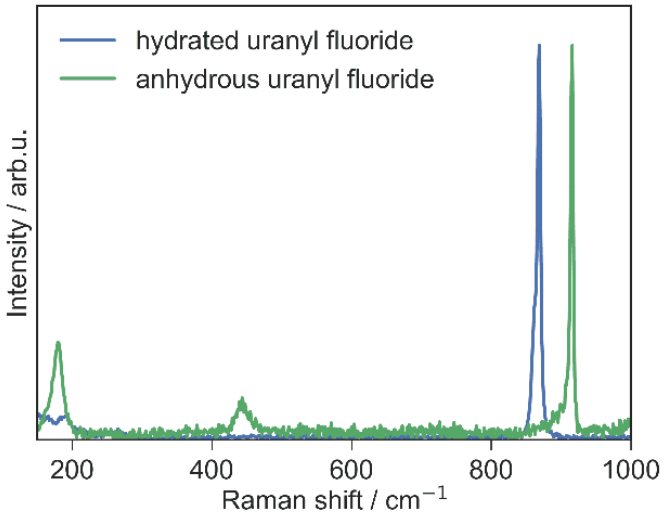

Figure 2.22: Characteristic Raman spectra of anhydrous uranyl fluoride (UO_2F_2) and hydrated uranyl fluoride ($[(UO_2F_2)(H_2O)]_7 \cdot 4\,H_2O$).

component was visible with the 785 nm laser at higher temperature. Figure 2.23 shows the changes in the Raman spectrum as the temperature was increased. A discrete phase transition from $[(UO_2F_2)(H_2O)]_7 \cdot 4\,H_2O$ to anhydrous UO_2F_2 occurred around 110°C, as evidenced by the disappearance of the uranyl stretching mode of $[(UO_2F_2)(H_2O)]_7 \cdot 4\,H_2O$ at 868 cm^{-1}, and the appearance of the uranyl stretching mode of UO_2F_2 at 915 cm^{-1}. The noted transition temperature is in agreement with the dynamic XRD data.

Because the uranyl stretching peaks of hydrated and anhydrous uranyl fluoride can be fully resolved, the relative heights of these peaks can be used to assess the progression of the phase transition. Figure 2.24 shows the normalized relative intensities of the two peaks over time during the temperature ramp. The phase transition occurs fairly rapidly when the transition temperature is reached. The transition temperature is again lower than previously reported [89], potentially because previous Raman temperature ramps were conducted under ambient humidity. To further assess the effect of humidity on the dehydration transition, additional temperature ramps were conducted using the same settings, but under an increased water vapor pressure of 0.85, 1.70, or 2.13 kPa (20%, 40%, and 50% RH relative to 30°C, respectively). Figure 2.25 shows the fraction of anhydrous UO_2F_2 in the sample as the temperature was increased, as measured by the intensity of the 915 cm^{-1} peak of UO_2F_2 relative to the 868 cm^{-1} peak of $[(UO_2F_2)(H_2O)]_7 \cdot 4\,H_2O$. The transition temperature increases with increased water vapor pressure. While the phase transition was noted to begin at approximately 101°C at 0.21 kPa, it does not start until 110°C at 0.85 kPa and 118°C at 1.70 and 2.13 kPa. This dependence on the environmental humidity is consistent with the previous findings of Lychev et al. [102].

Returning to Figure 2.23, it is clear that there is a slight shift in the uranyl stretching mode of the uranyl fluoride hydrate prior to the dehydration transition. This shift is more noticeable when expanding the uranyl stretching region of the spectrum, as shown in Figure 2.23b. In addition to a shift upwards, the peak is observed to broaden. This is better illustrated in Figure 2.26a, which shows the Raman spectra collected every 10°C overlaid on top of one another. The uranyl stretching mode begins to broaden slightly as low as 40–50°C, but significant broadening and a shift in frequency begin to occur at 70-80°C. This is the same temperature at which slight changes in the XRD pattern were noted,

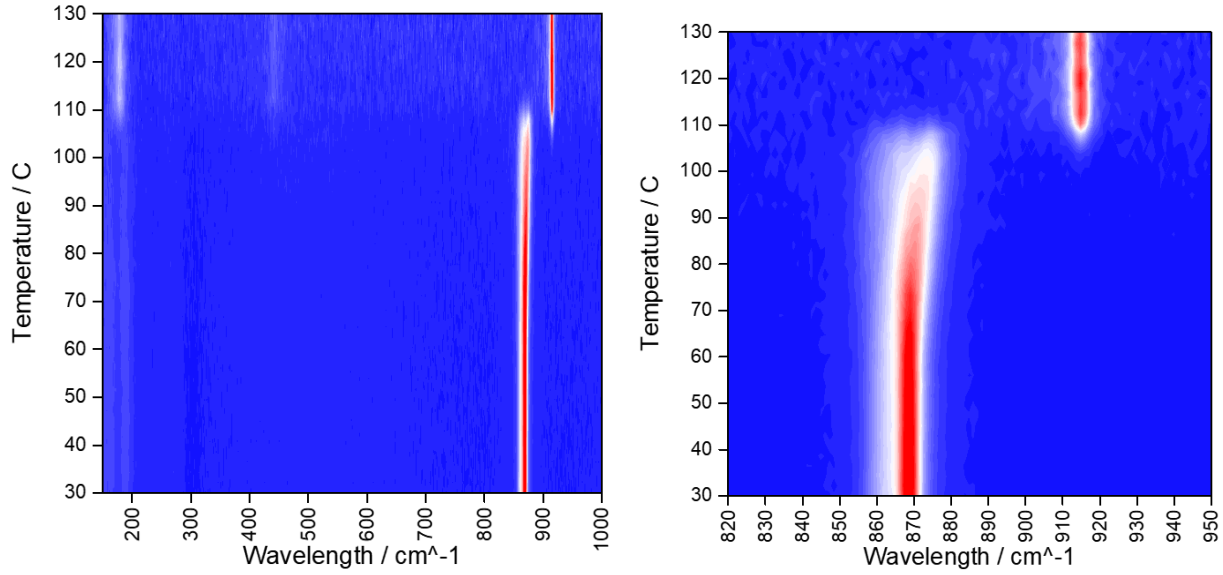

(a) **(b)**

Figure 2.23: (a) Waterfall plot showing changes in the Raman spectrum of uranyl fluoride as the sample temperature was ramped from 30°C to 130°C. Each spectrum was normalized independently to the sum of the areas of the $[(UO_2F_2)(H_2O)]_7 \cdot 4\,H_2O$ and UO_2F_2 uranyl stretching peaks at 868 and 915 cm^{-1}, respectively. (b) Expanded view of the uranyl stretching region of the same plot.

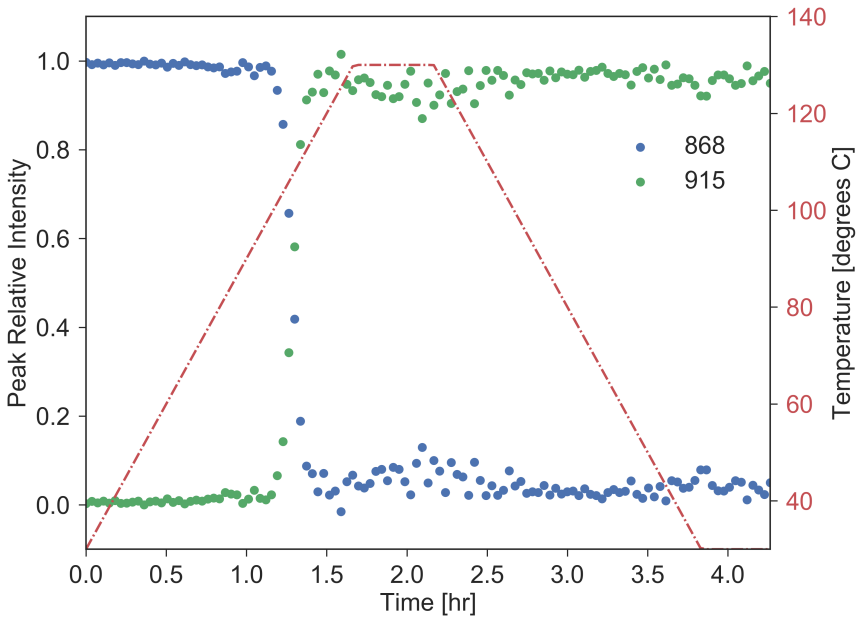

Figure 2.24: Normalized relative intensity of the uranyl stretching peak of hydrated uranyl fluoride (blue) and anhydrous uranyl fluoride (green) over time as the sample temperature was ramped from 30°C to 130°C and then cooled to 30°C. The dashed red line corresponds to the temperature over time. A transition from hydrated to dehydrated uranyl fluoride was observed to occur at approximately 110°C.

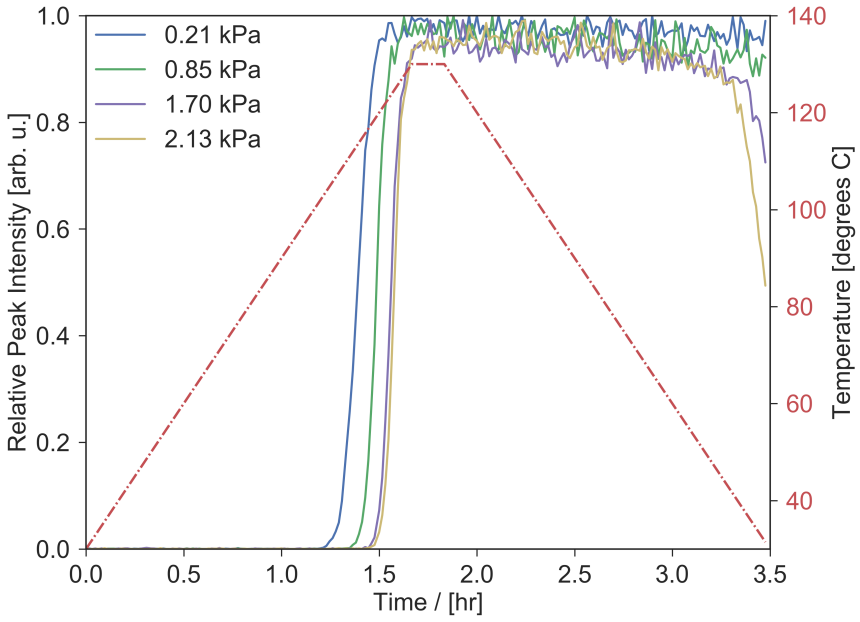

Figure 2.25: Fraction of UO_2F_2 present in a sample of uranyl fluoride, as measured by the intensity of the 915 cm^{-1} peak of UO_2F_2 relative to the 868 cm^{-1} peak of $[(UO_2F_2)(H_2O)]_7 \cdot 4\,H_2O$, at increasing temperature under four different water vapor pressures: 0.21, 0.85, 1.70, and 2.13 kPa, corresponding to 5%, 20%, 40%, and 50% RH at 30°C, respectively.

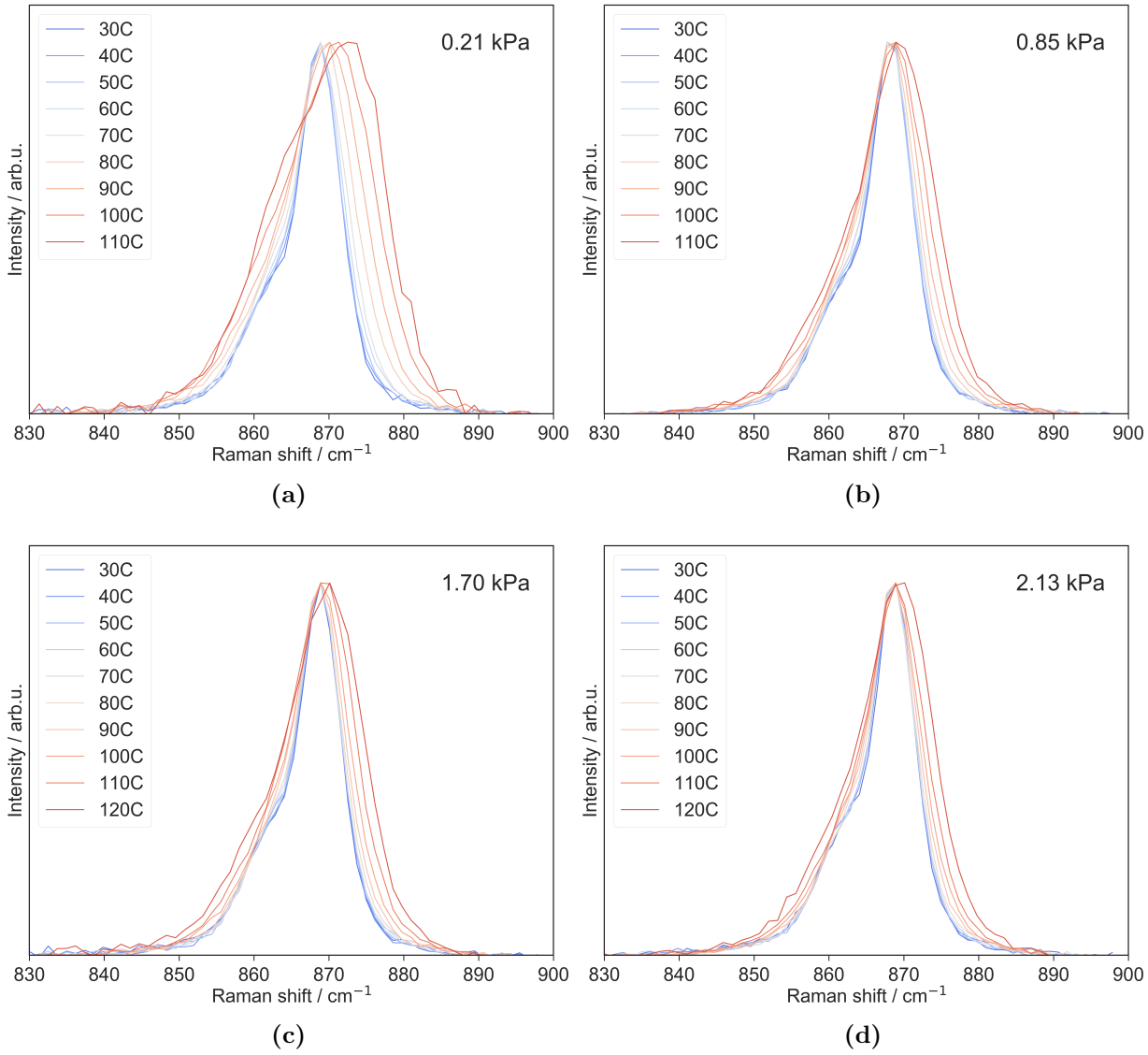

Figure 2.26: Raman spectrum of $[(UO_2F_2)(H_2O)]_7 \cdot 4\,H_2O$ at increasing temperature under a water vapor pressure of (a) 0.21 kPa, (b) 0.85 kPa, (c) 1.70 kPa, and (d) 2.13 kPa, corresponding to 5%, 20%, 40%, and 50% RH at 30°C, respectively. All spectra have been independently scaled to 1 for easier comparison of the broadening effect.

suggesting that these observations are correlated, and that the broadening and shifting of the uranyl stretching peak in the Raman spectrum is also related to the loss of hydrogen bonded water molecules in the pores of the $[(UO_2F_2)(H_2O)]_7 \cdot 4\,H_2O$ structure. The redshift of the peak is consistent with a strengthening of the uranyl bond due to the removal of water molecules that form hydrogen bonds with the uranyl oxygens. The broadening may be indicative of a decrease in crystallinity, [85] consistent with the buckling of fluorine ligands identified from the dynamic XRD data.

Interestingly, as shown in Figures 2.26b–2.26d, the shift and broadening of the uranyl stretching peak is much less pronounced for the temperature ramps conducted under higher water vapor pressure. The magnitude of the frequency shift in each of the four experiments was compared by fitting the uranyl stretching mode to two psuedo-Voigt functions at each time step. At ambient temperature, the uranyl stretching mode fits to two peaks centered at 869 cm^{-1} and 862 cm^{-1}. The frequency of the dominant higher energy peak is plotted in Figure 2.27 with increasing temperature. At 0.21 kPa, the peak shifts from 868.9 to 872.6 cm^{-1} before the transition to anhydrous uranyl fluoride occurs. At higher water vapor pressure, however, the peak only shifts to 870–870.5 cm^{-1} before the transition. It is unclear why the initial frequency of the uranyl stretching mode is slightly lower to start at 0.85 kPa than for the other three experiments. This may be indicative of a slightly different initial water content or other small structural deviation.

Hydration of anhydrous uranyl fluoride

As in the dynamic XRD experiment, the Raman sample was cooled back to 30°C after dehydration under a steady flow of dry air to prevent rehydration. To monitor the rehydration process via Raman spectroscopy, the humidity was increased to 50% RH after the sample had cooled to 30°C and been equilibrated for 12 hours. As shown in Figure 2.28, rehydration was found to occur readily at this humidity, and the UO_2F_2 uranyl stretching mode at 915 cm^{-1} was quickly replaced by a peak at 868 cm^{-1}, characteristic of the hydrated structure. No further changes were observed in the Raman spectrum as the sample was hydrated for 17 hours while scanning continuously. As with the dynamic XRD data, differences were noted in the Raman spectrum of the hydrated material initially and post

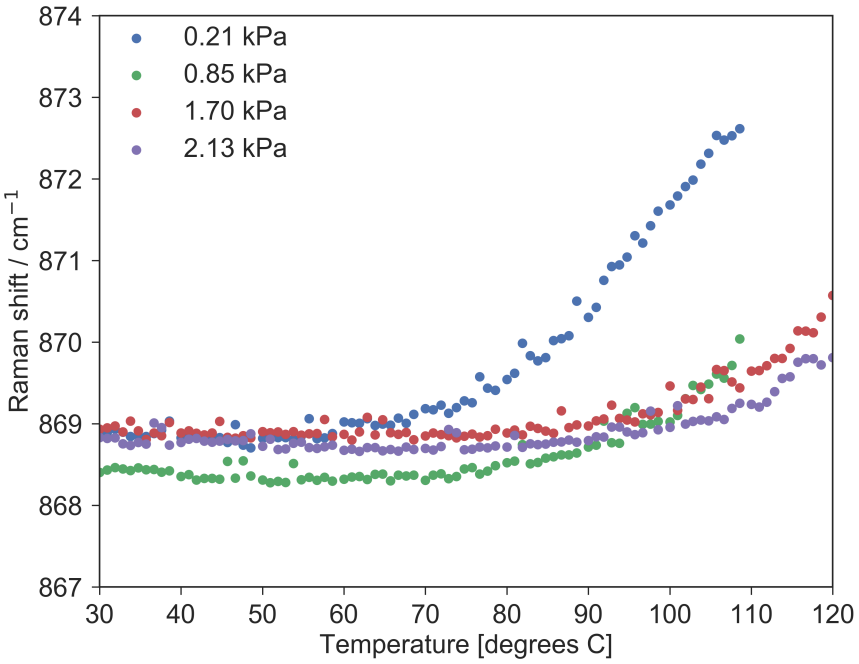

Figure 2.27: Frequency of the dominant uranyl stretching mode in the Raman spectrum of $[(UO_2F_2)(H_2O)]_7 \cdot 4\,H_2O$ with increasing temperature under four water vapor pressures: 0.21, 0.85, 1.70, and 2.13 kPa, corresponding to 5%, 20%, 40%, and 50% RH at 30°C, respectively.

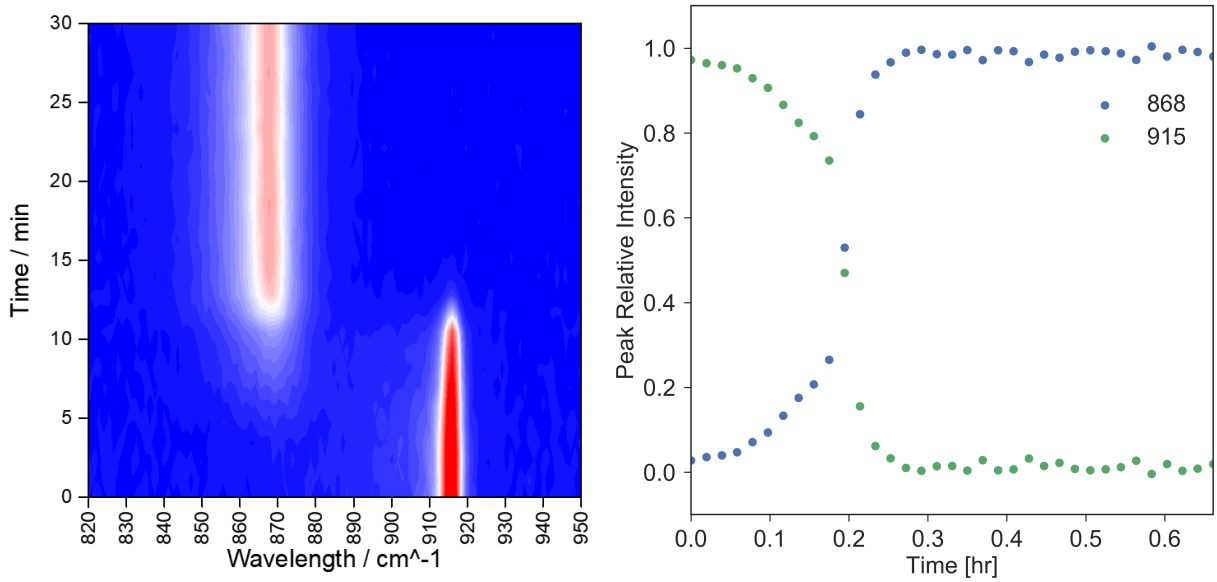

(a) (b)

Figure 2.28: (a) Waterfall plot showing changes in the Raman spectrum of uranyl fluoride over time as the sample was exposed to 50% RH at 30°C. (b) Normalized relative intensity of the uranyl stretching peak of anhydrous uranyl fluoride (green) and hydrated uranyl fluoride (blue).

dehydration/rehydration. This difference is illustrated in Figure 2.29. The uranyl stretching peak of the rehydrated material appears much broader than the starting material. Comparing the pseudo-Voigt fits of the uranyl stretching modes of the initial and rehydrated material, shown in Figure 2.30, suggests that the bulk of this broadening is actually the result of an increase in the intensity of the lower energy shoulder centered at 862 cm^{-1}.

As discussed in Section 2.2.2, the origin of the splitting of the uranyl stretching mode in $[(UO_2F_2)(H_2O)]_7 \cdot 4\,H_2O$ is not entirely clear and is likely the result of both differences in equatorial coordination as well as hydrogen bonding to the uranyl oxygens. The rehydrated material was shown to have a similar, albeit distinct, structure to the initial $[(UO_2F_2)(H_2O)]_7 \cdot 4\,H_2O$, especially in terms of lattice parameters. It is possible that the uranyl ions are slightly rearranged in the hydrated structure, allowing a greater fraction of them to participate in hydrogen bonds with water hydrogens. If the 862 cm^{-1} peak is interpreted as corresponding to the uranyl stretching mode of such uranyl ions, the observed increase in intensity is consistent with this description.

After hydrating for 17 hours, the sample was desiccated under dry air for an additional 26 hours. As shown in Figure 2.29, desiccation did not have a significant effect on the Raman spectrum. The Raman spectrum does not convert back to that of the initial material, suggesting that the structural changes between the initial and rehydrated material are not reversible—at least not on the timescale studied.

Understanding the effect of dehydration and rehydration on the structure of the uranyl fluoride hydrate is worth analyzing further but is not explored in this dissertation. The fact that the initial $[(UO_2F_2)(H_2O)]_7 \cdot 4\,H_2O$ material used in the dehydration/rehydration studies was also produced via hydration of anhydrous uranyl fluoride, albeit at a lower humidity over a longer timescale, suggests that the structural changes observed may be connected to hydration rate. Additionally, hydration in the dynamic experiments was carried out at 30°C to ensure temperature stability in the absence of a cooling mechanism. This slightly elevated temperature could also explain the formation of the altered rehydration product.

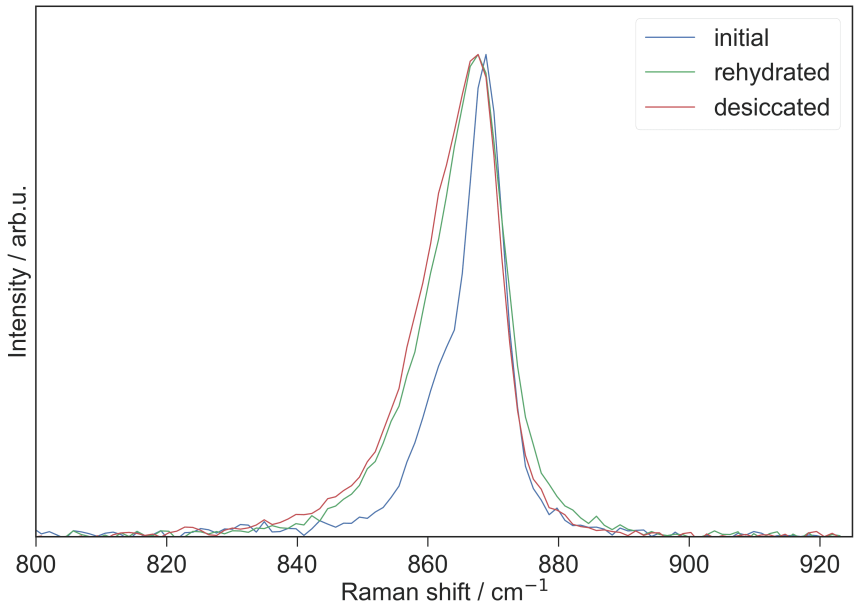

Figure 2.29: Comparison of the uranyl stretching region of the Raman spectrum of a sample of uranyl fluoride hydrate initially, after dehydration at 130°C and rehydration at 50% RH at 30°C, and after subsequent desiccation at 0% RH at 30°C.

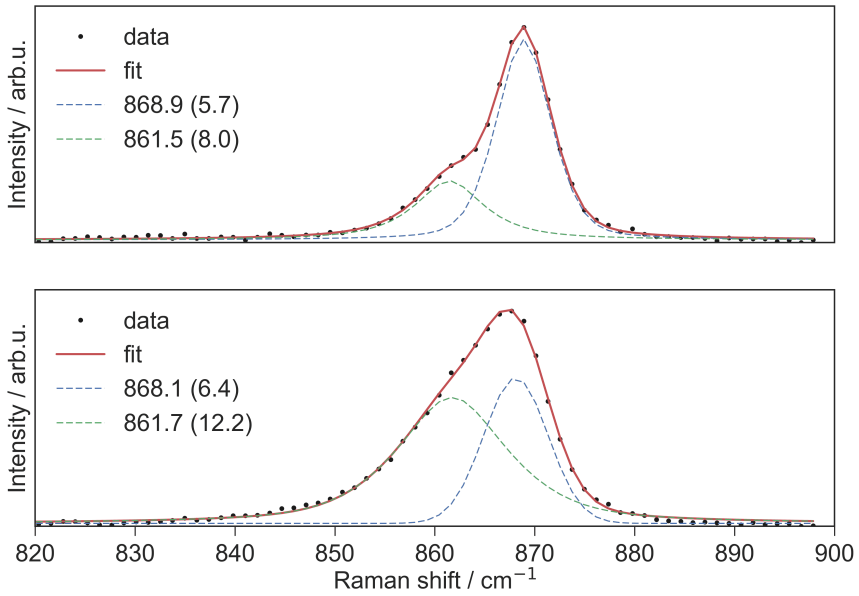

Figure 2.30: Comparison of the pseudo-Voigt fits of the uranyl stretching region of the Raman spectrum of a sample of uranyl fluoride hydrate initially (upper) and after dehydration at 130°C/rehydration at 50% RH (30°C) (lower). The center frequency and full-width-half-maximum of each curve are labeled.

2.4 Summary and future directions

In summary, this chapter presents a computational characterization of hydrated uranyl fluoride and clarifies the phase transition between hydrous and anhydrous uranyl fluoride. The structure and dynamics of the crystallographic water molecules in the $[(UO_2F_2)(H_2O)]_7 \cdot 4\,H_2O$ structure were solved computationally in the absence of clear experimental data. This represents the first computational study of this structure. Computational methods were also used to analyze the relationship between the hydrogen bonding network and the experimentally observed Raman spectrum. Several open questions remain regarding the characterization of the $[(UO_2F_2)(H_2O)]_7 \cdot 4\,H_2O$ structure. Despite an attempt to computationally assess the origin of the multiple Raman-active symmetric uranyl stretching modes, it remains uncertain whether the splitting is primarily due to differences of the equatorial environment of different uranyl ions or differences in hydrogen bonding to different uranyl oxygens.

This study marks the first time the phase transition between anhydrous and hydrated uranyl fluoride was studied experimentally in real time, clarifying the mechanism of this transition as well as the conditions under which it occurs. The consistency of the obtained XRD and Raman data with previous TGA analyses suggests that the crystallographic pore water molecules in $[(UO_2F_2)(H_2O)]_7 \cdot 4\,H_2O$ are driven off above 70°C, while the transformation to anhydrous uranyl fluoride occurs at 100–120°C. Both of these dehydration steps are shown to be dependent on the environmental humidity. In the future, dynamic IR spectroscopy could provide more detail regarding the loss of the interlayer water molecules because this technique is much more sensitive to water-related vibrational modes than Raman spectroscopy is.

The formation of a slightly altered hydrate structure after the dehydration and rehydration of $[(UO_2F_2)(H_2O)]_7 \cdot 4\,H_2O$ also requires further study. It is likely that these structural changes are related to the rate of hydration, motivating future work exposing anhydrous uranyl fluoride to a range of lower humidity environments and analyzing hydration over a much longer timescale than presented in this work. This more in-depth study may

also clarify how the structural changes upon rehydration relate to the observation of an amorphous intermediate by Miskowiec et al. [114].

Chapter 3

Chemical transformation of hydrated uranyl fluoride

Chapter 2 clarified characteristics of the two known structures of uranyl hydrate (UO_2F_2 and $[(UO_2F_2)(H_2O)]_7 \cdot 4\,H_2O$) and the phase transition between them. This chapter explores the chemical behavior of hydrated uranyl fluoride ($[(UO_2F_2)(H_2O)]_7 \cdot 4\,H_2O$) at elevated water vapor pressure. Uranyl fluoride is shown to be unstable above a threshold humidity, undergoing a complete loss of fluorine to form two hydration products. These products are tentatively identified in this chapter as uranyl hydroxide and uranyl peroxide species, respectively, from their Raman spectra. Components of this chapter come from the following papers:

> **M. C. Kirkegaard**, A. Miskowiec, M. W. Ambrogio, and B. B. Anderson. "Evidence of a nonphotochemical mechanism for the solid-state formation of uranyl peroxide." *Inorg. Chem.*, 2018, 57, 5711-5715.
>
> **M. C. Kirkegaard**, A. Miskowiec, M. W. Ambrogio, J. Langford, A. E. Shields, J. L. Niedziela, R. Kapsimalis, and B. B. Anderson. "Characterizing the chemical behavior of uranium compounds for nuclear forensics." Proceedings of the Institute for Nuclear Materials Management, 2018.

M. C. Kirkegaard, M. W. Ambrogio, A. Miskowiec, J. L. Niedziela, T. L. Spano, A. E. Shields and B. B. Anderson. "Characterization of the degradation of $[(UO_2F_2)(H_2O)]_7 \cdot 4\,H_2O$ under humid conditions." In preparation.

3.1 Previous studies of the hydration of uranyl fluoride

Although the Mikhailov hydrate ($[(UO_2F_2)(H_2O)]_7 \cdot 4\,H_2O$) is the only uranyl fluoride hydrate structure that has been solved, [111] previous studies suggest that additional hydrates may exist at higher water vapor pressures. For example, Marshall et al. suggested the existence of three different hydrates with the same approximate composition, $UO_2F_2 \cdot 2\,H_2O$ [104]. Brooks et al. observed the formation of an additional species, tentatively identified as a trihydrate, after equilibrating material at 100% RH for 144 hours [23]. Gromov et al. identified four distinct hydrates with X-ray and equilibrium vapor pressure measurements that could be formed by equilibrating uranyl fluoride powder with water vapor at varying temperatures over 2–8 weeks [160, 143]. On the other hand, Lychev et al. did not observe the formation of any additional species at elevated water vapor pressure [102]. The current literature thus leaves uncertainty regarding how many uranyl fluoride hydrate structures may exist. None of the above studies provide conclusive identification of chemical composition or crystal structures, meaning that it is feasible that some of the species observed may not have actually been uranyl fluoride hydrates, but rather other uranyl species produced in a chemical reaction with water vapor.

The hydration of uranyl fluoride has been studied more recently by Kips et al., who examined how the Raman spectrum of the uranyl fluoride hydrate evolves upon exposure to elevated water vapor pressure. Upon long-term exposure to a humid environment, a redshifted uranyl stretching mode around 845 cm^{-1} was observed in the Raman spectra in addition to the Raman peak characteristic of $[(UO_2F_2)(H_2O)]_7 \cdot 4\,H_2O$ at 868 cm^{-1}. This new peak was tentatively attributed to the absorption of water in the uranyl fluoride hydrate structure [86, 146]. Similar redshifting of uranyl modes upon hydration was previously observed via infrared (IR) spectroscopy as well, with the IR-active asymmetric stretching

mode shifting from 966 to 955 to 948 to 945 cm^{-1} in what were tentatively identified as hydrates with one, two, three, and four waters per uranium, respectively [161].

In a separate study, Kips et al. [87] also raised the possibility that uranyl fluoride undergoes a loss of fluorine upon exposure to elevated water pressure. Using scanning electron microscopy with energy dispersive X-ray spectroscopy (SEM-EDS) and ion-microprobe secondary ion mass spectrometry (IM-SIMS), the authors measured a reduction in the fluorine/uranium (F/U) ratio of uranyl fluoride particles that were aged in humid environments that was accelerated by UV exposure. The measured loss of fluorine supports the possibility that a chemical reaction with water vapor produces additional uranyl species. The measured loss of fluorine was not correlated with the authors' previously observed changes in the Raman spectrum, however, leaving it unclear if the additional peaks in the Raman spectra after hydration could be attributed to species other than uranyl fluoride hydrates.

3.2 Evidence of a chemical transformation of uranyl fluoride at high humidity

Uncertainty about whether or not additional hydrate structures exist motivated a more rigorous study of the behavior of hydrated uranyl fluoride at elevated water vapor pressures. This was achieved by exposing particles of $[(UO_2F_2)(H_2O)]_7 \cdot 4\,H_2O$ to a humid environment and monitoring changes in the particles over several months via micro-Raman spectroscopy. Particles of $[(UO_2F_2)(H_2O)]_7 \cdot 4\,H_2O$, produced via the same process described in Section 2.3, were deposited on three adhesive carbon tabs on SEM mounts, two of which were then suspended in capped glass vials above a NaCl saturated-salt solution in deionized water to achieve an environment of approximately 75% relative humidity (RH) at 20–23°C (corresponding to a water vapor pressure of 1.75–2.11 kPa) [26]. The third tab was suspended in an empty vial and thus exposed to ambient RH to act as a control. These sample conditions are summarized in Table 3.1. Multiple particles on each sample were tracked throughout the study, and the same region of each particle was analyzed each time.

Table 3.1: Sample conditions. The 75% RH environment was achieved by exposing samples to the headspace of a NaCl saturated-salt solution, and the 100% RH environment was achieved by replacing the saturated-salt solution with deionized water.

Sample	Equilibration conditions
a	75% RH for 238 days
b	75% RH for 190 days + 100% RH for 48 days
c	Ambient (40–55% RH) for 238 days

Initial Raman spectra of all three samples were characteristic of hydrated uranyl fluoride with a uranyl stretching peak at 868 cm^{-1} and shoulder around 862 cm^{-1} [89]. No significant changes were noted throughout the course of the experiment in sample *c*, which was left at ambient RH. For the particles on samples *a* and *b*, hydrated at 75% RH, however, the 868 cm^{-1} peak decreased in intensity, while additional peaks appeared at 845 and 820 cm^{-1} (Figure 3.1a). Over the first 30 days, significant color changes were observed for these particles as well, as shown in Figure 3.2. After this time, the color appeared fairly consistent, although the Raman spectra continued to change through the end of the experiment.

After 190 days of equilibrating at 75% RH, sample *b* was moved into a new vial and exposed to the headspace of pure deionized water as opposed to the NaCl saturated-salt solution, increasing the RH to 100% for an additional 48 days of equilibration. As shown in Figure 3.1b, this led to the complete disappearance of the 845 cm^{-1} peak and the rapid growth of the 820 cm^{-1} peak as well as a peak at 865 cm^{-1} similar in frequency to the initial uranyl fluoride peak. After 48 days of additional hydration at 100% RH, the Raman spectra of the particles on sample *b* were stable, and no further changes were observed. The disappearance of the 845 cm^{-1} peak suggests that the peaks at 845 and 820 cm^{-1} corresponded to two different species, while the correlated growth of the 820 and 865 cm^{-1} peaks suggests that these two peaks are related to the same species. It is therefore evident that the 865 cm^{-1} peak observed to grow in intensity with exposure to elevated water pressure is not related to the 868 cm^{-1} peak characteristic of $[(UO_2F_2)(H_2O)]_7 \cdot 4\,H_2O$, but instead corresponds to a mode in a different species with a coincidentally similar frequency. Thus, at least two hydration species are formed as $[(UO_2F_2)(H_2O)]_7 \cdot 4\,H_2O$ is exposed to elevated water vapor pressure, one with a characteristic peak at 845 cm^{-1} and another with characteristic peaks at 820 and 865 cm^{-1}.

A more mathematically rigorous analysis of the data was performed using multivariate curve resolution (MCR) to decompose the spectra collected at each time point into component spectra corresponding to different species. Singular value decomposition (SVD) suggested that there were three component species, consistent with a visual interpretation of the spectra. Figure 3.3 shows the resulting three deconvoluted spectral components, denoted β, γ, and δ. Some artifacts are noted, especially in the spectra of the second species, γ,

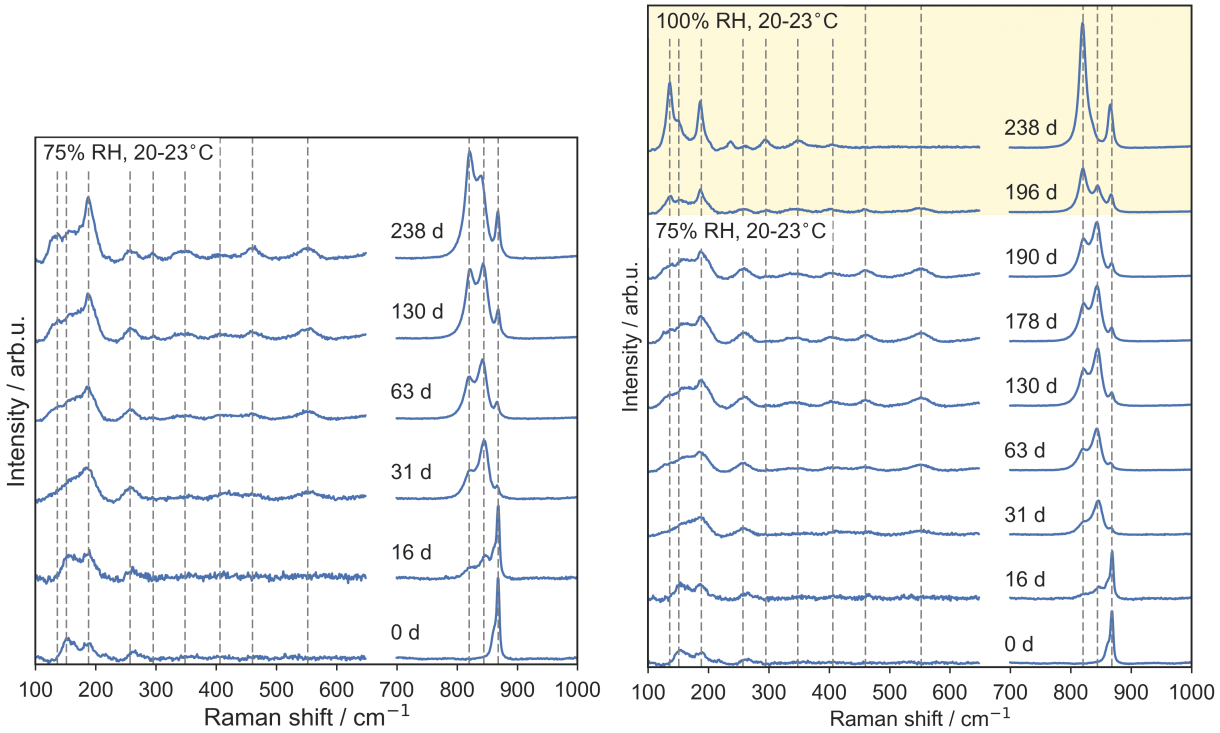

Figure 3.1: (a) Evolution of the micro-Raman spectrum of a representative particle of $[(UO_2F_2)(H_2O)]_7 \cdot 4\,H_2O$ from sample *a* after increasing amounts of time spent equilibrating in a 75% RH environment (20–23°C). (b) Evolution of the micro-Raman spectrum of a representative particle of $[(UO_2F_2)(H_2O)]_7 \cdot 4\,H_2O$ from sample *b* after increasing amounts of time spent equilibrating in a 75% RH environment and then 100% RH environment after 190 days (20-23 °C). In both figures, the lower wavenumber region of each spectrum has been scaled by a factor of three to show weaker intensity peaks more clearly. Vertical lines are at 136, 151, 188, 236, 257, 295, 348, 406, 460, 552, 820, 845, and 868 cm^{-1}. All spectra are normalized to the Rayleigh line intensity (not shown) to allow for better comparison of peak intensities among different days [88].

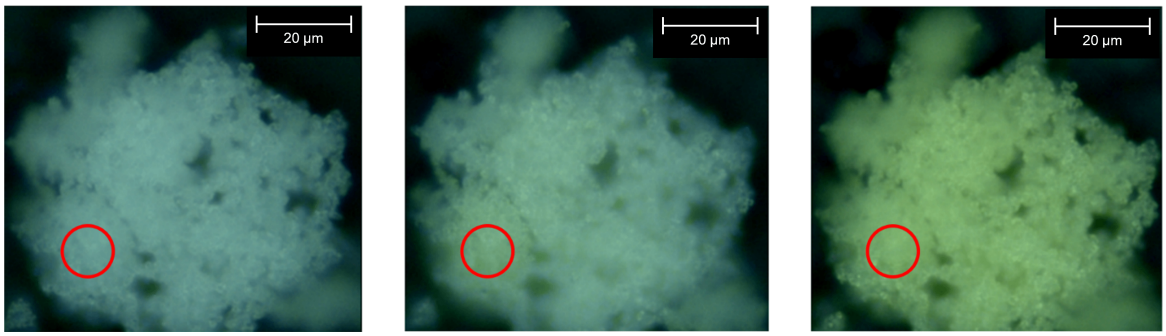

(a) **(b)** **(c)**

Figure 3.2: Microscope images of a representative particle of $[(UO_2F_2)(H_2O)]_7 \cdot 4\,H_2O$ from sample *a* (a) initially, (b) after hydrating at 75% RH for 16 days, and (c) after hydrating at 75% RH for 31 days. The red circles identify the location where Raman spectra were collected at each time point. Images are not white balanced.

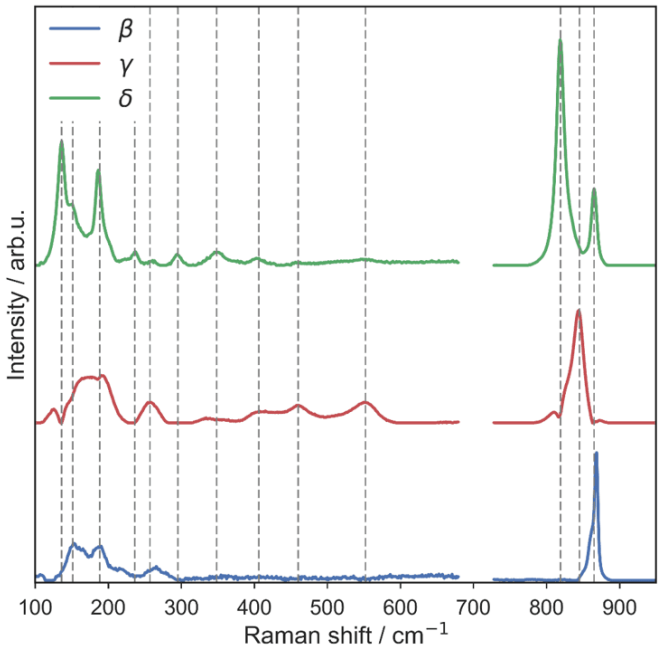

Figure 3.3: Deconvoluted spectral components. The lower wavenumber region of each spectrum has been scaled by a factor of three to show weaker intensity peaks more clearly. Vertical lines show peaks at 136, 151, 188, 236, 257, 295, 348, 406, 460, 552, 819, 845, and 868 cm^{-1} [88].

due to difficulties deconvoluting the overlapping peaks given the limited number of spectra collected. The γ species is characterized by peaks at 845, 552, and 460 cm^{-1}, while the δ species is characterized by peaks at 865, 820, 348, 295, 236, and 136 cm^{-1}. The normalized concentration profiles of these component species are shown in Figure 3.4. It is clear that the β species ($[(UO_2F_2)(H_2O)]_7 \cdot 4\,H_2O$) undergoes a transition to the γ and δ species over the course of several weeks at 75% RH, and that a transition from γ to δ, which happens slowly at 75% RH, occurs much more rapidly at 100% RH.

At the conclusion of the experiment, energy dispersive X-ray spectroscopy (EDX) was used to perform a qualitative elemental analysis of particles on both hydrated samples as well as a third sample of fresh $[(UO_2F_2)(H_2O)]_7 \cdot 4\,H_2O$. From the final Raman spectra of characteristic particles from each hydrated sample (Figure 3.5), it is apparent that particles on sample *a*, left at 75% RH throughout the entire experiment, were a mixture of the γ and δ species after 238 days of equilibration, while particles on sample *b*, which was further hydrated at 100% RH for 38 days, have undergone a complete transition to the δ product. On each sample, EDS spectra were collected on five particles and found to be consistent. As shown in the bottom-left panel of Figure 3.5, the EDS spectrum of a particle of $[(UO_2F_2)(H_2O)]_7 \cdot 4\,H_2O$ freshly mounted on a GSR tab has peaks attributed as uranium M-peaks (3.17 keV and 3.34 keV), a fluorine K-peak (0.67 keV), and a oxygen K-peak (0.53 keV). Peaks associated with carbon and nitrogen appear as well, attributed to the substrate and off-gassing, respectively. No obvious contaminants were observed.

The EDS spectra of particles on both samples *a* and *b* were found to contain all of the same peaks as fresh uranyl fluoride, with the exception of the peak attributed to fluorine. No measurable fluorine was noted in any of the hydrated particles studied via EDS. This confirms that neither the γ nor δ species are additional uranyl fluoride hydrates. Rather, the $[(UO_2F_2)(H_2O)]_7 \cdot 4\,H_2O$ starting material undergoes a chemical reaction with exposure to a humid environment, transforming into hydration products that contain only uranium and oxygen (and hydrogen, which cannot be detected via EDS). The presence of Raman active modes in the 750–900 cm^{-1} region of both of these species suggests that the uranyl ion remains intact. Thus, it is more likely that the γ and δ species correspond to uranyl hydroxides or peroxides than uranium oxides.

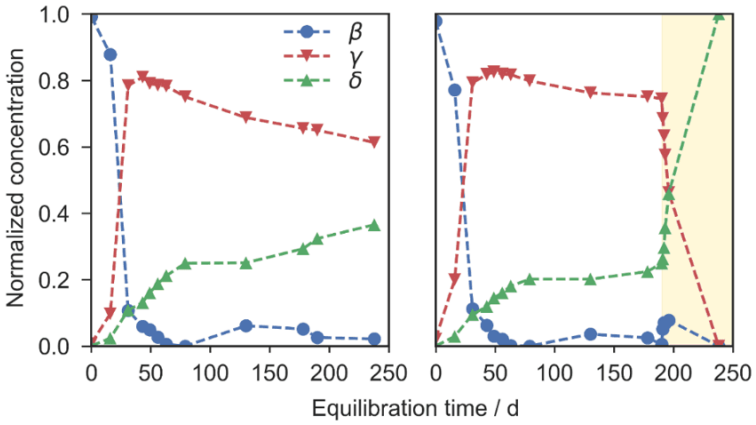

Figure 3.4: Normalized concentration gradients of the three component species as determined by MCR analysis for a representative particle on (a) sample *a*, exposed to 75% RH for 238 days and (b) sample *b*, exposed to 75% RH for 190 days and 100% RH for an additional 48 days, illustrated by the shaded portion of the graph [88].

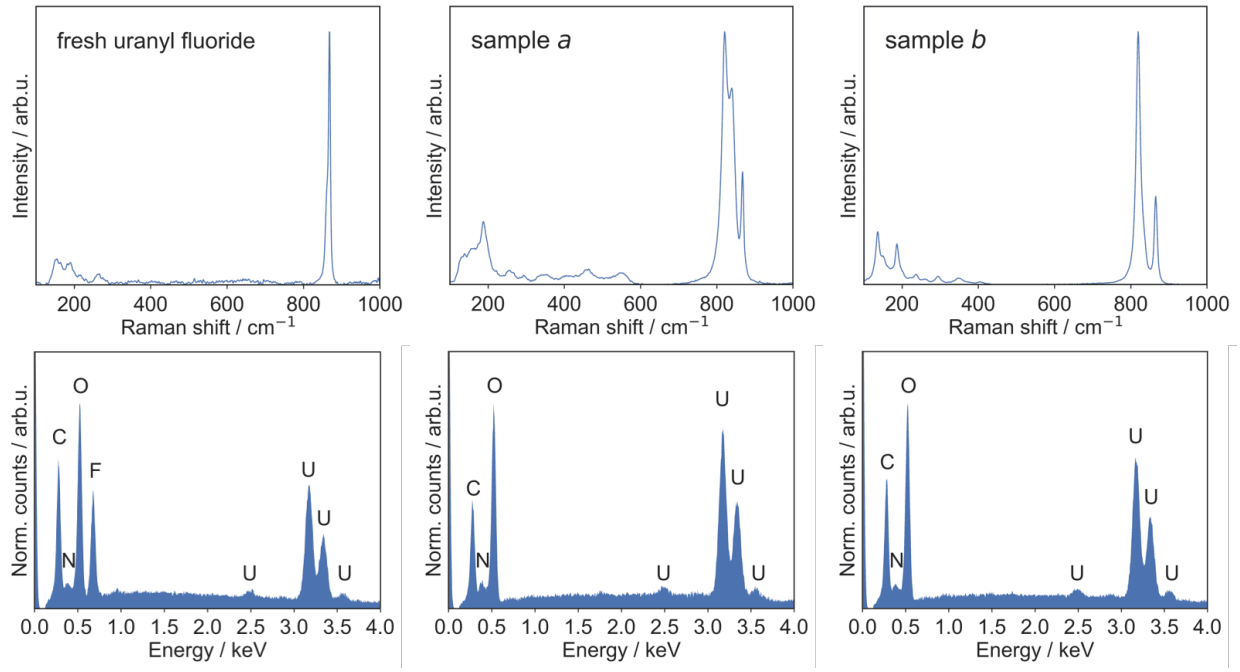

Figure 3.5: Raman (top row) and EDS spectra (bottom row) of a characteristic particle of (a) fresh $[(UO_2F_2)(H_2O)]_7 \cdot 4\,H_2O$, (b) sample *a*, $[(UO_2F_2)(H_2O)]_7 \cdot 4\,H_2O$ exposed to 75% RH for 238 days, and (c) sample *b*, $[(UO_2F_2)(H_2O)]_7 \cdot 4\,H_2O$ exposed to 75% RH for 190 days and then 100% RH for an additional 48 days.

3.3 Preliminary characterization of uranyl fluoride hydration products

One of the goals of this study was to not only determine under what conditions uranyl fluoride is unstable, but to rigorously characterize the products of these hydration reactions. Initial characterization is possible from the deconvoluted Raman spectra of these products (Figure 3.3). As shown in Figure 3.6, the deconvoluted Raman spectrum of δ is an excellent match with that of the mineral studtite, a uranyl peroxide hydrate of the form $[(UO_2)O_2(H_2O)_2] \cdot 2\,H_2O$ [29]. The Raman spectrum of studtite has been well characterized. Peaks at 819 and 864 cm^{-1} are assigned to the symmetric uranyl stretch and peroxide stretch, respectively [4, 17, 132, 31, 96, 18, 40]. Excellent agreement is noted between the hydrated particle and studtite for not only these two dominant peaks, but also for all of the lower energy peaks of studtite, at 68, 106, 135, 151, 163, 187, 237, 263, 294, 348, and 406 cm^{-1}. The slight shoulder at 835–840 cm^{-1} that appears in the spectrum of the hydrated particles is attributed to metastudtite ($(UO_2)O_2(H_2O)_2$), the dehydration product of studtite. While the structure of δ cannot be confirmed via Raman spectroscopy, the excellent agreement of these spectra leave little doubt that hydrated particles have transformed into a uranyl peroxide species with a local structure at least similar to that of studtite [88]. In addition, as shown in Figure 3.7, following vacuum exposure during SEM-EDS analysis, the Raman spectra of the fully hydrated particles matched that reported for metastudtite, with a uranyl stretching mode at 830 cm^{-1} [17, 96]. This is further evidence that the structure of this hydration product is studtite-like.

Characterization of the γ hydration product via Raman spectroscopy is less straightforward. The MCR analysis suggests that γ is characterized by dominant Raman peaks at 845, 552, and 460 cm^{-1}. These peaks are reasonably consistent with published Raman spectra of uranyl hydroxide hydrate minerals like schoepite ($(UO_2)_4O(OH)_6 \cdot 6\,H_2O$) and metaschoepite ($(UO_2)_4O(OH)_6 \cdot 5\,H_2O$), which are typically found to have a symmetric uranyl stretching frequency between 830 and 855 cm^{-1}, as well as peaks near 550 and 450 cm^{-1} attributed to stretching modes of equatorial ligands [4, 60, 132, 31, 2, 70, 69, 18]. However, as described in the following chapter, Raman spectra of uranyl hydroxide compounds in the literature

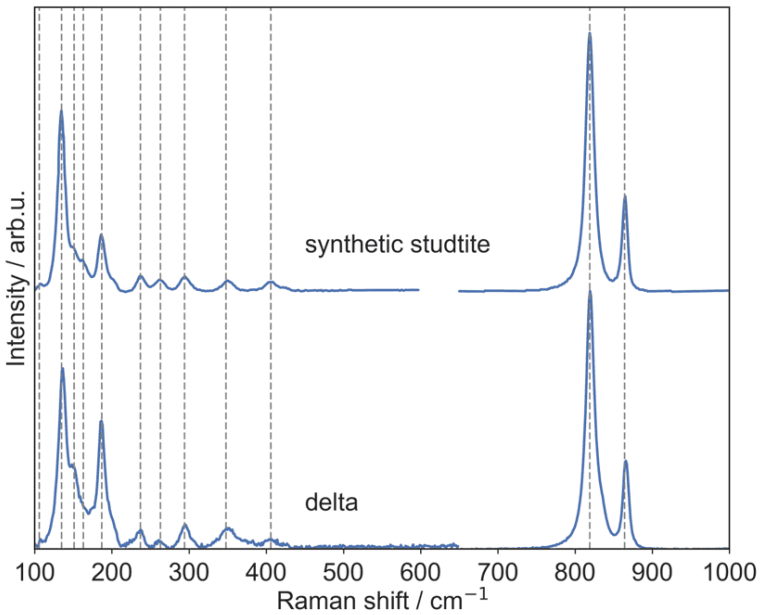

Figure 3.6: Raman spectrum of δ compared to published Raman spectrum of studtite, $[(UO_2)O_2(H_2O)_2] \cdot 2\,H_2O$ [88]. The structure of the studtite sample was confirmed XRD prior to the collection of Raman spectra.

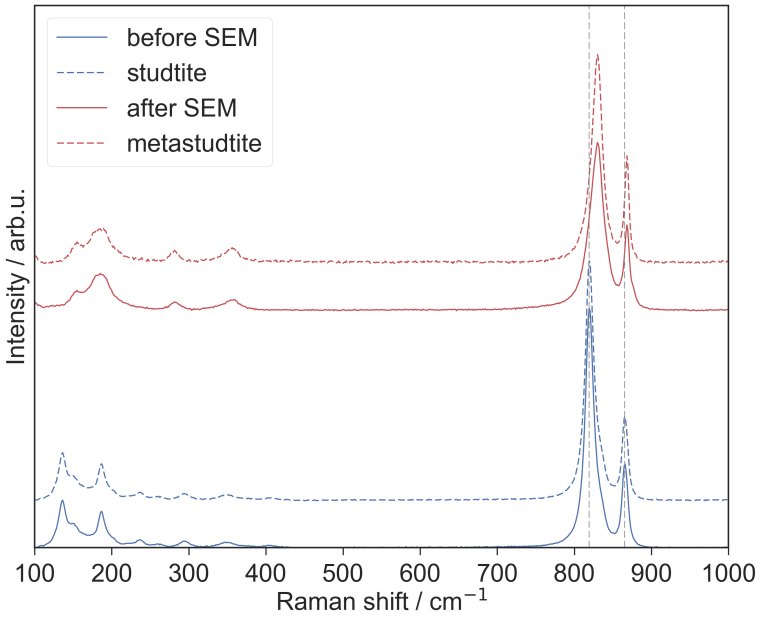

Figure 3.7: Raman spectra of a particle from sample *b* collected after 238 days of hydration, prior to and following SEM-EDS analysis (exposure to vacuum). The Raman spectra of studtite and metastudtite, collected from lab standards structurally confirmed via XRD, are shown for comparison. Dashed lines at 819 and 865 cm^{-1} show the location of the uranyl and peroxo stretching modes, respectively, in studtite.

are significantly varied, making identification of the species difficult from Raman data alone. This motivates the use of complementary structural techniques such as x-ray diffraction (XRD) to study this material. Further characterization of these hydration products will be discussed in Chapters 4 (γ) and 5 (δ).

3.4 Effect of temperature and water vapor pressure on the transformation of uranyl fluoride

The initial particle hydration study described in Section 3.2 demonstrated that hydrated uraynl fluoride ($[(UO_2F_2)(H_2O)]_7 \cdot 4\,H_2O$) is stable at room temperature (20–22°C) and ambient humidity (40–50% RH) but not at 75% RH. This finding motivated a follow-up study exposing particles to a wider range of conditions. Five different saturated-salt solutions were used to achieve varying humidity at two different environmentally relevant temperatures. In total, 10 samples were prepared with SEM tabs in a similar method as before, with the equilibration conditions summarized in Table 3.2. In the initial study, samples were removed from their equilibration environments each time they were analyzed via Raman spectroscopy. In this follow-up experiment, the SEM tabs were sealed in plastic containers with saturated-salt solutions throughout the entirety of the experiment, and Raman spectra were collected through glass windows on the top of the containers. Additionally, while the SEM tabs were suspended upside down in the initial experiment, they were oriented facing up in this follow-up experiment. The new sample setup is shown in Figure 3.8. Eight particles were tracked over time on each sample.

The stability of uranyl fluoride under this wider range of conditions was again assessed by tracking the evolution of the Raman spectra of particles on each sample over time. The evolution of the uranyl stretching region of the Raman spectrum for a characteristic particle on each sample is shown in Figure 3.9. The initial spectra collected on each sample were characteristic of hydrated uranyl fluoride, with a uranyl stretching peak at 868 cm^{-1} and shoulder around 862 cm^{-1} [89, 88]. The Raman spectra of particles on sample 1 (25°C, 33% RH) and sample 6 (35°C, 32% RH), did not change over the course of the 220-day

Table 3.2: Sample conditions. RH as measured for each saturated-salt solution by Greenspan [62]. Water vapor pressures were calculated using the Buck equation [26].

Sample	Temperature/°C	Sat. Salt	RH	Water Vapor Pressure/kPa
1	25	$MgCl_2$	32.8%	1.04
2	25	NaBr	57.6%	1.83
3	25	NaCl	75.3%	2.39
4	25	KCl	84.3%	2.67
5	25	KNO_3	93.6%	2.97
6	35	$MgCl_2$	32.0%	1.80
7	35	NaBr	49.9%	2.81
8	35	NaCl	74.9%	4.22
9	35	KCl	83.0%	4.67
10	35	KNO_3	90.8%	5.11

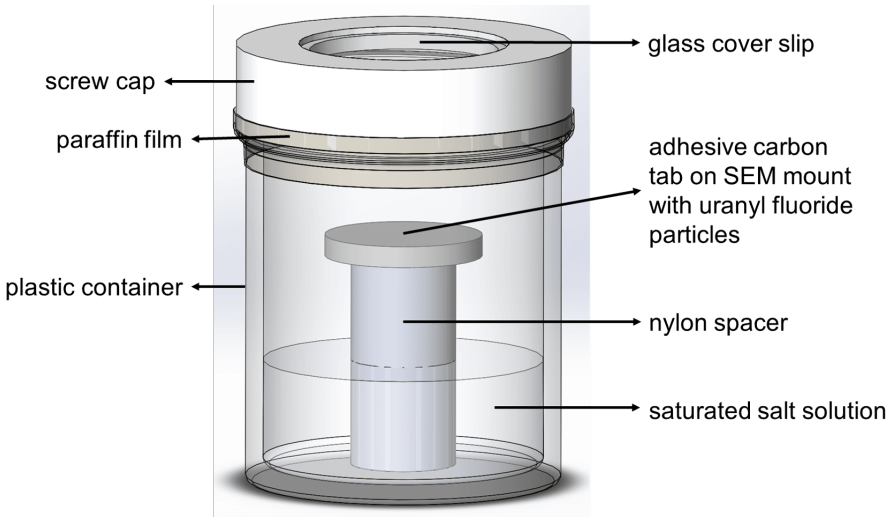

Figure 3.8: Diagram of the sample containers used to hydrate $[(UO_2F_2)(H_2O)]_7 \cdot 4\,H_2O$ particles. Each container was sealed throughout the course of the experiment and stored in incubators at either 25 or 35°C.

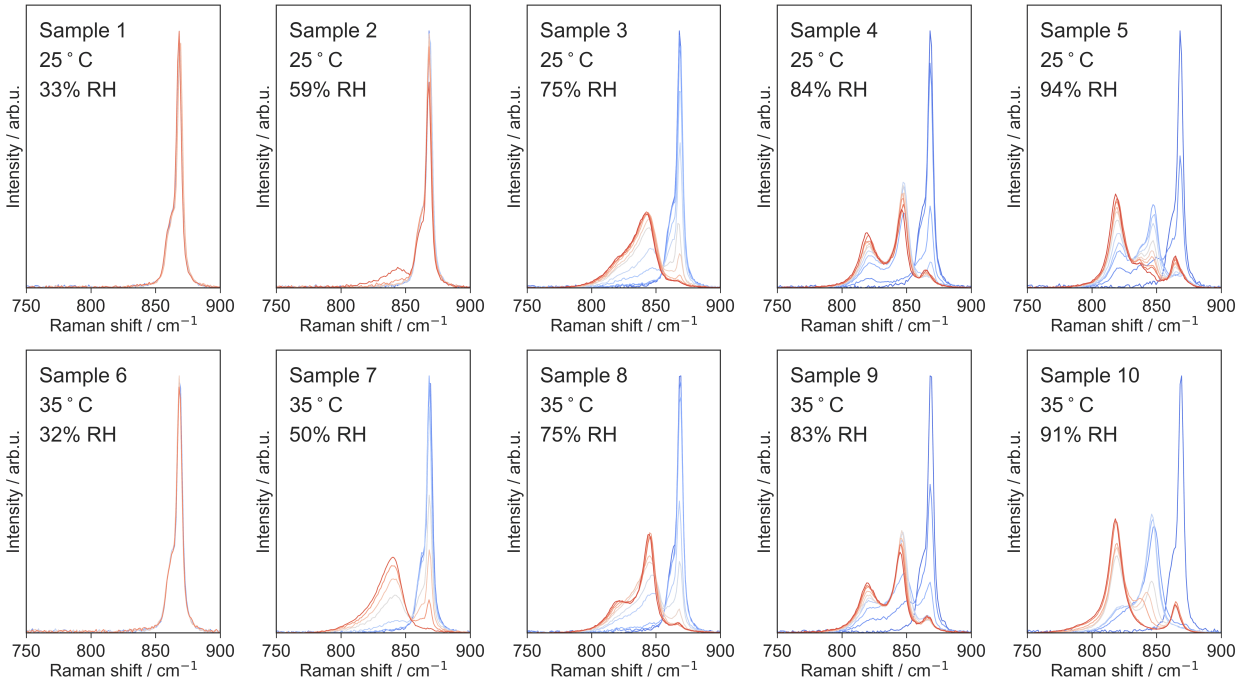

Figure 3.9: Evolution of the Raman spectrum of a representative particle of $[(UO_2F_2)(H_2O)]_7 \cdot 4\,H_2O$ on samples 1–10. Individual spectra are normalized by the peak area in the region shown to allow for easier comparison. Multiple scans were performed on the same particle over 220 days of equilibration (day 1 in dark blue, day 220 in dark red). Equilibration conditions are listed in each subfigure and in Table 3.2. $[(UO_2F_2)(H_2O)]_7 \cdot 4\,H_2O$ was found to be stable to hydration in samples 1 and 6 but underwent changes in more humid environments.

experiment, indicating that the uranyl fluoride hydrate is stable under these conditions, consistent with the prior finding that uranyl fluoride was stable at ambient temperature and humidity. In all remaining samples, changes were apparent in the uranyl stretching region of the Raman spectrum. This indicates that there is a threshold humidity between 33% and 59% RH at 25°C and between 32% and 50% RH at 35°C, above which uranyl fluoride begins to degrade.

The changes in the Raman spectra observed at humidities above this threshold were consistent with the findings of the previous study at 75% RH. In the uranyl stretching region of the Raman spectra, shown in Figure 3.9, hydration led first to the growth of a peak at 845 cm^{-1}, previously attributed to the γ hydration species [88]. At higher humidities, this peak is replaced by peaks at 820 and 864 cm^{-1}, attributed to the δ hydration species. The transformation of $[(UO_2F_2)(H_2O)]_7 \cdot 4\,H_2O$ to these hydration products was also marked by the appearance of additional peaks in the lower energy region, consistent with prior observations at 75% RH [88]. In addition to the changes in the Raman spectra, the particles underwent color changes at high humidity, illustrated in Figure 3.10.

Once again, at the conclusion of the 220-day experiment, each sample was analyzed via SEM-EDS. Five random particles were examined on each sample. Particles from samples 1–4 and 6–9 had similar subhedral/blocky morphology, consistent with the morphology of fresh $[(UO_2F_2)(H_2O)]_7 \cdot 4\,H_2O$ particles studied previously [88]. As shown in Figure 3.12, particles on sample 5 had a distinct fibrous/irregular morphology. Particles on sample 10 also looked distinct from the others, with a concentric morphology. The circular outline around the particle from sample 10 is evidence of deliquescence, which was also observable under the microscope when collecting Raman spectra. Some particles appeared to recrystallize over the course of the experiment, while others remained semiliquid-like.

Approximate oxygen/uranium (O/U) and F/U ratios calculated from the EDS data are shown in Figure 3.11. As expected from the Raman spectra, a fluorine peak was not resolvable above the background in any of the particles from samples 9, 10, 13, 14, and 15, while samples 7, 8, and 12 showed a reduction in fluorine relative to samples 6 and 11. In addition to a loss of fluorine, the EDS spectra showed an increase in the O/U ratio upon hydration. This is consistent with the formation of uranyl hydroxide/peroxide

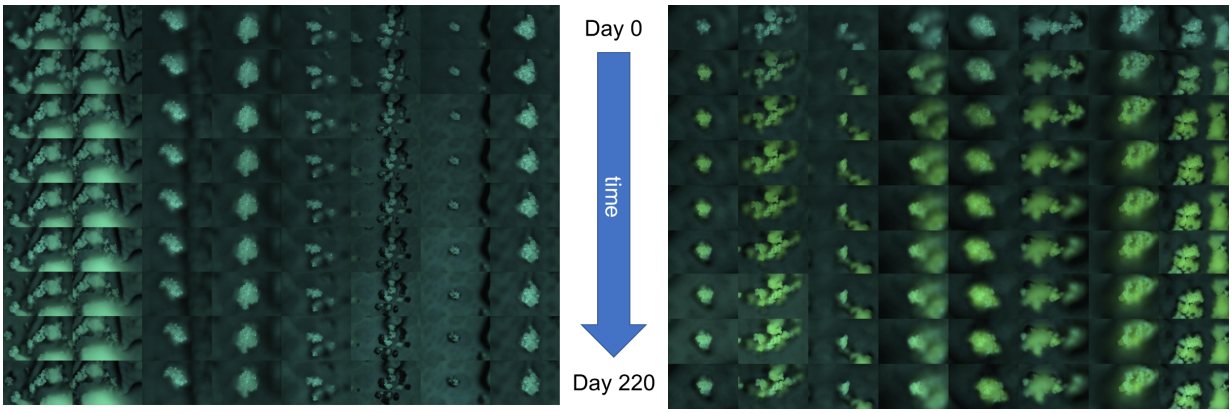

Figure 3.10: (a) Microscope images of the eight particles on sample 1 over time at 33% RH and 25°C. (b) Microscope images of the eight particles on sample 5 over time at 94% RH and 25°C. Images were taken with the same color-balance settings at each time point but are not white balanced.

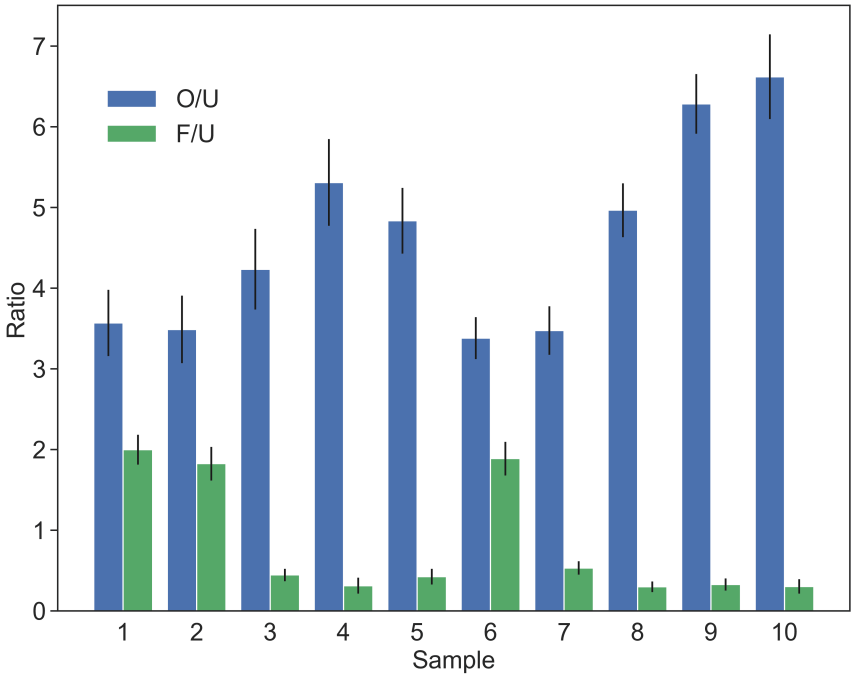

Figure 3.11: Approximate O/U and F/U ratios for each sample. Ratios were calculated by dividing the intensities of the dominant peak in the EDS spectra corresponding to each element. Results from five random particles are averaged for each sample; error bars show $\pm$ one standard deviation. Ratios have been normalized to sample 1 (25°C, 32% RH), which is assumed to be pure $[(UO_2F_2)(H_2O)]_7 \cdot 4\,H_2O$.

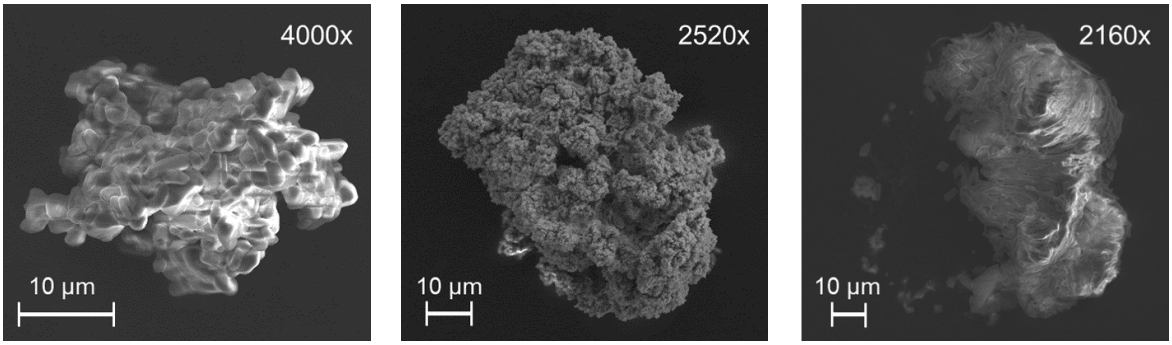

(a) **(b)** **(c)**

Figure 3.12: SEM images of a characteristic particle from (a) sample 1, (b) sample 5, and (c) sample 10. The morphology of particles on the remaining samples most closely matched that of sample 1.

species as the O/U ratio in known uranyl hydroxide and uranyl peroxide hydrates is higher than in $[(UO_2F_2)(H_2O)]_7 \cdot 4\,H_2O$. Calculated O/U ratios are likely underestimates since the vacuum conditions necessary for EDS have been observed to pull water from some crystal hydrates during the measurement. As discussed previously, the 820 cm^{-1} Raman peak was observed to shift upwards in energy in some samples after vacuum exposure, consistent with the dehydration of studtite to metastudtite ($(UO_2)O_2(H_2O)_2$), which has an O/U ratio of 6 instead of 8. Furthermore, the calculated elemental ratios are not intended to be quantitative since variables like particle orientation can significantly affect the intensity of different elemental contributions.

One of the goals of analyzing a wider range of humidity levels in this follow-up experiment was to assess whether any additional hydration products could be formed above or below 75% RH. In almost all of the samples, no additional peaks were noted in the Raman spectrum over time, suggesting that γ and δ are the only hydration products. For sample 5, however, at 25°C and 94% RH, an additional peak is visible near 838 cm^{-1}. Figure 3.13 expands this region of the Raman spectrum for sample 5 from Figure 3.9, starting with day 5 of hydration to focus on the peaks of the hydration products. At least four peaks are visible in the data. The peak at 847 cm^{-1} is attributed to γ, and the peaks at 819 and 864 cm^{-1} are attributed to δ. The remaining peak, near 838 cm^{-1}, was observed only in this sample and is difficult to assign. The intensity of this peak roughly follows that of the 847 cm^{-1} peak, although the ratio of these peaks changes over time. The 838 cm^{-1} peak is tentatively assigned to the uranyl stretch of a uranyl hydroxide species based on the frequency of the mode and the observed similarities to the 847 cm^{-1} peak. It is unclear if this peak corresponds to an additional uranyl hydroxide hydrate product distinct from γ, or to a redshifted mode in γ. Such redshifting could be the result of stronger hydrogen bonding interactions to uranyl oxygens due to the presence of additional water molecules at high humidity. While this peak was not observed for sample 10, equilibrated at a similarly high humidity, findings described in the next chapter suggest that the elevated temperature may limit water absorption in γ.

Part of the uncertainty regarding the attribution of this additional peak stems from the observed variability of the peak attributed to γ over time and across the different samples studied. While the Raman peak near 868 cm^{-1}, attributed to $[(UO_2F_2)(H_2O)]_7 \cdot 4\,H_2O$,

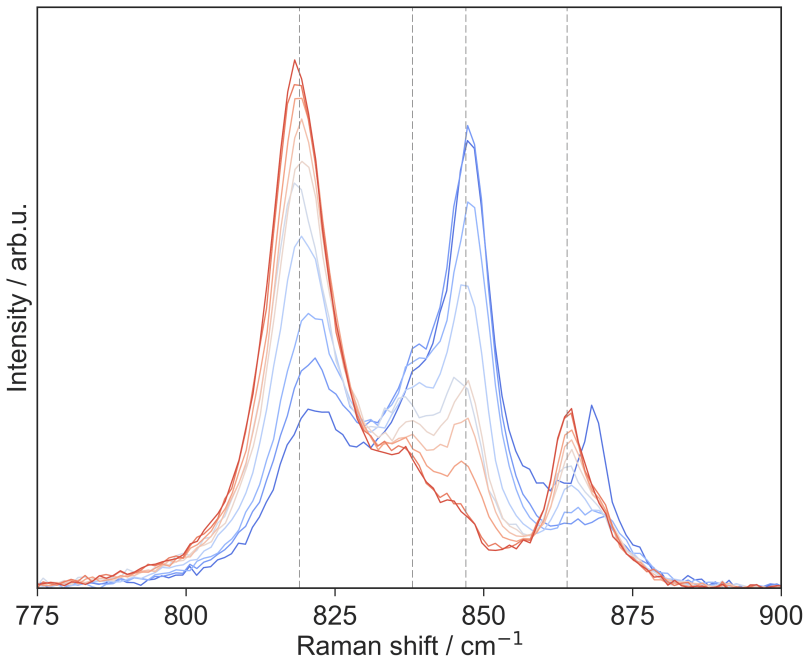

Figure 3.13: Evolution of the Raman spectrum of a representative particle on sample 5 (25°C and 94% RH). Data collected on the first 4 days of hydration is eliminated to highlight peaks corresponding to the hydration products. Day 5 is shown in dark blue, day 220 in dark red. Dashed lines at 819, 838, 847, and 864 cm^{-1} indicate the location of observed peaks.

appears at more or less the same frequency in each sample and was not observed to shift during the course of the experiment, the Raman peak near 845 cm^{-1}, attributed to γ, was observed to shift downwards in energy with hydration in nearly every sample where it appeared. Similar redshifting is observed for the 819 cm^{-1} peak attributed to δ in some samples (e.g., in Figure 3.13), but this shift is less exaggerated than the shift in the γ peak with continued hydration. Figure 3.14 shows a subset of the data presented in Figure 3.9 to highlight shifts in the γ peaks. Only spectra in which γ was the dominant component were included.

It is clear from Figure 3.14 that in addition to the shifting of this peak in each sample over time, the position of this peak differs significantly between samples. Figure 3.15 shows the final spectrum in Figure 3.14 for samples 3, 4, 5, 7, 8, 9, and 10 overlaid for easier comparison of the frequency and width of the peak attributed to γ. This peak is considerably wider and shifted down in energy in the samples stored at lower humidity, where δ was not observed to form. The wider peaks suggests that γ may be less crystalline when formed under these conditions. This lack of crystallinity can be explained by comparing the water content of $[(UO_2F_2)(H_2O)]_7 \cdot 4\,H_2O$ and the two hydration products. $[(UO_2F_2)(H_2O)]_7 \cdot 4\,H_2O$ has an H_2O/U ratio of 1.54. Studtite ($[(UO_2)O_2(H_2O)_2] \cdot 2\,H_2O$), on the other hand, has an H_2O/U ratio of 4. While the water content of δ may not exactly match that of studtite, the increased O/U ratio observed in the SEM-EDS spectra supports a significant increase in water content. The uranyl hydroxide hydrate schoepite ($[(UO_2)_4O(OH)_6] \cdot 6\,H_2O$) has an H_2O/U ratio of 1.5. Again, the water content of γ is likely not exactly the same as stoichiometric, crystalline schoepite, and further studies described in the next chapter suggest that γ may be additionally hydrated relative to schoepite. Still, by this comparison, the water content of γ is likely much closer to that of the initial $[(UO_2F_2)(H_2O)]_7 \cdot 4\,H_2O$ material than that of δ.

At moderate humidity (i.e., 50% RH at 35°C), the initial $[(UO_2F_2)(H_2O)]_7 \cdot 4\,H_2O$ transforms into γ, but the water vapor pressure is not high enough to induce further transformation to δ. The reaction from uranyl fluoride to γ is dependent on interactions with additional water molecules (see Section 3.5.1), but if the water content of crystalline γ is similar to that of $[(UO_2F_2)(H_2O)]_7 \cdot 4\,H_2O$, these water molecules are excess in the product

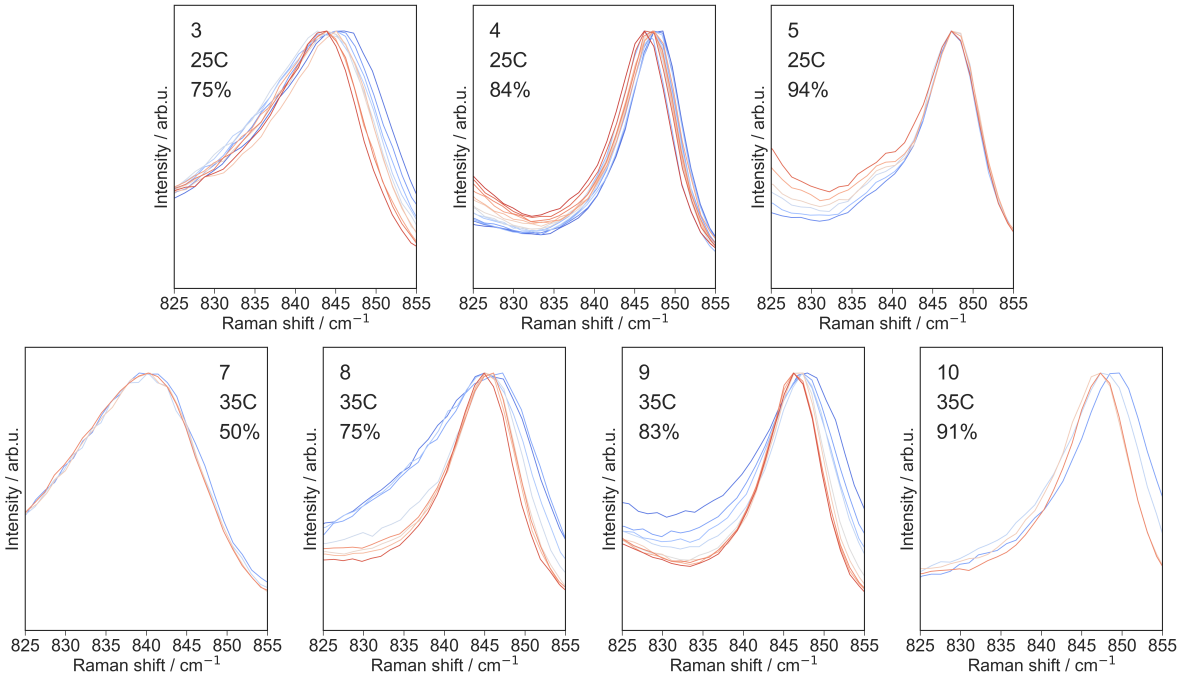

Figure 3.14: Subset of the Raman datasets on representative particles as shown in Figure 3.9 for samples 3, 4, 5, 7, 8, 9, and 10. Only spectra in which γ was the dominant component have been included. The first spectrum meeting this criterion is shown in dark blue, and last in dark red. Samples 1, 2, and 6 have been omitted since γ was never the dominant species in these samples. All spectra are shown normalized to the intensity of the γ peak to better highlight the shift in peak frequency over time. The first/last peak positions are: sample 3: 846.1/843.9 cm^{-1}, sample 4: 848.5/846.2 cm^{-1}, sample 5: 847.3/847.3 cm^{-1}, sample 7: 839.1/840.2 cm^{-1}, sample 8: 845.0/844.9 cm^{-1}, sample 9: 847.9/846.2 cm^{-1}, sample 10: 849.7/847.3 cm^{-1}.

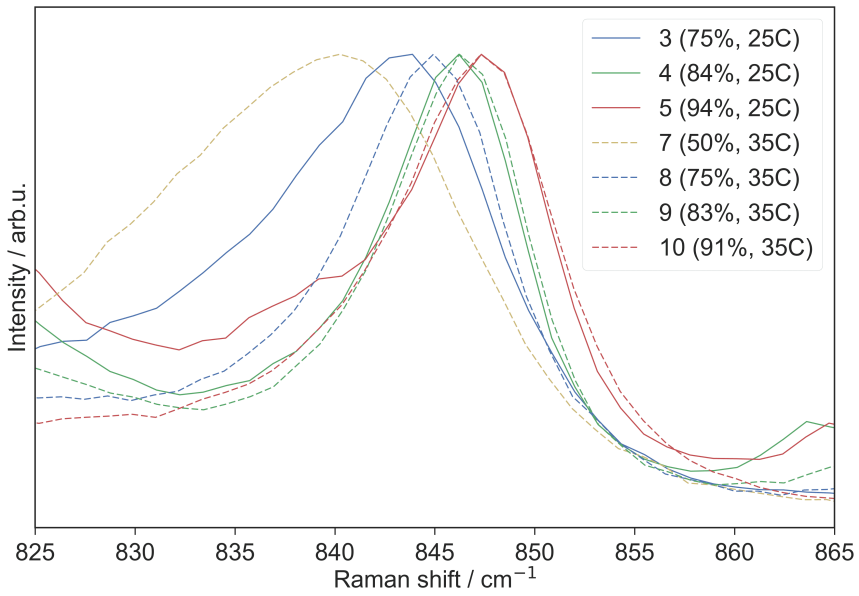

Figure 3.15: Comparison of the final spectra in Figure 3.14 for samples 3, 4, 5, 7, 8, 9, and 10. Spectra have been normalized to the intensity of the γ peak for better comparison.

structure and may reduce the crystallinity of the γ product. This explains the broadness of the γ Raman peak under these conditions, as well as the redshifted energy. At higher humidity, enough water vapor is present to cause the formation of the highly hydrated δ species from γ. Formation of δ pulls excess water from the γ structure, causing better crystallization that results in a much narrower Raman peak.

This assessment may also explain why the 845 cm^{-1} Raman peak attributed to γ was much sharper in the previous study conducted at 75% RH at ambient temperature than observed at 75% RH and 25°C in this follow-up study. In the initial study, the samples were removed from their hydration environments each time they were analyzed via Raman spectroscopy, exposing them to ambient humidity for short amounts of time. This likely resulted in the loss of some of the residual water from the γ structure, sharpening the Raman peak. Variation in the crystallinity of γ between experiments could also explain why formation of δ was observed to occur readily in the initial experiment at 75% RH but to a much smaller extent in the follow-up study. Alternatively, this discrepancy could be due to differences in the initial $[(UO_2F_2)(H_2O)]_7 \cdot 4\,H_2O$ material. As shown in Chapter 2, the Raman spectra of different batches of $[(UO_2F_2)(H_2O)]_7 \cdot 4\,H_2O$ material were observed to differ slightly, suggesting that the structural and chemical properties of the material might vary between batches, affecting the hydration reactions.

Variation in the position of Raman peak attributed to γ over time and between different samples complicated the utility of MCR analysis, which deconvolutes the real spectra into linear combinations of "pure" spectral components that are assumed to be static. In reality, as demonstrated in this case, changes in local environment can induce slight shifts in the "pure" spectra over time. An approximate analysis was conducted by inputting the Raman spectrum of pure γ, obtained via experiments described in Chapter 4. These experiments revealed that γ has a shoulder near 825–830 cm^{-1}, previously not identified because it was obscured by the overlap of the uranyl stretching mode of δ. This explains why sample 7 is observed to have a shoulder near 825–830 cm^{-1} despite the absence of δ, as indicated by the lack of a peak near 864 cm^{-1} corresponding to the peroxide stretching mode. To further constrain the MCR analysis, the Raman spectrum of δ, identified from the initial particle hydration study and not observed to be particularly humidity

dependent, was fixed during the iterative calculations. In addition, the concentration of the initial $[(UO_2F_2)(H_2O)]_7 \cdot 4\,H_2O$ material was set to zero after a complete transformation from $[(UO_2F_2)(H_2O)]_7 \cdot 4\,H_2O$ to γ was observed. This prevented the growth of the peroxide stretching mode at 864 cm^{-1} from being falsely attributed to reformation of $[(UO_2F_2)(H_2O)]_7 \cdot 4\,H_2O$, which can be ruled out as the sample was devoid of fluorine in the SEM-EDS analysis. With these constraints, convergence was achieved in the MCR analysis of each sample, although the resulting deconvoluted spectral components and normalized concentration gradients are approximate.

Because the position and width of the Raman peak attributed to γ was observed to vary significantly between samples, MCR was applied to each sample independently. Since the spectra of δ was fixed for all samples and the spectra of the initial uranyl fluoride is clear from the initial scan, only the predicted spectra of γ differed between samples. The deconvoluted spectral components obtained from the analysis of sample 5 are shown in Figure 3.16 and are very similar to the spectra deconvoluted in the previous hydration study, shown in Figure 3.3. That initial study likely overestimated the relative concentration of δ because the low-energy shoulder of the γ Raman peak had not been identified. The opposite is the case in this follow-up study; the deconvoluted spectra of γ is predicted to have a more pronounced shoulder than observed in a pure sample of γ (Figure 4.14), likely leading to a slight underestimate of δ in a majority of the samples.

The normalized concentration gradients for the majority of the samples are shown in Figure 3.17. Samples 1 (25°C, 33% RH) and 6 (35°C, 32% RH) have been omitted since no reaction was observed to occur for these samples. It is clear from Figure 3.17 that two separate reactions occur over the experimental timescale, consistent with the findings of the initial hydration experiment. The first hydration reaction, from $[(UO_2F_2)(H_2O)]_7 \cdot 4\,H_2O$ to β, occurred rapidly at higher humidity levels, while the second reaction, from γ to δ, occurred much more slowly. As noted previously, the rates of both of these reactions were observed to vary between particles on the same sample. This variation is potentially due to differences in the morphology and/or the initial water content of the individual particles tracked in the experiment [88].

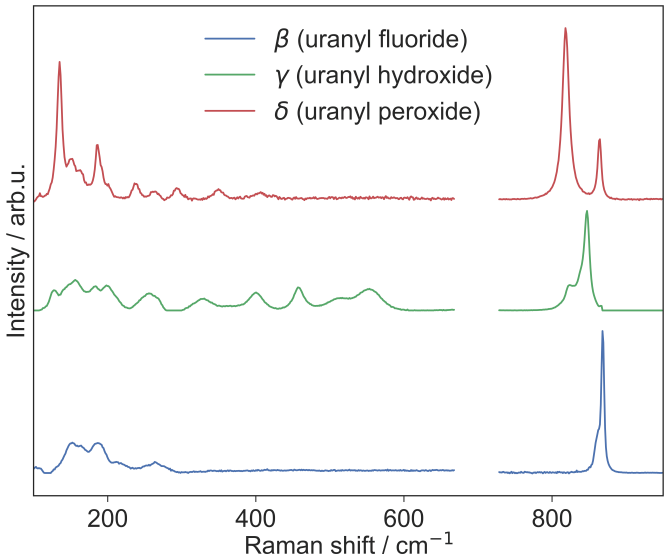

Figure 3.16: Deconvoluted spectral components from the MCR analysis of all particles on sample 5. The lower energy region of the Raman spectra has been scaled by a factor of three.

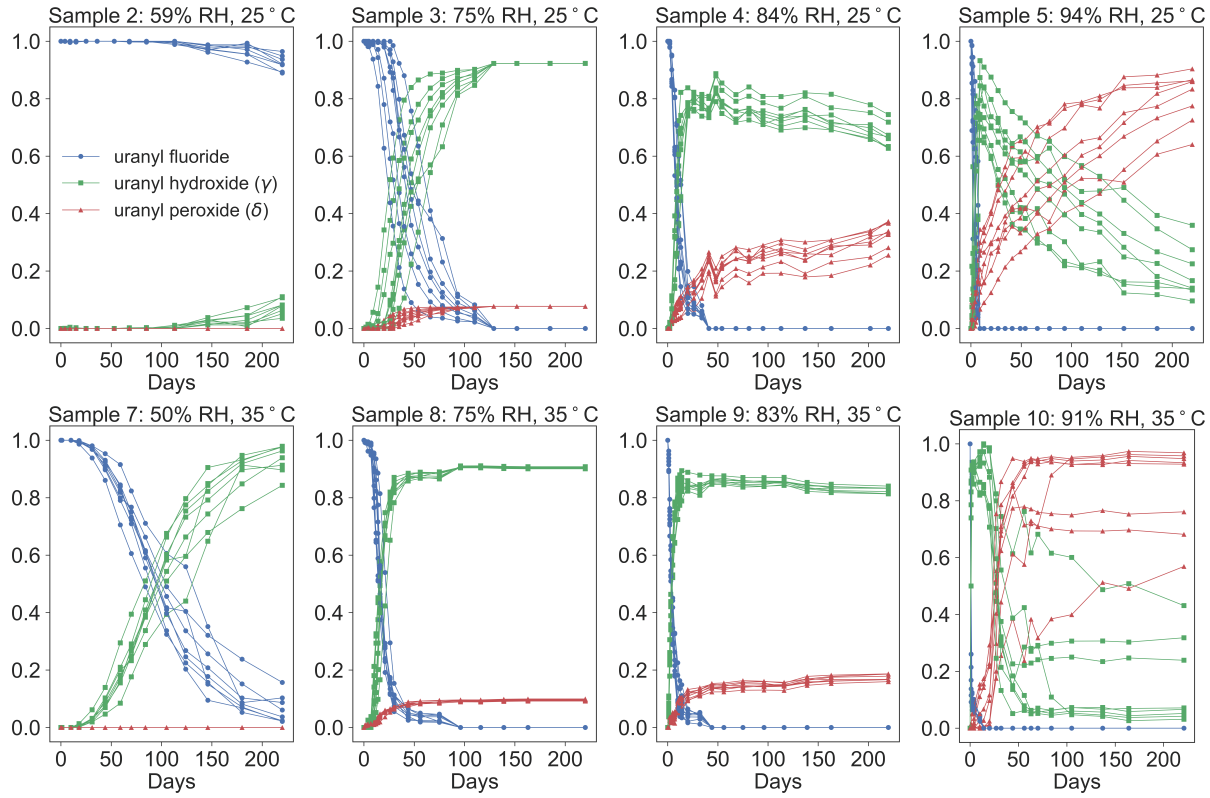

Figure 3.17: Normalized concentration of each species over time, as determined via MCR, on samples 2–5 and 7–10. Eight lines are shown for each sample, corresponding to the eight different particles analyzed over the course of the experiment.

To supplement the MCR analysis, the relative concentration of each species in each sample over time was also estimated directly from the relative peak intensities in the Raman spectra. A version of this method, using the relative intensities at 868, 845, and 820 cm^{-1} to correspond to the the fraction of $[(UO_2F_2)(H_2O)]_7 \cdot 4\,H_2O$, γ, and δ, respectively, was previously shown to produce similar concentration gradients to MCR [88]. Here, the method is updated to better account for observed peak overlap. For example, the observed intensity at 820 cm^{-1} was previously assumed to directly correlate to the concentration of δ present in the particle. However, further characterization of the γ hydration species, presented in Chapter 4, clarifies that γ has a shoulder near 825 cm^{-1} in its Raman spectrum in addition to a dominant peak near 845 cm^{-1}. This shoulder overlaps the uranyl stretching mode of δ. The ratio of the expected intensity at 820 cm^{-1} and 845 cm^{-1} for γ was determined to be 0.15 from the Raman spectrum of what is assumed to be pure γ (Figure 4.14). The intensity at 820 cm^{-1} corresponding to δ is therefore taken to be the raw intensity of the 820 cm^{-1} peak minus 0.15 times the intensity of the 845 cm^{-1} peak. Similarly, the amount of $[(UO_2F_2)(H_2O)]_7 \cdot 4\,H_2O$ is described by the intensity of the 868 cm^{-1} peak minus 0.28 times the amount of δ due to the overlap of the $[(UO_2F_2)(H_2O)]_7 \cdot 4\,H_2O$ uranyl stretching mode and δ peroxide stretching mode. Finally, the amount of γ in the sample is described by the intensity of the 845 cm^{-1} peak minus 0.06 times the intensity of the 820 cm^{-1} peak.

The resulting concentration gradients for each species over time are shown in Figure 3.18. The curves are again approximate, as the overlap ratios described above are expected to be temperature and humidity dependent. The results were reasonably similar to the MCR results in Figure 3.17. The most notable difference is for sample 7; the MCR analysis did not resolve δ in this sample, while the peak intensity method did. The lack of a peroxide stretching mode at 864 cm^{-1} in this sample after hydration (Figure 3.9), suggests that the concentration gradients calculated via MCR are more accurate, at least for this sample. On the other hand, the MCR analysis showed the γ and δ concentrations stabilizing towards the end of the experiment in samples 3 and 8. In Figure 3.9, it is clear that the ratio of the 845 cm^{-1} and 820 cm^{-1} peaks continues to change in these samples, as shown with the peak intensity method. These inconsistencies limit the feasibility of a quantitative kinetic analysis of the second reaction, from γ to δ.

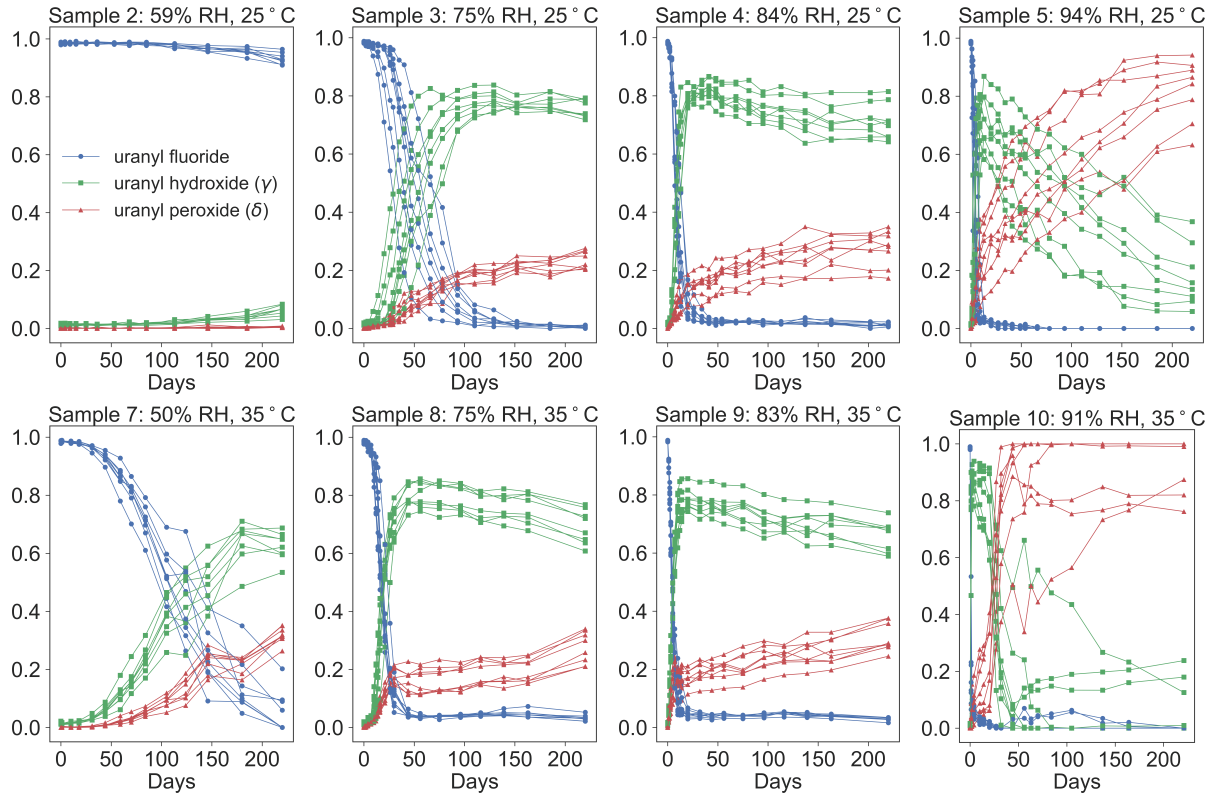

Figure 3.18: Normalized concentration of each species over time, as determined via ratios of the Raman intensity at 868 cm^{-1}, 845 cm^{-1}, and 868 cm^{-1}, on samples 2–5 and 7–10. Eight lines are shown for each sample, corresponding to the eight different particles analyzed over the course of the experiment.

3.5 Kinetic analysis

3.5.1 Uranyl fluoride to uranyl hydroxide (γ)

While neither analysis method seems to fully resolve the relative concentrations of the γ and δ across this dataset, the concentration gradients of the initial $[(UO_2F_2)(H_2O)]_7 \cdot 4\,H_2O$ material calculated with each method are quite consistent. The relative concentration of this species is easier to determine because the 868 cm^{-1} peak does not shift in frequency or broaden significantly with hydration. The quantification of this species over time allows for a more detailed kinetic analysis of the first reaction, from $[(UO_2F_2)(H_2O)]_7 \cdot 4\,H_2O$ to γ, to reveal mechanistic information.

Figure 3.19 shows the concentration gradient of $[(UO_2F_2)(H_2O)]_7 \cdot 4\,H_2O$ for a characteristic particle on samples 2, 3, 4, 7, and 8 to better illustrate the curve shape. The remaining samples were excluded because the transformation from $[(UO_2F_2)(H_2O)]_7 \cdot 4\,H_2O$ to γ either did not proceed significantly over the experiment timescale (samples 1 and 6), or occurred too rapidly to collect an adequate number of data points along the reaction curve (samples 5, 9, and 10). The concentration of $[(UO_2F_2)(H_2O)]_7 \cdot 4\,H_2O$ over time follows a sigmoidal shape; this is most apparent for sample 7, where the complete conversion of $[(UO_2F_2)(H_2O)]_7 \cdot 4\,H_2O$ occurs over roughly the same timescale as the experiment. The rate of conversion from $[(UO_2F_2)(H_2O)]_7 \cdot 4\,H_2O$ to γ is slow at first but then accelerates as the conversion proceeds. As the amount of $[(UO_2F_2)(H_2O)]_7 \cdot 4\,H_2O$ is reduced, the rate of conversion again slows.

This sigmoid shape is suggestive of some sort of nucleation-and-growth mechanism, which often describes the kinetics of crystallization and solid-state phase transitions [99]. Nucleation reactions occur in three phases, as illustrated in Figure 3.20. Nuclei begin to form during the initial induction phase. As these nuclei begin to grow and additional nuclei are formed, the reaction rate increases significantly. Finally, the reaction slows as the growing particles come into contact with each other and as the amount of remaining reactant where nuclei can form is decreased.

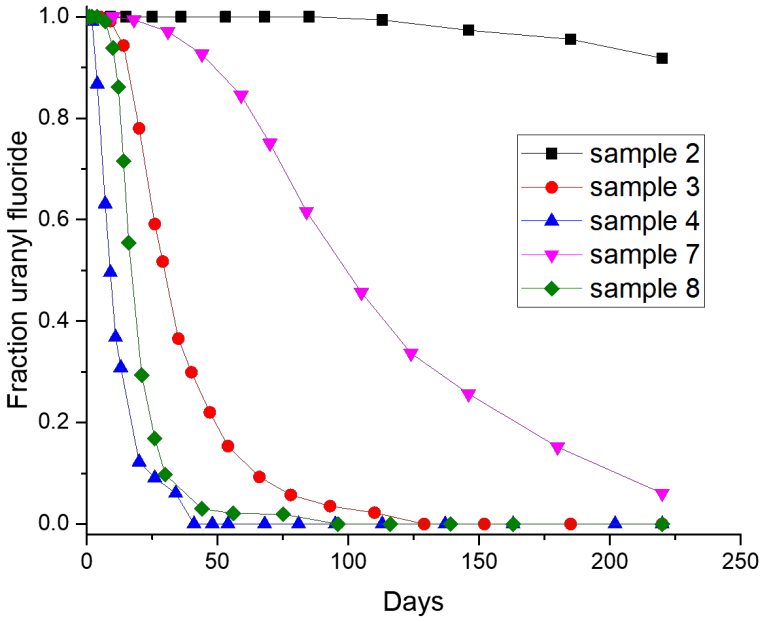

Figure 3.19: Normalized concentration gradients of $[(UO_2F_2)(H_2O)]_7 \cdot 4\,H_2O$ for a characteristic particle on samples 2, 3, 4, 7, and 8 over the 220 day hydration experiment.

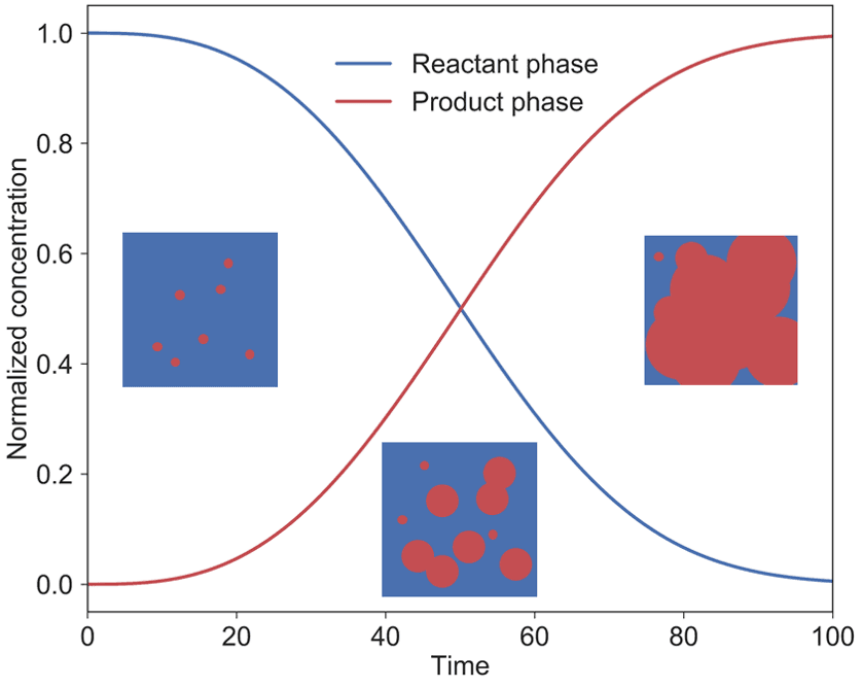

Figure 3.20: Normalized concentration curves of the reactant and product phases in a solid-state nucleation reaction. Insets show a schematic of the three-phase nucleation-and-growth process. Nuclei begin to form during the initial induction phase. As these nuclei begin to grow and additional nuclei are formed, the rate increases significantly. Finally, the rate slows as the growing particles come into contact with each other and as the amount of remaining reactant where nuclei can form is decreased.

The simplest nucleation reaction model is described by the Avrami equation [12, 13],

$$y = e^{-(kt)^n}, \tag{3.1}$$

where $y(t)$ is the normalized concentration of the reactant species over time, and n and k are constants that describe the rate. From the derivation of the Avrami equation, n is related to the number of dimensions in which nuclei growth occur, and is thus sometimes fixed or constrained to be an integer value. However, due to the often irregular shape of nuclei as well as the assumptions of this model, n is also often determined to be noninteger. The other fit parameter in the Avrami model, k, is a time independent rate constant, with units [1/time]. Thus, one of the assumptions of the Avrami equation is that the nucleation and growth rate are not dependent on time or the extent of the reaction. Additionally, nucleation is assumed to occur randomly and homogeneously.

The Avrami equation (Equation 3.1) can be rewritten,

$$\ln(-\ln(1 - y(t))) = n\ln(k) + n\ln(t), \tag{3.2}$$

allowing for the determination of n and k by plotting $\ln(-\ln(y(t)))$ vs. $\ln(t)$, which will be linear for reactions following Avrami behavior. Figure 3.21 shows $\ln(-\ln(y(t)))$ vs. $\ln(t)$ plotted for representative particles on samples 2, 3, 4, 7, and 8. The curves for samples 2 and 7 look approximately linear, but the curves for the remaining samples are clearly nonlinear, indicating that the simplistic Avrami model cannot accurately describe the kinetics of the observed reaction. This is also clear from Figure 3.22, which shows the $[(UO_2F_2)(H_2O)]_7 \cdot 4\,H_2O$ concentration curves for a representative particle on samples 3, 4, 7, and 8 fit to the Avrami model. While the Avrami model reproduces the general shape of these curves, it overestimates the reaction rate as the conversion proceeds toward completion. This indicates that the nucleation and growth rates in this reaction are time dependent.

While the Avrami model is still widely used to interpret solid-state reaction mechanisms [99], newer dispersive kinetic models have attempted to account for time-dependent nucleation and growth rates. Prominent examples inslude the acceleratory and deceleratory

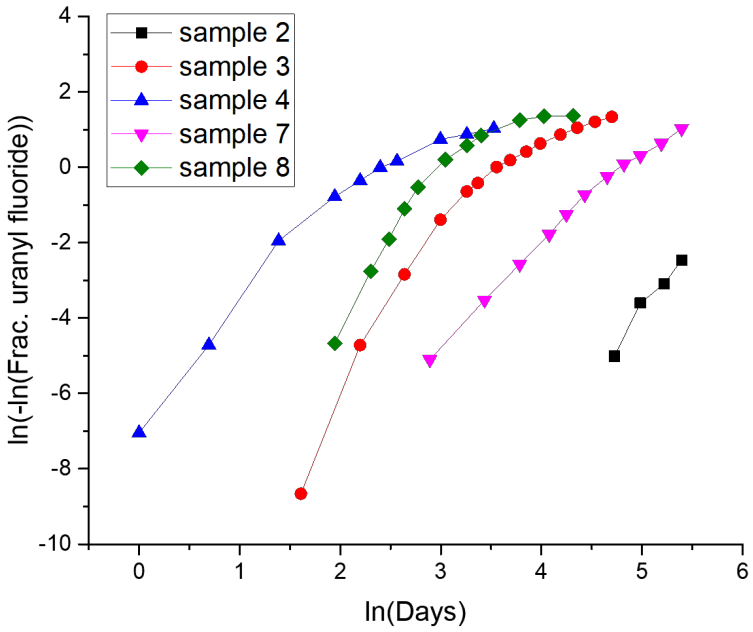

Figure 3.21: $\ln(-\ln(y(t)))$ vs. $\ln(t)$ plotted for the uranyl fluoride concentrations over time for representative particles on samples 2, 3, 4, 7 and 8.

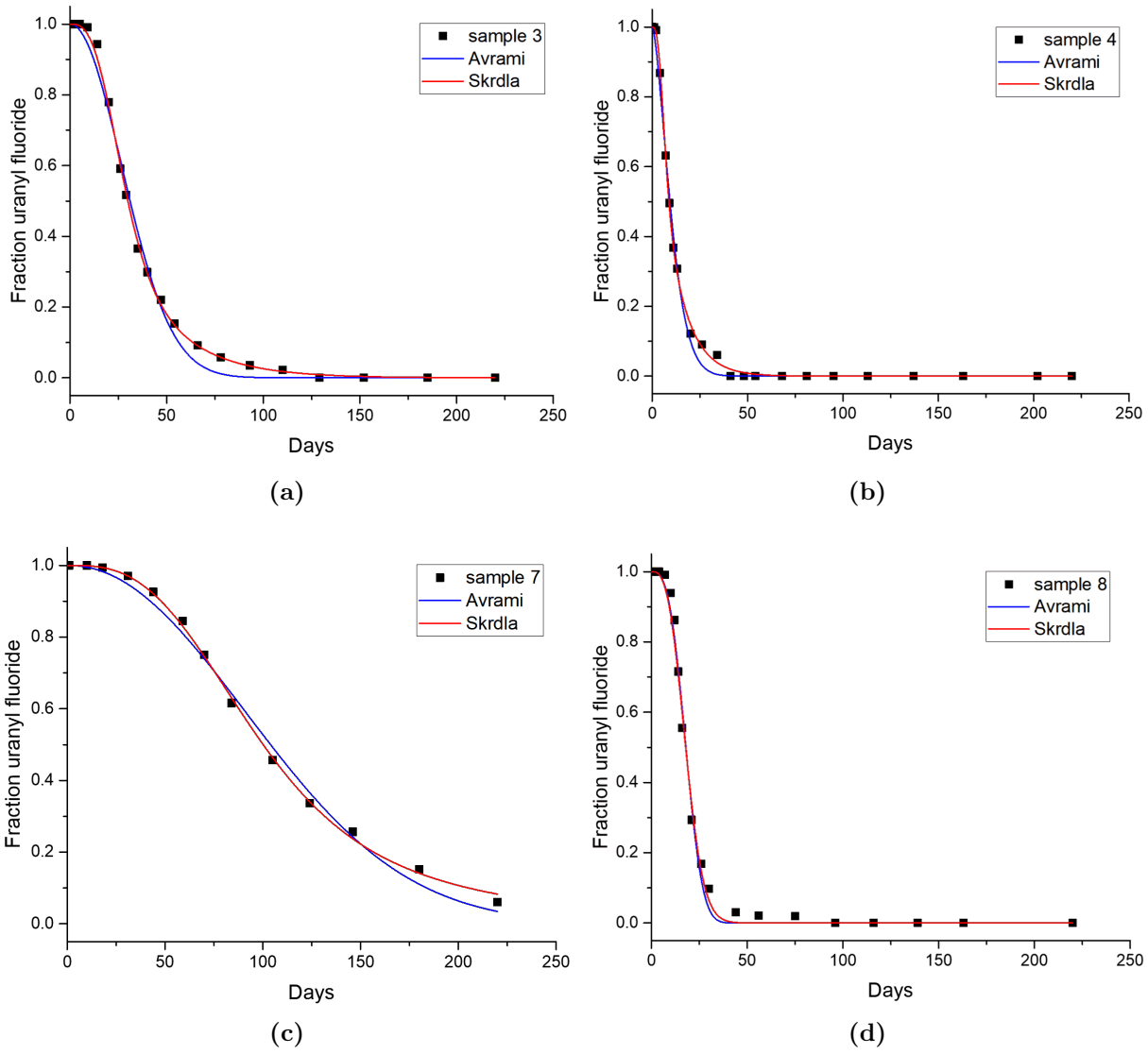

Figure 3.22: Normalized concentration gradients of $[(UO_2F_2)(H_2O)]_7 \cdot 4\,H_2O$ for a representative particle on (a) sample 3, (b) sample 4, (c) sample 7, and (d) sample 8 over the 220-day hydration experiment, fit to the Avrami and Skrdla deceleratory dispersive models. The Avrami n/k[1/hr] parameters were 2.0/0.069, 1.55/0.085, 2.1/0.0082, and 3.0/0.0491 for samples 3, 4, 7, and 8, respectively. The Skrdla α[1/hr]/β[1/hr^2] parameters were 0.037/0.00112, 0.095/0.024, 0.0115/0.000092, and 0.2/0.0006.

dispersive models introduced by Skrdla in 2009 [145]. These models are described by Equation 3.3 (acceleratory) and Equation 3.4 (deceleratory). In these models, the rate "constant", k, is, in fact, no longer constant, but rather either increases or decreases as a function of time. The fit parameters, α and β, describe the initial rate and the evolution of the rate over time, respectively. Skrdla presents a physicochemical interpretation of these parameters as well, relating α and β to the activation enthalpy and entropy, respectively [145].

$$y(t) = e^{(-\alpha/t)(e^{\beta t^2}-1)}; \quad k(t) = \alpha e^{\beta t^2} \tag{3.3}$$

$$y(t) = e^{(\alpha t)(e^{-\beta t^2}-1)}; \quad k(t) = \alpha e^{-\beta t^2} \tag{3.4}$$

A comparison of the general shape of both Skrdla models and the Avrami model is shown in Figure 3.23. Based on the fact that the time-independent rate constant of the Avrami model seems to overestimate the conversion rate toward the end of the conversion (Figure 3.22), the deceleratory Skrdla model was fit to the data. These fits, shown compared to the Avrami fits in Figure 3.22, reduced the residuals in each case. Additional sigmoidal models, such as the Prout-Tompkins [134, 24] model, were also fit to the data but resulted in larger residuals than the Skrdla deceleratory model and are not shown in Figure 3.22.

The deceleratory nature of the conversion from $[(UO_2F_2)(H_2O)]_7 \cdot 4\,H_2O$ to γ suggests that it is denucleation, rather than nucleation, driven [145]. This means that formed nuclei promote the dissociation of the reactant species ($[(UO_2F_2)(H_2O)]_7 \cdot 4\,H_2O$) rather than the formation of the product species (γ). Denucleation reactions tend to be deceleratory because the reaction rate is correlated to the volume of unreacted reactant where new nuclei can form, which is small toward the end of the conversion [145].

As discussed in Chapter 2, it is likely that the $[(UO_2F_2)(H_2O)]_7 \cdot 4\,H_2O$ structure can absorb additional water molecules into its pores with exposure to elevated water vapor pressure. A quasi-elastic neutron scattering study by Miskowiec et al. found that these absorbed water molecules could not be removed upon desiccation [113], suggesting that these water molecules form strong hydrogen bonds to the uranyl framework, as anticipated from the structure. A plausible denucleation mechanism involves the incorporation of water molecules into specific positions within the crystal structure that drives the dissociation of

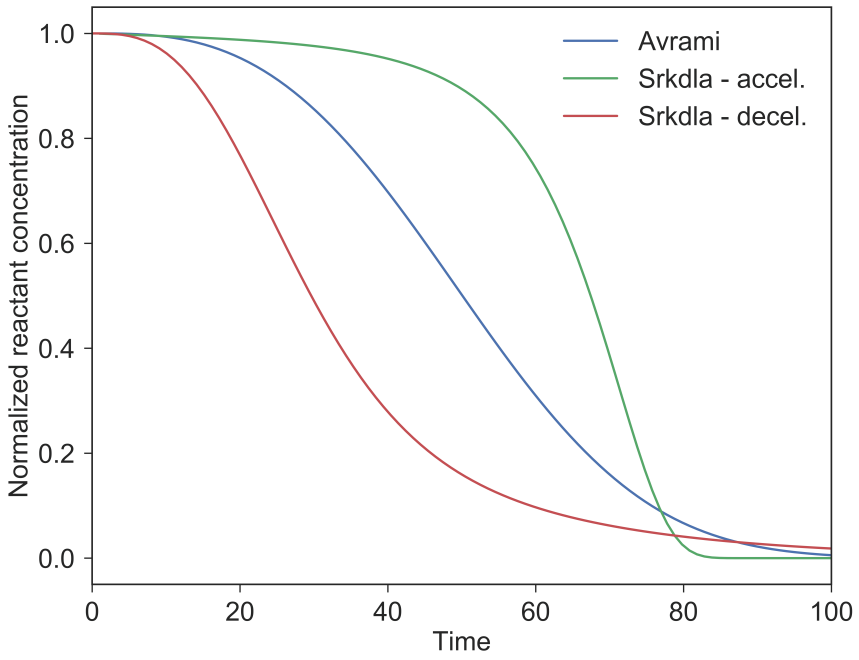

Figure 3.23: Comparison of the Avrami and acceleratory/deceleratory dispersive models of Skrdla. The example parameters are Avrami: k=0.0176 1/hr, n=1.912, Skrdla - accel.: α=0.5 1/hr, β=0.001 1/hr^2, Skrdla - decel.: α = 0.04 1/hr, β = 0.001 1/hr^2.

the fluorine ligands at these sites, forming hydroxy ligands and releasing HF gas that leaves the crystal matrix. A dissociative reaction mechanism is consistent with findings of Kips et al. that the loss of fluorine can be accelerated with UV irradiation [87].

Attempts to fit all of the $[(UO_2F_2)(H_2O)]_7 \cdot 4\,H_2O$ concentration curves to the Skrdla model were only successful for samples 3, 4, 7 and 8. The fitted α and β parameters for all particles on these four samples are shown in Figure 3.24, plotted against the water vapor pressure. Both α and β increase with increasing water vapor pressure, although the relationship is dependent on the temperature as well. Using the average α and β values each of the four samples analyzed, the calculated time-dependence of the respective reaction rates are shown in Figure 3.25. It is clear that at higher water vapor pressure, the initial rate of the denucleation is high but also decreases more rapidly. The rate curves in Figure 3.25 are qualitatively similar to the $[(UO_2F_2)(H_2O)]_7 \cdot 4\,H_2O$ concentration curves of the same samples, further supporting a reactant-driven denucleation mechanism.

The relationship between the reaction rate and water vapor pressure is unclear from Figure 3.24 since only two samples could be fit at each temperature. To get a clearer picture of the effect of temperature and water vapor pressure on the rates, the concentration curves for all of the particles on samples 2–5 and 7–9 of the curves were fit to the simpler Avrami model. Sample 10 was excluded from this analysis because the data collected during this first rapid hydration reaction were sparse, and because it is unclear how the observed deliquescence of particles on this sample would effect the reaction mechanism. To achieve convergent fits for the remaining particles and better compare the k values, n was arbitrarily fixed at 2.5 for all fits.

Figure 3.26 shows the resulting k values as a function of the water vapor pressure. The water vapor pressure dependence at each individual temperature is qualitatively as expected, but the two sets of data do not follow the same trendline. The reaction rates for samples stored at 35°C are lower than predicted solely by extrapolating the results from 25°C to higher water vapor pressure. This is likely explained by the effect that temperature has on the water sorption isotherm; at constant water activity, the amount of absorbed water is reduced with increasing temperature [44]. The first step of the proposed denucleation reaction involves the absorption of additional water molecules into the pores of the $[(UO_2F_2)(H_2O)]_7 \cdot 4\,H_2O$

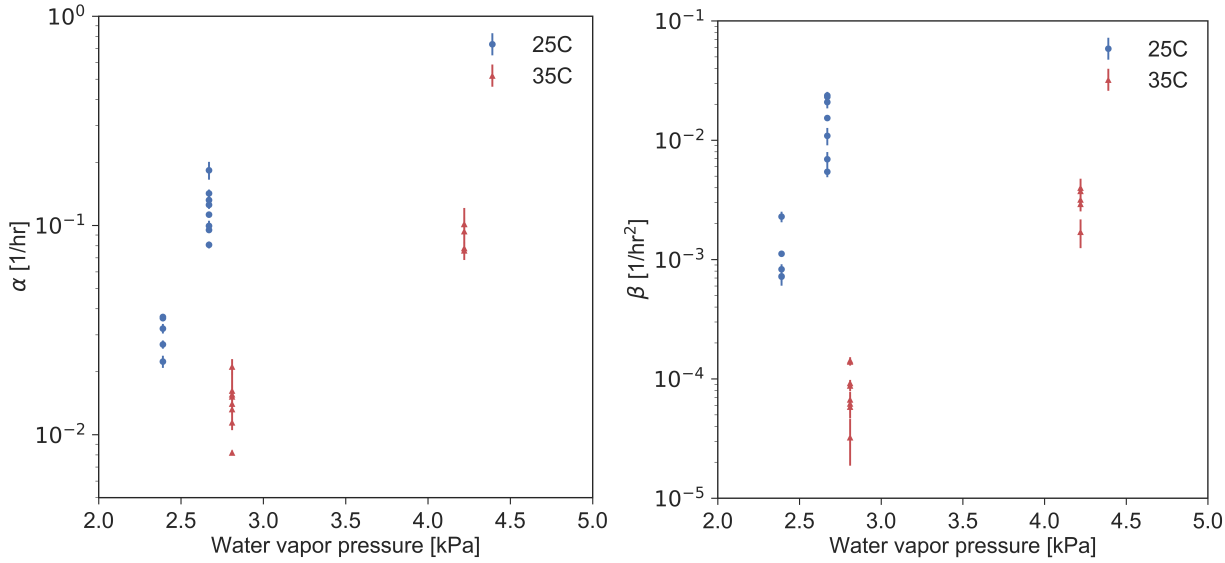

Figure 3.24: Skrdla (a) α and (b) β parameters vs. water vapor pressure for particles on samples 3, 4, 7 and 8. Particles from samples 3 and 4 (25°C) are shown in blue, and particles from samples 7 and 8 (35°C) are shown in red. Note the logarithmic y-axes.

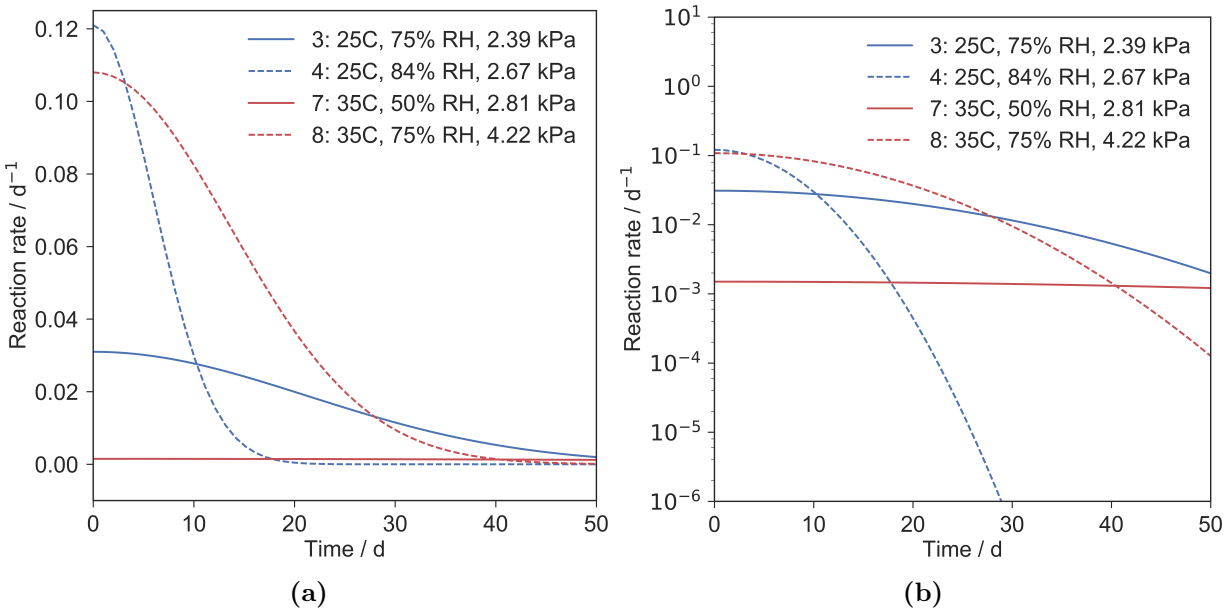

Figure 3.25: Time dependence of the reaction rate based on the average α and β parameters for samples 3, 4, 7, and 8, shown with a (a) linear and (b) logarithmic y-scale.

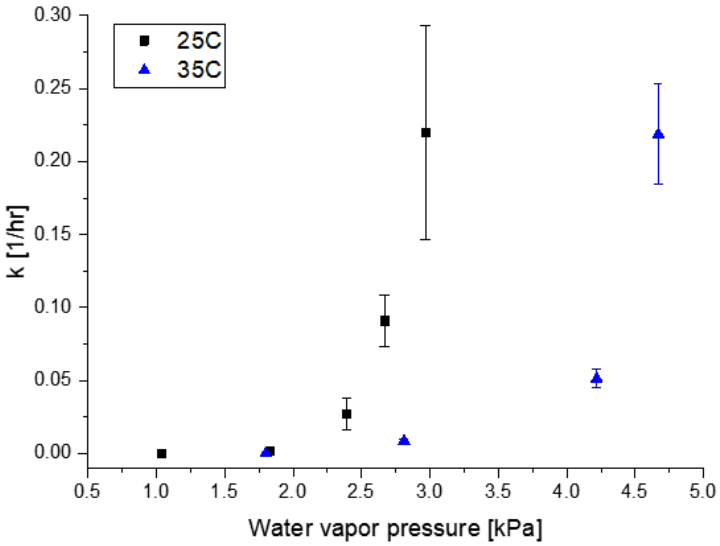

Figure 3.26: Avrami k parameter vs. water vapor pressure, including fits from all particles on samples 2–5 and 7–9. Particles from samples 2–5 (25°C) are shown in black, particles from samples 7–9 (35°C) are shown in blue. n has been fixed at 2.5 in all fits.

structure. At higher temperatures, less water is absorbed, which has a negative effect on the overall reaction rate. Repeating this experiment over a wider temperature range would help clarify this effect.

3.5.2 Uranyl hydroxide (γ) to uranyl peroxide (δ)

As discussed previously, a thorough kinetic analysis of the second reaction, from γ to δ, is impeded by the inability to accurately resolve the relative concentrations of these two species due to variation in the shape and location of the Raman peak attributed to γ. Figure 3.27 shows the approximate concentration gradients of δ over time as calculated by the MCR and point ratio methods. While precise rate information cannot be extracted from these approximations, it is clear that formation of δ is dependent on the water vapor pressure. The δ species was the dominant species by the end of the experiment in samples 5 and 10, which were exposed to the highest RH. Temperature again seems to have a negative effect on the reaction rate. Samples 8 and 9 were stored under higher vapor pressure than sample 5 (4.22 and 4.67 kPa vs. 2.97 kPa, respectively), yet the rate of δ formation was much greater in sample 5, indicating that the elevated temperature of samples 8 and 9 impeded formation. This can be potentially explained again by the negative effect that temperature has on water absorption. Alternatively, this effect may be related to the finding, described in the next chapter (Section 4.5), that the structure of γ is sensitive to small changes in temperature. A contraction in the interlayer spacing of the γ structure could have a significant effect on the reactivity of the species.

3.6 Summary and future directions

Two particle hydration studies have demonstrated that uranyl fluoride is unstable in humid conditions, with a threshold humidity of 30–60% RH depending on the temperature (25°C vs. 35°C). Above this threshold, uranyl fluoride undergoes a transformation to γ, tentatively identified in this chapter as a uranyl hydroxide hydrate species. Further characterization of this species is discussed in Chapter 4. With exposure to high enough water vapor pressure, γ can be transformed into δ, identified as a uranyl peroxide hydrate species similar to studtite.

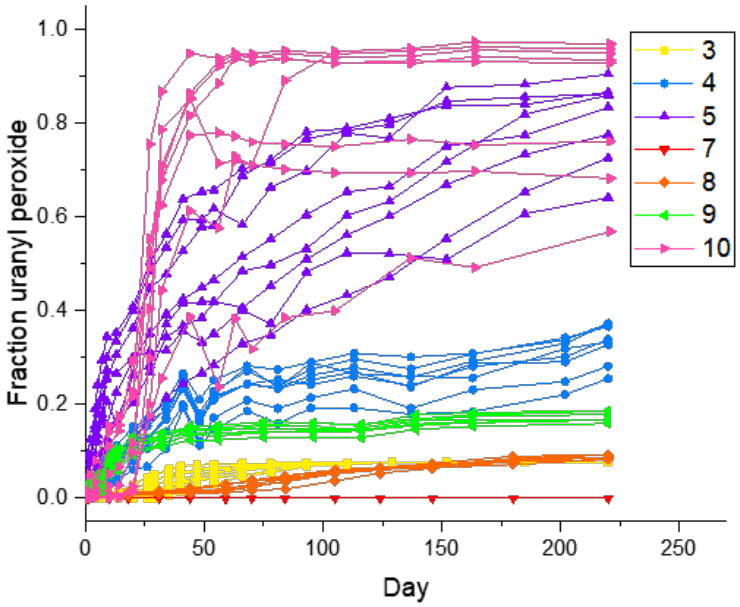

(a)

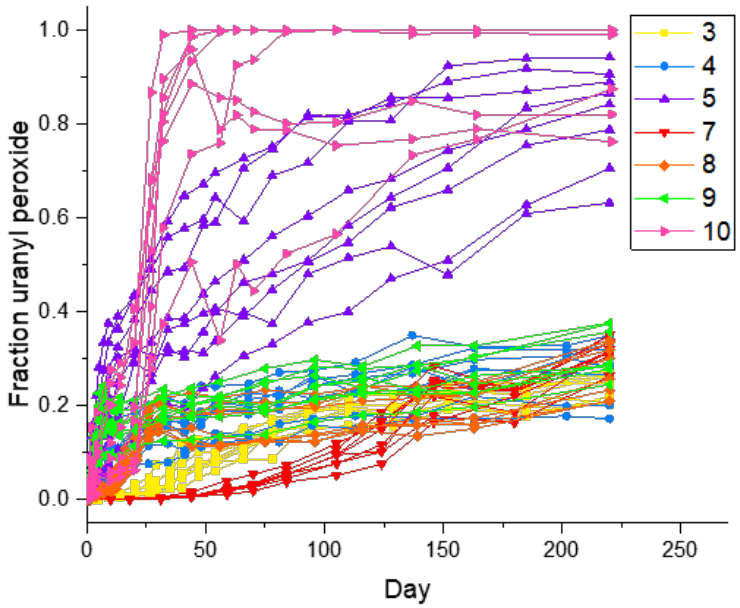

(b)

Figure 3.27: Concentration gradients for uranyl peroxide (δ) over time for samples 3–5 and 7–10 as calculated via (a) MCR and (b) the point ratio method. Samples 1, 2, and 6 are omitted, as δ was not observed to form in the timescale examined.

The Raman spectra of these three species overlap significantly, necessitating the tracking of particles over time to deconvolute the pure spectra and reveal the concentration gradients.

A partial loss of fluorine in uranyl fluoride particles upon hydration was first documented by Kips et al. via SEM-EDS and IM-SIMS. [87] The hydration studies discussed in this chapter confirm this finding, clarifying that a complete loss of fluorine is expected under a humid environment. Analysis of the same particles over several months provides a much more complete understanding of this reaction and insight into the reaction mechanism. The deceleratory sigmoidal shape of this conversion is consistent with a denucleation reaction mechanism, suggesting that the absorption of additional water into the $[(UO_2F_2)(H_2O)]_7 \cdot 4\,H_2O$ structure creates reactive sites where water molecules interact with fluorine ligands, leading to the dissociation of the fluorine ligands and release of HF gas. The observed effect of temperature on the reaction rate is consistent with a multistep mechanism involving water absorption; the increase in the rate at elevated temperature was not observed to fully scale with the correlated increase in water vapor pressure because the amount of water absorbed into the $[(UO_2F_2)(H_2O)]_7 \cdot 4\,H_2O$ structure is reduced with increasing temperature. Additional experiments at fixed water vapor pressure and a wider temperature range would help clarify the temperature dependence of the rate, providing additional mechanistic insight. Future computational studies could also further clarify the mechanistic details of this reaction. In particular, nudged elastic band calculations could provide insight about potential transition states in the water–fluorine interaction.

The formation of a uranyl peroxide species from the uranyl hydroxide intermediate was also observed on multiple samples stored at high humidity. This reaction is clearly dependent on the water vapor pressure; in the first particle hydration study, the rate of uranyl peroxide formation was significantly accelerated when the RH was increased from 75% to 100%. A detailed analysis of the water vapor pressure and temperature dependence of this second reaction is complicated, however, by the water vapor pressure and temperature dependence of the structure of the uranyl hydroxide intermediate. A worthwhile follow-up experiment would be to track the uranyl peroxide reaction under a variety of conditions starting from the same pure γ starting material.

Chapter 4

Characterization of a novel layered uranyl hydroxide hydrate (γ) from the hydration of uranyl fluoride

Chapter 3 demonstrated that uranyl fluoride is not stable under humid environments, but instead transforms into two hydration products, γ and δ. SEM-EDS measurements confirm that neither γ nor δ contain fluorine, identifying them as uranyl hydroxide or peroxide species rather than additional uranyl fluoride hydrates. The Raman spectrum of the first hydration product, γ, is generally consistent with uranyl hydroxide hydrates like the minerals schoepite ($[(UO_2)_4O(OH)_6] \cdot 6\,H_2O$) and metaschoepite ($[(UO_2)_4O(OH)_6] \cdot 5\,H_2O$). This chapter presents a more thorough characterization of γ, in part via a comparative analysis with respect to synthetic metaschoepite. The structure of γ is shown to be similar to that of schoepite and metaschoepite, but with a significantly expanded layer spacing that allows for the incorporation of additional interlayer water molecules. This structural distinction explains differences in the vibrational spectra of γ and synthetic metaschoepite, as well as in the chemical behavior upon desiccation and dehydration. Components of this chapter come from the following papers:

M. C. Kirkegaard, J. L. Niedziela, A. Miskowiec, A. E. Shields, and B. B. Anderson. "Elucidation of the structure and vibrational spectroscopy of synthetic metaschoepite and its dehydration product." Accepted to *Inorg. Chem.*

M. C. Kirkegaard, M. W. Ambrogio, T. L. Spano, J. L. Niedziela, A. Miskowiec, A. E. Shields and B. B. Anderson. "Formation of a uranyl hydroxide hydrate via hydration of $[(UO_2F_2)(H_2O)]_7 \cdot 4\,H_2O$." Submitted to *Dalton Trans.*

4.1 Literature review of uranyl hydroxide hydrates

4.1.1 Known uranyl hydroxide hydrate structures

Much of the current understanding of solid-state uranyl hydroxide species comes from the study of minerals [130]. The hydrated uranyl hydroxide mineral schoepite, $[(UO_2)_4O(OH)_6] \cdot 6\,H_2O$, was first described by Walker et al. in 1923 [164] and was partially characterized in the following decades [34]. In the 1990s, a full structure determination was made by Finch et al. from a naturally occurring sample. X-ray diffraction (XRD) confirmed that the uranyl ion in schoepite is coordinated to five hydroxy groups, creating edge-sharing UO_7 pentagonal bipyramids that form 2D layers (Figure 4.1). Water molecules exist between the layers, hydrogen bonded to the hydroxy groups. These water molecules can also act as hydrogen bond donors to uranyl oxygens [53].

It was noted in the 1960s that multiple distinct uranyl hydroxide hydrates exist, and that conversion between these forms occurs readily upon hydration/dehydration [34, 33]. The most notable example of this is the slow dehydration of schoepite in air to a partially dehydrated form known as metaschoepite [54]. Because this transformation occurs under ambient conditions, schoepite and metaschoepite are often found together in nature [55, 54].

The stoichiometry of metaschoepite was identified as $[(UO_2)_4O(OH)_6] \cdot 5\,H_2O$, with one fewer water molecule than schoepite [45, 71, 54]. Metaschoepite is difficult to distinguish from schoepite with powder XRD, suggesting that they have similar crystal structures and leading Finch et al. to propose that the dehydration transition involves the simple removal of specific water molecules [54]. However, while metaschoepite and schoepite display very

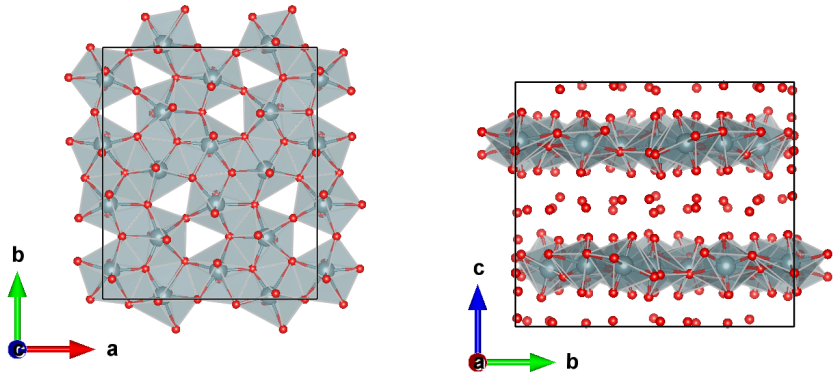

(a) **(b)**

Figure 4.1: (a) Top-down and (b) side views of the crystal structure of schoepite, $[(UO_2)_4O(OH)_6] \cdot 6\,H_2O$, as determined by Finch et al.[53] Oxygen atoms in between the layers of uranyl polyhedra correspond to water molecules; hydrogen atoms are omitted as their location was not solved experimentally.

similar powder XRD patterns, they are readily distinguishable via single-crystal diffraction [34]. In 1999, Weller et al. finally produced large enough single crystals of synthetic metaschoepite for full structural characterization via this method [171].

Single-crystal diffraction studies confirmed that metaschoepite has a very similar structure to schoepite, with the same layers of edge-sharing pentagonal bipyramids in layers. Slight differences in the orientation and tilt of the pentagonal bipyramids were noted, as well as differences in the organization of the interlayer water molecules. In schoepite, there are the same number of hydroxy groups and water molecules, such that each hydroxy group forms a strong hydrogen bond with a water molecule. In metaschoepite, this is no longer the case and two water molecules interact with hydroxy groups in both layers, forming weaker hydrogen bonds [171]. This leaves one remaining water molecule that does not interact with a hydroxy group but rather forms hydrogen bonds with the other waters and the uranyl oxygens [171]. While Finch et al. suggested that the dehydration transition involved the simple removal of specific water molecules, the distinct arrangement of water molecules in metaschoepite suggests that the dehydration transition is more complicated and that the removal of four water molecules in the unit cell is followed by shifts in the remaining oxygen positions [171]. The minor structural differences between schoepite and metaschoepite are shown in Figure 4.2.

Due to these minor structural differences, schoepite and metaschoepite can be distinguished by their a and b lattice parameters [171, 90]. An analysis of all crystallographic studies of schoepite [19, 133, 34, 53, 131] and metaschoepite [34, 171, 93, 25, 90] finds that while the a and b lattice parameters are both statistically distinct ($p = 5.5 \cdot 10^{-5}$ and 0.026, respectively), the c lattice parameter, which defines the interlayer spacing, is not statistically distinct ($p = 0.48$). This is illustrated in Figure 4.3. Thus, removal of interlayer water molecules in the transition from schoepite to metaschoepite does not change the interlayer spacing.

An additional uranyl hydroxide hydrate mineral, paraschoepite, was identified by Schoep and Stradiot in 1947 [142] and later partially characterized via powder XRD by Christ and Clark in 1960 as a component of a mixed phase mineral sample [34]. No further evidence of paraschoepite has been presented. The existence of paraschoepite was more

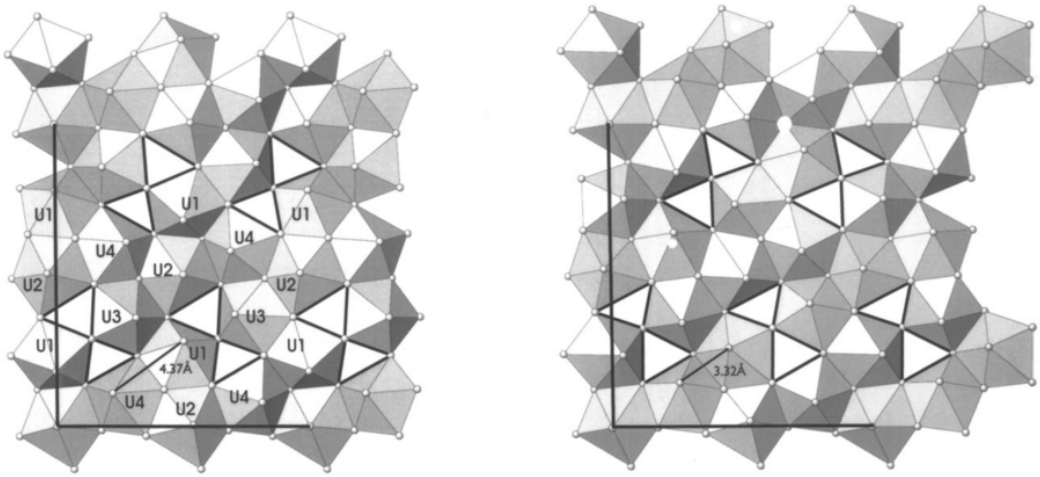

(a)

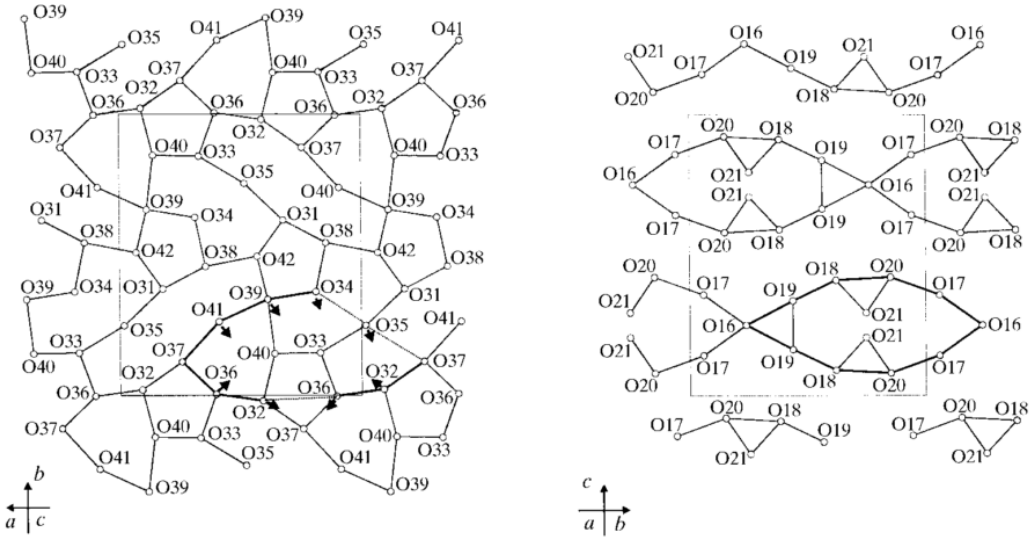

(b)

Figure 4.2: (a) Comparison of the uranyl layers in schoepite (left) and metaschoepite (right). Reproduced from Weller et al. 2000 [171]. (b) Comparison of the position of oxygen atoms in the interlayer water layers in schoepite (left) and metaschoepite (right). Reproduced from Weller et al. 2000 [171].

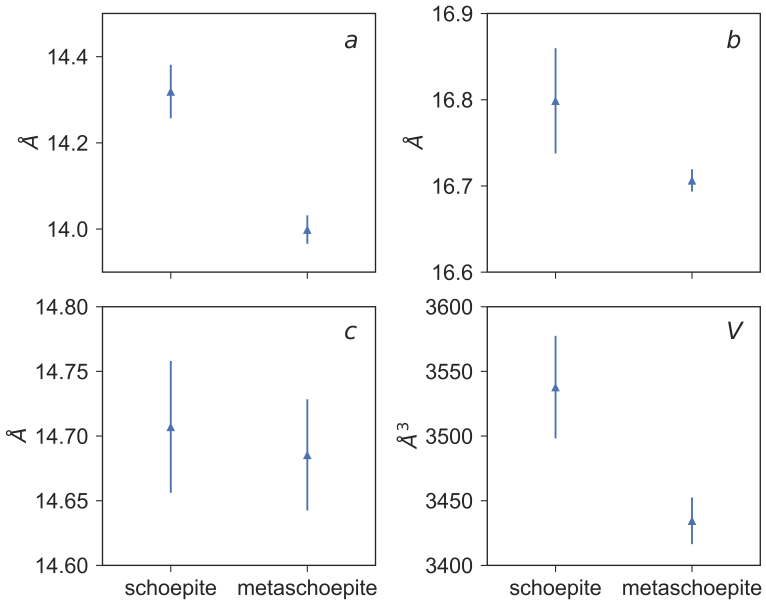

Figure 4.3: Average lattice parameters reported from structural characterization of schoepite [19, 133, 34, 53, 131] and metaschoepite [34, 171, 93, 25, 90]. Error bars are $\pm\sigma$. For consistency, lattice parameters for both schoepite and metaschoepite are defined as reported for schoepite, which belongs to the Pbcn space group. The c parameter is normal to the uranyl layers.

recently questioned by Burns et al., who suggested that the extraneous diffraction maxima in a schoepite sample that Christ and Clark assigned to paraschoepite may have been due to crystallographically oriented inclusions of the mixed-valence uranium oxide hydrate ianthinite, $[U_2{}^{4+}(UO_2)_4O_6(OH)_4(H_2O)_4] \cdot 5\,H_2O$ [28]. Alternatively, paraschoepite has been interpreted as a mixture of schoepite, metaschoepite, and "dehydrated schoepite" [55]. Thus, there remains lingering uncertainty over the number of different uranyl hydroxide hydrate species that exist, whether as minerals or produced synthetically. The identification of a likely uranyl hydroxide hydrate species formed from the hydration of uranyl fluoride is particularly interesting in this light, and further characterization of this species is motivated to elucidate how this species is distinct from other known or predicted species.

4.1.2 Vibrational spectroscopy of uranyl hydroxide hydrates

While natural and synthetic uranyl hydroxides hydrates have been studied at length, there is significant variation among published vibrational spectra supposedly corresponding to the same species. Raman spectra of uranyl hydroxide species typically have at least one symmetric uranyl stretching mode in the 830-855 cm^{-1} range, as well as peaks near 550 and 450 cm^{-1}, but are not very consistent, as illustrated in Figure 4.4 [4, 60, 132, 31, 2, 70, 69, 18, 165]. Infrared (IR) spectra, while rarer in the literature, are similarly inconsistent [71, 3]. Characterizing pure species is difficult since transitions between the different states of hydration occur at ambient conditions. Naturally occurring samples of uranyl hydroxide have been shown via single-crystal diffraction to contain multiple phases, [55, 54] so it is not surprising that Raman spectra of natural samples are inconsistent and show multiple peaks in the uranyl stretching region (Figure 4.4).

However, this discrepancy persists among synthetically produced samples as well. This can be explained at least in part by the sensitivity of these species to dehydration, whether via laser heating or desiccating storage conditions. It was recently demonstrated in a study related to this present work, described elsewhere [90], that synthetic metaschoepite is not stable to dehydration when stored for 4–6 weeks at 16% or 40% RH, leading instead to the formation of anhydrous uranyl hydroxide [90]. In addition, synthetic metaschoepite was shown to be very sensitive to laser heating [90]. Figure 4.5 shows the Raman spectrum

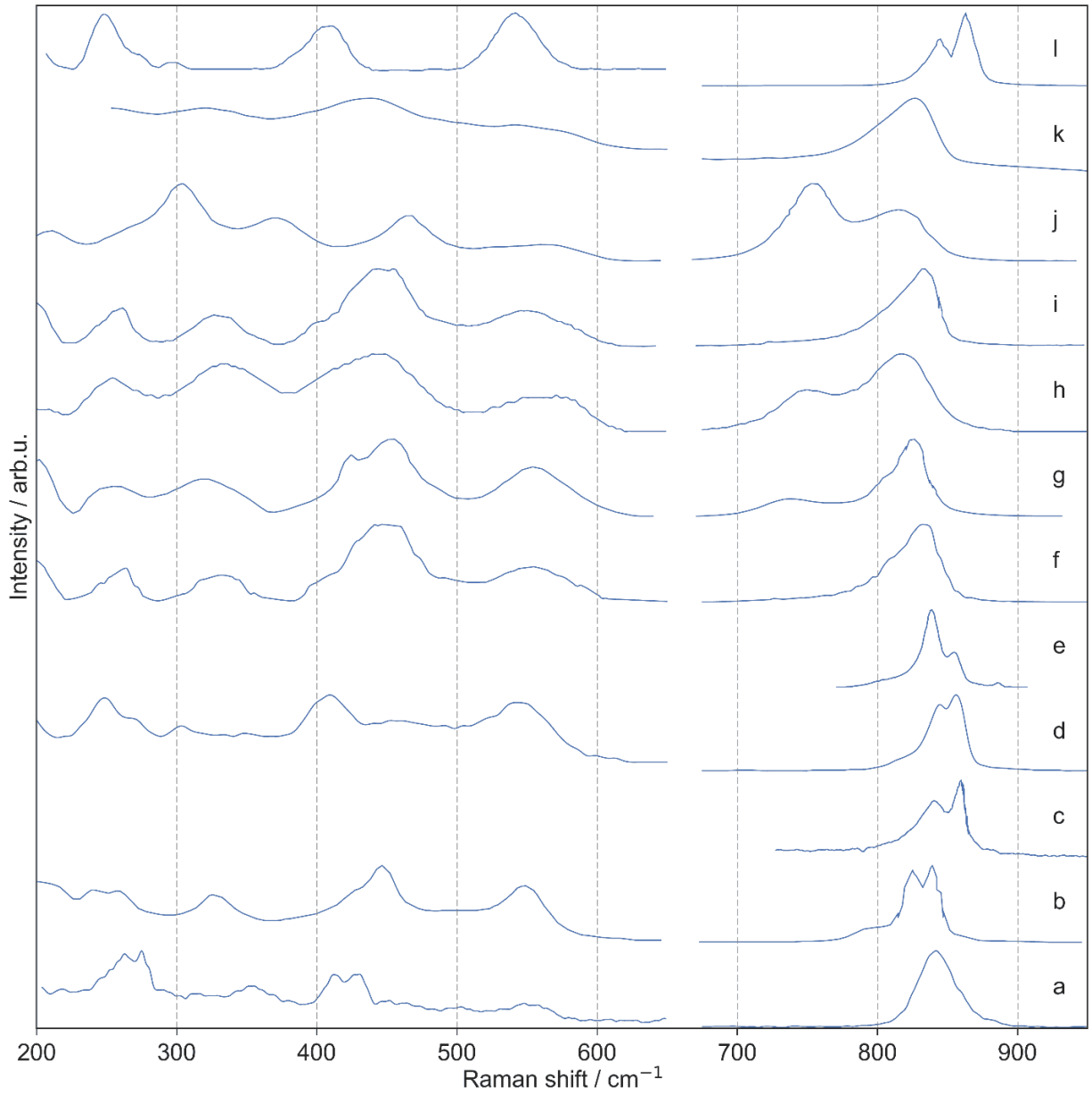

Figure 4.4: Raman spectra of various uranyl hydroxide hydrates in the literature. (a) Sweet 2013 [149] (metaschoepite), (b) Alam 2016 [2] (metaschoepite), (c) Maya 1981 [107] (schoepite), (d) Amme 2002 [4] (schoepite), (e) Frost 2007 [60] (schoepite), (f) Ho Mer Lin 2014 [70] (schoepite), (g) Ho Mer Lin 2015[69] (schoepite, Alligator), (h) Ho Mer Lin 2015 [69] (schoepite, Belgian Congo), (i) Ho Mer Lin 2015 [69] (schoepite, North Span), (j) Ho Mer Lin 2015 [69] (schoepite, synthetic), (k) Berlizov 2016 [18] (schoepite), (l) Walshe 2017 [165] (schoepite, synthetic). The higher and lower energy regions of each spectrum have been normalized independently to allow for ease of comparison.

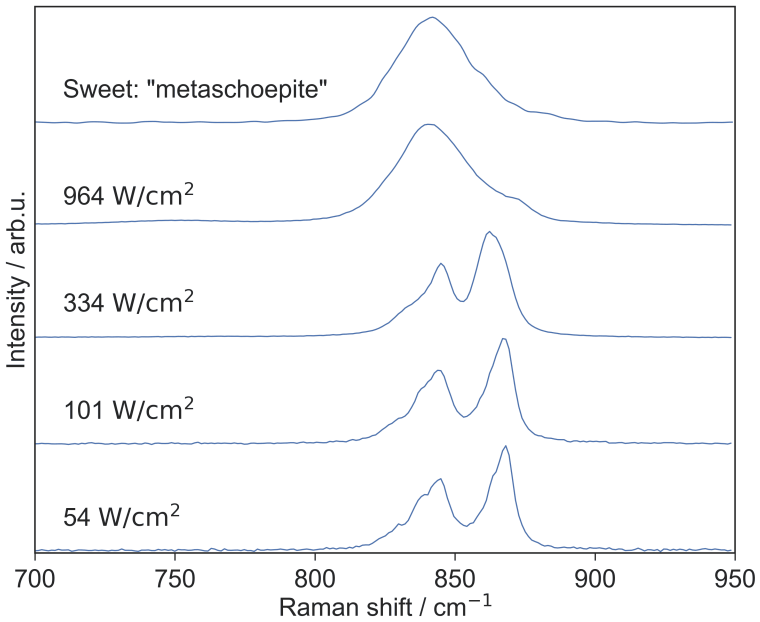

Figure 4.5: Uranyl stretching region of the Raman spectrum of a representative particle of uranyl hydroxide hydrate examined under increasing laser power density compared to the Raman spectrum of synthetic "metaschoepite" determined by Sweet et al. [149]. The sample studied by Sweet et al. may have been dehydrated during laser exposure. The Raman spectra presented in this study were obtained with a laser power density of 101 W/cm^2 to avoid unintended alteration of the samples.

of synthetic metaschoepite obtained with increasing laser power density. Changes in the Raman spectra were observed with a laser power density of 334 W/cm^2, while at 964 W/cm^2, dehydration via laser heating produced a Raman spectrum consistent with anhydrous uranyl hydroxide [90]. Inadvertent dehydration of metaschoepite, whether due to storage conditions or laser heating, likely explains why Sweet et al. found the Raman spectra of metaschoepite and $\alpha-UO_2(OH)_2$ to be nearly indistinguishable, despite XRD patterns consistent with the distinct structural forms [149] and why several Raman spectra of natural uranyl hydroxide hydrate samples are more consistent with anhydrous uranyl hydroxide [70, 69, 18]. To minimize the likelihood of sample alteration when studying uranyl hydroxide hydrates for this work, the laser power density was kept at 101 W/cm^2 in all subsequent Raman studies.

4.2 Structural characterization of γ

The uranyl fluoride particle hydration experiments described in Chapter 3 revealed that uranyl fluoride is not stable at high relative humidity (RH), but rather undergoes a complete loss of fluorine to form a uranyl hydroxide species. Structural information was unattainable from these particle studies, however, motivating a follow-up experiment involving the hydration of much larger samples of uranyl fluoride suitable for XRD analysis. XRD and Raman spectroscopy data were collected periodically on two different samples of uranyl fluoride stored at approximately 84% RH at 25 and 35°C, respectively. Each sample was produced by depositing approximately a few mg of uranyl fluoride hydrate ($[(UO_2F_2)(H_2O)]_7 \cdot 4\,H_2O$) onto zero-background silicon XRD plates along with a small amount of silicon powder to act as a standard. No solvent was used in the preparation of the XRD plates to prevent dehydration or other alteration of the material. The two plates were then placed on top of mounts in separate plastic containers filled with a small amount of a KCl saturated-salt solution and stored in different incubators set to 25 and 35°C. The water vapor pressures of the two samples were approximately 2.67 and 4.67 kPa. Samples were removed from their hydration containers for periodic XRD and Raman analysis, and measurements were carried out at ambient conditions. Multiple micro-Raman spectra were collected in different regions of the sample during each analysis to assess homogeneity.

Both uranyl fluoride samples, equilibrated at 84% RH at 25 or 35°C, were observed to undergo a chemical transformation upon hydration, as characterized by both XRD and Raman spectroscopy. At 25°C (P_{H_2O} = 2.67 kPa), this hydration reaction proceeded very slowly over the course of the 140-day experiment, as visible from both the XRD pattern and the uranyl stretching region of the Raman spectrum (Figure 4.6). At 35°C (P_{H_2O} = 4.67 kPa), however, a complete transformation occurred over this time frame, as shown in Figure 4.7. The changes in the Raman spectra were consistent with the reaction from uranyl fluoride to a uranyl hydroxide hydration product previously identified in hydrated $[(UO_2F_2)(H_2O)]_7 \cdot 4\,H_2O$ particles, although the hydration reaction was found to occur much more slowly in bulk. For comparison, complete transformation of uranyl fluoride particles to uranyl hydroxide at 75% RH at ambient temperature (20–22°C) was observed to take approximately 50 days [88], while the same reaction had barely progressed after 140 days at 84% RH and 25°C. Increasing the temperature and thus water vapor pressure was found to significantly accelerate the reaction such that complete conversion of a bulk sample was attainable in several months.

Collection of multiple micro-Raman spectra during each analysis revealed that the sample did not hydrate homogeneously. This is illustrated in Figure 4.8. While the initial uranyl fluoride material was found to be homogeneous as characterized via Raman spectroscopy, formation of the uranyl hydroxide product occurred more rapidly in some regions than others, potentially due to variations in the surface morphology of the sample. This is consistent with prior observations that the rate of hydration varied somewhat among different particles on the same sample [88]. After 140 days, the sample hydrated at 35°C had completely transformed from uranyl fluoride to uranyl hydroxide as evident from the XRD data (Figure 4.7a). At this point, as shown in Figure 4.8, the Raman spectra were once again consistent across the sample, with no evidence of remaining $[(UO_2F_2)(H_2O)]_7 \cdot 4\,H_2O$.

After 140 days of hydration, there was also no evidence of the uranyl peroxide species that was previously observed to form in hydrated particulate samples. While it is difficult to rule out the presence of a peak near 820 cm^{-1} corresponding to the uranyl stretching mode in this species due to overlap with the uranyl hydroxide peak, the presence of uranyl peroxide in the hydrated sample would be evident by a peroxo stretching mode near 865 cm^{-1} [88, 40].

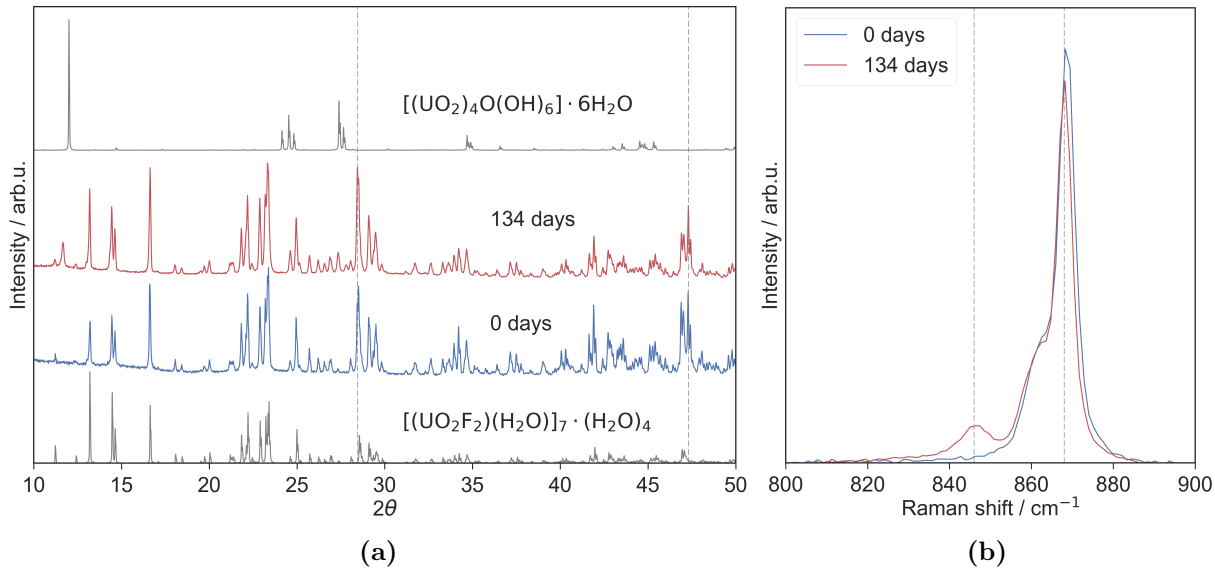

Figure 4.6: (a) XRD patterns over time of a sample of $[(UO_2F_2)(H_2O)]_7 \cdot 4\,H_2O$ stored at 84% RH at 25°C ($P_{H_2O} = 2.67$ kPa) compared to the expected patterns of uranyl fluoride hydrate ($[(UO_2F_2)(H_2O)]_7 \cdot 4\,H_2O$) and schoepite ($[(UO_2)_4O(OH)_6] \cdot 6\,H_2O$). Dashed lines show the position of peaks corresponding to the silicon standard added to the sample. (b) The uranyl stretching region of the Raman spectrum of the same sample over time. Dashed lines at 868 and 846 cm^{-1} highlight the location of the dominant uranyl stretching modes of $[(UO_2F_2)(H_2O)]_7 \cdot 4\,H_2O$ and the new hydration product (γ), respectively.

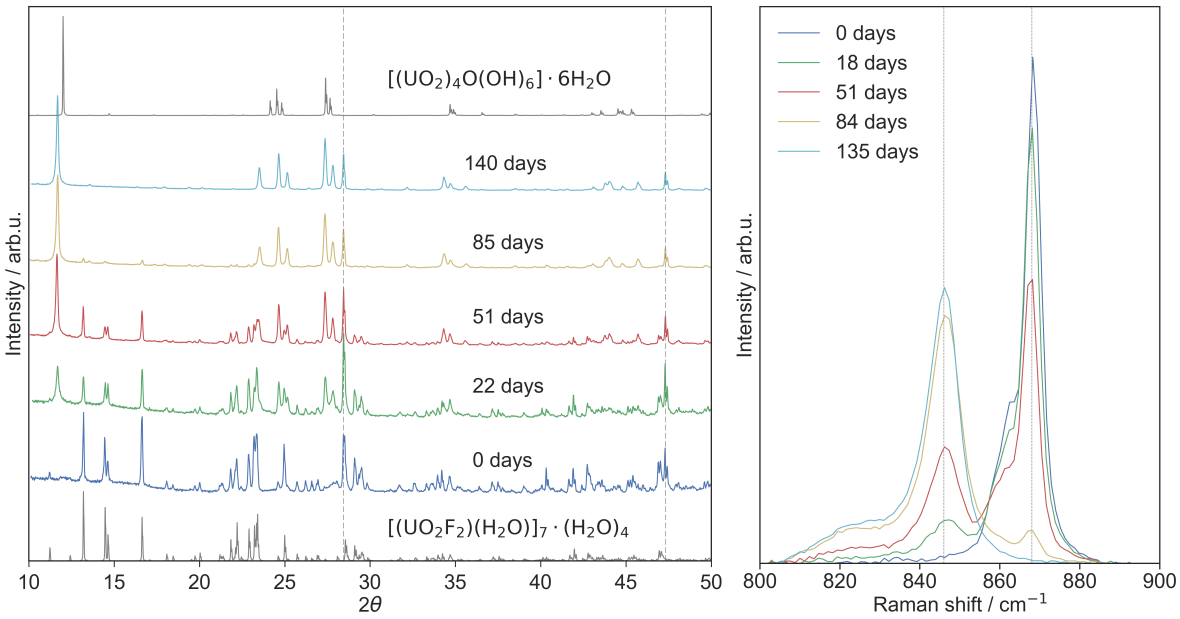

(a) **(b)**

Figure 4.7: (a) XRD patterns over time of a sample of $[(UO_2F_2)(H_2O)]_7 \cdot 4\,H_2O$ stored at 84% RH at 35°C ($P_{H_2O} = 4.67$ kPa) compared to the expected patterns of uranyl fluoride hydrate ($[(UO_2F_2)(H_2O)]_7 \cdot 4\,H_2O$) and schoepite ($[(UO_2)_4O(OH)_6] \cdot 6\,H_2O$). Dashed lines show the position of peaks corresponding to the silicon standard added to the sample. (b) The uranyl stretching region of the Raman spectrum of the same sample over time. Dashed lines at 868 and 846 cm^{-1} highlight the location of the dominant uranyl stretching modes of $[(UO_2F_2)(H_2O)]_7 \cdot 4\,H_2O$ and the new hydration product (γ), respectively.

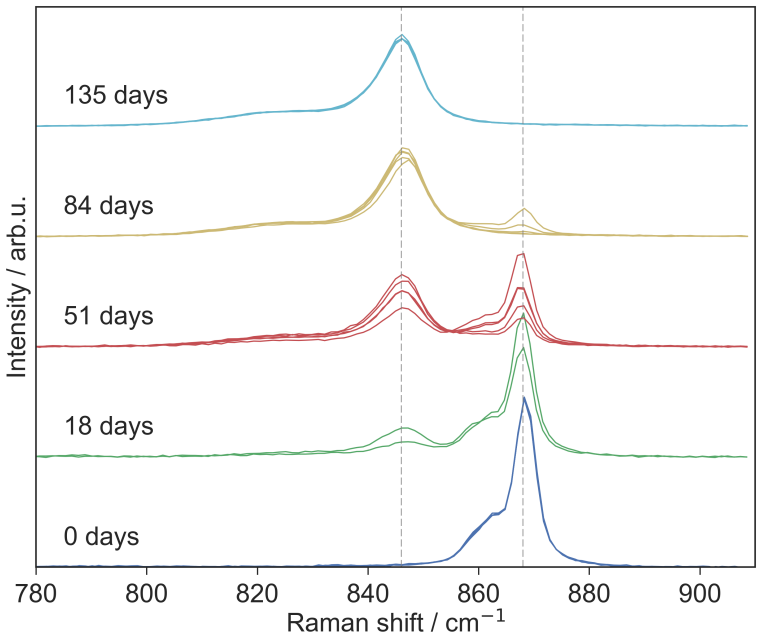

Figure 4.8: The uranyl stretching region of the Raman spectrum over time of a sample of $[(UO_2F_2)(H_2O)]_7 \cdot 4\,H_2O$ stored at 85% RH at 35°C ($P_{H_2O} = 4.67$ kPa). Five Raman spectra were collected from random regions of the sample on each day, with the exception of after 18 days of hydration, when only two spectra were collected. Dashed lines at 868 and 846 cm^{-1} highlight the location of the dominant uranyl stretching modes of $[(UO_2F_2)(H_2O)]_7 \cdot 4\,H_2O$ and the new hydration product (γ), respectively.

The absence of this second hydration product of uranyl fluoride is not surprising given the much slower hydration rate observed for the bulk vs. particle samples. As described in Chapter 3, on a particle scale, the formation of this uranyl peroxide species from the uranyl hydroxide intermediate is already observed to occur much more slowly than the first hydration reaction from uranyl fluoride to uranyl hydroxide. Complete transformation of the bulk uranyl fluoride sample to uranyl hydroxide in this study took at least 100 days at 35°C, suggesting that it could possibly take years to form a significant quantity of the peroxide species.

As shown in Figure 4.7, the diffraction maxima of the hydration species are similar to those expected of the schoepite, $[(UO_2)_4O(OH)_6] \cdot 6\,H_2O$. The most notable difference between the two patterns is a shift in the (002) and (004) peaks near $2\theta = 12$ and 24°, respectively, indicative of an expanded layer spacing. Rietveld refinement was used to determine the lattice parameters of γ using the crystal structure of schoepite as an initial structure. A satisfactory fit was obtained, with major reflections assigned, as shown in Figure 4.9. The refined lattice parameters are shown in Table 4.1 compared to other uranyl hydroxide hydrates. The primary distinction of γ from the known structures schoepite and metaschoepite is an expanded c lattice parameter (the c direction has been redefined to be perpendicular to uranyl sheets in both schoepite and metaschoepite). This lattice parameter is approximately 14.73 Å in both schoepite and metaschoepite, compared with 15.118 Å as measured for γ.

The expanded layer spacing in γ relative to schoepite or metaschoepite is reminiscent of the proposed mineral paraschoepite [142]. As shown in Figure 4.10, the diffraction maxima of γ match reflections of paraschoepite reported by Christ and Clark from a mixed-phase mineral sample [34]. While ianthinite has a similarly expanded layer spacing relative to schoepite and metaschoepite, the presence of ianthinite in this sample seems unlikely due to lack of prominent peaks in the $2\theta = 26$–27° region of the powder diffraction pattern. The diffraction maxima of γ cannot be attributed to a mixture of schoepite and its dehydration products either. The sharpness of the diffraction maximum at $2\theta = 12°$ and the homogeneity of collected Raman spectra suggests that γ consists of a single phase. While it is impossible to confirm whether γ is a synthetic analog of paraschoepite, the existence of a uranyl hydroxide

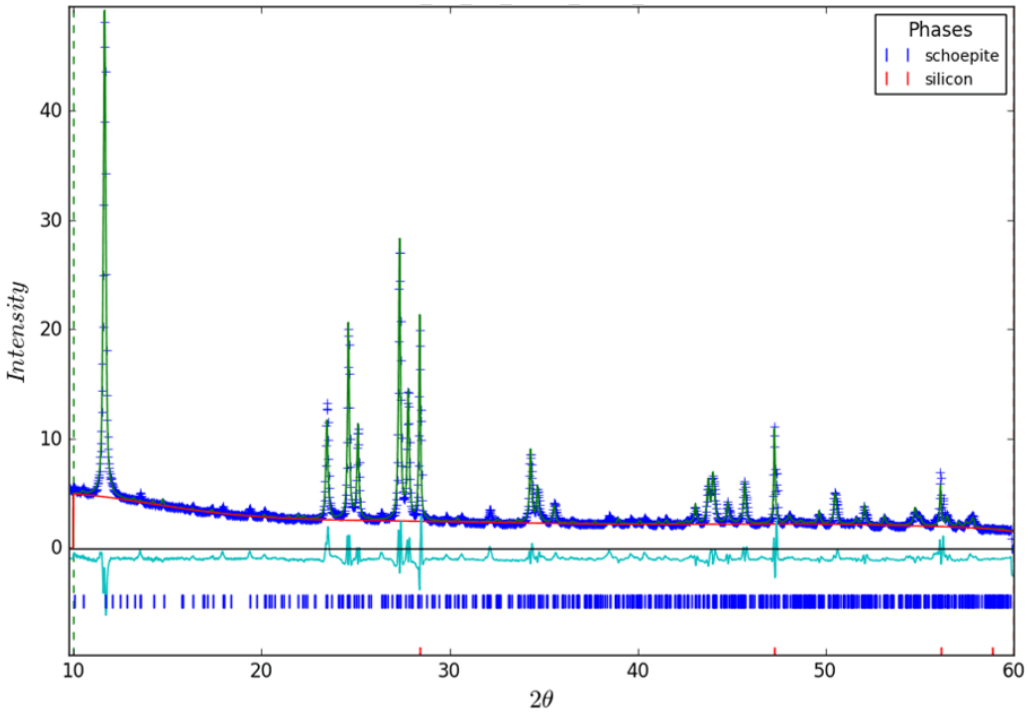

Figure 4.9: Rietveld refinement of γ using the crystal structure of schoepite [53]. Silicon powder was added to the sample as a standard.

Table 4.1: Rietveld refinement parameters of γ compared to other uranyl hydroxide hydrates. Lattice parameters are oriented so that the c-axis is perpendicular to the uranyl sheets. All distances are in Å, and all lattice angles are 90 degrees.

Sample	a	b	c
schoepite [53]	14.337(3)	16.813(5)	14.731(4)
syn. metaschoepite [171]	14.050(2)	16.709(2)	14.7291(2)
aged metaschoepite [171][a]	14.112	16.768	15.143
syn. metaschoepite [90]	14.037	16.678	14.622
paraschoepite [34][b]	14.12	16.83	15.22
γ	14.168	16.741	15.118

[a] Weller et al. found that a crystal of metaschoepite cooled to 150K and then warmed to room temperature and left at ambient conditions for several months transformed to a distinct structure with the composition $UO_3 \cdot 2.25\,H_2O$ and space group Pbna. A full structural solution of this species was not made.
[b] Christ and Clark also refer to this species as schoepite-III.

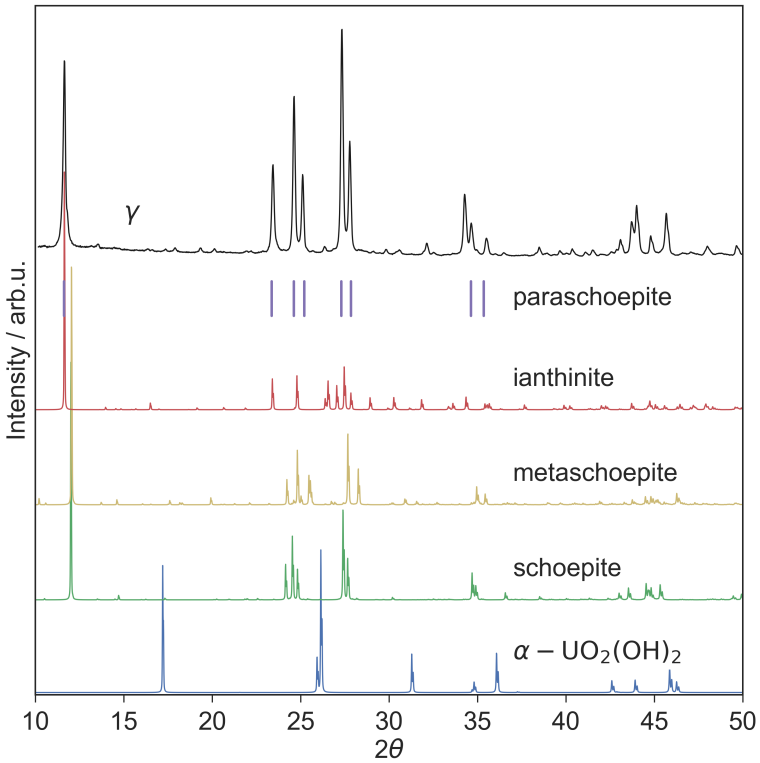

Figure 4.10: XRD pattern of γ compared to the reflections reported for the debated species "paraschoepite" [34] (also referred to as schoepite-III by Christ and Clark) and the known patterns of ianthinite [28], metaschoepite [171], schoepite [53], and anhydrous uranyl hydroxide (α−$UO_2(OH)_2$) [152].

hydrate with similarly expanded layer spacing adds weight to claims that this mineral may exist.

There is additional evidence of synthetic uranyl hydroxide hydrate species with expanded layer spacing. As shown in Table 4.1, Weller et al. found that a crystal of metaschoepite cooled to 150K and then warmed to room temperature and left at ambient conditions for several months transformed to a distinct structure with an expanded layer spacing. A full structural solution of this species was not made, and the relationship between metaschoepite and this distinct species is unclear. However, the composition of the aged sample was determined to be $UO_3 \cdot 2.25\,H_2O$, with more water per unit cell than metaschoepite, which has the empirical formula $UO_3 \cdot 2\,H_2O$. This suggests that the layer spacing expands to incorporate additional water molecules. Since γ is formed at high RH, it may have a similarly elevated water content in comparison to schoepite and metaschoepite.

4.3 Hydration of synthetic metaschoepite

The hypothesis that the uranyl hydroxide hydration product may contain more interlayer water molecules than schoepite and metaschoepite raises the question of whether or not it is possible to form this species via the hydration of these known materials. Synthetic metaschoepite can be readily produced for such a hydration experiment. It was demonstrated previously that the structure of bulk synthetic metaschoepite is not altered by long-term exposure to a 75% RH environment [90]. A follow-up experiment was carried out to investigate whether synthetic metaschoepite might transform into a γ-like species with expanded layer spacing upon equilibration in a more humid environment.

Synthetic metaschoepite material was prepared from the hydration of amorphous UO_3 as described previously [90]. Uranyl nitrate hexahydrate crystals (depleted, from SPI-Chem) were first ground into a powder and then heated in air at 300°C for 24 hours to produce dark red x-ray–amorphous UO_3. The heat was then reduced to 80°C, and deionized water was introduced while stirring continuously. After the solution turned bright yellow (approximately 10 minutes), it was removed from the heat and allowed to evaporate in ambient conditions (approximately 22°C and 60% RH). Once dry, the bright yellow powder

was rinsed twice with deionized water to remove residual nitrates and again allowed to dry at ambient conditions. The XRD pattern of the resulting material (Figure 4.11) was consistent with synthetic metaschoepite, $[(UO_2)_4O(OH)_6] \cdot 5\,H_2O$[171], with a minor component attributable to anhydrous uranyl hydroxide, $\alpha{-}UO_2(OH)_2$. Because synthetic metaschoepite was found to be unstable to dehydration at moderate and low humidity [90], the uranyl hydroxide material was stored in a glass jar with a NaCl saturated-salt solution, providing approximately 75% RH at ambient temperature (22–23°C).

To further hydrate the synthetic metaschoepite, an XRD sample was prepared from this synthesized material and stored in a container with a KNO_3 saturated-salt solution at 35°C (91% RH, $P_{H_2O} = 5.11$ kPa) for 127 days. XRD and Raman data were collected periodically over this time period. While collecting XRD data required removing the sample from the hydrating environment, scans were limited to 45 minutes to minimize potential dehydration during measurement. Figure 4.12 shows the XRD pattern over time. An initial analysis suggests that the (002) peak shifts to lower 2θ slightly upon hydration, indicating expansion of the layer spacing. However, based upon comparison to the initial pattern and the predicted location of this peak from previous studies of metaschoepite, it is more plausible that the material was slightly dehydrated during some measurements relative to others, contracting the interlayer spacing to a small degree. This is not surprising since XRD measurements were conducted under ambient conditions, and the interlayer spacing of synthetic metaschoepite has been shown to be highly dependent on the RH of the environment (see Section 4.5).

While the XRD pattern of this hydrated sample was not indicative of a major structural change, Raman spectra collected on the sample over time showed changes in the uranyl stretching region (Figure 4.13). In particular, the initial Raman peak near 868 cm^{-1} was observed to redshift significantly upon hydration, while peaks at 845 cm^{-1} and below were observed to broaden slightly but did not shift notably. Collection of multiple spectra in different regions of the sample on each date of analysis revealed that these changes did not occur homogeneously across the sample. However, the 868 cm^{-1} peak(s) were consistently redshifted.

No changes were observed in the lower energy peaks of the Raman spectrum over time, suggesting that the equatorial environment of the uranyl ions remains unchanged upon

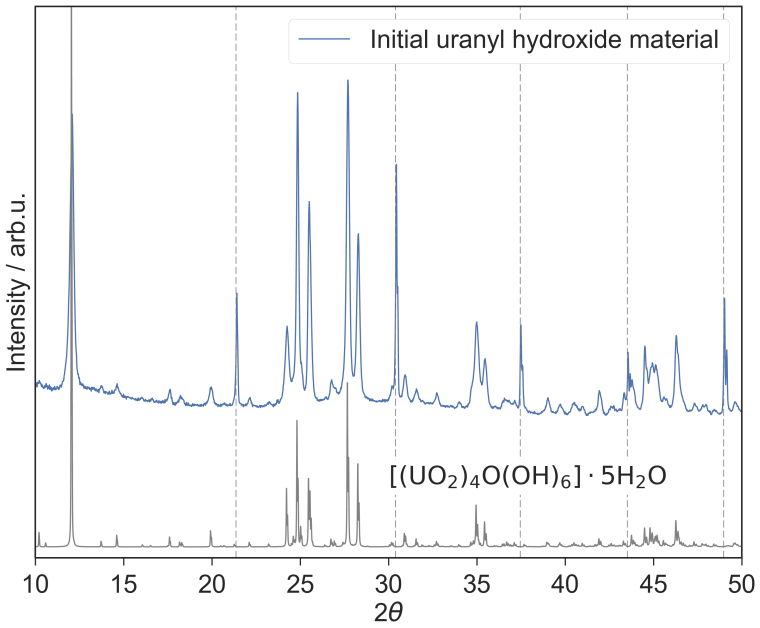

Figure 4.11: XRD pattern of the initial uranyl hydroxide powder used to form samples for hydration. Pattern matching identifies this material as synthetic metaschoepite, $[(UO_2)_4O(OH)_6] \cdot 5\,H_2O$[171], with no noticeable impurities. Dashed lines correspond to the location of peaks associated with the LaB_6 standard added to the sample.

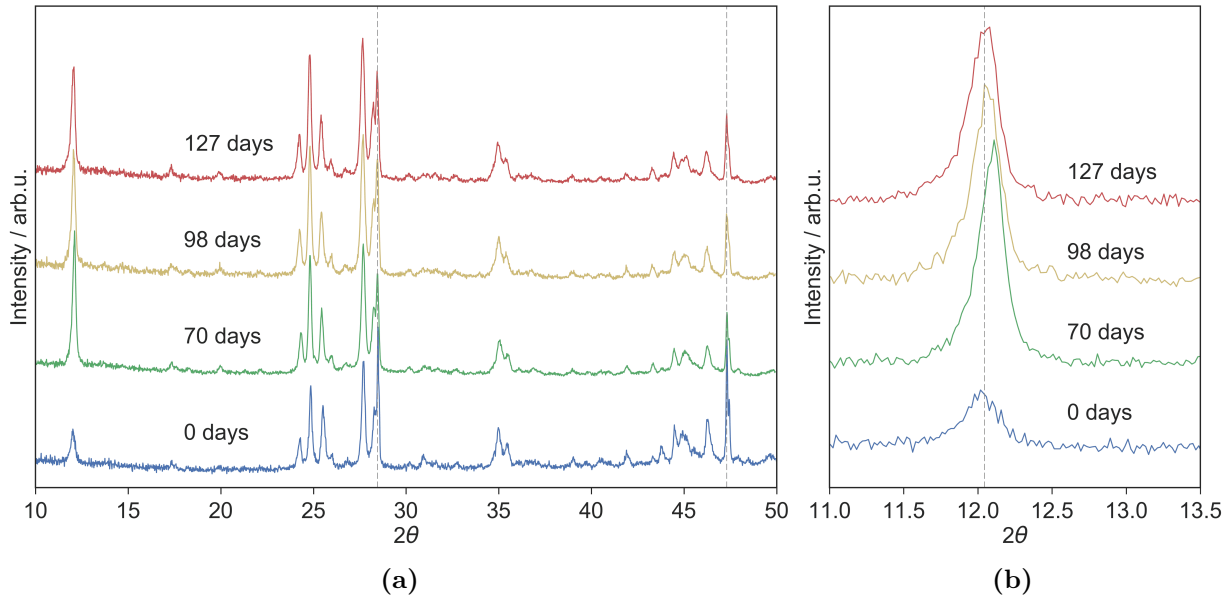

Figure 4.12: (a) XRD pattern of synthetic metaschoepite upon increasing time spent exposed to 95% RH at 35°C. (b) Expanded view of the (002) peak.

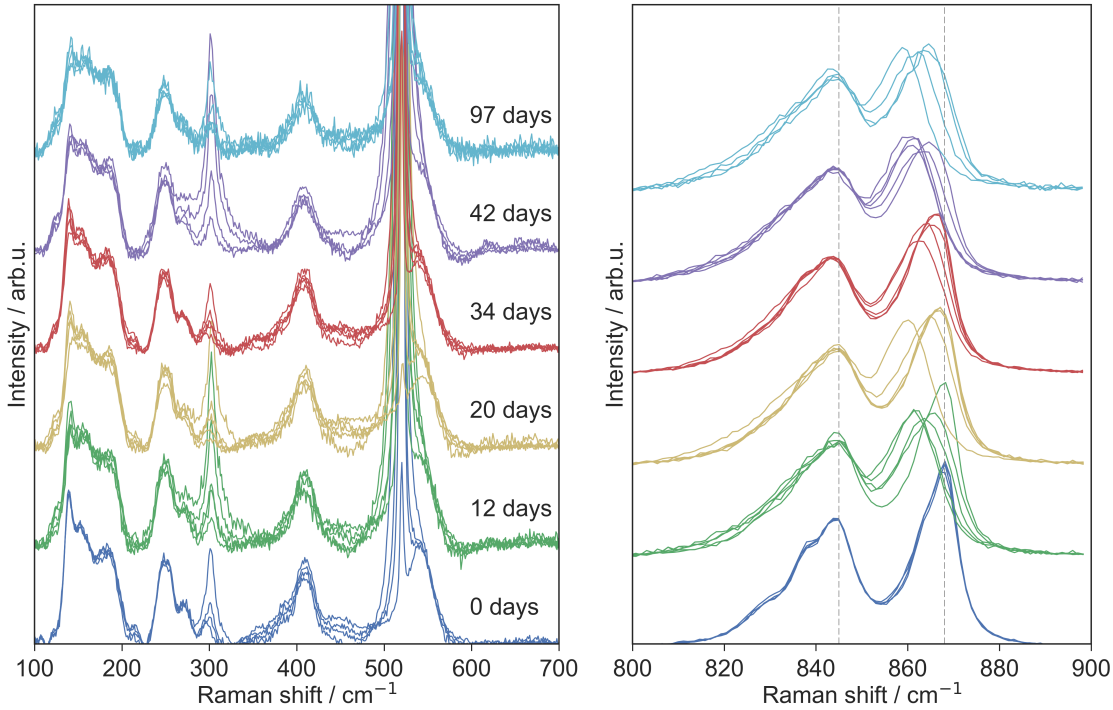

Figure 4.13: Raman spectra collected on a sample of synthetic metaschoepite equilibrated for increasing amounts of time in a 95% RH, 35°C environment. The multiple spectra at each point of hydration correspond to Raman spectra collected on different regions of the sample on the same day. Dashed lines at 868 and 845 cm^{-1} show the initial location of the two dominant uranyl stretching modes. Peaks at 521 and 301 cm^{-1} are attributed to the silicon XRD plate.

hydration. This is consistent with the lack of structural change concluded from the XRD pattern. This means that the redshift in the higher energy uranyl stretching mode cannot be explained by a change in equatorial coordination. Instead, it appears that the local environment of a subset of the uranyl ions changes without any effect on the long-range structure or equatorial bonding. This is consistent with a change in the interlayer water structure that strengthens hydrogen bonding interactions to some of the uranyl ions. The nature of these changes deserves additional study but is beyond the scope of this dissertation. This experiment suggests that is not possible to form the novel γ species via hydration of synthetic metaschoepite.

4.4 Comparison of the vibrational spectra of γ and synthetic metaschoepite

Production of essentially pure γ via hydration of XRD samples allows for better characterization of the vibrational spectra of γ. Material from the fully hydrated XRD plate was subjected to Raman and IR spectroscopy. The full Raman spectrum of γ, including low-energy modes, is shown in Figure 4.14. The Raman spectrum of synthetic metaschoepite, as previously reported [90], is shown for comparison. Pseudo-Voigt fits of the Raman peaks of γ are shown in Figure 4.15. The uranyl stretching region of the Raman spectrum of γ is characterized by a dominant peak at 846 cm^{-1} with a shoulder centered at 830 cm^{-1}. The presence of two uranyl stretching modes indicates the existence of multiple uranyl ion environments that may differ by equatorial coordination or hydrogen bonding interactions. Additional Raman peaks appear at 555, 515, 459, 400, 330, 257, 199, 158, and 127 cm^{-1}. Many of the peaks in this lower-energy region are distinct from those observed in synthetic metaschoepite, suggesting that the arrangement of equatorial hydroxy and oxide ligands in two structures is distinct. This potentially explains why γ cannot be formed from the hydration of synthetic metaschoepite, as discussed in Section 4.3.

IR spectroscopy was performed to assess higher-energy water and hydroxy-related modes. These modes were not visible in the Raman spectrum due to the low incident laser power used

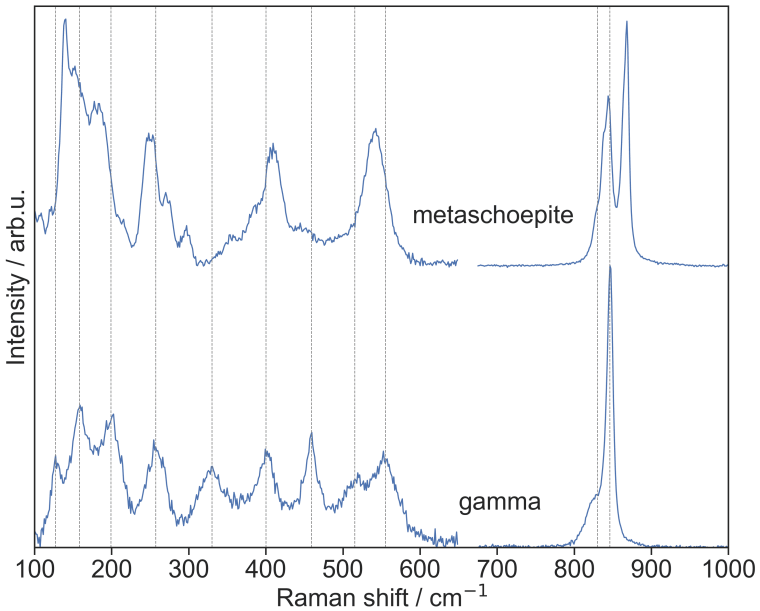

Figure 4.14: Comparison of the Raman spectrum of γ and synthetic metaschoepite. The lower-energy region of the spectra is scaled by a factor of five.

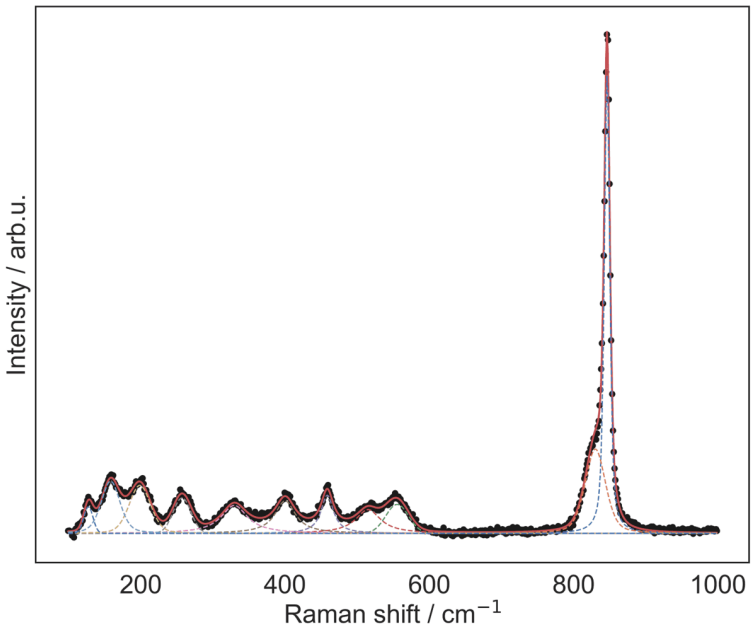

Figure 4.15: Pseudo-Voigt fits of the Raman peaks of γ.

to avoid unintentionally altering the sample and because water is a weak Raman scatterer. Figure 4.16 shows the IR spectrum of γ, again compared to that of synthetic metaschoepite [90]. OH stretching modes appear between 2500 and 3700 cm^{-1}. This region of the spectrum can be adequately fit to five pseudo-Voigt curves (Figure 4.17a) centered at 3569, 3483, 3258, 3037, and 2833 cm^{-1}. The 3569 and 3483 cm^{-1} peaks are attributed to the OH stretching mode of interlayer water molecules, while the remaining peaks are attributed to the OH stretching mode of hydroxy ligands. The presence of multiple stretching modes for both water and hydroxy groups suggests that some water and hydroxy ligands in the structure participate in stronger hydrogen bonding than others. In general, the OH stretching modes in γ are slightly redshifted compared to synthetic metaschoepite, suggesting the presence of stronger hydrogen bonds. Stronger hydrogen bonding also explains the broadening of peaks between 3400 and 3600 cm^{-1} relative to metaschoepite.

The peak at 1624 cm^{-1} (Figure 4.17b) is attributed to the bending mode of the interlayer water molecules. The frequency of this mode is consistent with the frequency of the same mode in synthetic metaschoepite, suggesting that the crystallographic water molecules experience similar hydrogen bonding interactions. However, the δ(U−O−H) bending mode is blueshifted in the uranyl hydroxide hydration product (1043 cm^{-1}) compared to synthetic metaschoepite (1005 cm^{-1}). Based on a comparison of the computationally predicted vibrational spectra of schoepite and metaschoepite (Figure 4.18), this mode is demonstrated to be the most sensitive to differences in the interlayer water structure and hydrogen bonding network.

A peak at 1423 cm^{-1} in the experimental IR spectrum is not easily attributable. A much smaller peak in this region was noted previously in the IR spectrum of synthetic metaschoepite. Since no peaks were predicted in this region in the computational study of metaschoepite, this peak, along with a small peak at 1335 cm^{-1}, was attributed to the presence of impurities in the sample, possibly unreacted uranyl nitrate. The presence of this peak in the IR spectrum of γ cannot be explained by the presence of uranyl nitrate, however, since uranyl nitrate was not part of the synthetic process. Curiously, a peak in this region was also noted by Urbanec and Cejka in a natural sample of schoepite, although it was not assigned [162]. The energy of this peak is similar to that of the ν_3 vibrational

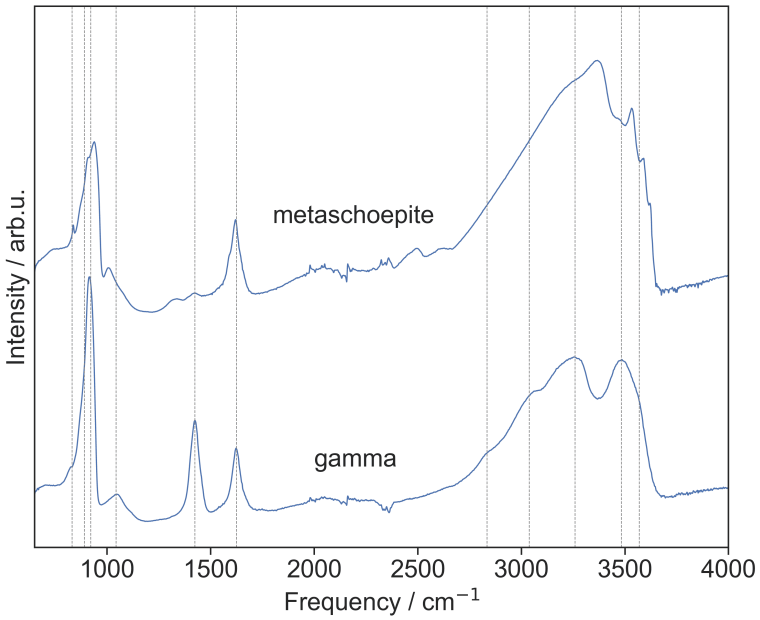

Figure 4.16: Comparison of the IR spectrum of γ and synthetic metaschoepite.

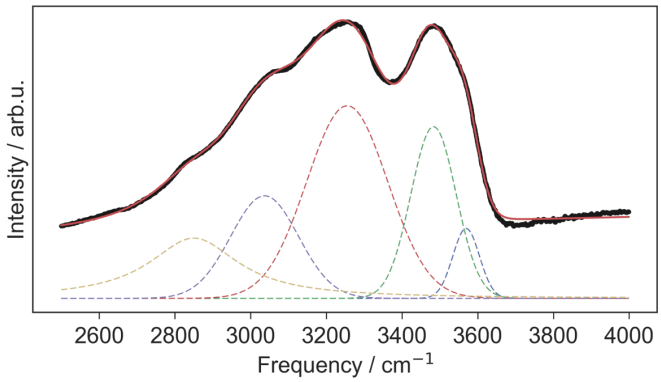

(a)

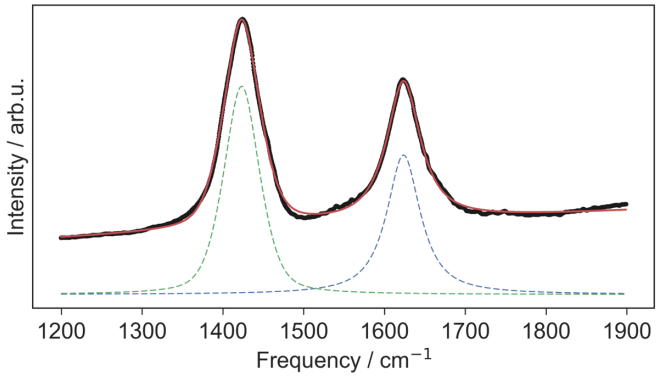

(b)

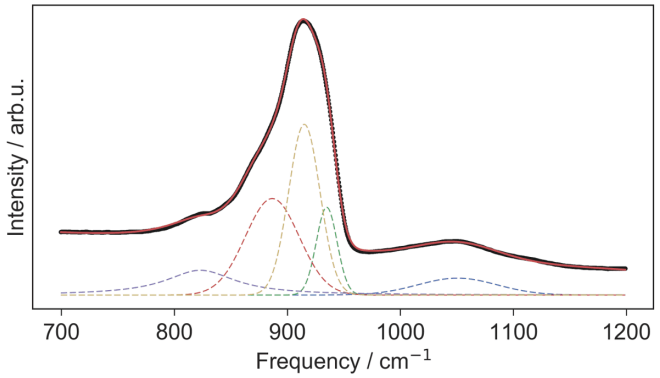

(c)

Figure 4.17: Pseudo-Voigt fits of the IR peaks of γ.

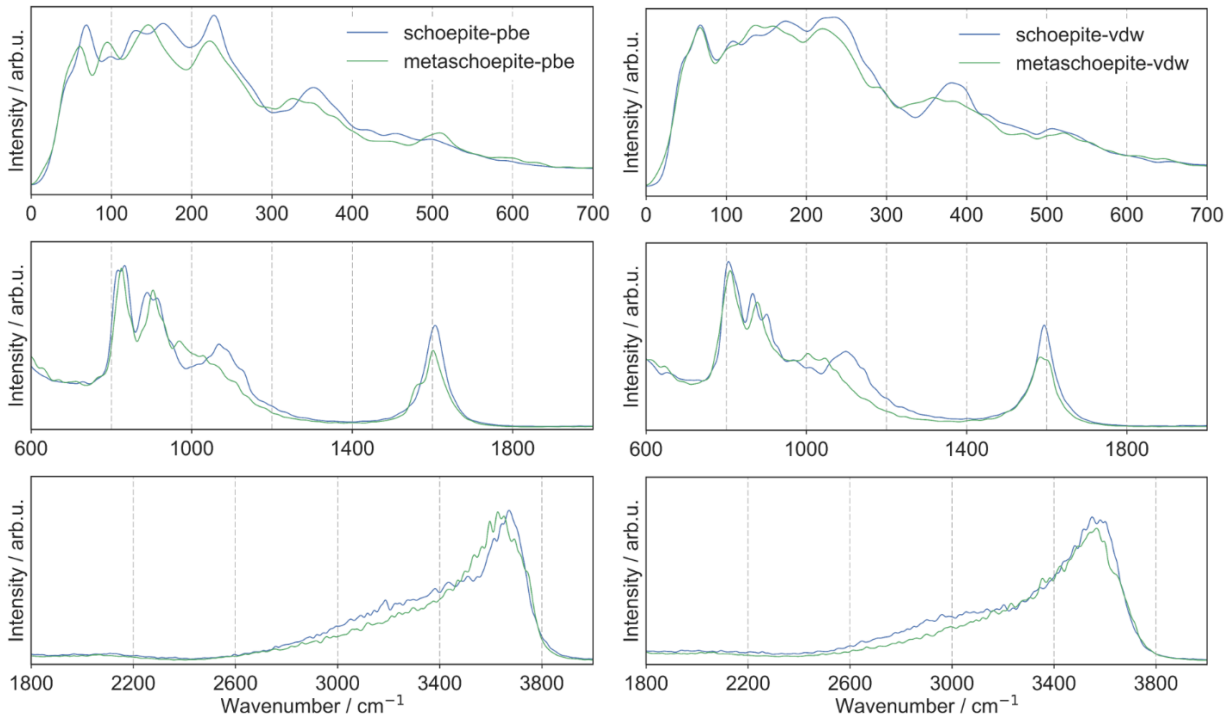

Figure 4.18: Comparison of the power spectra of schoepite and metaschoepite calculated from ab initio molecular dynamics simulations calculated with the (a) PBE [128] functional or (b) op!86-vdW [91, 92] functional. In both cases, the U-O-H bending mode near 1000 cm^{-1} is demonstrated to be the most sensitive to the differences between schoepite and metaschoepite.

mode of the carbonate ion in the uranyl carbonate minerals rutherfordine and sharpite [162]. The presence of carbonate in this species is not infeasible since CO_2 from the atmosphere is soluble near neutral pHs and could become concentrated in hydrated regions on the material. However, if carbonate were present, the symmetric carbonate stretch would be expected in the Raman spectrum near 1000–1100 cm^{-1} [58], and such a peak is not observed for γ.

To assess whether or not carbon is present in the γ structure, particles of γ were analyzed via scanning electron microscopy–energy dispersive x-ray spectroscopy (SEM-EDS). The particles studied were produced from the hydration of uranyl fluoride on a silicon XRD plate and transferred to another silicon substrate for EDS analysis to prevent carbon contamination. Multiple particles were analyzed on the sample and found to be relatively consistent. Figure 4.19 shows a representative EDS spectrum. Uranium, oxygen, and silicon (from the background) are identified as the major elemental components, as expected. A small peak near 0.68 keV is attributed to residual fluorine, which is not unexpected since this material was produced from the hydration of uranyl fluoride and likely still contains a minor component of uranyl fluoride. It is difficult to make a definitive conclusion regarding the presence of carbon in this sample due to the overlap of the carbon K_α peak (expected at 0.28 keV) and a satellite uranium peak near 0.29 keV (Figure 4.19b). Carbon was not identified as a component species in the EDS spectral matching software. Ultimately, while the presence of carbon in the system cannot be definitively ruled out, carbon is not identified as a major elemental component, suggesting that the mysterious 1423 cm^{-1} peak cannot be attributed to the stretching mode of the carbonate group. The origin of this peak thus remains unknown and deserves further study. Characterization of the thermal degradation of γ with dynamic IR spectroscopy could potentially help identify the mode.

The uranyl stretching region of the IR spectrum can be fit to three curves at 921, 890, and 830 cm^{-1} (Figure 4.17c). The peaks at 921 and 890 cm^{-1} are assigned to asymmetric uranyl stretching modes. The presence of two modes again indicates multiple uranyl environments. The peak in the IR spectrum at 830 cm^{-1} the location of the uranyl stretching shoulder in the Raman spectrum. Hydrogen bonding interactions are known to break the symmetry of the uranyl ion, causing a symmetric stretching mode to appear in the IR spectrum. This peak is thus tentatively assigned to the symmetric stretch of uranyl ions that are characterized by

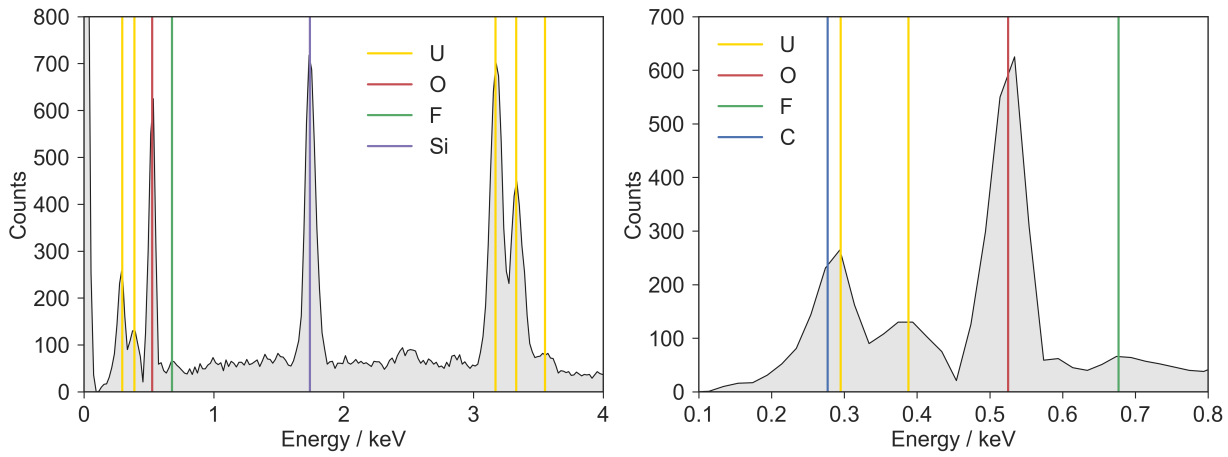

Figure 4.19: (a) SEM-EDS spectrum of a representative particle of γ on a silicon substrate. Peaks are attributed to U, O, F, and Si as shown. (b) Expanded view of the low-energy region of the same spectrum.

strong hydrogen bonding interactions with interlayer water molecules. The corresponding asymmetric mode appears at 890 cm^{-1}. Uranyl ions that are not characterized by strong hydrogen bonding have a symmetric stretching mode at 846 cm^{-1} and an asymmetric stretching mode at 921 cm^{-1}.

A list of the IR and Raman peaks and their assignments is shown in Table 4.2.

4.5 Relative humidity dependence of the interlayer spacing of γ and synthetic metaschoepite

In previous studies of synthetic metaschoepite [90], variation was noted in the crystal structure, as determined by XRD, depending on the environmental conditions of the sample. In particular, the interlayer spacing was demonstrated to be sensitive to the RH under which the sample was studied. Dynamic XRD experiments with humidity control were carried out to further probe this behavior. Figure 4.20 shows the interlayer spacing, determined from the position of the (002) reflection, as a sample of synthetic metaschoepite was exposed to increasing humidity at 30 °C. The interlayer spacing is clearly humidity dependent, increasing by roughly 0.025 Åas the RH was increased from 40 to 60%. Expansion of the layer spacing occurs rapidly as the humidity is increased, and remained fairly stable over 12 hours at each humidity level. While the interlayer spacing determined at 40% RH (∼7.384 Å) was still expanded relative to literature values for schoepite and metaschoepite, which range between 7.31 and 7.375 Å [19, 133, 34, 53, 131], and 7.3065 and 7.365 Å [34, 171, 93, 25, 90], respectively (Figure S8), these values were measured under an ambient RH that may have been lower than 40%.

The lower limit of the interlayer spacing was explored by desiccating another sample of synthetic metaschoepite under dry air at 30°C. One-hour XRD scans were again collected consecutively. As shown in Figure 4.21, the (002) and (004) reflections were observed to shift towards higher angles upon desiccation, indicating a contraction of the c lattice parameter and thus interlayer spacing ($c/2$). The (002) reflection stopped shifting after 24 hours of desiccation. At this point, the sample was rehydrated by increasing the RH to 50%. The

Table 4.2: Raman and IR spectroscopy peaks.

IR / cm^{-1}	Raman/ cm^{-1}	Assignment
3569		ν(OH) (water)
3482		ν(OH) (water)
3258		ν(OH) (hydroxy)
3037		ν(OH) (hydroxy)
2833		ν(OH) (hydroxy)
1624		$\delta(H_2O)$
1423		???
1043		δ(U−O−H)
921		$\nu_{as}(UO_2^{2+})$
890		$\nu_{as}(UO_2^{2+})$
	846	$\nu_s(UO_2^{2+})$
830	830	$\nu_s(UO_2^{2+})$
	555	$\nu(U{=}O_{eq})/\nu$(U=(OH))
	515	$\nu(U{=}O_{eq})/\nu$(U=(OH))
	459	ν(U=(OH))/γ(U−(OH)−U)
	400	ν(U=(OH))/γ(U−(OH)−U)
	330	ν(U=(OH))/γ(U−(OH)−U)
	257	$\delta(UO_2^{2+})/\delta$(U−(OH)−U)
	199	$\delta(UO_2^{2+})/\delta$(U−(OH)−U)
	158	$\delta(UO_2^{2+})$/lattice modes
	127	$\delta(UO_2^{2+})$/lattice modes

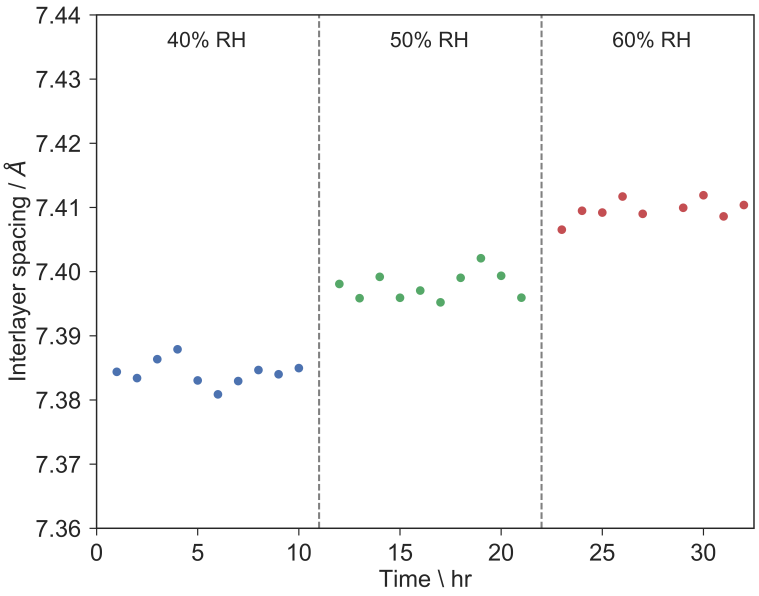

Figure 4.20: Interlayer spacing of synthetic metaschoepite at 40%, 50%, and 60% RH at 30°C, as determined by the position of the (002) reflection. A series of one-hour XRD scans were collected consecutively at each humidity level after equilibrating the sample for one hour.

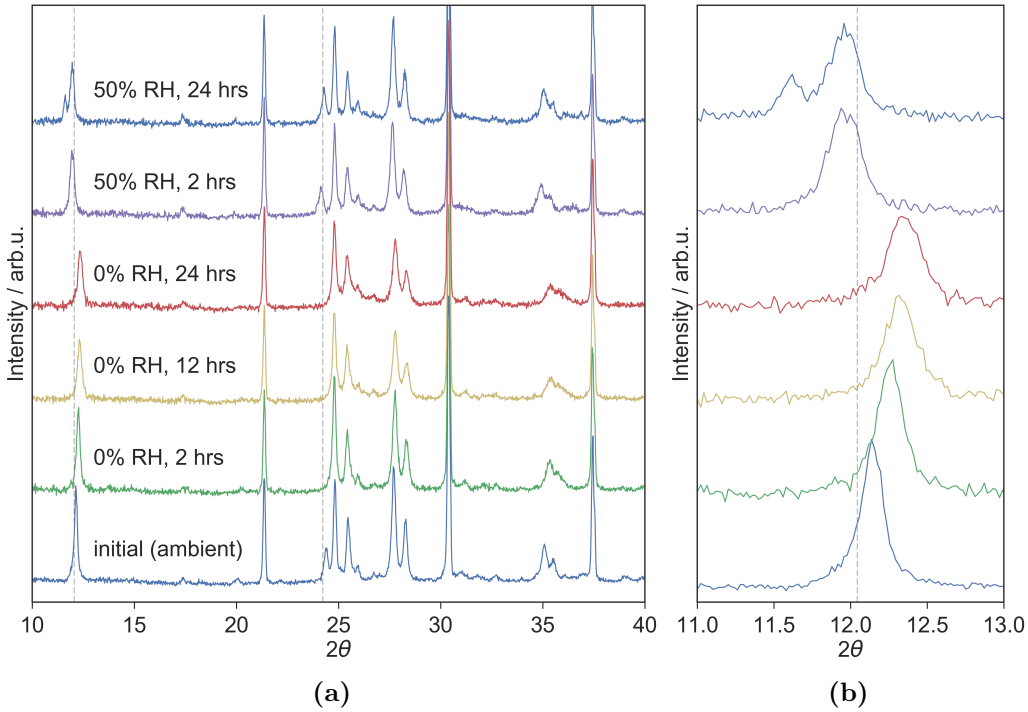

Figure 4.21: (a) XRD pattern of synthetic metaschoepite upon dessication under dry air. (b) Expanded view of the (002) reflection. Dashed lines show the expected location of the (002) and (004) reflections of synthetic metaschoepite at $2\theta = 12.043^\circ$ and $2\theta = 24.2216^\circ$ [171]. Peaks at $2\theta = 21.36$, 30.38, and 37.44° correspond to the LaB_6 standard added to the sample.

(002) and (004) reflections shifted back toward lower angles, indicating a rapid re-expansion of the layer spacing. As the sample was rehydrated at 50% RH for several hours, a second peak becomes visible at $2\theta = 11.6°$. The position of this peak matches the position of the (002) peak of γ at 50% RH, suggesting that a component of the synthetic metaschoepite is converted to a γ-like species with expanded layer spacing. This peak cannot be definitely attributed, however, due to the absence of a corresponding (004) reflection near $2\theta = 23.43°$. Further experiments are necessary to identify this component and assess whether or not γ can be formed from synthetic metaschoepite after all, via rehydration following an initial desiccation. It is plausible that desiccation induces some disorder in the uranyl layers such that the hydrogen bonding interactions that link the layers via interlayer water molecules are weakened. This would allow the interlayer to be more easily expanded via absorption of additional water molecules.

After the RH had been held at 50% for 24 hours, the dessication and rehydration cycle was repeated a second time (24 hr 0% RH, 24 hr 50% RH). As demonstrated in Figure 4.22, the contraction and expansion of the c lattice parameters, indicated by the shifting of the (002) and (004) reflections, was found to be reversible over both cycles. Unlike the (002) and (004) reflections, the (240) and ($\bar{4}$00) reflections did not shift significantly over the course of the experiment, indicating that the a and b lattice parameters of synthetic metaschoepite are stable to changes in the environmental humidity. This is illustrated in Figure 4.23, which shows the three lattice parameters over the course of the experiment, as calculated via sequential Rietveld refinement (see Chapter 1 for details on Rietveld refinement). The b lattice parameter was found to be very constant throughout the experiment. The sudden changes in RH had small effect on the a parameter, although this effect does not appear to be correlated to the direction of the humidity change and is much smaller in magnitude than the observed variation in the c lattice parameter.

The humidity dependence of the c lattice parameter and thus interlayer spacing may explain the variability of this parameter in the literature for measurements of schoepite and metaschoepite (see Figure 4.3). Figure 4.24 shows the interlayer spacing ($c/2$) over the course of the experiment compared to past measurements of schoepite and metaschoepite, conducted at ambient RH. Upon desiccation, the interlayer spacing contracts, approaching

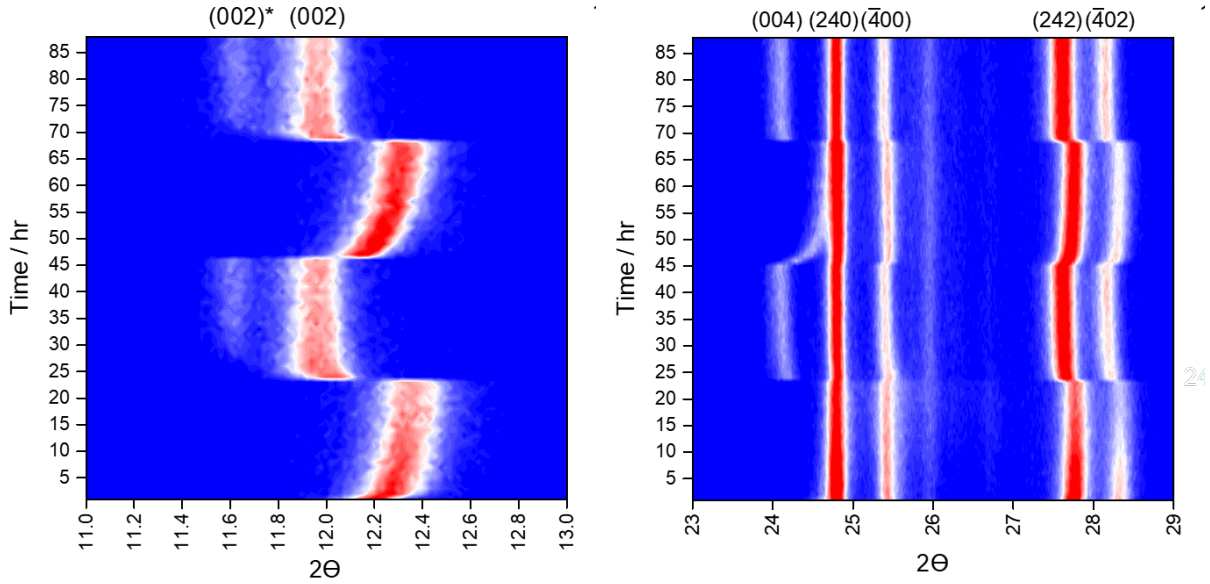

Figure 4.22: Position of dominant reflections in synthetic metaschoepite as the environmental humidity was cycled between 0% and 50% RH (30°C): 24 hr 0% RH, 24 hr 50% RH, 24 hr 0% RH, 24 hr 50% RH. One-hour XRD scans were collected consecutively throughout the entire experiment, with no delay between.

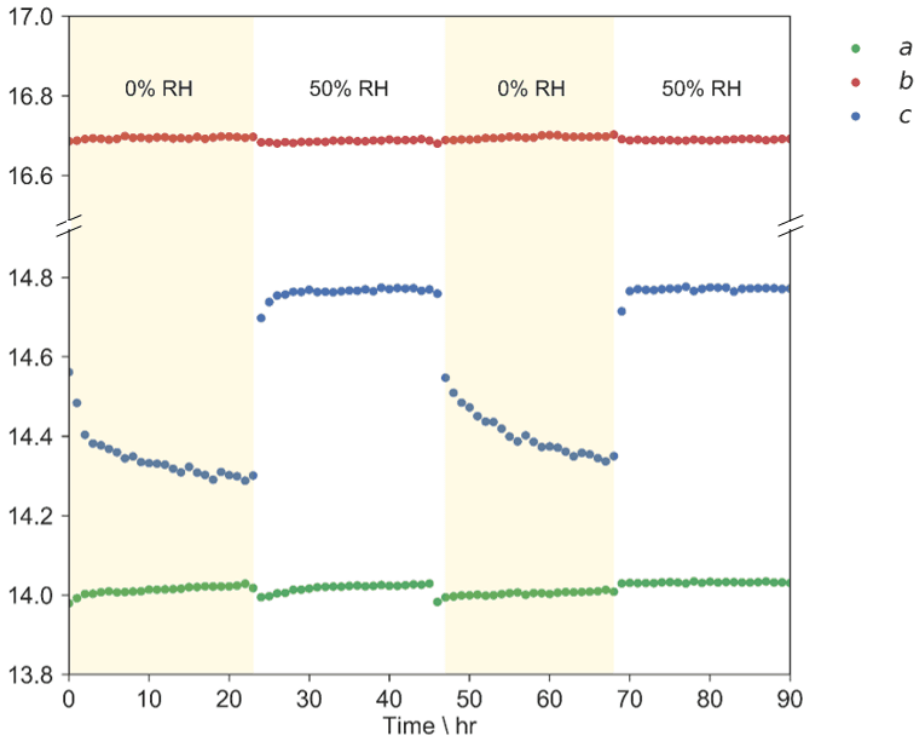

Figure 4.23: Lattice parameters of synthetic metaschoepite with the environmental humidity cycled between 0% and 50% RH (30°C), as determined via sequential Rietveld refinement. One-hour XRD scans were collected consecutively throughout the entire experiment, with no delay between.

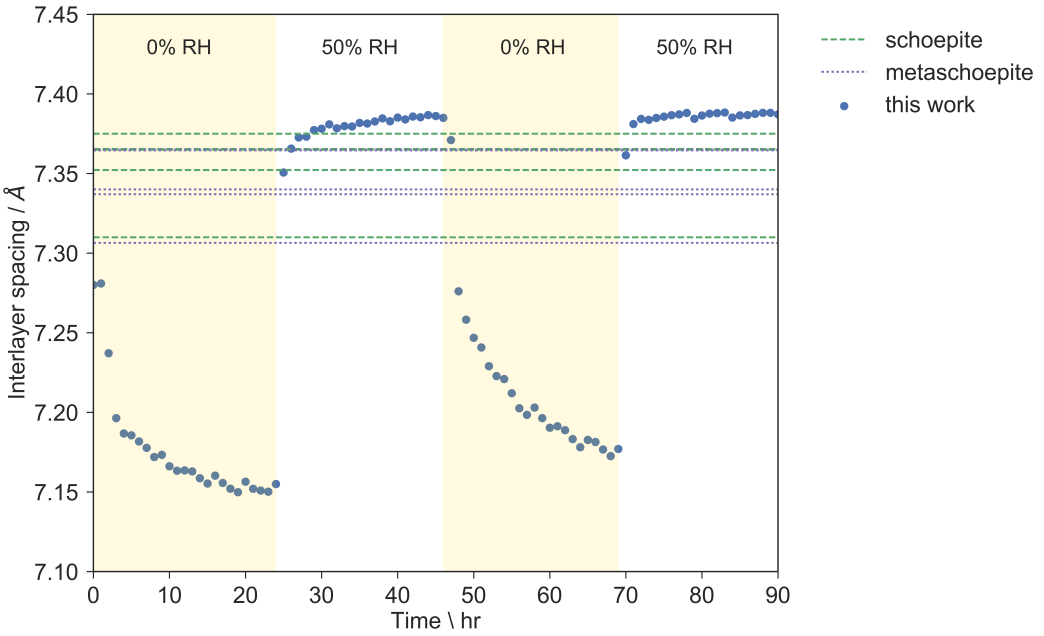

Figure 4.24: Interlayer spacing of synthetic metaschoepite with the environmental humidity cycled between 0% and 50% RH (30°C), as determined via sequential Rietveld refinement. One-hour XRD scans were collected consecutively throughout the entire experiment, with no delay between. Horizontal lines show reported values in the literature for schoepite [19, 133, 34, 53, 131] and metaschoepite [34, 171, 93, 25, 90].

approximately 7.15 Å after 24 hours. Rehydration at 50% RH leads to a rapid re-expansion of the spacing to a stable maximum value of approximately 7.38 Å after 5–6 hours. All of the reported values in the literature fall between these two values. The minimum interlayer spacing after the second desiccation cycle was found to be slightly expanded relative to the first, likely due to an introduction of some disorder in the metaschoepite uranyl layers that limits the contraction. However, it is also possible that the interlayer spacing would have continued to contract slowly had the desiccation period been extended.

The relative stability of the a and b lattice parameters, as well as the observed reversibility of this change in interlayer spacing, suggests that there was no significant structural change in the uranyl layers. The contraction and expansion of the c lattice parameter is presumably due to the removal and replacement of a portion of the interlayer water molecules. This behavior is somewhat unexpected given the strong hydrogen bonding network in metaschoepite [2, 90]. Water molecules are hydrogen bonded not only to each other, but to the hydroxy groups in the uranyl layers as well. The removal of each of these interlayer water molecules would thus require the breaking of multiple fairly strong hydrogen bonds.

Density Functional Theory (DFT) calculations were carried out to better understand the structural effect of removing a subset of the interlayer water molecules. Schoepite was used in place of metaschoepite for this study because the increased symmetry lessened the computational effort. A series of calculations were carried out in which the schoepite unit cell was re-optimized upon the removal of different numbers of water molecules. The 48 interlayer water molecules in the schoepite unit cell are organized in 12 symmetrically distinct positions. One or more of these 12 groups of water molecules were removed in each calculation. Selection among the 12 groups was random. Because the choice of the specific water molecules removed was expected to affect the resulting interlayer spacing, three separate calculations were run at each water content. An additional two calculations were run with 40 and 44 waters molecules removed due to greater variation in the optimized structures at this water content level. Structural optimization was done in two steps. Following removal of the water molecules, the atomic positions of the remaining atoms were optimized while keeping the lattice parameters fixed. Once the atomic positions were optimized, the lattice parameters were allowed to relax as well, and the atomic positions were optimized for a second time.

The DFT-optimized interlayer spacing of each of these calculations is shown in Figure 4.25 as a function of the number of water molecules removed. As water molecules are removed from the structure, the interlayer contracts as expected. When all or almost all of the interlayer water molecules are removed, the structure collapses in the c direction, and hydrogen bonds form between the uranyl oxygens and hydroxy groups in adjacent layers (see Figure 4.33). This full dehydration was previously demonstrated to occur in synthetic metaschoepite upon extended exposure to a desiccating environment [90]. This irreversible phase transition is distinct from the reversible contraction and expansion of the layer spacing that occurs more quickly upon changes in the humidity. Figure 4.25 suggests that the removal of about half of the water molecules in the unit cell of schoepite would result in the 2–3% interlayer contraction observed experimentally without causing the irreversible collapse of the structure. This is a very rough comparison however. The average water dissociation energy over all of the calculations was 0.686 eV, likely an underestimate as the PBE functional underestimates the strength of long-range van der Waals interactions [66, 65].

Since γ was identified as a layered uranyl hydroxide hydrate with structural similarity to schoepite and metaschoepite, the humidity dependence of the structure was investigated for comparison. An XRD sample of γ was desiccated and rehydrated two times as in the experiment with synthetic metaschoepite. The initial scan of the material under ambient conditions, shown in Figure 4.26, roughly matches that measured previously (Section 4.2), with the exception of a shoulder on the (002) reflection that indicates that a component of the sample has a smaller interlayer spacing and may be partially dehydrated relative to the rest of the material. Upon desiccation, the (002) peak was observed to shift to higher 2θ, indicating a contraction of the layer spacing similar to that observed in synthetic metaschoepite. Unlike for metaschoepite, however, where this shift occurred continuously after the first hour of desiccation (Figure 4.22), a discrete jump in the peak position was observed to occur after about 12 hours of desiccation, likely due to a rearrangement of the remaining interlayer water molecules. The XRD pattern was stable after 24 hours of desiccation. A low-angle shoulder on the (002) reflection after desiccation indicates that a minor component of the species retained a slightly larger layer spacing, potentially due to additional disorder in the uranyl layers.

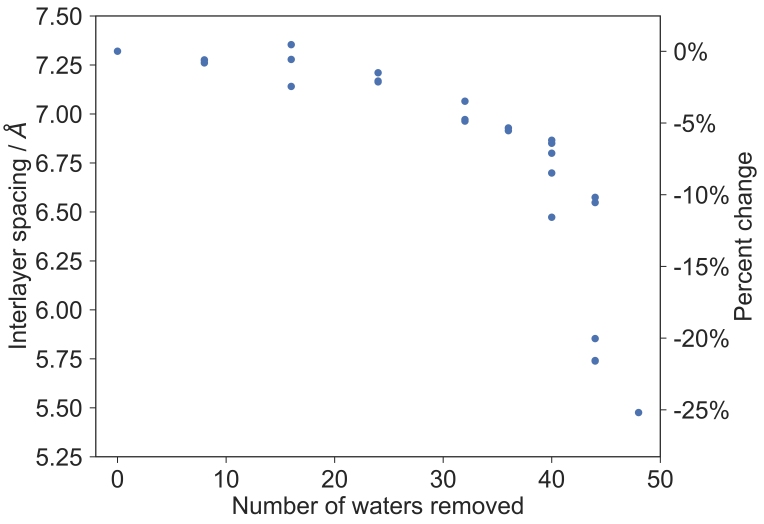

Figure 4.25: DFT-optimized interlayer spacing of schoepite with varying number of water molecules removed from the unit cell. Interlayer spacing of metaschoepite with an increasing number of interlayer water molecules removed.

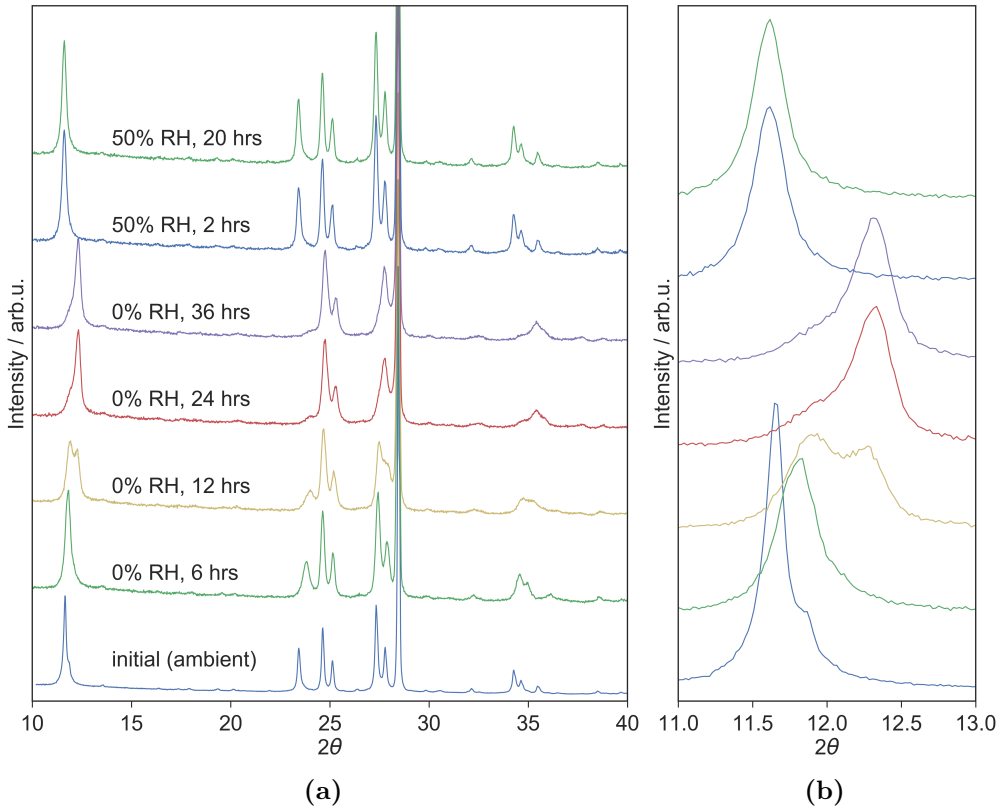

Figure 4.26: (a) XRD pattern of γ upon dessication under dry air. (b) Expanded view of the (002) reflection. The peak at $2\theta = 28.443^{\circ}$ corresponds to the Si standard added to the sample.

After desiccating for 36 hours, the sample of γ was rehydrated at 50% RH. As with synthetic metaschoepite, rehydration induced a rapid re-expansion of the interlayer spacing, as evidenced by a shift in the (002) and (004) reflections. This contraction and expansion of the interlayer spacing was again found to be repeatable over two dessication–rehydration cycles, as shown in Figure 4.27. The discrete shift of the (002) reflection that occurs approximately 10–12 hours into each period of dessication is clearly visible in Figure 4.27 as well. Unlike observed for synthetic metaschoepite, the (240) and ($\bar{4}$00) reflections do shift appreciably over the course of the experiment, indicating that the a and b lattice parameters in γ are also sensitive to changes in humidity, albeit to a much smaller degree than the c parameter.

While sequential Rietveld refinement of all scans was not successful due in part to the splitting of the (002) reflection and the overlap of the ($\bar{4}$02) reflection with a peak from the Si standard, Table 4.3 shows the lattice parameters of γ, as well as synthetic metaschoepite, calculated from Rietveld refinements of single scans at 0% RH and 50% RH. At 50% RH, the interlayer spacing of γ is significantly expanded relative to synthetic metaschoepite. The interlayer spacing of γ is still larger than synthetic metaschoepite after both species were desiccated, although the values become closer. The a and b lattice parameters of γ shrink by -0.5 and -0.4% upon dessication relative to 50% RH, indicating that the uranyl layers in γ are less rigid than in synthetic metaschoepite. This is potentially explained by a less rigid hydrogen bonding network of interlayer water molecules in γ.

After the first desiccation cycle, the interlayer spacing of γ was still expanded relative to synthetic metaschoepite (Table 4.3); however, after the second desiccation cycle, which is shown in Figure 4.28, the interlayer spacings were comparable. This is likely due to an introduction of some disorder in the metaschoepite uranyl layers that already existed in γ. However, it is clear that these desiccated species are still structurally distinct since upon rehydration at 50% RH, the interlayer spacings are re-expanded to the previous distinct values at 50% RH. Differences in the arrangement of equatorial hydroxy and oxide groups, alluded to by differences in the Raman spectra of γ and synthetic metaschoepite (Section 4.4), could potentially explain the distinct rehydration behavior.

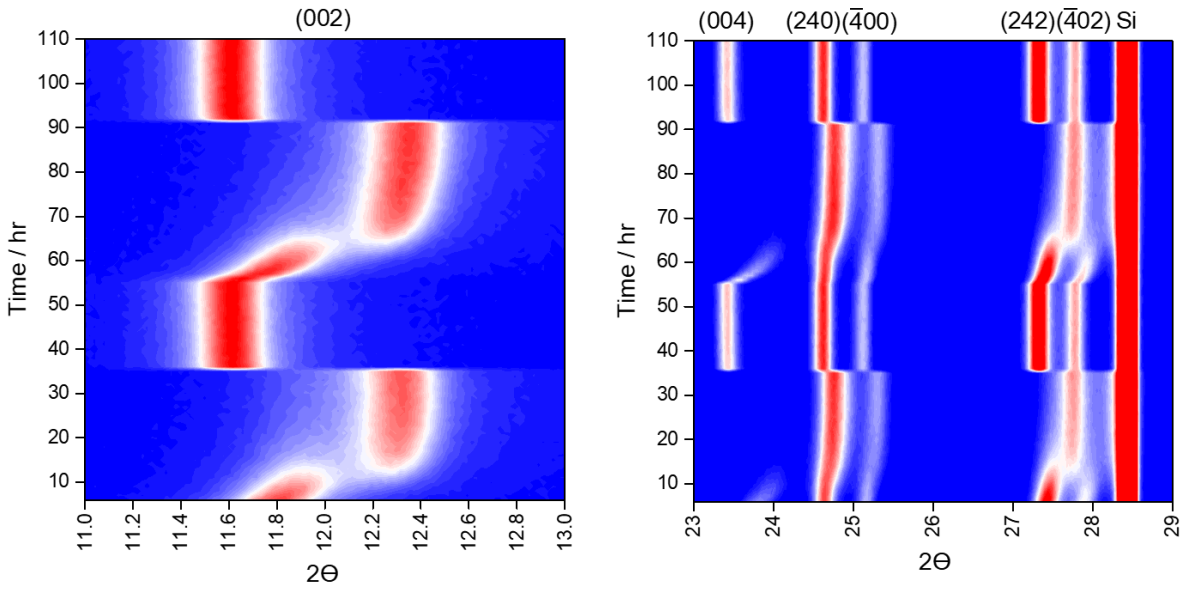

Figure 4.27: Position of dominant reflections in synthetic metaschoepite as the environmental humidity was cycled between 0% and 50% RH (30°C): 36 hrs 0% RH, 21 hrs 50% RH, 35 hrs 0% RH, 18 hrs 50% RH. Unfortunately, data was not collected for the first six hours of desiccation due to an instrument malfunction. The peak at 2θ=28.443° corresponds to the Si standard added to the sample.

Table 4.3: Rietveld refinement parameters of γ and synthetic metaschoepite after equilibration at 50% RH and 0% RH (30°C). Lattice parameters are oriented so that the c axis is perpendicular to the uranyl sheets. All distances are in Å, and all lattice angles are 90°.

Sample	a	b	c	V
syn. metaschoepite, 50% RH	13.985(7)	16.684(9)	14.728(8)	3436(2)
syn. metaschoepite, 0% RH	13.9985(1)	16.7179(1)	14.17017(9)	3316.18(7)
percent change	0.1%	0.2%	−3.8%	−3.5%
γ, 50% RH	14.156(1)	16.786(2)	15.183(2)	3608.8(5)
γ, 0% RH	14.080(9)	16.716(8)	14.387(5)	3386(2)
percent change	−0.5%	−0.4%	−5.2%	−6.2%

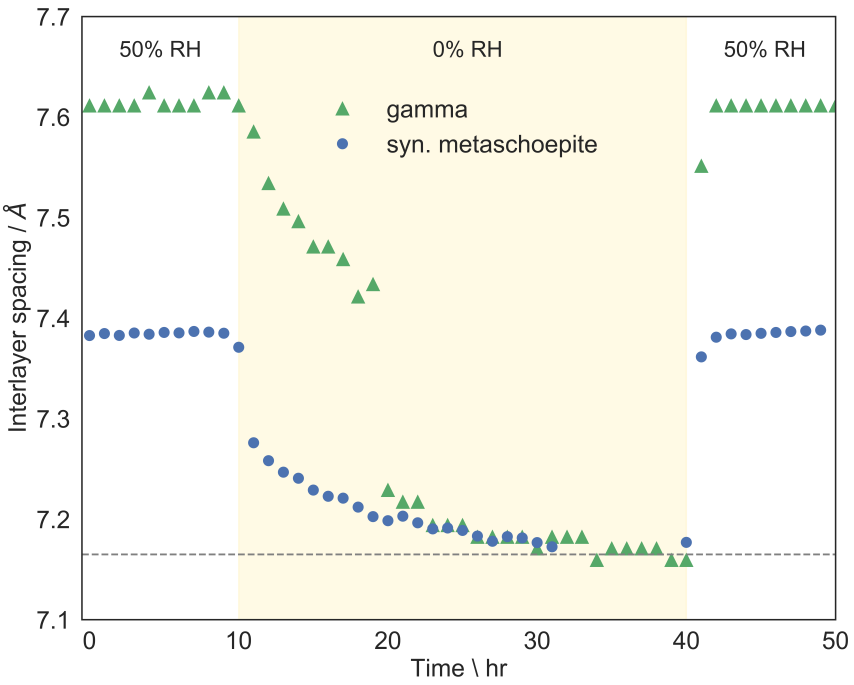

Figure 4.28: Interlayer spacing of synthetic metaschoepite (blue circles) and γ (green triangles) over a portion of the rehydration and second dessication cycle. The RH was set to 50% (at 30°C) for the first 10 hours, and then 0% for the remainder for the time shown. One-hour XRD scans were collected consecutively throughout the entire experiment, with no delay between. The interlayer spacing of synthetic metaschoepite was calculated via sequential Rietveld refinement, while the interlayer spacing of γ was calculated from the position of the (002) reflection. The dashed line at 7.165 Å shows the approximate interlayer spacing of both desiccated structures.

4.6 Thermal stability of γ and synthetic metaschoepite

Differences between γ and synthetic metaschoepite were further assessed by studying the thermal dehydration of each species via dynamic XRD and Raman spectroscopy with temperature control. Figure 4.29 shows the XRD pattern of synthetic metaschoepite with increasing temperature. Two-hour XRD scans were collected at 10°C increments between 30 and 100°C, then at 20°C increments up to 200°C, and at 250 and 300°C. The temperature was ramped 1°C/min between scans and the sample was equilibrated at each temperature for 30 minutes prior to data collection. The dehydration reaction occurs in two steps. Shifts in the (002) and (004) reflections between 30 and 70°C (Figure 4.30) indicate a contraction of the layer spacing similar to that observed upon desiccation. As shown in Figure 4.31, the magnitude of this contraction is comparable in each case, suggesting that the dehydration mechanism is the same. In addition to this contraction in the c direction, a slight expansion occurs in the a and b directions, as evident via sequential Rietveld refinement (Figure 4.32).

At 80°C and above, a phase transition to anhydrous uranyl hydroxide ($\alpha-UO_2(OH)_2$, Figure 4.33) occurs. This transition is similar to the complete dehydration of synthetic metaschoepite that was previously demonstrated to occur upon prolonged exposure to a desiccating environment at ambient temperature [90]. However, as shown in Figure 4.34, the anhydrous product of the heating experiment is considerably more amorphous than the anhydrous sample produced via dessication at ambient temperature. This is unsurprising since the anhydrous product crystallized much more slowly (i.e., over weeks) via desiccation than dehydration.

This dehydration phase transition was also examined via Raman spectroscopy. Figure 4.35 shows the Raman spectrum of synthetic metaschoepite at increasing temperature. There is again evidence of two dehydration steps, consistent with the XRD data. Between 30 and 70°C, the higher energy uranyl stretching peak redshifts from an original position of 869 cm^{-1} to 862 cm^{-1}. This shift is illustrated in Figure 4.36. The lower uranyl stretching peak(s) do not change notably over this temperature range, nor do any of the lower energy peaks. By comparison of the XRD and Raman data, the redshifting of the upper uranyl stretching peak is correlated with the contraction of the layer spacing. It is plausible that

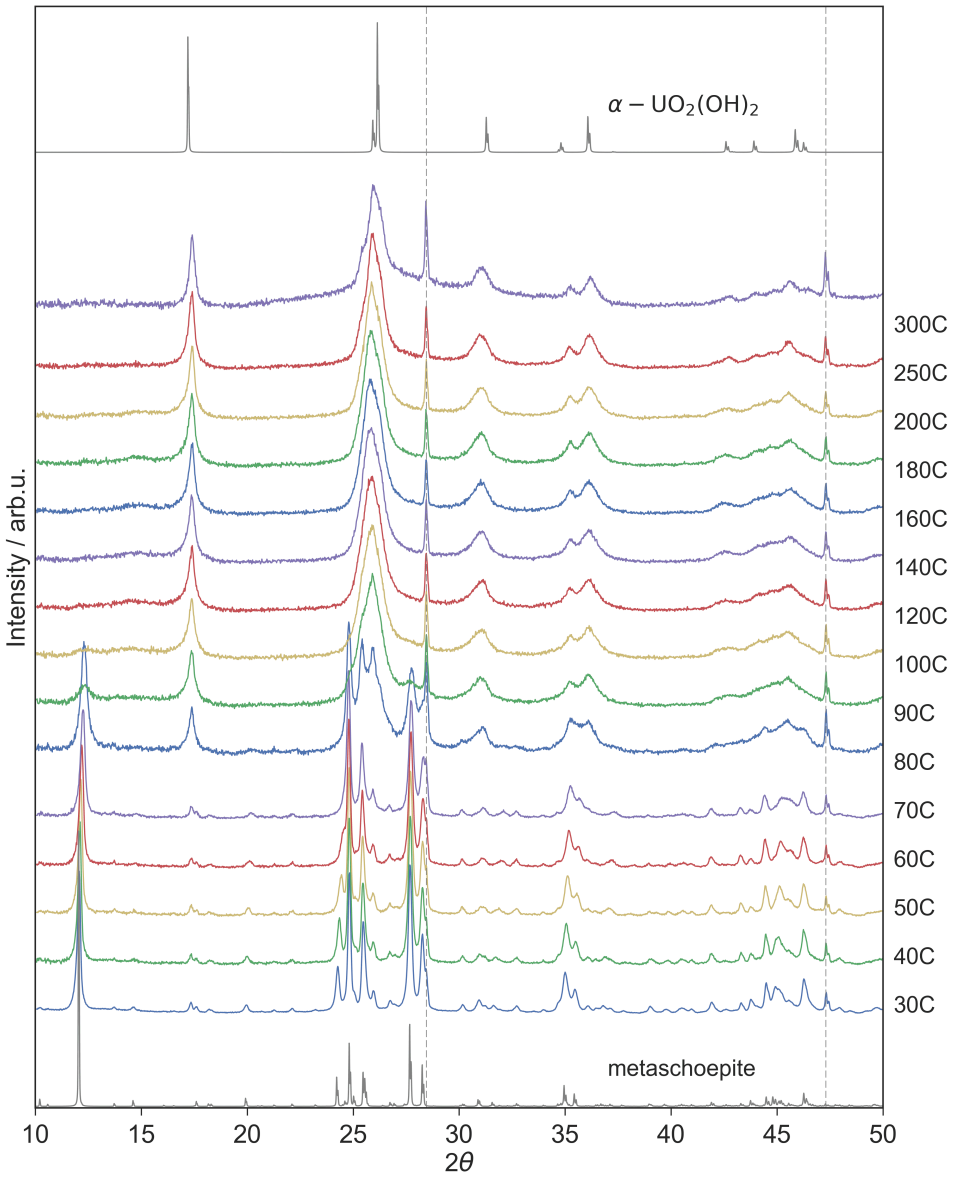

Figure 4.29: XRD pattern of synthetic metaschoepite at increasing temperature, from 30 to 300°C. The temperature was ramped 1°C/min between scans, and the sample was equilibrated at each temperature for 30 minutes prior to data collection. Each XRD pattern was collected over 2 hours. The expected patterns of metaschoepite [171] and anhydrous uranyl hydroxide [152] are shown for comparison.

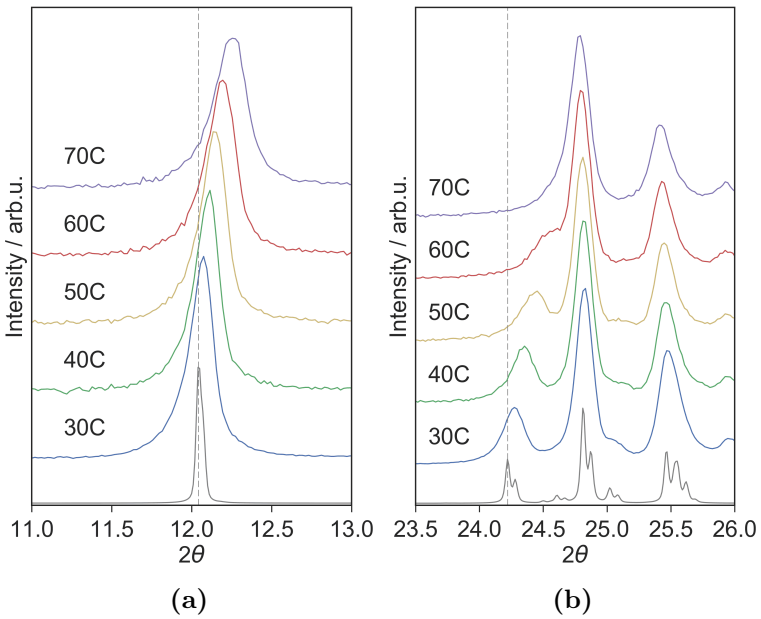

Figure 4.30: Regions of the XRD pattern of synthetic metaschoepite at increasing temperature, showing shifts in the (a) (002) reflection, and (b) (004) reflection. Dashed lines at $2\theta = 12.043°$ and 2θ=24.2216° show the expected location of the (002) and (004) reflections, as determined by Weller et al. [171].

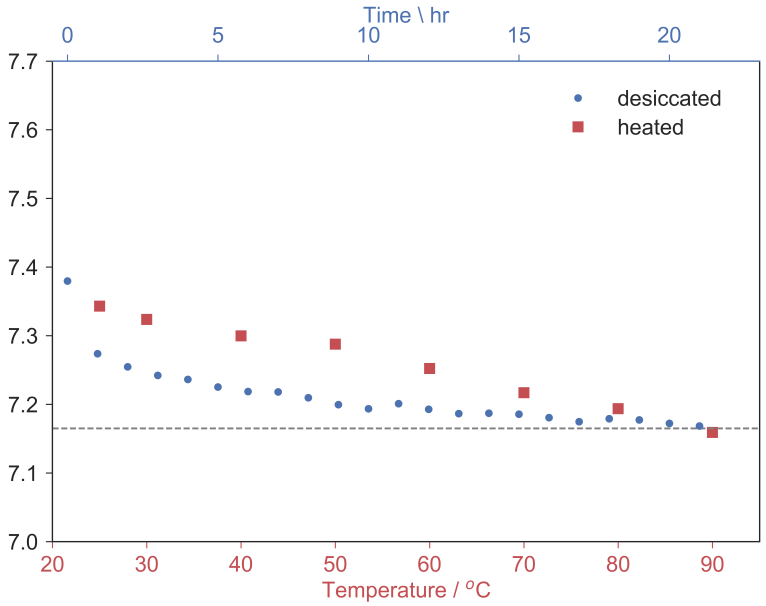

Figure 4.31: Interlayer spacing of synthetic metaschoepite as a function of temperature (red squares) and as a function of desiccation time (blue circles). The dashed line at 7.165 Å shows the approximate minimum layer spacing upon desiccation and upon heating before a discrete phase transition occurred >90°C.

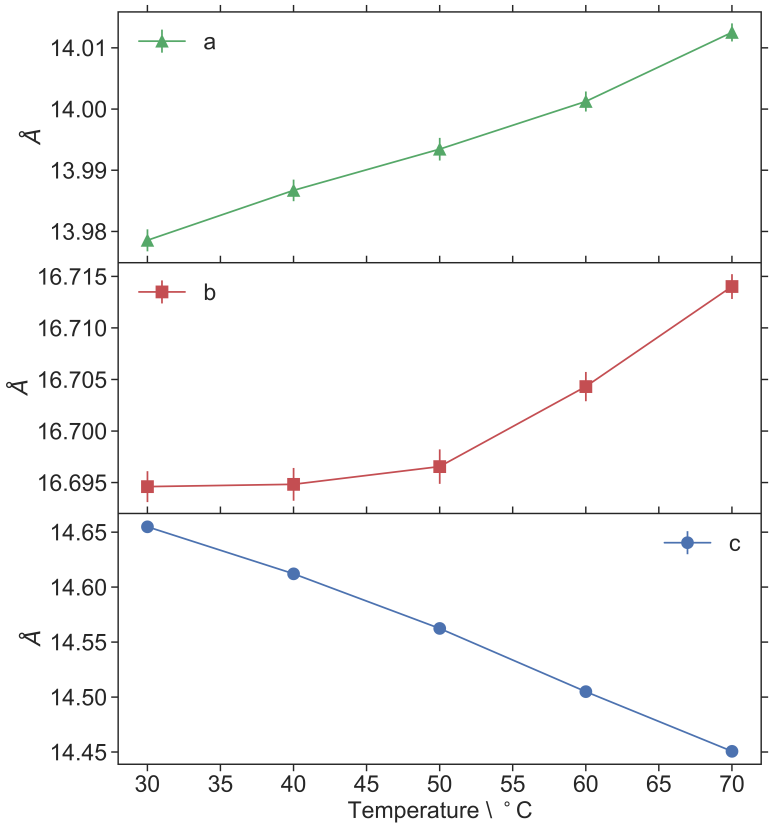

Figure 4.32: Lattice parameters of synthetic metaschoepite between 30 and 70 °C, as determined via sequential Rietveld refinement.

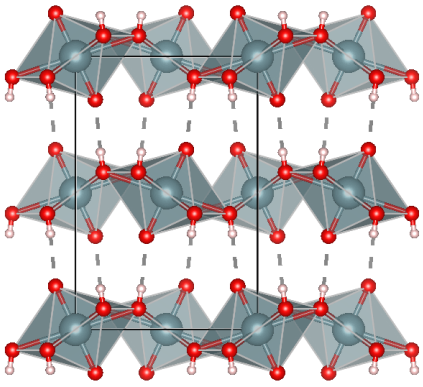

Figure 4.33: Crystal structure of $\alpha-(UO_2(OH)_2$, as determined by Taylor [152].

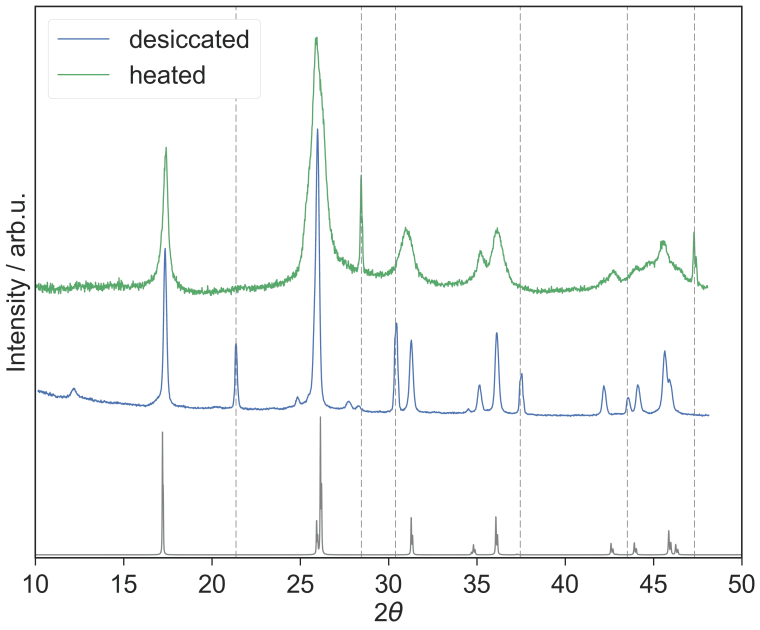

Figure 4.34: Comparison of the XRD pattern of anhydrous uranyl hydroxide produced by desiccating synthetic metaschoepite for 6 weeks at 16% RH and ambient temperature (22°C) and of anhydrous uranyl hydroxide produced by heating synthetic metaschoepite to 250°C. The predicted XRD pattern of $\alpha-UO_2(OH)_2$ [152] is shown for comparison. Dashed lines show the locations of peaks corresponding to LaB_6 or Si powder standards, which should be ignored in a comparison of the two samples.

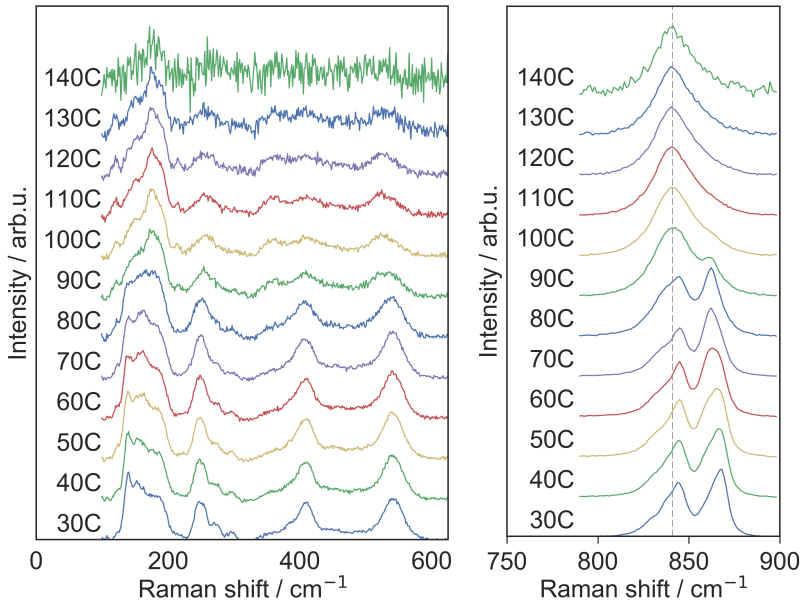

Figure 4.35: Raman spectrum of synthetic metaschoepite at increasing temperature from 30 to 140°C. The temperature was ramped at 0.2°C/min.

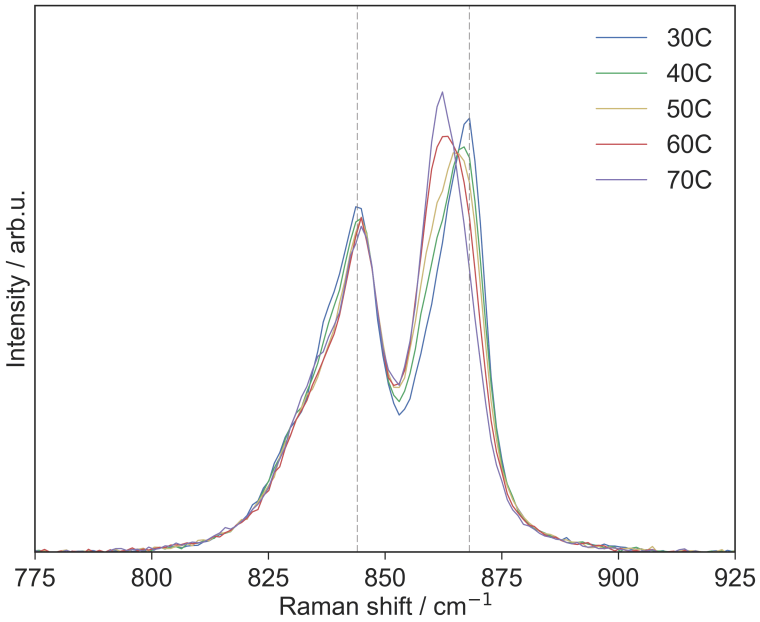

Figure 4.36: Raman spectra of synthetic metaschoepite at 30 to 70°C overlaid. The temperature was ramped at 0.2°C/min. Dashed lines at 868, 845, and 841 cm^{-1} highlight the location of the two dominant uranyl stretching modes of synthetic metaschoepite at ambient temperature [90].

this contraction promotes increased hydrogen bonding interactions to a subset of the uranyl ions, redshifting the stretching mode of those uranyl ions. The upper uranyl stretching peak was previously attributed to the subset of uranyl ions in the metaschoepite structure that are equatorially bound to five hydroxy groups, as opposed to four hydroxy groups and an oxide group. It is unclear why contraction of the layer spacing would selectively affect these uranyl ions, and it is possible that this assignment needs to be re-examined. Additional computational experiments could help assess which uranyl ions are predicted to be most affected by changes in the interlayer spacing.

As observed in the XRD experiment, a phase transition to anhydrous uranyl hydroxide occurs between 80 and 100°C. The resulting single uranyl stretching mode centered at 841 cm^{-1} is consistent with previous measurements of anhydrous uranyl hydroxide [149]. However, this transition temperature is significant lower than has been previously reported for metaschoepite. Nipruk et al. studied the dehydration transition from schoepite to metaschoepite to anhydrous uranyl hydroxide via thermogravimetric analysis (TGA) and found the two transitions to occur near 116 and 156°C [123]. It is possible that starting from the more hydrated schoepite affects the dehydration temperature, however, complicating a direct comparison to the data presented in this work. In addition, the IR spectrum of metaschoepite presented by Nipruk et al. is not a perfect match with the IR spectrum of the material used in this study, suggesting that there may be slight structural differences in the samples. Finch et al. previously noted that a sample of schoepite was partially dehydrated to anhydrous uranyl hydroxide by heating at 120°C for one hour [54]. While this observation was made for schoepite and not metaschoepite, the finding suggests that it is possible to dehydrate uranyl hydroxide hydrates at lower temperatures than determined by Nipruk et al.

The same dynamic XRD and Raman temperature experiments were repeated with samples of γ to compare the thermal stability of this new material to synthetic metaschoepite. The same experimental settings were used in each case. Figure 4.37 shows the XRD pattern of γ at increasing temperature. Between ambient temperature and 50°C, the (002) and (004) peaks were observed to shift upwards, indicating a contraction of the layer spacing consistent with that observed upon desiccation. As found for metaschoepite, the magnitude of this

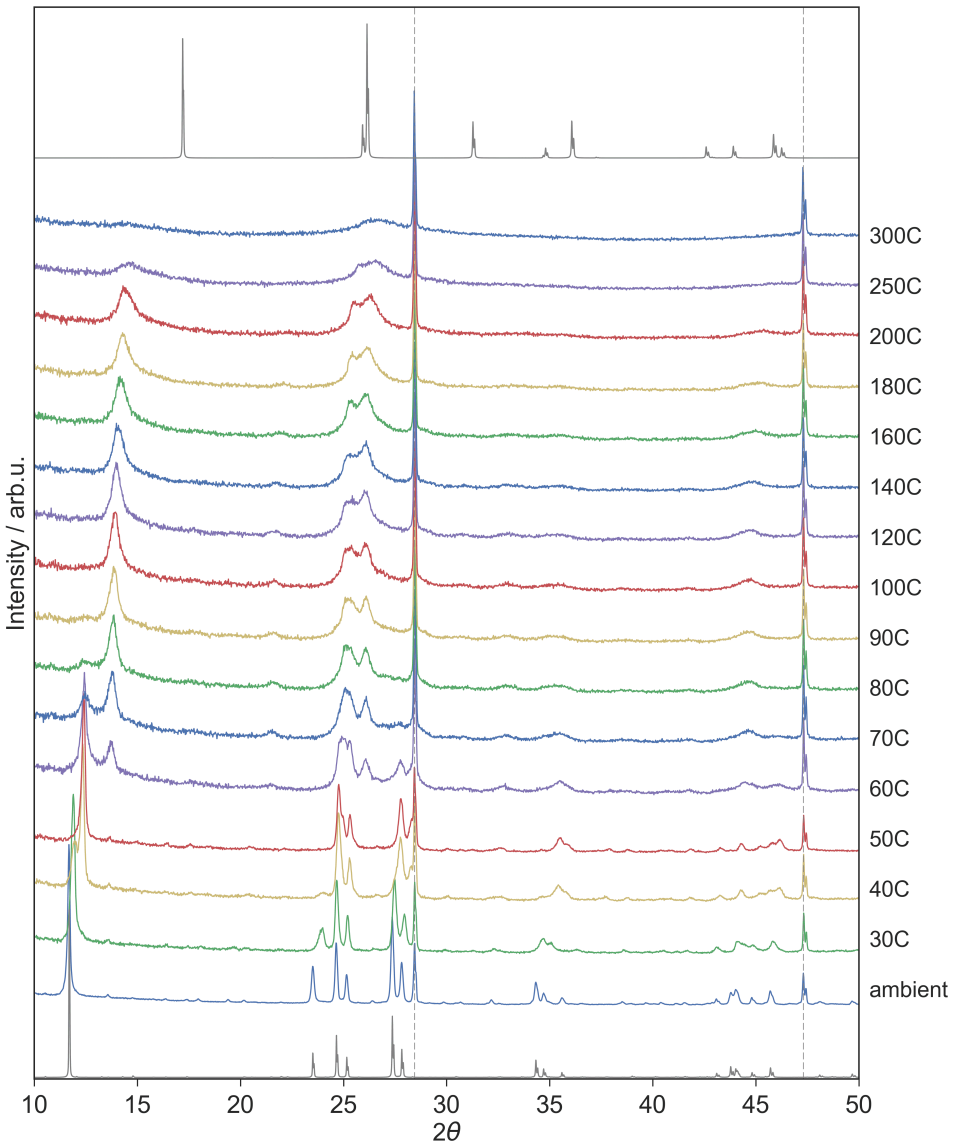

Figure 4.37: XRD pattern of γ at increasing temperature, from ambient to 300°C. The temperature was ramped 1°C/min between scans, and the sample was equilibrated at each temperature for 30 minutes prior to data collection. Each XRD pattern was collected over 2 hours. The previously determined expected pattern of the γ structure is shown for comparison, as well as that of anhydrous uranyl hydroxide [152].

contraction in each case is comparable (Figure 4.38). Distinct from synthetic metaschoepite, the a and b parameters of the new uranyl hydroxide hydration product contract along with the c lattice parameter prior to the phase transition (Figure 4.39), suggesting that the uranyl polyhedra begin to buckle as water molecules are removed. The contraction of the c lattice parameter occurs more rapidly between 25 and 40 °C and at the same slower rate as synthetic metaschoepite between 40 and 70 °C. If this species is hydrated relative to synthetic metaschoepite, and there are more water molecules than hydroxy ligands, the excess water molecules cannot form strong hydrogen bonds with hydroxy groups. These water molecules may be removed from the structure more easily, leading to the initial rapid contraction of the interlayer spacing.

Beginning at 60°C, a phase transition is indicated by a discrete shift of the (002) peak, more clearly illustrated in Figure 4.40. At 250 and 300°C, the XRD pattern indicates a predominantly amorphous material, with no well-defined Bragg reflections. Unlike observations of synthetic metaschoepite, a discrete phase transition to anhydrous uranyl hydroxide never occurs. Instead, the position of the (002) reflection indicates that the layer spacing contracts upon heating to approximately 6.19 Å, in between the spacing observed for the hydrates at room temperature (7.34 Å for synthetic metaschoepite and 7.56 Å for γ) and the spacing observed for anhydrous uranyl hydroxide (5.09 Å).

This difference in the dehydration behavior between synthetic metaschoepite and γ is illustrated in Figure 4.41, which shows the interlayer spacing of each species as a function of temperature. The spacing at each temperature was determined by the position of the (002) reflection (or (020) in anhydrous uranyl hydroxide, which is oriented with the uranyl layers normal to the b-direction [152]). In the cases where multiple (002)/(020) reflections were observed due to a phase mixture, both corresponding interlayer spacings are shown.

Why the γ dehydration product has an expanded interlayer spacing relative to anhydrous uranyl hydroxide is unclear. It is possible that the uranyl polyhedra are buckled in the structure such that they cannot stack as tightly as observed in anhydrous uranyl hydroxide; unfortunately the a and b lattice parameters cannot be adequately determined for this structure due to the limited number of broad reflections. Above 200 °C, the structure becomes X-ray amorphous, suggesting that, as a result of buckling or other disorder,

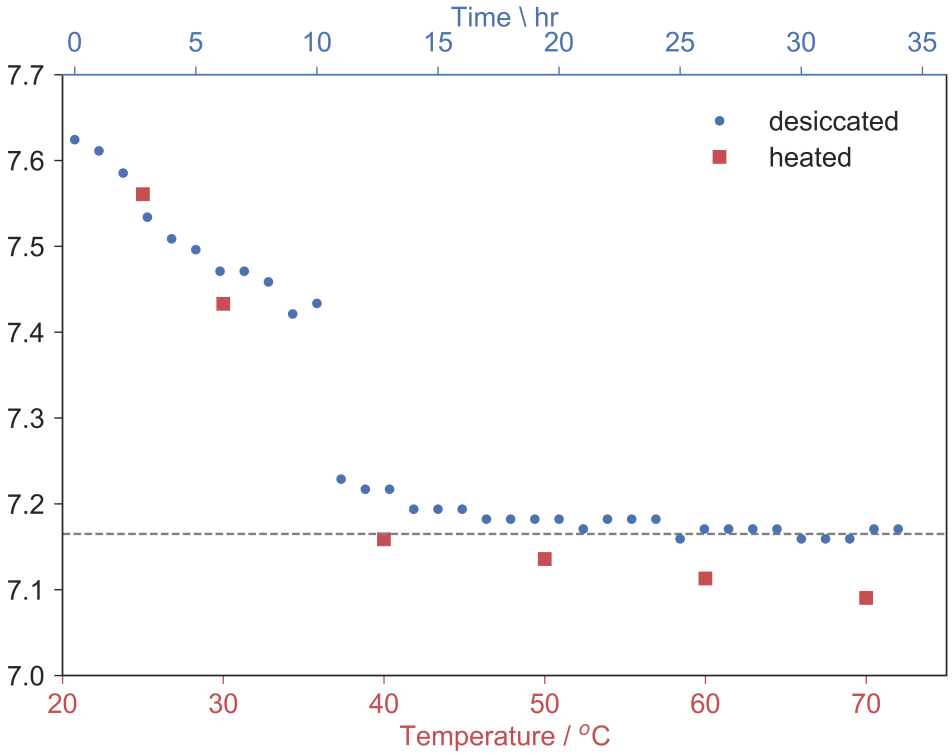

Figure 4.38: Interlayer spacing of γ as a function of temperature (red squares) and as a function of desiccation time (blue circles). The dashed line at 7.165 Å shows the approximate minimum layer spacing upon desiccation.

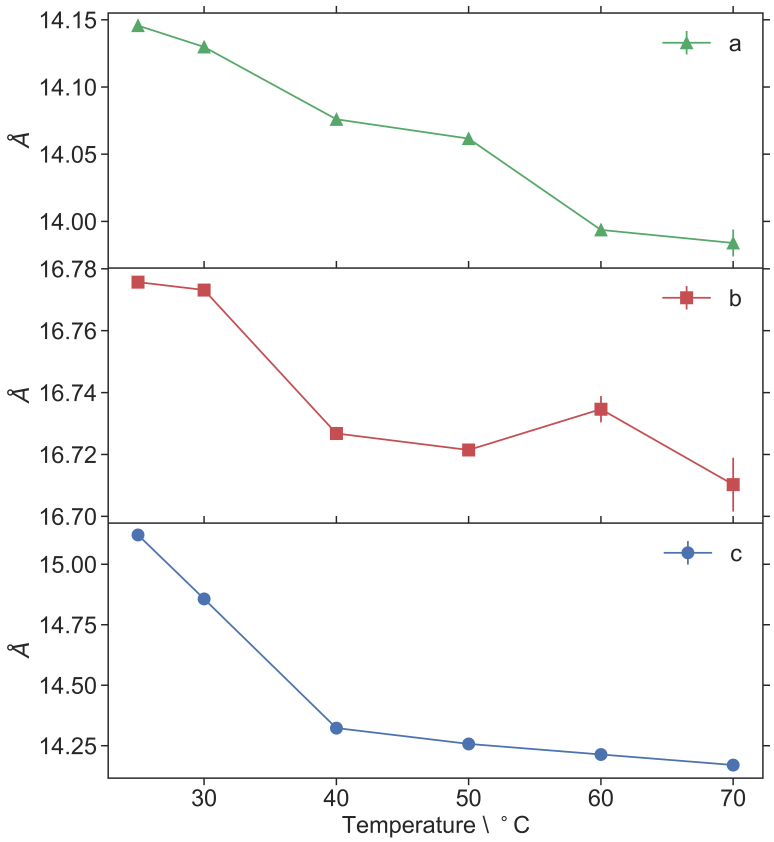

Figure 4.39: Lattice parameters of γ between 30 and 70 °C, as determined via sequential Rietveld refinement.

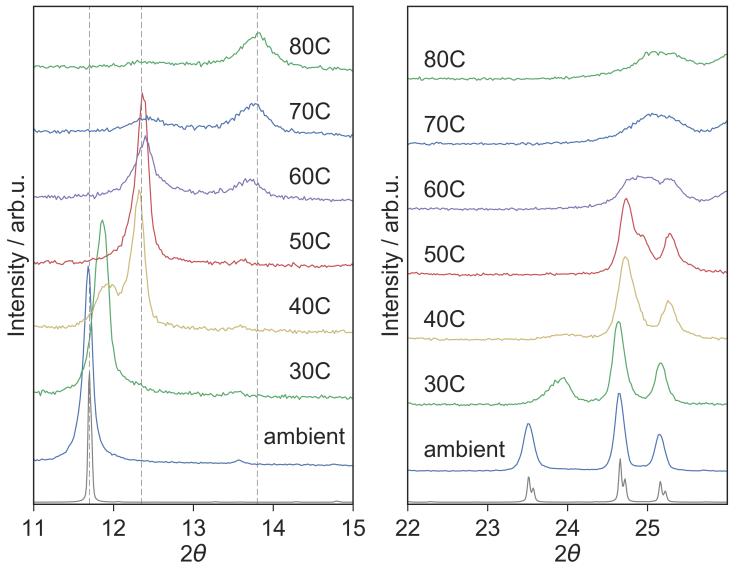

Figure 4.40: Regions of the XRD pattern of γ at increasing temperature, showing shifts in the (a) (002) reflection, and (b) (004) reflection.

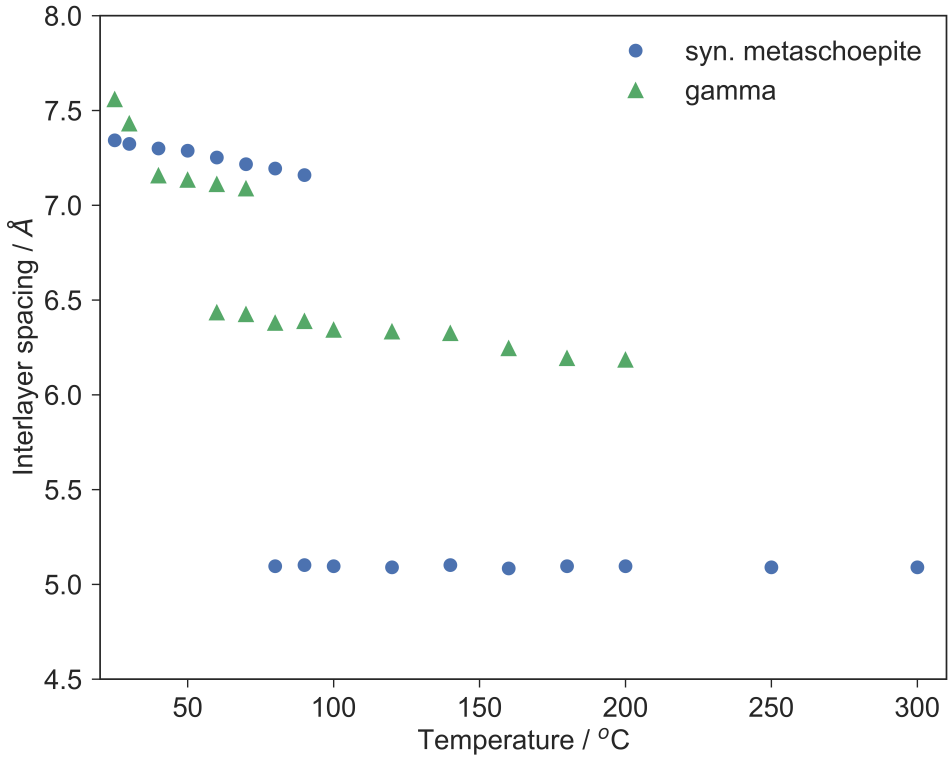

Figure 4.41: Interlayer spacing of synthetic metaschoepite (blue circles) and γ (green triangles), as determined by the position of the (002) reflection (or corresponding reflection in the anhydrous species), as a function of temperature.

the dehydration product does not have the same organized hydrogen bonding scheme as anhydrous uranyl hydroxide (Figure 4.33) which promotes stability at higher temperatures.

It is also possible that there is something between the layers preventing them from collapsing completely. If a subset of the interlayer water molecules were not removed in the phase transition, the interlayer spacing of the dehydration product would be expanded relative to anhydrous uranyl hydroxide. The structural effect of residual water molecules was explored computationally in the study of the effect of water removal on the layer spacing of schoepite described in Section 4.5. Figure 4.42 shows the optimized unit cells in two different cases where 44 of the 48 interlayer water molecules in the schoepite unit cell were removed. In one case (Figure 4.42a), the remaining water molecules keep the layers from forming hydrogen bonds to each other, maintaining a layer spacing of 6.55 Å. In the other, hydrogen bonds between the layers do form, and the water molecules become trapped in pockets formed by the tilting of surrounding uranyl polyhedra. The layer spacing in this case was calculated to be 5.85 Å, still expanded relative to the experimental value for purely anhydrous uranyl hydroxide (5.151 Å [152]). The expanded water spacing of the γ dehydration product is observed to persist up to 200°C, where it would be highly unexpected for hydrogen bonded water molecules to remain in the structure. It is unclear, however, how strongly remaining water molecules could be bonded in these uranyl pockets.

To better understand both the structure of the γ dehydration product and how this dehydration transition occurs, γ was studied via Raman spectroscopy upon heating. Figure 4.43 shows the Raman spectrum of γ at increasing temperature. Unlike metaschoepite, no change was observed in Raman spectrum below 110°C (Figure 4.44). This was unexpected given the significant changes that occur in the XRD pattern over this range. The two samples of γ used in the XRD and Raman heating experiments were produced independently via the hydration of two different batches of uranyl fluoride, and while the initial XRD patterns and Raman spectra of each sample were consistent, it is possible that differences could have existed that were not observable with these techniques. A follow-up study using the same batch of material for both experiments is necessary to clarify these findings.

Around 120°C, a transition finally occurs in the Raman spectrum. The initial uranyl stretching mode at 846 cm^{-1} broadens and shifts slightly to 841 cm^{-1}. In addition, a broad

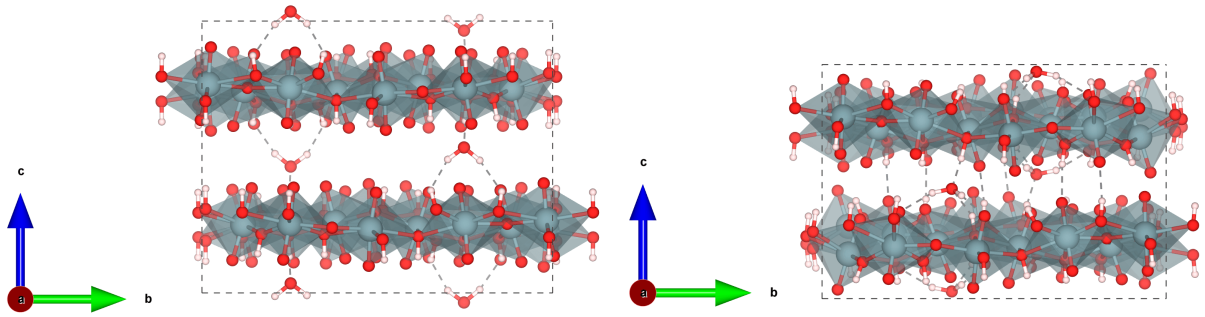

(a) **(b)**

Figure 4.42: Two different optimized structures of schoepite after the random removal of 11 of the 12 groups of interlayer water molecules in schoepite. The interlayer spacing is calculated to be (a) 6.55 Å and (b) 5.85 Å.

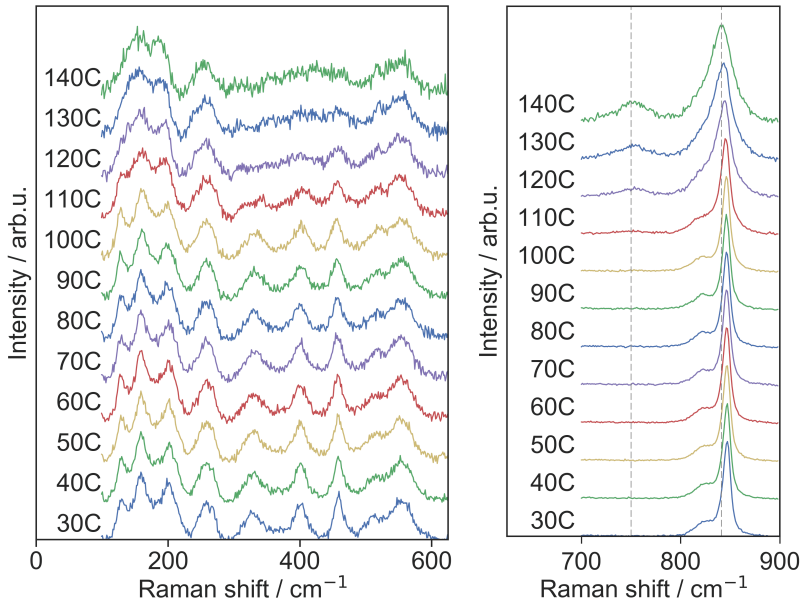

Figure 4.43: Raman spectrum of γ at increasing temperature, from 30 to 140°C. The temperature was ramped at 0.2°C/min.

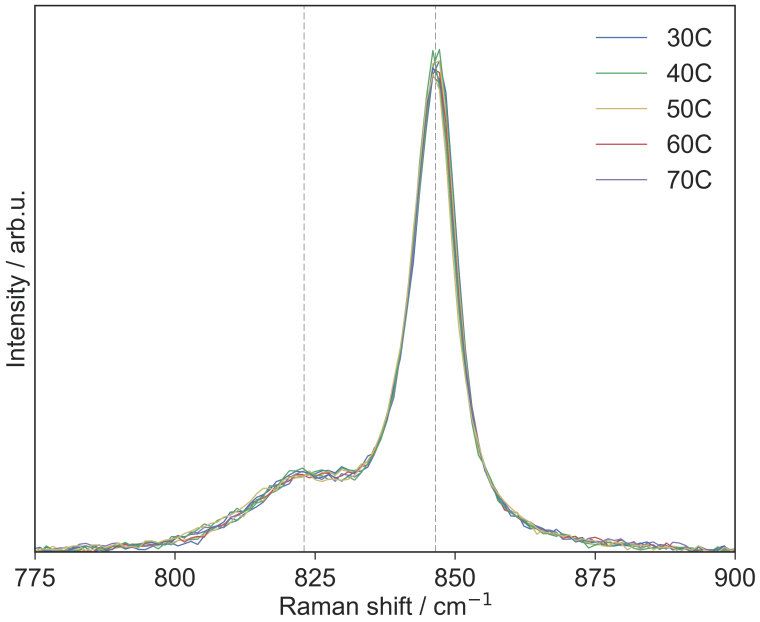

Figure 4.44: Raman spectra of γ at 30 to 70°C overlaid. The temperature was ramped at 0.2°C/min. Dashed lines at 846 and 823 cm^{-1} highlight the location of the uranyl stretching modes of γ at ambient temperature.

weak peak grows in at 750 cm^{-1}. The origin of this peak is unclear; it is somewhat low in energy to be a second uranyl stretching mode. The uranyl stretching mode at 841 cm^{-1} is consistent with previous studies of anhydrous uranyl hydroxide and with the dehydration product of synthetic metaschoepite observed in this work. The similarities between the high-temperature spectra suggest that the dehydration products have structural similarities, at least in terms of the equatorial coordination of the uranyl ion. The higher temperature required to dehydrate γ in this Raman study is consistent with the previously discussed hypothesis that γ is characterized by stronger hydrogen bonds between hydroxy groups and interlayer water molecules. However, the dynamic XRD study of γ suggested that it was *less* stable than synthetic metaschoepite at increasing temperature. Additional studies are necessary to clarify these inconsistencies.

4.7 Summary and future directions

In summary, the initial hydration product of uranyl fluoride, γ, has been characterized using a variety of complementary methods. In Chapter 3, this species was tentatively identified as a uranyl hydroxide species based on the SEM-EDS and Raman spectra. XRD confirms this identification, showing structural similarities between γ and the known uranyl hydroxide hydrate minerals schoepite and metaschoepite. Rietveld refinement of the XRD pattern shows that γ has a significantly expanded layer spacing relative to these known species. This structure has never been isolated previously.

The structure and chemical behavior of γ has been further analyzed through a comparative study to synthetic metaschoepite. Comparison of the Raman and IR spectra of γ with synthetic metaschoepite suggests that the uranyl layers in each differ slightly and that γ is characterized by stronger hydrogen bonding interactions between the uranyl layers and the interlayer water molecules. The fact that γ transforms into a dehydration product distinct from anhydrous uranyl hydroxide when heated is further evidence that γ has notable structural differences from synthetic metaschoepite. However, dynamic XRD and Raman temperature scans of samples of γ found different transition temperatures and cannot be reconciled without a follow-up study. One of the present limits to the characterization

of γ is the inability to produce large samples of material in a reasonable amount of time. Formation of γ via hydration of uranyl fluoride is slow, particularly in bulk. This limits the ability to replicate experiments or perform complementary experiments on the same batch of material, introducing additional uncertainty into the analysis. The origin of a strong IR peak at 1423 cm^{-1} in γ also requires further study.

Future work should focus on identifying ways of accelerating the formation of γ from uranyl fluoride or identifying alternate synthesis routes. The inability to form γ via hydration of synthetic metaschoepite at ambient temperature and pressure was demonstrated in this work. However, the formation of a minor component species with an expanded layer spacing in the rehydration of synthetic metaschoepite following desiccation suggests that a synthesis method from synthetic metaschoepite should be further explored. It is possible that a hydrothermal synthesis route from either uranyl fluoride or uranyl hydroxide starting material could be identified. The ability to produce larger samples of γ would enable the application of additional complementary techniques such as TGA and neutron scattering that could provide additional insight into the water content and structure. In addition, multiple experiments could be carried out on samples from the same batch of material, reducing uncertainties in the correlating of data sets. Production of a single crystal of γ, if feasible, would allow for a more detailed structural analysis and better understanding of how the uranyl layers differ in γ relative to schoepite and metaschoepite.

Chapter 5

Elucidation of a novel formation mechanism for solid-state uranyl peroxide (δ)

Chapter 4 presented efforts to characterize γ, the uranyl hydroxide hydrate formed via hydration of uranyl fluoride. As discussed in Chapter 3, at high enough humidity, γ can be further converted into δ. This product was proposed to be a uranyl peroxide species based on the excellent agreement of the Raman spectrum with that of the uranyl peroxide hydrate mineral studtite, $[(UO_2)O_2(H_2O)_2] \cdot 2\,H_2O$. The formation of a uranyl peroxide species in this system was unexpected given the lack of hydrogen peroxide (H_2O_2). The excellent agreement of all peaks leaves no doubt that a uranyl peroxide species has been produced, but Raman spectroscopy does not provide direct structural information for confirmation. This chapter presents additional structural characterization of δ as well as elucidation of the novel nonphotochemical formation mechanism for uranyl peroxide. The unexpected formation of uranyl peroxide in this system is attributed to oxidation of water by the uranyl ion. While this reaction is expected to require photoexication of the uranyl ion, the environment of the uranyl ion in the uranyl hydroxide reagent appears to facilitate the redox reaction from the uranyl ground state.

Components of this chapter come from the following papers:

M. C. Kirkegaard, M. W. Ambrogio, A. Miskowiec, J. L. Niedziela, T. L. Spano, A. E. Shields and B. B. Anderson. "Characterization of the degradation of $[(UO_2F_2)(H_2O)]_7 \cdot 4\,H_2O$ under humid conditions." In preparation.

M. C. Kirkegaard, T. L. Spano, A. Miskowiec, J. L. Niedziela, A. E. Shields and B. B. Anderson. "Evidence of unusual uranyl ion reactivity in uranyl hydroxide hydrates." In preparation.

5.1 Literature review of uranyl peroxide hydrate species

5.1.1 Known uranyl peroxide hydrate structures

Uranyl peroxides were first identified by Zachariasen in 1944 [175]. Subsequent studies showed that two different uranyl peroxide species, of the form $[(UO_2)O_2(H_2O)_2] \cdot 2\,H_2O$ and $(UO_2)O_2(H_2O)_2$, can be synthesized by adding H_2O_2 to uranyl solutions at differing temperature. It was also observed that $[(UO_2)O_2(H_2O)_2] \cdot 2\,H_2O$ can be converted to $(UO_2)O_2(H_2O)_2$ by drying in air at 100°C or under vacuum at room temperature [140]. The minerals studtite and metastudtite were later shown to be structurally identical to synthetic $[(UO_2)O_2(H_2O)_2] \cdot 2\,H_2O$ and $(UO_2)O_2(H_2O)_2$, respectively [163, 46]. Studtite and metastudtite remain the only known peroxide-containing minerals [94].

The full structure of studtite was solved by Burns and Hughes in 2003 [29]. Each linear uranyl group is bonded to six additional oxygens, two of which are water ligands and the other four of which comprise peroxide groups. The O−O bonds of two peroxide groups thus make up two equatorial edges of each uranyl hexagonal bipyramid, as shown in Figure 5.1. The uranyl polyhedra share peroxide groups, forming chains that are linked together by hydrogen bonds between water molecules.

Unlike studtite, no refined structure of metastudtite has been published. In the absence of single-crystal x-ray data, first-principle calculations have been used to attempt to refine the structure of metastudtite [127, 170]. Weck et al. predicted an orthorhombic cell with structural similarities to studtite that matches experimental data well (Figure 5.2) [170]. Metastudtite is thought to form by the loss of interlayer water in studtite [29]. This

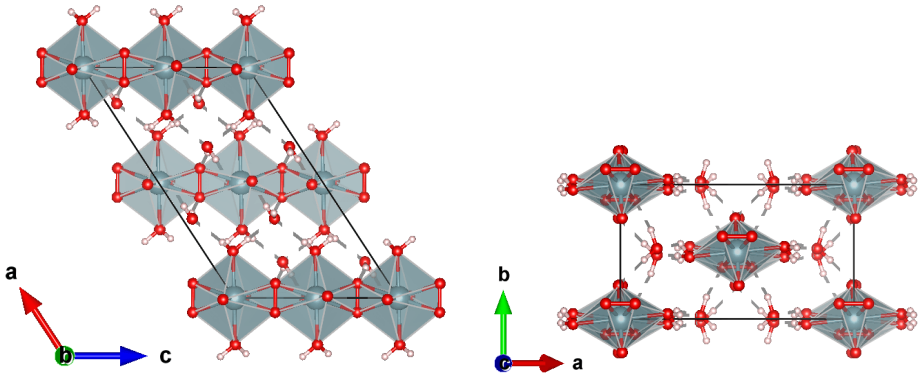

(a) **(b)**

Figure 5.1: (a) Top-down and (b) side views of the crystal structure of studtite, $[(UO_2)O_2(H_2O)_2] \cdot 2\,H_2O$, as determined by Burns and Hughes [29].

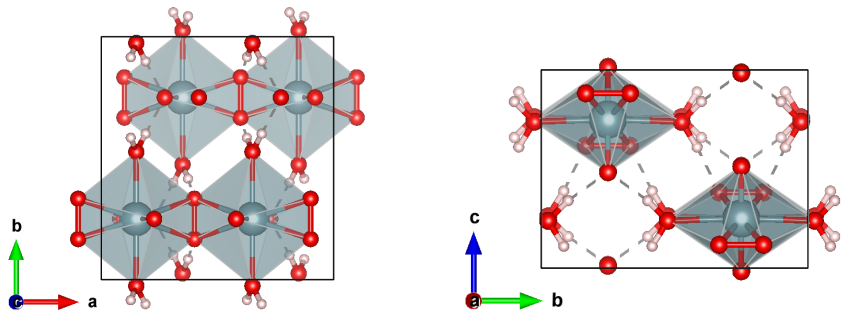

(a) **(b)**

Figure 5.2: (a) Top-down and (b) side views of the crystal structure of metastudtite, $(UO_2)O_2(H_2O)_2$, as predicted computationally by Weck et al. [170].

dehydration transition has been demonstrated to be irreversible [64, 126], presumably due to the formation of strong hydrogen bonds between adjacent uranyl chains.

The most thorough experimental study of metastudtite is presented in the thesis of S. Labs [96]. X-ray diffraction (XRD) analysis showed that the chains of uranyl polyhedra move slightly toward each other upon dehydration. Labs also attempted to refine the structure of metaschoepite via neutron scattering. Starting with the computationallypredicted structure from Weck et al. [170], refinement shortened one uranyl bond and lengthened the other, tilting one of the uranyl oxygens toward the peroxo group and leaving the uranyl unit bent at a fairly extreme 143° angle. Labs noted that this refined structure is somewhat questionable, but that the tilt of the uranyl oxygen towards the peroxo unit allows for intramolecular hydrogen bonding, which could explain why the dehydration transition is irreversible.

Thermogravimetric analysis (TGA) by Labs showed that the dehydration reaction from studtite to metastudtite occurs around 80°C. However, a variable temperature XRD analysis showed dehydration occurring much sooner, between 30 and 60°C. Above 56°C, studtite could no longer be detected in the XRD pattern. Labs suggested that a structural change may occur at lower temperatures, but the water released from the crystal structure remains adsorbed to the surface and thus no weight loss is detected until higher temperatures [96]. Alternatively, Colmenero et al. noted that this dehydration reaction occurs at higher temperatures in the presence of water [40]. It is possible that the TGA and XRD studies performed by Labs were conducted under different water vapor pressures, which could thus also explain the discrepancy.

Labs also used inelastic incoherent neutron scattering (IINS) to look at water bonding in studtite and metastudtite. Water librational modes were resolvable in studtite only, suggesting that hydrogen-bonded water exists in studtite but not metastudtite. Strong UOH and HOH bending vibrations are visible in metastudtite, suggesting that water is more restricted in metastudtite than studtite. These observations offer further support of the structural model of metaschoepite proposed by Weck et al. [169].

5.1.2 Vibrational spectroscopy of uranyl peroxide hydrates

Studtite and metastudtite have also been characterized via vibrational spectroscopy. Infrared (IR) spectra of studtite and metastudtite published by Labs [96] are shown in Figure 5.3. As expected, there are some differences between the two species in the bands associated with water. For example, studtite has two peaks in the water bending region (1500–1750 cm^{-1}) corresponding to the two different types of water in the structure. The most notable difference in the 400–1000 cm^{-1} region of the spectra is the presence of a broad feature around 730 cm^{-1} in studtite, which Labs tentatively attributed to a symmetric uranyl stretching mode [96] but which might alternatively correspond to water librational modes. Raman spectra collected by Labs [96] are shown in Figure 5.4. The peroxo stretching mode is nearly identical for both species, at 866 cm^{-1} in studtite and 867 cm^{-1} in metastudtite, while the uranyl stretching mode shifts from 819 cm^{-1} in studtite to 833 cm^{-1} in metastudtite. These spectra are in good agreement with those of both natural and synthetic samples published by others [4, 17, 132, 31, 18, 40]. The published Raman spectra of studtite and metastudtite are much more consistent than those of schoepite and metaschoepite.

5.1.3 Rising interest in uranyl peroxide species

As illustrated in Figure 5.5, uranium peroxide species have gained significant attention in recent years. Interest in these species has grown in a number of different areas, from fundamental solution chemistry to radiochemistry. Studtite and metastudtite are the only known peroxide-containing minerals, prompting investigation into how the complex electronic structure of uranium might stabilize these units [127]. The discovery that uranium peroxide units can self-assemble into large stable cage clusters has garnered additional interest [144, 135]. On the more applied side, uranyl peroxide species have been observed to form in spent nuclear fuel that comes in contact with water [67], creating safety concerns due to off-gassing and motivating additional study of the long-term stability of these species [14, 126]. Increased interest in uranyl peroxide species further motivated a more thorough characterization of δ and its formation mechanism from γ.

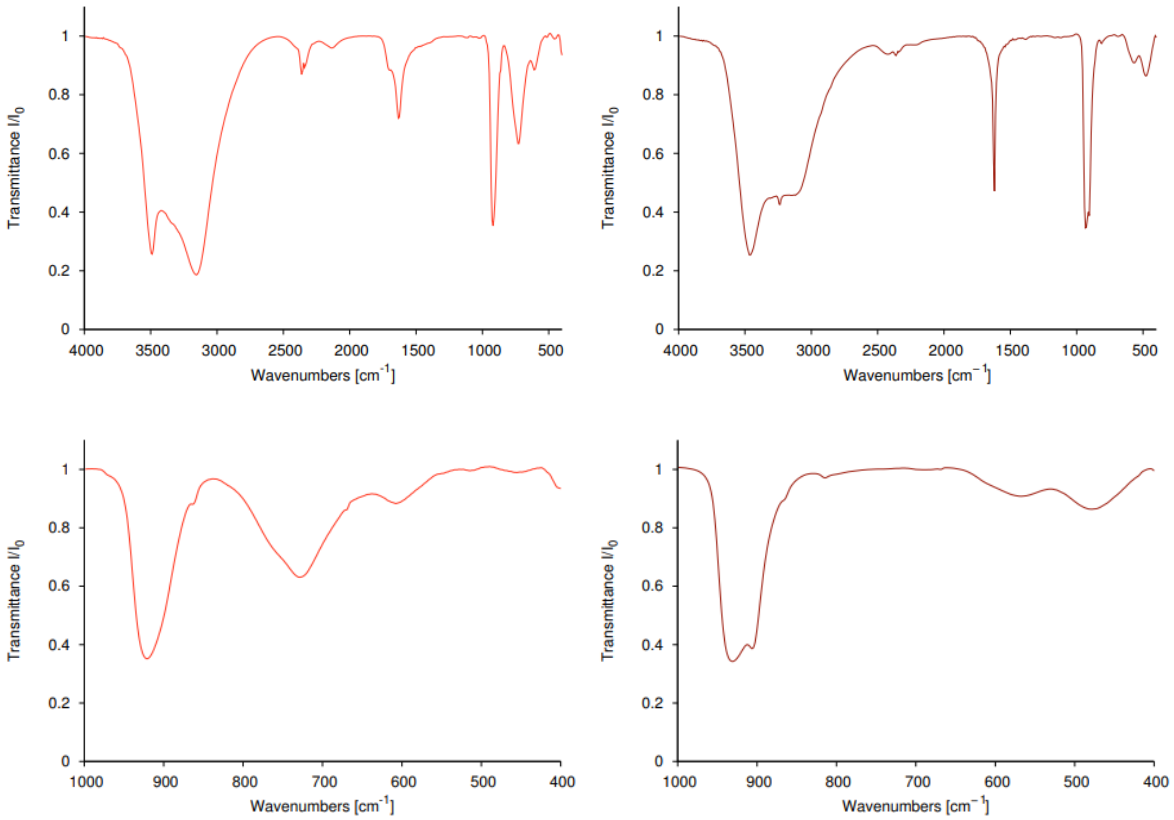

Figure 5.3: IR spectra of studtite (left) and metastudtite (right). Reproduced from Labs 2015 [96].

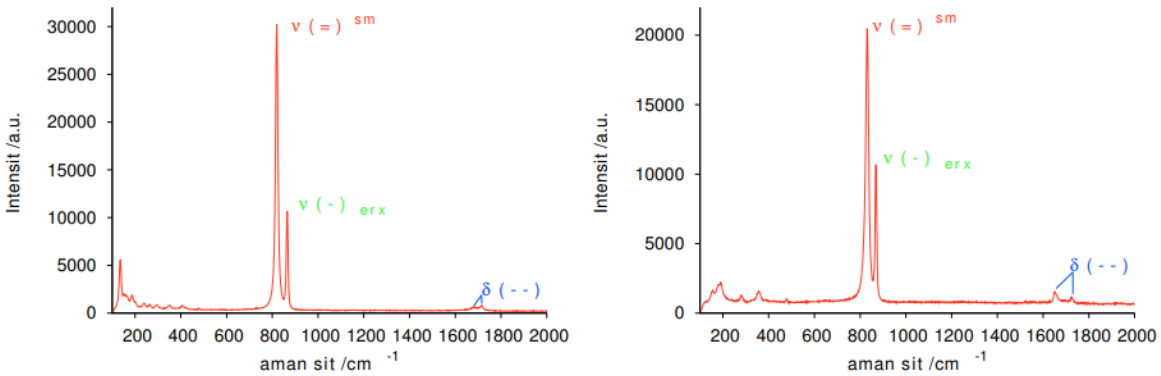

Figure 5.4: Raman spectra of studtite (left) and metastudtite (right). Reproduced from Labs 2015 [96].

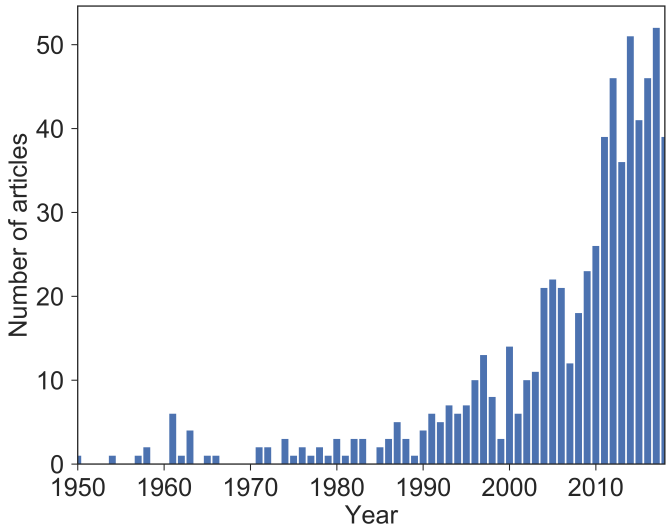

Figure 5.5: Number of publications in the Web of Science database per year matching the keywords "uranium/uranyl peroxide" or "studtite."

5.2 Structural characterization of δ

The formation of δ, a proposed uranyl peroxide species, from the hydration of uranyl fluoride was introduced in Chapter 3. Analysis of the concentration curves over time suggested that δ forms upon further hydration of the initial hydration product of uranyl fluoride, γ, which was characterized as a uranyl hydroxide hydrate in Chapter 4. While the excellent agreement of the Raman spectrum of δ with the uranyl peroxide hydrate studtite is strong evidence that δ has peroxo ligands and a similar overall structure, Raman spectroscopy is not a direct structural technique. To confirm the production of a peroxide species in this system, a larger sample of uranyl fluoride was hydrated to obtain XRD data. The previous chapter described the hydration of two XRD samples of uranyl fluoride to form the uranyl hydroxide hydrate species, γ. A third XRD sample was similarly prepared by depositing $[(UO_2F_2)(H_2O)]_7 \cdot 4\,H_2O$ powder on a silicon XRD plate with silicon powder standard. This sample was hydrated for a longer period of time than the samples described in Chapter 4 — 185 days at 83% relative humidity (RH) and 35°C ($P_{H_2O} = 4.67$ kPa), and then an additional 62 days at 91% RH and 35°C (P_{H_2O}=5.11 kPa).

Figure 5.6 shows the XRD pattern of this sample initially and at two different stages of hydration. After 76 days, the initial $[(UO_2F_2)(H_2O)]_7 \cdot (H_2O)_4$ material has undergone a complete transformation and the XRD pattern is a good match to the γ species previously identified. The Raman spectrum of the sample at this point matches the previously determined Raman spectrum of γ, with a dominant uranyl stretching mode near 845 cm^{-1} and lower shoulder centered near 825 cm^{-1}.

After 247 days of hydration, the Raman spectrum shows the growth of δ, with characteristic peaks at 820 and 865 cm^{-1}. The Raman peak attributed to the γ species near 845 cm^{-1} has shifted down slightly in frequency, suggestive of strengthened hydrogen bonding due to the absorption of additional water molecules. In general, the Raman spectrum at this point is consistent with particles in the particle hydration study that were determined to be a mix of the γ and δ species. In addition to these changes in the Raman spectrum, there are additional peaks in the XRD diffractogram compared to after 76 days. The location of many of these peaks matches the location of the expected diffraction maxima of studtite

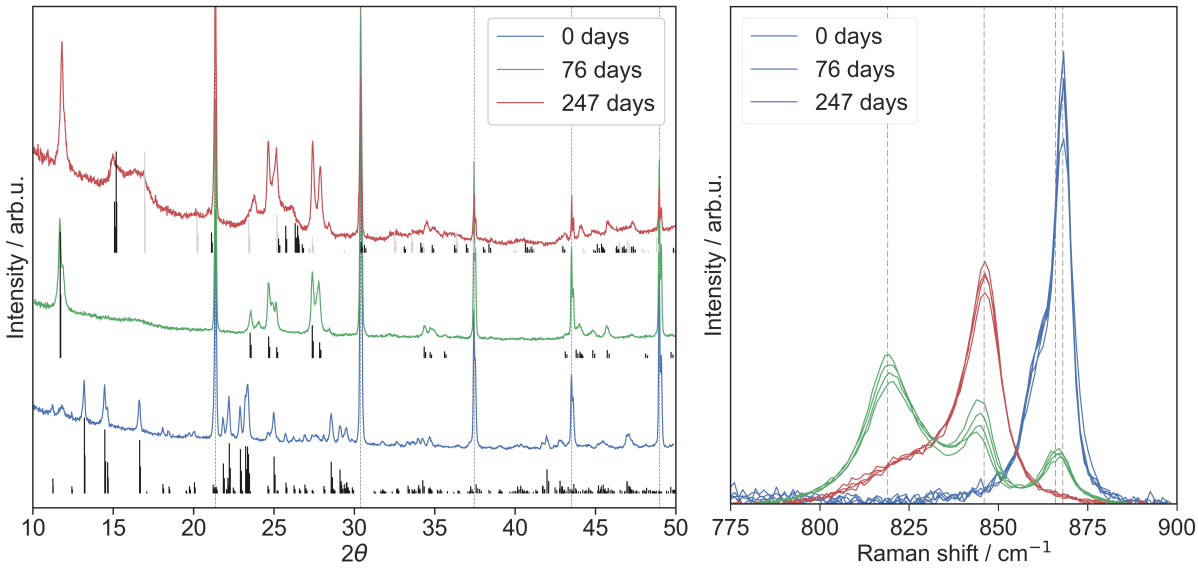

Figure 5.6: (a) XRD patterns over time of a sample of $[(UO_2F_2)(H_2O)]_7 \cdot (H_2O)_4$ stored at 85% RH at 35°C (P_{H_2O} = 4.67 kPa). The initial pattern is shown compared to the expected pattern of $[(UO_2F_2)(H_2O)]_7 \cdot (H_2O)_4$. After 76 days, the pattern matches the expected pattern of the γ species, as determined via Rietveld refinement in the previous chapter. The pattern after 247 days of hydration is shown compared to the expected patterns of $[(UO_2)O_2(H_2O)_2] \cdot 2\,H_2O$ (black) and $[(UO_2)(O_2)(H_2O)_2]$ (gray). Dashed lines show the position of peaks corresponding to the LaB_6 standard added to the sample. (b) The uranyl stretching region of the Raman spectrum of the same sample over time. Dashed lines at 868, 846, and 820 cm^{-1} highlight the location of the dominant uranyl stretching modes of $[(UO_2F_2)(H_2O)]_7 \cdot (H_2O)_4$, γ, and $[(UO_2)O_2(H_2O)_2] \cdot 2\,H_2O$, respectively.

($[(UO_2)O_2(H_2O)_2] \cdot 2\,H_2O$) and metastudtite ($(UO_2)O_2(H_2O)_2$). In particular, new peaks are visible near 2θ = 15, 21, and 26°, as in studtite. Broader peaks near 2θ = 17, 20, and 23° are suggestive of the presence of a more amorphous metastudtite-like component. The dominant uranyl stretching peaks in the Raman spectrum at 820 cm^{-1} is more characteristic of studtite than metastudtite, but the peak is fairly broad, suggesting that a second peak near 830 cm^{-1} corresponding to a metastudtite-like component may simply not be resolvable. This is supported by previous observations of a shoulder on this peak in the particle hydration study.

The water content of $[(UO_2F_2)(H_2O)]_7 \cdot (H_2O)_4$ and its hydration products may explain why δ appears to be much more amorphous than γ. As discussed in Chapter 3, the H_2O/U ratio for studtite is 4, compared to 1.54 in $[(UO_2F_2)(H_2O)]_7 \cdot (H_2O)_4$. Two of the four water molecules per uranium in studtite are equatorially bound to the uranium atoms, while the remaining two are hydrogen-bonded between the chains of peroxo-linked uranyl polyhedra. These crystallographic water molecules are not present in metastudtite, which has a H_2O/U ratio of 2. The water content of the γ species remains unknown, but based on the characterization of this species as structurally similar to schoepite, it is hypothesized that the water content is closer to that of schoepite (H_2O/U = 1.5) than of studtite. The formation of a uranyl peroxide species structurally similar to studtite from a uranyl hydroxide species similar to schoepite thus requires the incorporation of a large number of additional water molecules.

If a limited number of water molecules are present in the formation of δ from γ, as is the case of a reaction occurring at a solid–gas interface, it is plausible that peroxo-linked uranyl polyhedra chains form, but additional water molecules are not available to crystallize these chains with long-range order through a hydrogen bonding network. This would result in a mixture of poorly crystalline synthetic studtite and metastudtite with a variable amount of crystallographic water throughout, consistent with the observed XRD pattern. Additional hydration would not necessarily result in the formation of more crystalline studtite because once hydrogen bonds form directly between the chains of uranyl polyhedra, as found in metastudtite, they are unlikely to be broken to allow for the incorporation of additional water

molecules. Previous studies have found that the dehydration of studtite to metastudtite is irreversible for this reason [64, 126].

This XRD hydration experiment confirms the identification of δ as a uranyl peroxide species. Formation of a uranyl peroxide species from a uranyl hydroxide species (γ) was not expected in this system given the absence of added H_2O_2. The novelty of this reaction prompted an investigation to further elucidate the formation mechanism.

5.3 Known uranyl peroxide formation reactions

The formation of a uranyl peroxide species from the hydration of uranyl fluoride through a uranyl hydroxide intermediate has not been demonstrated previously. In fact, there are no prior examples of formation of uranyl peroxide species in the solid state at all. The lack of observed solid-state reactions is not particularly surprising since the high water content of studtite makes crystallization challenging in a nonaqueous environment. As demonstrated in this work, a very high water vapor pressure is required to induce the formation of δ from γ.

While this reaction is the first evidence of a solid-state formation mechanism, multiple aqueous formation mechanisms for uranyl peroxide species are described in the literature. The simplest involves the addition of H_2O_2 to uranium oxides. Uranyl peroxides have been observed to form on the surface of UO_2 disks or precipitate out of uranyl solutions when exposed to a H_2O_2 solution of at least $5 \cdot 10^{-4}$ M [166, 4, 94, 36, 67, 42, 31]. Since H_2O_2 was not added in this study, this formation mechanism is less relevant and will not be discussed further. The remaining mechanisms generally involve the in situ production of H_2O_2 in the system, whether by radiolysis or a photochemical reaction. These mechanisms and their potential relevance to the reaction observed in this work will be discussed in turn.

5.3.1 Radiolytic

Uranyl peroxides have been observed to form in systems where H_2O_2 is produced in situ via water radiolysis, such as on the surface of fresh UO_2 fuel pellets irradiated in water [141, 42, 63, 31], on the surface of spent fuel pellets exposed to de-ionized water [67], and in

irradiated samples of hydrated uranyl hydroxide [74]. H_2O_2 is produced via water radiolysis by the combination of two hydroxyl radicals ($^{\cdot}OH + {}^{\cdot}OH \longrightarrow H_2O_2$), as summarized in Figure 5.7.

In these examples, the activity of the sample or external source is significant—several orders of magnitude above the activity of the depleted uranium material used in this study. However, the radiolytic production of H_2O_2 was also suggested to be responsible for the formation of the uranyl peroxide mineral studtite in nature. While ^{238}U and ^{235}U have very long half-lives (4.5 billion and 700 million yrs, respectively), uraninite minerals can be relatively radioactive due to a build-up of radioactive daughter products. Assuming an α activity of 35,000 dpm/cm^2 at the surface of uraninite, Kubatko and Burns calculated that the H_2O_2 concentration could reach $3.5 \cdot 10^{-3}$ M in the layer of water between uraninite crystals in just 4 years [94].

The possibility of forming uranyl peroxide radiolytically at much lower activity levels seems to make a radiolytic mechanism more likely in this system. However, there are significant differences between this work and the assumptions made by Kubatko and Burns. For one, the material in this study was made with depleted uranium (0.03% ^{235}U), which has an α activity that is a fraction of that of uraninite at secular equilibrium with its radioactive daughter products. Given that the initial uranyl fluoride material was purified from any radioactive daughters during the UF_6 hydrolysis reaction, the α activity of this material is estimated to be approximately 8.6 Bq/mg, compared to 91 Bq/mg for UO_2 in secular equilibrium with all of its daughter products. In this work, δ was also observed to form in days at elevated humidity rather than years [88]. A proposed radiolytic mechanism would need to account for why the observed peroxide formation mechanism is several orders of magnitude faster than expected based on previous studies.

One possible explanation for a radiolytic mechanism is that the radiolytic yield of hydrogen peroxide is higher than expected. In their calculations of uranyl peroxide formation from uraninite, Kubatko and Burns assume a radiolytic yield of 0.985 H_2O_2 molecules/100 eV [35]. Thus, every 4.27 MeV α particle released from ^{238}U produces approximately 42,700 molecules of H_2O_2. It is possible that this value needs to be reassessed. In addition, Kubatko and Burns only consider the α activity of the mineral in their calculations [94]. The initial

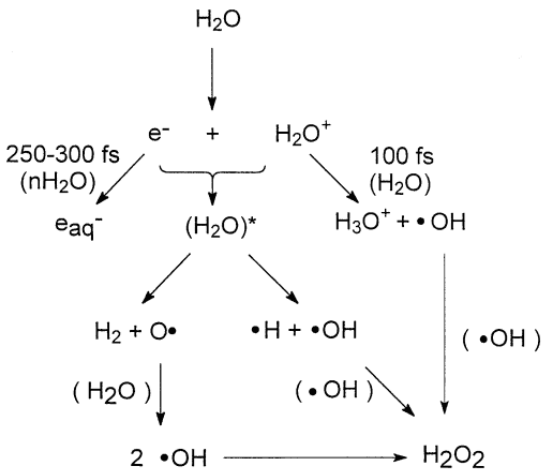

Figure 5.7: Schematic for the decomposition of water leading to the formation of H_2O_2. Reproduced from Hiroki et al. [68]

material used in this study has some β and γ activity after aging for a few months due to the growth of the short-lived daughter products ^{234}Th and ^{234m}Pa, and β and γ radiolysis have been known to cause hydrogen peroxide formation as well [148, 97, 77, 50]. However, adjusting the radiolytic yield to account for β and γ radiolysis still cannot explain the acceleration of the rate by several orders of magnitude, as observed in this work.

Most relevant radiolysis studies have focused on the interaction of bulk materials with liquid water. As described in Chapter 4, the uranyl hydroxide reactant γ has a layered structure with interlayer water molecules. If a radiolytic mechanism does describe peroxide formation in this system, the generation of H_2O_2 likely occurs between these layers. It is possible that the radiolytic yield from these confined water molecules differs significantly from radiolytic yields in bulk water. Previous studies have observed increased yields of radiolytic products, including H_2O_2, with the γ irradiation of hydrated oxides or porous species with confined water [120, 118, 119, 129, 56, 138, 98]. This result was explained as evidence of an efficient energy transfer from the crystal to the confined or surface water. Ionizing radiation produces excitons that migrate to the surface of the oxide and react with surface hydroxy groups to produce surface radical oxygens. Water molecules then interact with these surface radicals, producing hydroxyl radicals which can combine to form H_2O_2 [98].

The existence of a similar catalytic effect must be considered as a potential mechanism for the formation of H_2O_2 in the system studied in this work, especially since the uranyl hydroxide reactant, γ, has hydroxy groups that could form hydroxyl radicals. However, it is important to note that this effect has only been observed in the case of γ radiolysis, not α radiolysis, and the estimated γ energy rate of the source material ($4{\cdot}10^{-8}$ Gy/s) is many orders of magnitude below the γ dose rates in these studies (0.03–1.8 Gy/s) [120, 118, 119, 129, 56, 138, 98]. Le Caer et al. found that H_2O_2 formation actually decreased when the system was irradiated with 10 MeV electrons instead of a γ source, because the higher-energy radiation caused defects in the crystal structure rather than excitons [98]. It is likely that α particles would cause similar defects and not result in a catalytic effect.

In summary, while water radiolysis has been shown to produce uranyl peroxide species, there is no clear explanation for the significantly reduced timescale of uranyl peroxide

formation observed in this work. The possibility of a radiolytic mechanism is revisited in Section 5.5.2 following additional experiments to elucidate the origin of the peroxo oxygens.

5.3.2 Photochemical

Uranyl peroxide species can also be generated in systems where H_2O_2 is produced in situ via a photochemical rather than radiolytic reaction. A few different photochemical mechanisms have been proposed to explain the production of multiple uranyl peroxide species found to form without adding H_2O_2 as a reagent [137, 156, 155, 81, 105, 1, 48, 32, 151, 153].

Uranyl-promoted autoxidation

The primary photochemical mechanism for uranyl peroxide formation involves autoxidation of the photoexcited uranyl ion, which generates H_2O_2 as a byproduct. When UO_2^{2+} is exposed to light, $^*UO_2^{2+}$ is generated. $^*UO_2^{2+}$ can be reduced by H abstraction or electron transfer to produce UO_2^{+}, which can then be reoxidized by atmospheric oxygen (Reaction 5.1) to regenerate UO_2^{2+} and produce H_2O_2 in the process. Thangavelu and Cahill recently demonstrated that this mechanism was responsible for the production of three uranyl peroxo complexes [153]. These species were observed to form in uranyl solutions exposed to ambient light or sun, but not when syntheses were performed in the absence of light. Peroxo species also failed to form when the synthesis was carried out under nitrogen, indicating that atmospheric O_2 was required to form in situ hydrogen peroxide, consistent with Equation 5.1.

$$2\,UO_2^{+} + O_2 + 2\,H^{+} \longrightarrow 2\,UO_2^{2+} + H_2O_2 \tag{5.1}$$

Oxidative coupling of hydroxy bridges

A recent study by McGrail et al. [110] presents an alternative mechanism for the formation of a uranyl peroxide species, in which the peroxo bridge is formed via the oxidative coupling of water or hydroxy bridges (Figure 5.8). The authors still observed the formation of this uranyl peroxide species after light exposure in the absence of atmospheric oxygen, suggesting

Scheme 1. Proposed Overall Reaction for Uranyl Peroxide Formation in Pyridine[a]

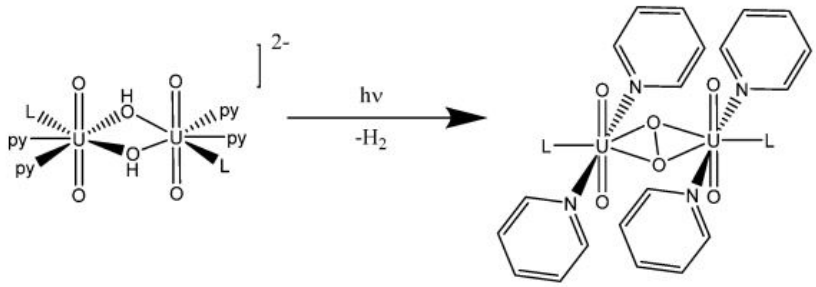

[a] L = $^{-}$OAc, NO_3^{-}.

Figure 5.8: Oxidative coupling reaction scheme proposed by McGrail et al. [110].

that autoxidation via Equation 5.1 was not occurring. Isotopic labeling confirmed that the peroxo ligand resulted from the oxidative coupling of two water or hydroxy ligands, with the observed evolution of H_2 gas supporting this proposed mechanism. This mechanism has since been proposed to explain the formation of uranyl peroxide species from two other hydroxy-bridged compounds [76, 158]. However, Jayasinghe et al. [80] recently suggested that peroxide formation in this system could instead be the result of the photoexcitation of the diethyl ether solvent, which is a known peroxide former. Such a mechanism would not be dependent on the presence of gaseous O_2 and would result in the release of H_2, as noted in this study. Thus, the mechanistic details of this proposed oxidative coupling reaction are in question.

5.4 Confirmation of a nonphotochemical mechanism

To determine whether or not a photochemical reaction is responsible for the formation of uranyl peroxide in this system, the uranyl fluoride particle hydration experiment was replicated in the absence of light. Particles of uranyl fluoride hydrate ($[(UO_2F_2)(H_2O)]_7 \cdot 4\,H_2O$) were again deposited onto an adhesive carbon tab and exposed to a 75% RH environment at 35°C (P_{H_2O}=4.22 kPa). The sample container was wrapped in aluminum foil to prevent light exposure to the particles during the experiment. Figure 5.9 shows the evolution of the Raman spectrum over time. Peaks at 845 cm^{-1} and 820 cm^{-1} once again appear in the uranyl stretching region upon hydration, and the peaks at 820 and 865 cm^{-1} increase in intensity relative to the peak at 845 cm^{-1} between 57 and 81 days. It is thus clear that both γ and δ form when particles of $[(UO_2F_2)(H_2O)]_7 \cdot 4\,H_2O$ are hydrated in the dark, ruling out a photochemical reaction mechanism for the formation of either species [88].

For thoroughness, a similar experiment was carried out starting with particles of the isolated uranyl hydroxide intermediate γ. Particles of γ were hydrated in a 84% RH environment at 25°C (P_{H_2O}=2.57 kPa) for 45 days. The sample container was again wrapped in aluminum foil to prevent light exposure during hydration. The evolution of the uranyl stretching region of the Raman spectrum of a representative particle is shown in Figure 5.10. The decrease in the intensity of the 847 cm^{-1} peak, attributed to γ, and

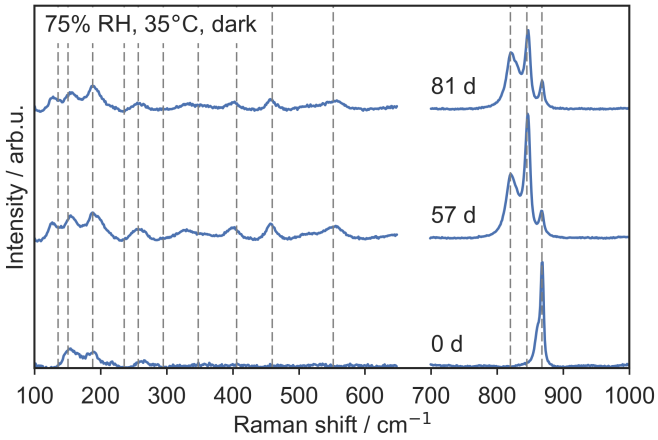

Figure 5.9: Representative micro-Raman spectra of a uranyl fluoride particle ($[(UO_2F_2)(H_2O)]_7 \cdot 4\,H_2O$ at t = 0) after increasing amounts of time spent equilibrating in a 75% RH environment at 35°C in the dark. After 57 and 81 days of hydration, it is clear that both of the hydration products observed previously (uranyl hydroxide and uranyl peroxide) are present.

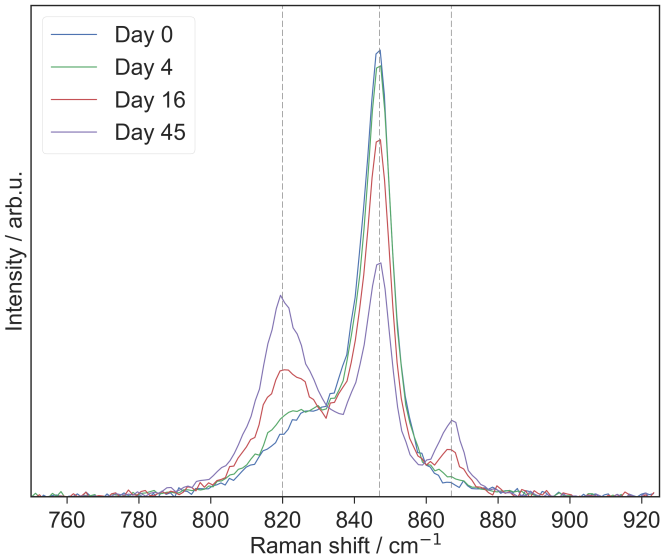

Figure 5.10: Uranyl stretching region of the Raman spectrum of a representative particle of γ hydrated in a 85% RH environment at 25 °C). The sample was wrapped in tinfoil during equilibration to minimize light exposure. The lower energy region of each spectrum is scaled by a factor of 3. Dashed lines at 820, 847, and 867 cm^{-1} highlight peak locations. The decrease in the intensity of the 847 cm^{-1} peak and increase in the intensities of the 820 and 867 cm^{-1} peaks indicate the transformation of γ into the uranyl peroxide species δ.

increase in the intensities of the 820 and 867 cm^{-1} peaks, attributed to δ, clearly indicates that the conversion of γ to δ proceeds in the absence of light.

Demonstration of the formation of δ from uranyl fluoride in the dark was the first evidence of a nonphotochemical mechanism for the formation of uranyl peroxide in the absence of significant radiation [88]. While never proposed previously, the existence of a nonphotochemical, nonradiolytic mechanism could explain previous unexpected observations of uranyl peroxide species in the literature. For example, studtite was recently identified in addition to metaschoepite as a corrosion product found on depleted uranium ammunitions retrieved from soil in Bosnia and Herzegovina [168]. The authors attributed the formation of studtite to the same radiolytic reaction mechanism responsible for the formation of studtite from natural uraninite. However, as noted previously, the α activity of depleted uranium is significantly reduced compared to uraninite in secular equilibrium with its radioactive daughter products.

Since the publication of nonphotochemical formation of δ [88], another study has presented evidence of the formation of a uranyl peroxide species in solution by nonphotochemical means. Jayasinghe et al. [80] demonstrated transformation of a uranyl carbohydrate coordination polymer into two different uranyl peroxide coordination complexes in the presence and absence of light. The proposed mechanism for the reaction that occurred in the presence of light involved the photoexcitation of the uranyl ion and in situ formation of H_2O_2 via autoxidation of the tetrahydrofuran (THF) solvent (Figure 5.11) [80]. Formation of a uranyl peroxide compound in the absence of light led the authors to conclude that photoexcitation of the uranyl ion is not a requirement for peroxide formation, which was again explained by autoxidation of the THF solvent.

5.5 Elucidation of the peroxide formation reaction

It is evident that water molecules play a mechanistic role in the formation of the uranyl peroxide species because the rate of formation increases with water vapor pressure. In addition, any potential role of the carbon substrate in the particle hydration experiments is ruled out since the same reaction was observed on silicon substrates employed for XRD

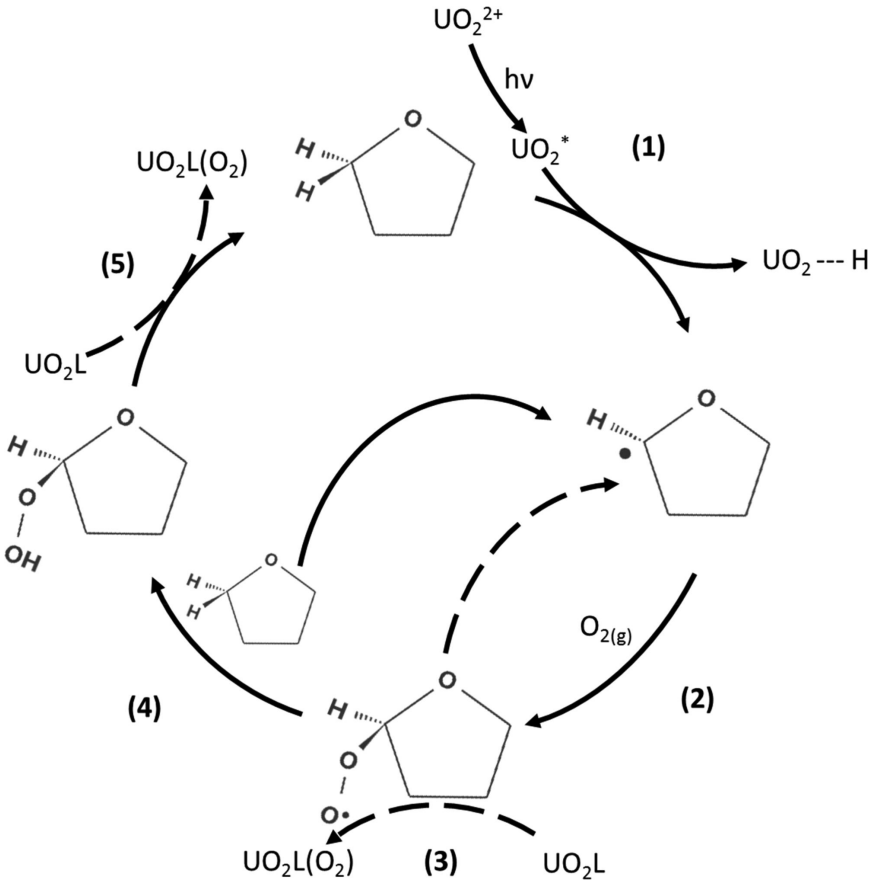

Figure 5.11: Proposed catalytic cycle for the formation of H_2O_2 from the autoxidation of THF. Reproduced from Jayasinghe et al. [80].

studies. However, the mechanistic details remain unclear from the hydration experiments presented thus far. Additional experiments were undertaken to elucidate these details.

5.5.1 Formation of uranyl peroxide from uranyl hydroxide starting material

The confirmation of γ as a uranyl hydroxide hydrate raised the question of whether other known uranyl hydroxide species can be likewise converted into uranyl peroxide at high humidity. To test this, multiple particles of synthetic metaschoepite ($[(UO_2)_4O(OH)_6] \cdot 5\,H_2O$) were monitored via micro-Raman spectroscopy while equilibrating at 25°C and 75% RH/85% RH/ 95% RH for 58 days. The synthetic metaschoepite material came from the synthesis decribed in Section 4.3. The initial Raman spectra of the particles on each sample were consistent with prior findings, with the uranyl stretching region showing strong peaks at 869 and 845 cm^{-1} [90]. Figure 5.12 shows the evolution of the Raman spectrum of a representative particle of synthetic metaschoepite at each humidity.

Upon hydration at 75% RH, the 869 cm^{-1} peak is observed to redshift to 855 cm^{-1}, where it is stable for the remainder of the experiment. This shift was observed at each humidity level, and as discussed in Section 4.3, is tentatively attributed to a change in the interlayer water structure that strengthens hydrogen bonding interactions to some of the uranyl ions. No comparable shift was observed for the 845 cm^{-1} peak, again consistent with the findings in Section 4.3. At 75% RH, however, a broad lower shoulder grows in on the 845 cm^{-1} peak. It is unclear if this shoulder corresponds to the formation of uranyl peroxide or structural changes within the uranyl hydroxide structure. At 85% RH, a clear peak grows in at 819 cm^{-1}, at the same frequency of the uranyl stretching mode in studtite. A peak near 866 cm^{-1} likely corresponds to the peroxide stretch of a uranyl peroxide hydration product, but it is difficult to confirm given potential overlap with the initial uranyl hydroxide peak at 869 cm^{-1}. At 95% RH, the transformation to uranyl peroxide is much clearer; after 58 days, the Raman spectrum is dominated by strong peaks at 819 and 864 cm^{-1}. The formation of uranyl peroxide from uranyl hydroxide confirms that fluorine or hydrogen fluoride gas released from

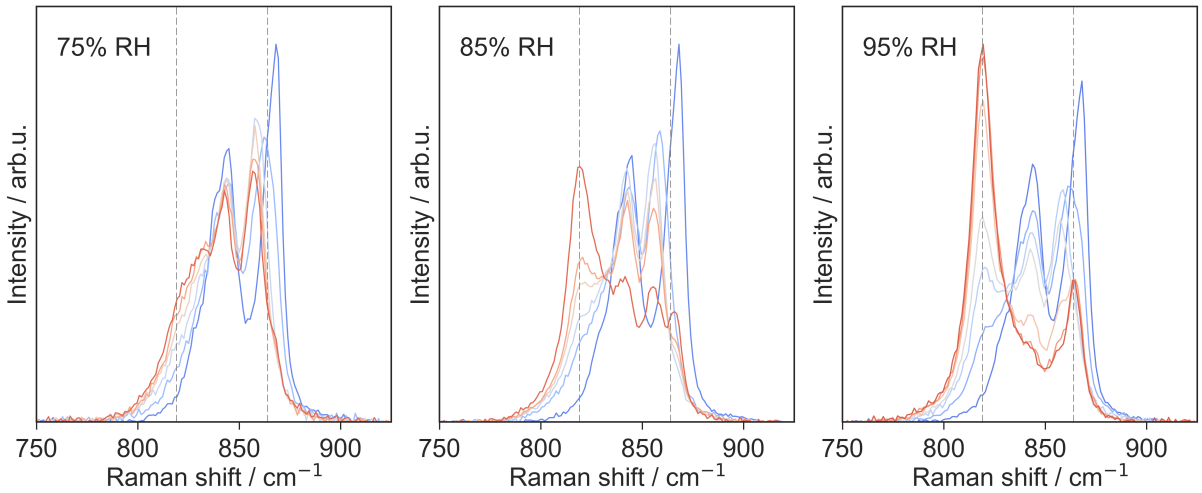

Figure 5.12: Evolution of the Raman spectrum of a representative particle of synthetic metaschoepite at 25°C and (a) 75% RH, (b) 85% RH, and (c) 95% RH. Multiple scans were performed on the same particle over 58 days of equilibration (day 1 in dark blue, day 58 in dark red). Individual spectra are normalized by the peak area in the region shown to allow for easier comparison. Dashed lines at 819 cm^{-1} and 864 cm^{-1} show the expected location of peaks corresponding to the uranyl and peroxo stretching modes of uranyl peroxide.

uranyl fluoride was not somehow responsible for the formation of uranyl peroxide from uranyl fluoride.

5.5.2 Origin of the peroxo groups

The origin of the peroxide oxygens in the uranyl peroxide species produced via the hydration of synthetic metaschoepite was assessed through an isotopic labeling study. Given the similarities between synthetic metaschoepite and γ, it is assumed that uranyl peroxide forms via hydration of each species by the same mechanism. Labeled synthetic metaschoepite was produced in the same manner described in Section 4.3 but using 97% $H_2{}^{18}O$. Raman spectra collected on the labeled material indicate the exchange of a majority of both the uranyl and equatorial oxygens (i.e., formation of $[(U^{18}O_2)_4{}^{18}O(^{18}OH)_6] \cdot 5\,H_2O$ (Figure 5.13). Because peaks corresponding to the bending and stretching modes of the interlayer water molecules do not appear in the Raman spectrum, it is not possible to determine whether these oxygen atoms have been exchanged as well.

Particles of this labeled uranyl hydroxide material were deposited onto an adhesive carbon tab and exposed to the headspace of a KCl saturated-salt solution (84% RH) in the same configuration described in Chapter 3. The sample was stored in an incubator maintained at 25°C. Raman spectra of several different particles on the sample were collected initially and after 2, 4, and 11 days of hydration. Changes observed in the uranyl stretching region of the Raman spectra for a representative particle over this time are shown in Figure 5.14. Initially, the dominant Raman peaks are at 819 and 796 cm^{-1}, corresponding to doubly labeled uranyl ions ($^{18}OU^{18}O$) in the synthetic metaschoepite starting material (Table 5.1 for a list of relevant expected frequencies). Initial intensity between 825 and 875 cm^{-1} is indicative of incomplete exchange of the uranyl oxygens during synthesis.

After hydrating for two days, the 819 cm^{-1} peak shifts to 806 cm^{-1}, consistent with the redshift observed in this mode (869 to 855 cm^{-1}) when hydrating samples of isotopically natural synthetic metaschoepite (Section 5.5.1). The changes in the Raman spectrum over this time period were further analyzed by subtracting the spectrum after two days of hydration from the initial spectrum (Figure 5.15). In addition to the shift in the 819 cm^{-1} peak, there is a decrease in the intensity of the 796 cm^{-1} peak, which is attributed to

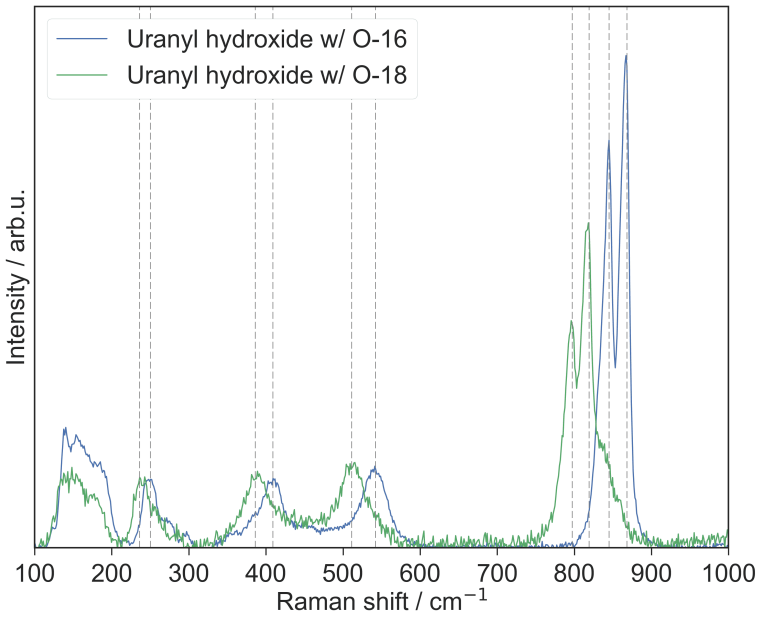

Figure 5.13: Representative Raman spectrum of synthetic metaschoepite made with H_2O and $H_2{}^{18}O$. The spectrum of the labeled sample was weaker in intensity and has been scaled by a factor of 2.5 to allow for better comparison of the peak frequencies. Isotopic shifts in both the uranyl stretching region (750–900 cm^{-1}) and equatorial stretching region (200–600 cm^{-1}) confirms replacement of these ^{16}O atoms with ^{18}O. Uranyl stretching modes observed at 868 and 845 cm^{-1} shift to 819 and 797 cm^{-1}, respectively, while modes at 542 and 409 cm^{-1} shift to 511 and 386 cm^{-1}, respectively. Modes below 200 cm^{-1} correspond primarily to uranium motion, and thus do not experience the same isotopic shift upon exchange of the oxygen atoms. Weaker peaks that correspond to unlabeled or partially labeled uranyl ions are observed in the labeled sample, a not-unexpected finding since the water used in synthesis was only 97% $H_2{}^{18}O$.

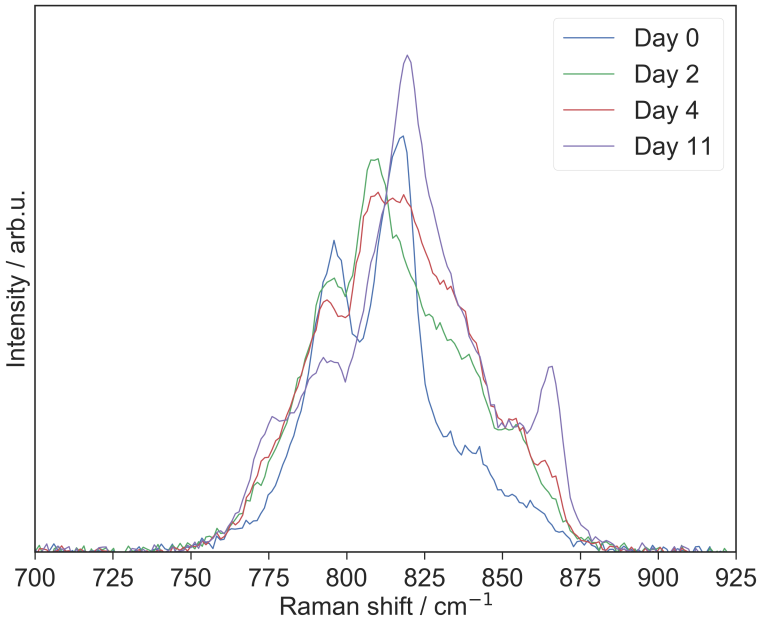

Figure 5.14: Evolution of the uranyl stretching region of the Raman spectrum of a characteristic particle of labeled synthetic metaschoepite upon hydration at 85% RH, 25°C. All Raman spectra have been normalized to the intensity of the Rayleigh peak (not shown).

Table 5.1: Expected frequencies of the uranyl ν(OUO) and peroxo ν(OO) stretching modes with the labeling of one or both oxygen atoms. Frequencies for $\nu(^{16}OU^{16}O)/\nu(^{16}O^{16}O)$ stretches come from observations described in this work. Frequencies for isotopically labeled stretches are estimated based on the square root of the isotopic masses.

Species	Stretch	$^{16}O^{16}O$	$^{16}O^{18}O$	$^{18}O^{18}O$
uranyl hydroxide	ν(OUO)	869/855[a]	845/831	819/806
	ν(OUO)	845	821	797
uranyl peroxide	ν(OUO)	820	797	773
	ν(OO)	865	841	816

[a] As shown in Figure 5.12, this peak undergoes a significant redshift upon hydration.

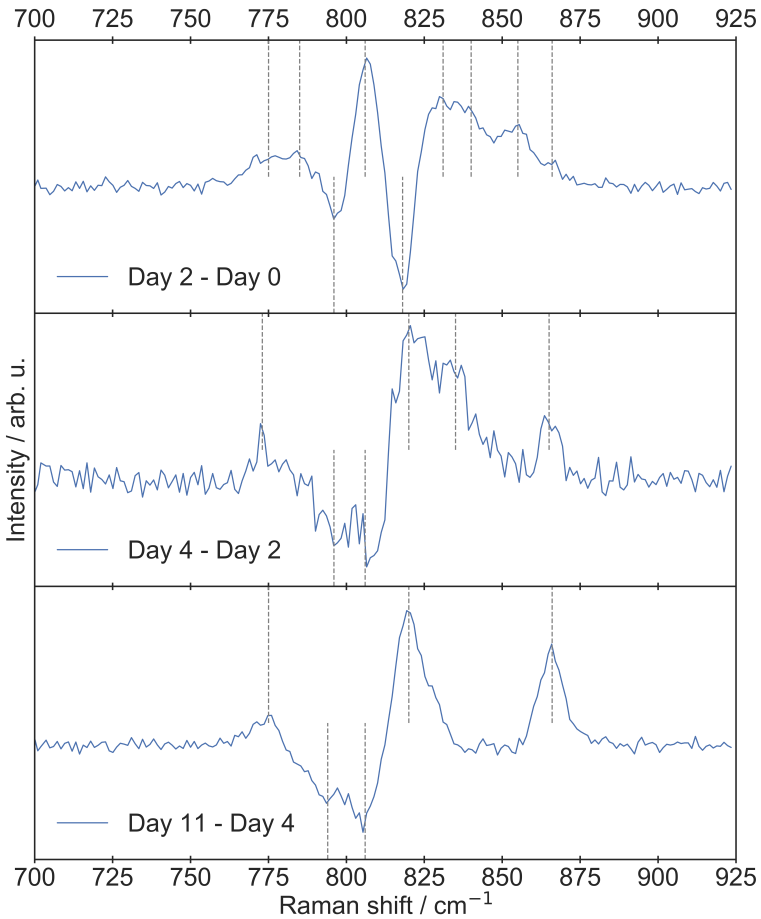

Figure 5.15: (Top) Subtraction of the normalized Raman spectra for Days 0 and 2 shown in Figure 5.14. Dashed lines at 775, 806, 831, 840, 855, and 866 cm^{-1} identify peaks that increase in intensity over this time period; dashed lines at 796 and 818 cm^{-1} identify peaks that decrease in intensity. (Middle) Subtraction of the normalized Raman spectra for days 2 and 4 shown in Figure 5.14. Dashed lines at 773, 820, 835, 865 cm^{-1} identify peaks that increase in intensity over this time period; dashed lines at 794 and 806 cm^{-1} identify peaks that decrease in intensity. (Bottom) Subtraction of the normalized Raman spectra for days 4 and 11 shown in Figure 5.14. Dashed lines at 775, 820, and 866 cm^{-1} identify peaks that increase in intensity over this time period; dashed lines at 794 and 806 cm^{-1} identify peaks that decrease in intensity.

$^{18}OU^{18}O$ ions in the uranyl hydroxide starting material. On the other hand, a peak grows in at 855 cm^{-1} as well as between 830 and 845 cm^{-1}. These peaks are consistent with the stretching modes of $^{16}OU^{16}O$ ions in the hydrated isotopically natural uranyl hydroxide species. Thus, it is clear that in the first two days of hydration, a subset of the uranyl ions in the uranyl hydroxide species undergo oxygen exchange with the unlabeled water vapor. This a significant finding given the expected stability of the uranyl ion in the solid state, and is discussed further in Section 5.5.3.

There is also some evidence of formation of the uranyl peroxide species in the first two days of hydration. A broad peak between 775 and 785 cm^{-1} is attributed to labeled uranyl ions ($\nu(^{18}OU^{18}O)$) in the uranyl peroxide species, while a small peak that begins to form at 865 cm^{-1} is attributed to the *unlabeled* peroxo stretch ($\nu(^{16}O^{16}O)$) in the same species [40]. It is difficult to resolve other peaks that may correspond to the uranyl peroxide species due to significant overlap with the uranyl hydroxide species.

Beyond two days of hydration, the uranyl hydroxide peak at 806 cm^{-1} does not redshift further. Between two and four days of hydration, this peak decreases in intensity along with the peak at 796 cm^{-1} identified as the other uranyl stretching mode in the same species. The decrease in these peaks indicates a transformation of the uranyl hydroxide species as expected upon hydration. These peaks are replaced by peaks at 775, 820, 835, and 865 cm^{-1}. The 775 cm^{-1} peak is again identified as corresponding to $^{18}OU^{18}O$ ions in the uranyl peroxide species, while the 865 cm^{-1} peak is identified as corresponding to unlabeled peroxo groups. The 820 cm^{-1} peak is tentatively assigned to $^{16}OU^{16}O$ ions in this species. While a $\nu(^{16}OU^{18}O)$ mode of the uranyl hydroxide species could appear at a similar frequency, previous studies have found that the exchange of both uranyl ions in a concerted mechanism is more likely than the exchange of just one [57]. The fact that there is no additional growth of uranyl hydroxide $\nu(^{16}OU^{16}O)$ peaks at 845 and 855 cm^{-1} also suggests that the 820 cm^{-1} peak is unrelated to the incorporation of ^{16}O into the uranyl oxo ligands of the uranyl hydroxide species.

Changes in the Raman spectrum between days 4 and 11 help clarify the assignment of the 820 cm^{-1} peak, which grows significantly over this time period, along with the peak at 866 cm^{-1}. The correlated growth of these two peaks is consistent with their respective

assignments as the unlabeled uranyl and peroxo stretching modes of the uranyl peroxide hydration product.

The significant presence of $^{16}OU^{16}O$ ions in the uranyl peroxide product was unexpected and indicative of additional uranyl oxygen exchange, explored further in Section 5.5.3. The 775 and 866 cm^{-1} peaks still correspond to labeled uranyl ions and unlabeled peroxo groups, respectively, while the decrease in the peaks at 794 and 806 cm^{-1} indicates the continued loss of uranyl hydroxide as it is converted into uranyl peroxide.

The goal of this experiment was to determine the origin of the peroxo oxygens in the uranyl peroxide product. It is clear from Figure 5.15 that unlabeled peroxo groups are present in the product, suggesting that the peroxo oxygens come from water vapor or atmospheric oxygen rather than the hydroxide ligands in the uranyl hydroxide starting material, the majority of which were labeled.

An alternative possibility to consider is that the hydroxide ligands in the uranyl hydroxide material, which were initially labeled, undergo exchange with water and/or atmospheric oxygen prior to the formation of the peroxo groups. This can be analyzed by examining the lower-energy region of the Raman spectra collected over hydration. As shown in Figure 5.13, the labeling of the uranyl hydroxide material shifts the major equatorial oxide/hydroxy modes from 542 and 409 cm^{-1} to 511 and 386 cm^{-1}, respectively. If oxygen exchange was occurring in these equatorial groups, peaks would be expected to grow in at 542 and 386 cm^{-1} as observed in isotopically natural metaschoepite (see Section 4.3 or [90]). However, as shown in Figure 5.16, this was not the case.

It should also be considered that labeled peroxo groups could form from the labeled hydroxy groups and then undergo oxygen exchange with the water vapor or atmospheric oxygen, resulting in the unlabeled peroxo groups identified in the spectra in Figure 5.15. There is no evidence that such exchange occurs on the same timescale as the uranyl hydroxide to uranyl peroxide transition, which would result in the increase and subsequent decrease of peaks attributed to labeled peroxo groups near 816 cm^{-1} ($\nu(^{18}O^{18}O)$) and 841 cm^{-1} ($\nu(^{16}O^{18}O)$). Instead, as shown in Figure 5.15c, the growth of the unlabeled peroxo stretching mode at 866 cm^{-1} is correlated with the disappearance solely of the uranyl hydroxide species and not with labeled peroxide groups. It is possible that exchange of the peroxide oxygens

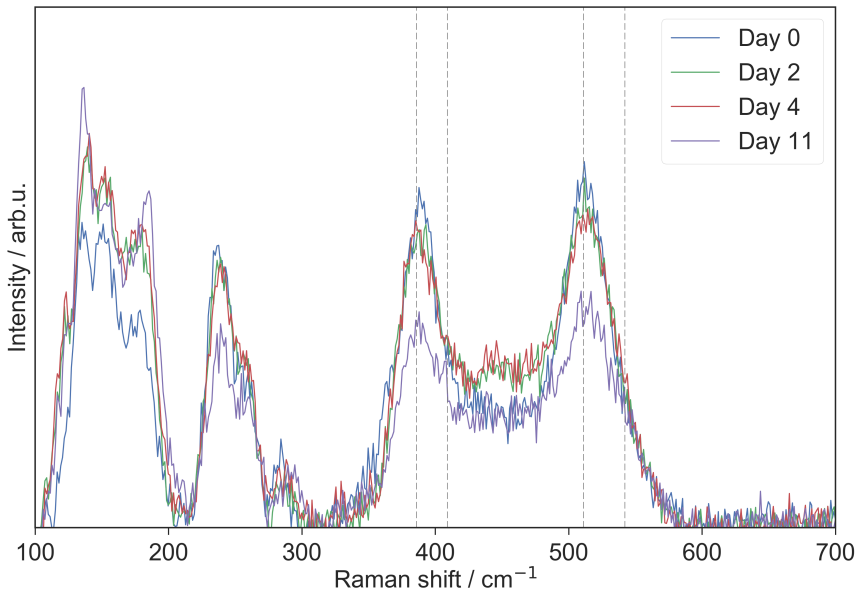

Figure 5.16: Evolution of the low-energy region of the Raman spectrum of a characteristic particle of labeled synthetic metaschoepite upon hydration at 85% RH, 25°C. All Raman spectra have been normalized to the intensity of the Rayleigh peak (not shown).

does occur, just at a much faster rate than the rate of peroxide formation. This cannot be ruled out from the collected data, but is deemed unlikely in the solid-state. Additional experiments to probe oxygen exchange in peroxo groups should to carried out to clarify this possibility.

Identifying the peroxo oxygens as most likely originating from water or atmospheric oxygen provides further insight regarding the applicability of potential radiolytic mechanisms presented in Section 5.3.1. As discussed there, previous studies have found an increase in expected radiolytic yields with the γ irradiation of hydrated species where water molecules are present on the surface or within pores of the material [120, 118, 119, 129, 56, 138, 98]. The increased yield of radiolytic products, including H_2O_2, has been explained as the result of the production of radical oxygens from surface hydroxy groups following interactions with excitons. If a similar mechanism were to explain the formation of uranyl peroxide from the uranyl hydroxide hydrate γ, the peroxo oxygens would be expected to come from the hydroxy groups in γ and thus be predominantly labeled in this experiment. While this finding does not rule out a radiolytic mechanism, it raises additional questions as to how the observed fast reaction rate could be explained via radiolysis.

5.5.3 Uranyl oxygen exchange

The isotopic labeling study discussed in the previous section revealed that uranyl oxygen exchange occurs slowly in synthetic metaschoepite upon exposure to elevated water vapor. This was unexpected given the general stability of the uranyl ion. In fact, it was the very slow exchange of the oxo ligands that initially identified the characteristic strength of relative inertness of the uranyl bond [43]. Uranyl oxygen exchange can occur in solution depending on the speciation of the uranyl ion, and can be accelerated by UV irradiation [57]. There was no evidence of deliquescence during the metaschoepite hydration experiment from the Raman microscope images, however, and uranyl oxygen exchange has never been reported across a solid–gas interface.

The chemical makeup of synthetic metaschoepite may explain why the uranyl oxygens are more susceptible to exchange than expected for a uranyl solid. In solution, uranyl hydroxide compounds have been observed to undergo uranyl oxygen exchange with solvent

water molecules at a much faster rate than observed for other uranyl species [37, 150]. This behavior has been attributed to a weakening of the uranyl bond due to reduced ionic bonding generated in part by the σ-donating ability of the hydroxy ligands [75]. It is possible that a similar charge transfer weakens the uranyl bonds in synthetic metaschoepite, increasing the rate of uranyl oxygen exchange with nearby water molecules. Additional computational calculations could investigate how the electronic structure of this compound may explain the observed reactivity.

The uranyl oxygen exchange observed in synthetic metaschoepite upon hydration still occurs fairly slowly; after 11 days, most uranyl ions in the remaining uranyl hydroxide fraction are still labeled. Much faster uranyl oxygen exchange is demonstrated to occur during the uranyl hydroxide to uranyl peroxide conversion, as evidenced by the growth of a Raman peak at 820 cm^{-1} corresponding to $^{16}OU^{16}O$ ions in the uranyl peroxide product. Since the majority of the uranyl ions in the uranyl hydroxide reactant were labeled with ^{18}O, the uranyl ions in the peroxide product were expected to be labeled as well, with a stretching frequency near 775 cm^{-1}. As shown in Figure 5.15c, a peak does grow in at 775 cm^{-1}, but it is much less intense than the peak at 820 cm^{-1} corresponding to unlabeled uranyl ions.

The presence of unlabeled uranyl ions in the uranyl peroxide product cannot be explained solely by uranyl oxygen exchange that occurs in the uranyl hydroxide species prior to conversion to the peroxide product. Figure 5.14 shows that the growth of the 820 cm^{-1} peak corresponding to $^{16}OU^{16}O$ ions in the uranyl peroxide product is correlated with a decrease in the peaks corresponding to $^{18}OU^{18}O$ ions in the uranyl hydroxide material. This indicates that significant exchange of the uranyl oxygens occurs during the reaction, an unexpected finding again considering the general stability of the uranyl ion. The absence of $^{16}OU^{18}O$ ions in the peroxide product is consistent with previous findings that a concerted exchange of both uranyl oxygens actually occurs at a faster rate than the exchange of just one [57].

The exchange of uranyl oxygen atoms during this reaction was further analyzed by conducting the opposite labeling study, exposing isotopically natural uranyl hydroxide to isotopically labeled water vapor. A droplet of deionized water spiked with 97% $H_2{}^{18}O$ was placed next to particles of synthetic metaschoepite that were adhered to a carbon tab. This

system was sealed and stored at 25°C. The RH of the sample chamber was not monitored, but deliquescence of the particles was not observed. The hydration of the particles was measured via Raman spectroscopy initially and after 6 and 12 days of hydration.

The evolution of the Raman spectrum of a representative particle is shown in Figure 5.17. The initial spectrum is characteristic of synthetic metaschoepite, with dominant uranyl stretching modes at 869 and 845 cm^{-1}. After 6 days of hydration, the 869 cm^{-1} peak redshifts to 855 cm^{-1}, as observed previously. In addition, a broad peak begins to form at 820 cm^{-1} with a broad low-energy shoulder. After 12 days of hydration, the uranyl hydroxide stretching modes decreased in intensity, replaced by dominant peaks at 820 and 866 cm^{-1} corresponding to the unlabeled uranyl and peroxo stretching modes of the uranyl peroxide product. In addition, a clear peak appears at 797 cm^{-1}. As shown in Table 5.1, the peak could be interpreted either as the $\nu(^{18}OU^{18}O)$ stretching mode in uranyl hydroxide or the $\nu(^{16}OU^{18}O)$ stretching mode in uranyl peroxide. However, there are two dominant uranyl stretching modes in uranyl hydroxide, and an increase in a peak corresponding to one of the $\nu(^{18}O^{18}O)$ stretching modes in uranyl hydroxide is expected to be accompanied by an increase in the other $\nu(^{18}OU^{18}O)$ stretching mode. Such a peak, expected near 806 cm^{-1}, is not observed. The absence of this peak could in theory be explained by a preferential exchange within the uranyl ions with lower-energy stretching frequency; however, this is deemed unlikely since both of the uranyl hydroxide uranyl stretching peaks were observed to shift due to oxygen exchange in the labeling experiment described in Section 5.5.2. Thus, it is more likely that the 797 cm^{-1} peak corresponds to the $\nu(^{16}OU^{18}O)$ stretching mode in uranyl peroxide.

Two separate isotopic labeling studies show evidence that significant uranyl oxygen exchange occurs with water during the formation of the uranyl peroxide species. This exchange occurs much more rapidly than the oxygen exchange observed in synthetic metaschoepite prior to the conversion, and cannot be explained solely by a weakening of the uranyl bond due to σ donation of the hydroxy ligands. This suggests that interactions with water molecules further facilitate this exchange.

The heightened reactivity of the uranyl ion in this system is similar to that observed in the photoexcited uranyl ion. Photoexcitation of the uranyl ion has long been known to facilitate

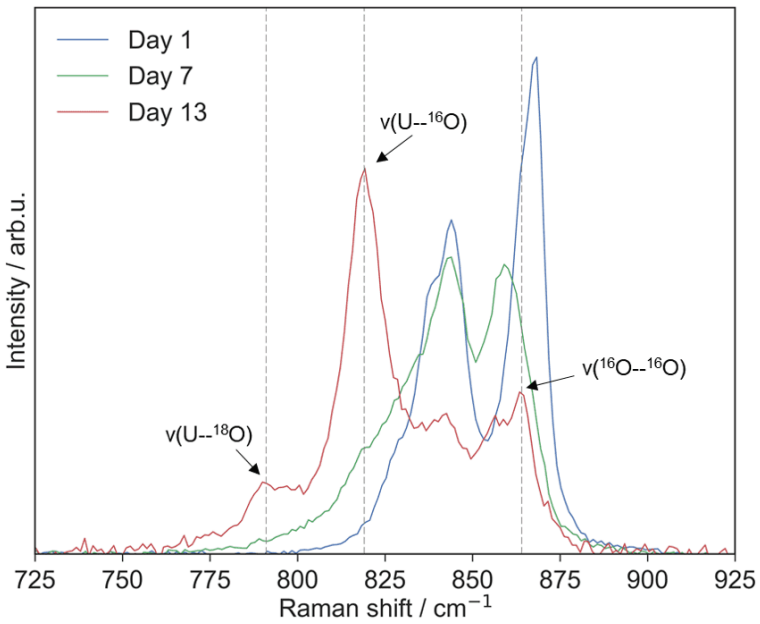

Figure 5.17: Uranyl stretching region of the Raman spectrum of a representative particle of synthetic metaschoepite adjacent to a droplet of deionized water spiked with $H_2{}^{18}O$.

exchange of the uranyl oxygens [57]. Importantly, the geometry of the uranyl ion is altered in the excited state, with one or both of the uranyl bonds elongated depending on the specific excited state. The more distant oxygen atoms acquire some radical character, becoming a strong hydrogen or proton acceptor [136]. A computational study by Réal et al. determined that the first step of the uranyl oxygen exchange mechanism involves intramolecular hydrogen or proton transfer from a coordinated water molecule to the photoexcited uranyl ion through a second-sphere water molecule that acts as a proton/hydrogen shuttle (Figure 5.18). As shown in Figure 5.18, the lengthening of one of the uranyl bonds due to photoexcitation is crucial to this interaction, as is the presence of a hydrogen bonding network that facilitates hydrogen/proton shuttling. Isomerization of the two hydroxy ligands formed as a result of this mechanism (Figure 5.18) was concluded to be responsible for uranyl oxygen exchange [136].

It is unclear exactly how a similar mechanism could explain the observed uranyl oxygen exchange in solid-state synthetic metaschoepite. Exchange appears to be occurring intermolecularly rather than intramolecularly since all of the equatorial hydroxy ligands were also labeled. The proton transfer mechanism shown in Figure 5.18 is plausible in the system given the presence of interlayer water molecules that are known to act as hydrogen bond donors to uranyl oxygens. The orientation of the uranyl ions and interlayer water molecules upon exposure to increased water vapor pressure may be such that excitation of the uranyl ion is not required to promote a proton transfer mechanism that further weakens the uranyl bond and facilitates oxygen exchange.

5.5.4 Interactions between the uranyl ion and water

The unexpected uranyl oxygen exchange and formation of peroxide both appear to be driven by interactions between the uranyl ion and vapor phase water molecules. These interactions were studied computationally through ab initio molecular dynamics (AIMD) simulations of the uranyl hydroxide species schoepite. The strength of these interactions can be examined through the pair distribution functions (PDFs) of all pairs of nearest-neighbor uranyl oxygen atoms and water hydrogen atoms and uranyl oxygen atoms, shown in Figure 5.19 in the schoepite and metaschoepite unit cells, averaged over the 18 ps AIMD simulation. Results

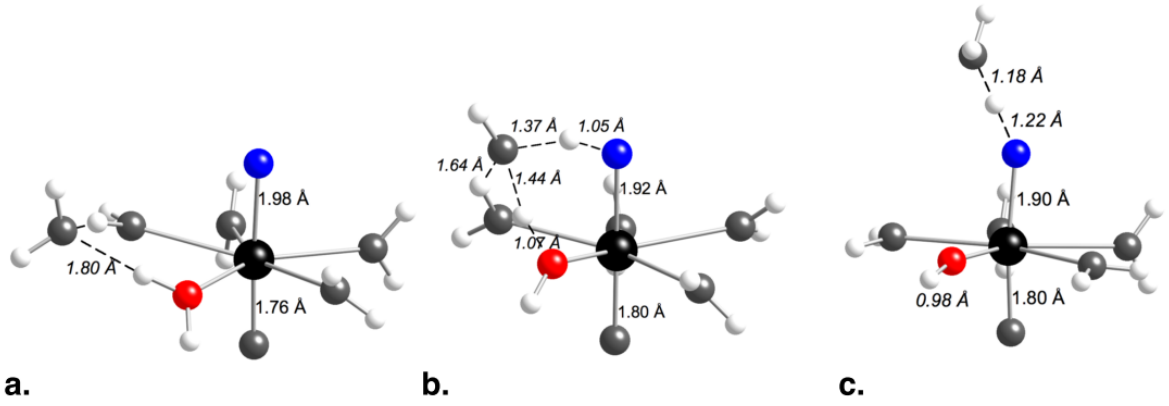

Figure 5.18: Schematic of hydrogen or proton transfer to the excited uranyl ion. Reproduced from Réal et al. [136].

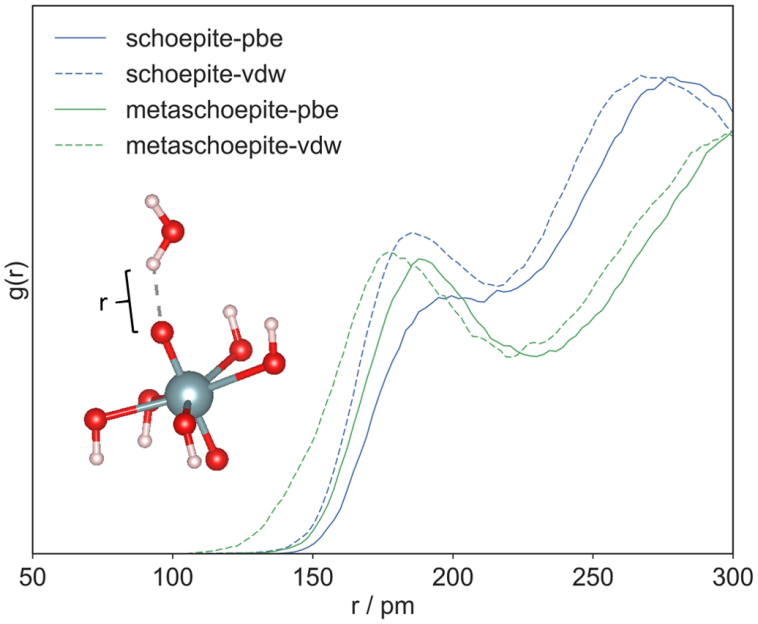

Figure 5.19: Radial distribution functions of uranyl oxygens and nearest neighbor water hydrogens in schoepite and metaschoepite with the PBE and optB86b-vdW functionals.

are presented for both schoepite and metaschoepite with the Perdew-Burke-Ernzerhof (PBE) [128] and op!86b-vdW (vdW) [91, 92]) functionals (see Chapter 1 for additional detail).

As evidenced by the bimodal shape of the curves, the interlayer water structure in schoepite and metaschoepite is such that only a subset of the uranyl oxygens interact significantly with water molecules. In both simulations of schoepite and the PBE simulation of metaschoepite, the hydrogen bonds that do form between uranyl oxygens and water hydrogens can be characterized as medium in strength; the hydrogen bond distances are rarely less than 150 pm over the course of the simulation. However, in the vdW simulation of metaschoepite, significantly stronger hydrogen bonding interactions are observed, with $O_{yl}\cdots H_{water}$ hydrogen bonds as short as 110 pm in some instances. This short distance suggests that some hydrogen atoms are even briefly coordinating with uranyl ions over the course of this simulation, supporting the hypothesis that hydrogen or proton transfer can occur in uranyl hydroxide hydrate systems in the absence of photoexcitation of the uranyl ion.

5.6 Proposed mechanism

The occurrence of uranyl oxygen exchange in the uranyl peroxide formation mechanism suggests that hydrogen abstraction occurs without photoexcitation of the uranyl ion. This helps to explain the unexpected nonphotochemical formation of uranyl peroxide. Despite the lack of photoexcitation of the uranyl ion, the peroxide formation mechanism is likely very similar to previously determined photochemical mechanisms [153]. In the first step, uranyl ions in the uranyl hydroxide product are reduced by water via hydrogen abstraction (Reaction 5.2/5.3). Autoxidation of the reduced uranyl ion can then proceed in the presence of atmospheric oxygen, generating H_2O_2 (Reaction 5.4) that reacts with the regenerated uranyl ions to form the uranyl peroxide product (Reaction 5.5). Formation of additional H_2O_2 molecules via the recombination of hydroxyl radicals formed in Reaction 5.2/5.3 is also possible (Reaction 5.6).

$$UO_2^{2+} + H_2O \longrightarrow UO_2^{+} + {}^{\cdot}OH + H^{+} \tag{5.2}$$

$$UO_2^{2+} + H_2O \longrightarrow UO_2H^{2+} + {}^{\cdot}OH \tag{5.3}$$

$$2\,UO_2^{+} + O_2 + 2\,H^{+} \longrightarrow 2\,UO_2^{2+} + H_2O_2 \tag{5.4}$$

$$UO_2^{2+} + H_2O_2 + xH_2O \longrightarrow [(UO_2)_2(O_2)(H_2O)_x] \tag{5.5}$$

$$2\,{}^{\cdot}OH \longrightarrow H_2O_2 \tag{5.6}$$

The demonstration of water as the reducing agent of the uranyl ion in this system is noteworthy. While photo-oxidation of water by the uranyl ion has been observed previously [30, 116, 84, 172, 173], examples of the photochemical formation of uranyl peroxide have all relied on hydrogen abstraction from organic substrates or solvents such as methanol [117, 106, 139, 167, 108, 103, 153]. A computational study by Tsushima offers an explanation of why water is less likely to act as a uranyl reducing agent. Tsushima found that the distance between uranyl oxygens and the hydrogen atoms in methanol or ethanol contracted significantly when the uranyl ion was excited, while a similar contraction was not observed in interactions with a water molecule [159]. In the proposed hydrogen abstraction mechanism (Reaction 5.2/5.3) this effect is overcome due to the existence of a rigid hydrogen bonding network in uranyl hydroxide hydrates that facilitates strong hydrogen bonding interactions between uranyl oxygens and water hydrogens.

Photoexcitation of the uranyl ion is not a requisite for this redox reaction due to specific attributes of the uranyl hydroxide reactant. The strong σ-donating character of the hydroxy ligands and hydrogen bonding interactions between uranyl oxygens and water hydrogens both weaken the uranyl ion even prior to hydration. Elevation of the water vapor pressure presumably strengthens the interaction between the uranyl ions and water molecules, prompting hydrogen abstraction. In the absence of these particular structural characteristics, photoexcitation of the uranyl ion is necessary to trigger a similar reaction.

The significance of the structure of the uranyl hydroxide reactant explains why uranyl peroxide was unexpectedly found with metaschoepite as a corrosion product found on depleted uranium ammunitions [168]. However, uranyl hydroxide species do not appear to uniquely satisfy the conditions necessary to facilitate hydrogen abstraction in the absence of photoexcitation, as evidenced by the recent demonstration of nonphotochemical uranyl

peroxide formation in a uranyl solution with THF solvent. It is worth further probing interactions between the uranyl ion and THF molecules computationally to understand what similarities may exist in the geometry and electronic structure of this system relative to uranyl hydroxide hydrates.

Elucidation of a nonphotochemical mechanism for the formation of uranyl peroxide from hydrated uranyl hydroxide raises the question of whether the mechanism explaining the formation of the uranyl peroxide mineral studtite needs to be revisited. Due to the absence of light below ground, Kubatko and Burns proposed that studtite formation must be radiolytic, pointing to the fairly high activity of uraninite in secular equilibrium with its radioactive daughters [94]. However, this work suggests that it is plausible that studtite forms from the uranyl hydroxide hydrate minerals schoepite or metaschoepite via a nonphotochemical autoxidation reaction. The existence of a second mechanistic route could help explain the prevalence of uranyl peroxide minerals.

5.7 Summary and future directions

In summary, the formation of a uranyl peroxide species (δ) via further hydration the uranyl hydroxide hydrate γ has been confirmed via XRD. The resulting species is structurally similar to the known uranyl peroxide minerals studtite and metastudtite, but with reduced crystallinity because, unlike formation from a solution phase, there are not enough water molecules readily available in the solid-state system to crystallize the peroxo-linked uranyl chains.

This reaction is demonstrated to be nonphotochemical and is also likely nonradiolytic based on the limited α activity of the system. These findings thus appear to indicate the existence of a novel uranyl peroxide formation mechanism. The fact that the same reaction is observed upon hydration of synthetic metaschoepite suggests that the structure and resulting chemical environment of uranyl hydroxide hydrates is relevant to promoting a reaction that otherwise would be unlikely to proceed without photochemical or radiolytic excitation. It is hypothesized that the significant σ-donating character of the hydroxide ligands and the strong hydrogen bonding network in these species both weaken the uranyl

ion such that increasing the water vapor pressure induces reduction of the uranyl ion via hydrogen abstraction and subsequent autoxidation via atmospheric oxygen. This proposed mechanism is very similar to that described by Thangavelu and Cahill [153] except that, in this work, photoexcitation of the uranyl ion is not required to trigger the reaction. The observation that significant uranyl oxygen exchange occurs during the formation of the uranyl peroxide species is consistent with a hydrogen abstraction mechanism.

Further work could help confirm the proposed mechanism. Repeating the isotopic labeling studies with γ labeled with ^{18}O in place of synthetic metaschoepite would help support the Raman peak assignments made in this chapter and confirm that formation of uranyl peroxide from γ and synthetic metaschoepite proceeds by the same mechanism as expected. The isotopic labeling studies presented here were somewhat complicated by the fact that synthetic metaschoepite has two dominant uranyl stretching modes, one of which redshifts significantly upon hydration. However, isotopic experiments with γ require the identification of an alternative synthetic route for γ, a challenge identified in Chapter 4. Complementary IR spectroscopy experiments would be a useful addition to future labeling studies, and could also provide additional structure characterization of the uranyl hydroxide product, such as how water molecules are arranged relative to the peroxo-linked uranyl chains. Determining whether or not the discovered mechanism relies on atmospheric oxygen would also clarify how autoxidation of the reduced uranyl ion occurs.

Chapter 6

Conclusions

6.1 Clarifying the chemical behavior of uranyl fluoride

The findings described in this work significantly clarify the chemical behavior of uranyl fluoride. Understanding the degradation pathways of uranyl fluoride in environmentally relevant conditions was one of the primary motivations of this study, and considerable progress has been made on this topic.

The phase transition between anhydrous uranyl fluoride (UO_2F_2) and hydrated uranyl fluoride ($[(UO_2F_2)(H_2O)]_7 \cdot 4\,H_2O$) was clarified through dynamic experiments. The dehydration transition is demonstrated to occur in two steps, with the removal of the hydrogen-bonded water molecules present in the pores of the uranyl fluoride hydrate structure occurring before a transformation to anhydrous uranyl fluoride. The rehydration of anhydrous uranyl fluoride is also clarified; while rehydration occurs readily in moderate humidity (>40% relative humidity (RH)), the rehydrated material appears to differ slightly in structure from the initial material. This suggests that the structure and water content of the uranyl fluoride hydrate may be dependent on factors such as the rate of rehydration.

Above a temperature-dependent threshold humidity (30–60% RH), particles of the uranyl fluoride hydrate undergo a complete loss of fluorine, resulting in the formation of a uranyl hydroxide hydrate. This reaction is demonstrated to be denucleation driven; water molecules are absorbed into the uranyl fluoride structure, driving fluorine dissociation at these sites through strong F···H interactions. This conversion occurs in just days for particles stored at

very high humidity (95% RH), although conversion is observed to occur much more slowly in the bulk phase.

The uranyl hydroxide hydration product of uranyl fluoride (γ) is demonstrated to be structurally similar to the uranyl hydroxide hydrate mineral schoepite, with layered uranyl sheets and interlayer water molecules. The layer spacing of γ is significantly expanded relative to schoepite, however. Analysis of the vibrational spectra of γ and synthetic metaschoepite suggest that hydrogen bonding between hydroxide ligands and interlayer water molecules is enhanced in γ, potentially due to the presence of additional interlayer water molecules.

At high enough water vapor pressure, γ can be further hydrated to form a second hydration product, δ, that is identified via x-ray diffraction (XRD) and Raman spectroscopy as a uranyl peroxide species similar to the known uranyl peroxide hydrate minerals studtite and metastudtite with chains of peroxo-linked uranyl ions. In studtite, these chains are linked by hydrogen-bonded water molecules; in metastudtite, these water molecules have been removed, and the chains are hydrogen bonded directly to each other. This explains why δ is more amorphous than γ. The limited number of available water molecules at the solid-gas interface compared to synthesis in solution prevents crystallization of the peroxo-linked chains, leading to a poorly crystalline uranyl peroxide species with regions structurally similar to both studtite and metastudtite.

This work has clarified the conditions under which uranyl fluoride is unstable and expected to undergo a chemical transformation. While evidence of fluorine loss with exposure to humidity indicated that some sort of transformation occurred over time, the two hydration products of uranyl fluoride characterized in this work have not been identified previously. The identification of the elemental and vibrational signatures of these products in particular is a significant contribution to the nuclear materials community, as these species will now be more easily identifiable in the future.

6.2 Characterization of uranyl species

This work provides a broader contribution to the understanding of solid-state uranyl compounds. As stressed in Chapter 1, very few solid-state uranyl compounds have been

rigorously characterized. Identification of uranyl compounds is often made via indirect structural techniques such as vibrational spectroscopy, but a clear understanding of how to correlate vibrational spectra to structures can be lacking. Presentation of complementary XRD, Raman, infrared (IR), and computational data of the structures studied in this work essentially expands a database that can be used to help interpret data collected from unknown materials in the future. Identification of significant phenomena that could affect measurements like the humidity dependence of the interlayer spacing in uranyl hydroxide hydrates is an essential component of this contribution as well.

6.3 Re-visiting uranyl reactivity

The identification of a novel non-photochemical uranyl peroxide formation mechanism represents a significant contribution to uranyl chemistry on its own. Further elucidation of this mechanism has revealed that the reaction proceeds because of an unexpected reactivity of the uranyl ion in uranyl hydroxide hydrates caused by the combination of σ-donating ligands and strong interactions between uranyl oxygens and interlayer water molecules. This is a novel finding with broad impact in uranyl chemistry research.

While the uranyl ion has been historically regarded as fairly inert, this work adds to a growing body of research that demonstrates that in specific cases, the oxo ligands can be much more chemically reactive than previously thought. Renewed interest in investigating uranyl ion reactivity was catalyzed in 2008 when Arnold et al. [8] demonstrated the first instance of selective functionalization of the uranyl oxo ligand. This was achieved by using a flexible ligand to simultaneously bind the uranyl ion and two potassium ions, creating a "Pac-Man" structure in which one of the uranyl oxygens donates electrons to the potassium ions. This charge transfer weakens the strong uranyl bonds, reducing the uranium and allowing the formation of a silicon–oxygen bond at the other oxo group [8, 21]. This work has since prompted a reevaluation of uranyl reactivity, and similar functionalization has been demonstrated in other systems as well [9, 10].

The potential for manipulation of the uranyl ion has garnered considerable interest because it has wide-reaching applications in nuclear waste management and environmental

remediation, among others. In this study, it was demonstrated that the uranyl bonds in uranyl hydroxide hydrates are weakened such that increased water vapor pressure can induced interactions that would typically require photoexcitation. As found by Arnold, the geometry of the system is crucial in facilitating this reaction. The 2008 study by Arnold et al. introduced "Pac-Man" structures that facilitate oxo ligand functionalization [8]. Multiple variants of these structures have now been identified. Similarly, this work demonstrates a class of layered uranyl hydroxide hydrates with novel uranyl reactivity. It is likely that additional structures exist with similar chemistry. In this manner, this work will help drive basic uranyl chemistry investigations for years to come.

6.4 Future directions

While this work significantly clarifies the chemical behavior of uranyl fluoride, the discovery of new reactions raises several additional areas of future study. Many of the specific remaining questions related to this work are discussed at the end of each chapter. General themes of future exploration are summarized here.

6.4.1 Probing the structure of water in hydrated uranyl fluoride

The uranyl fluoride hydrate solved by Mikhailov, $[(UO_2F_2)(H_2O)]_7 \cdot 4\,H_2O$, contains both equatorially bound and hydrogen-bonded water molecules. A computational analysis of the water structure in $[(UO_2F_2)(H_2O)]_7 \cdot 4\,H_2O$ is presented in Chapter 2, but there is remaining work to be done to experimentally characterize how water interacts with the crystal structure. The dehydration and rehydration of this structure is demonstrated to result in slight structural changes, potentially due to a rearrangement of this water network. It is also likely that the structure can incorporate a variable number of water molecules and that the hydrogen bonding network varies significantly based on the water content.

Clarifying these points will provide important insight regarding the hydration reaction from $[(UO_2F_2)(H_2O)]_7 \cdot 4\,H_2O$ to the uranyl hydroxide species, γ. This reaction has been demonstrated to occur above a threshold humidity, presumably due to the absorption of additional water molecules that interact strongly with fluorine ligands. The mechanistic

details of this reaction can be further probed with additional computational calculations. In particular, nudged elastic band calculations may prove useful for identifying the transition state of the fluorine–water interaction.

6.4.2 Further characterization of the structure of γ

Chapter 4 describes characterization of γ, a novel uranyl hydroxide hydrate formed from the hydration of uranyl fluoride. XRD analysis reveals that γ has a layered structure similar to the known uranyl hydroxide hydrate mineral species schoepite and metaschoepite. However, the interlayer spacing in γ is significantly expanded. Comparison of the IR spectrum of γ and synthetic metaschoepite also suggests that γ is characterized by stronger hydrogen bonds between the uranyl layers and interlayer water molecules. Both of these findings, along with the fact that γ is formed at high humidity, suggest that γ may have a higher water content than schoepite or metaschoepite. Future thermogravimetric analysis would help clarify this hypothesis.

Powder XRD allowed for a partial structural determination of γ in this study, namely the determination of the lattice constants. Comparison of the Raman spectrum of γ and synthetic metaschoepite suggests that the equatorial environment of the uranyl ions differs in the two structures, motivating additional structural studies. Full structural characterization of this species could be made via single-crystal XRD. However, this requires determination of a direct synthetic route. The identification of an alternative synthetic route would also allow for the production of larger quantities of γ, allowing the application of additional characterization methods such as neutron scattering techniques, as well as the the ability to replicate experiments or perform complementary experiments on the same batch of material.

Future computational studies would also be useful in determining structural characteristics of γ such as the position and dynamics of interlayer water molecules. Now that the lattice constants of γ have been assessed via XRD, a computational model of the structure including interlayer water molecules can be built. Carrying out ab initio molecular dynamics simulations on this structure may also help clarify why the vibrational spectra of γ and synthetic metaschoepite differ.

6.4.3 Further elucidation of peroxide formation reaction

The uranyl peroxide species δ, produced via hydration of γ or synthetic metaschoepite, is partially characterized in Chapter 5. Characterization of this species is complicated by the long formation time. Additional long-term hydration experiments may result in higher quality XRD patterns that could further clarify the structure of this species. IR spectroscopy, which was not obtained in this study, would be a useful complementary technique to probe the water structure within the crystal.

The novel nonphotochemical reaction by which δ deserves significant follow-up study as well. The mechanistic details of this reaction are elucidated in Chapter 5 in part via the hydration of isotopically labeled synthetic metaschoepite. If an alternative synthetic route for the formation of γ can be identified, repeating these experiments with labeled γ would help support the conclusions made in Chapter 5 and confirm whether or not the formation of uranyl peroxide via γ and synthetic metaschoepite proceeds by the same reaction. Additional hydration studies in an inert atmosphere would clarify how atmospheric oxygen is involved in the proposed autoxidation reaction.

In addition to further clarification of the specific mechanistic details of this reaction, future work should also focus on better understanding the unusual uranyl ion reactivity demonstrated in uranyl hydroxide hydrates. As discussed in Chapter 5, this is proposed to arise due to the combined effect of the strong σ-donating character of the hydroxy ligands and strong hydrogen bonding interactions between uranyl ions and interlayer water molecules. The electronic structure of these species should be assessed computationally to more thoroughly understand the effect of these structural characteristics. The observed uranyl oxygen exchange that occurs as a result of the weakening of the uranyl bonds can also be quantified through additional isotopic labeling studies.

Bibliography

[1] Aladzheva, I. M., Bykhovskaya, O. V., Nelyubina, Y. V., Klemenkova, Z. S., Petrovskii, P. V., and Odinets, I. L. (2011). Uranium complexes of cyclic O,O–bidentate ligands with the P–N–P backbone. *Inorganica Chim. Acta*, 373(1):130–136. 207

[2] Alam, T. M., Liao, Z., Nyman, M., and Yates, J. (2016). Insight into hydrogen bonding of uranyl hydroxide layers and capsules by use of ^{1}H magic-angle spinning NMR spectroscopy. *J. Phys. Chem. C*, 120(19):10675–10685. 84, 127, 128, 161

[3] Allen, P. G., Shuh, D. K., Bucher, J. J., Edelstein, N. M., Palmer, C. E. A., Silva, R. J., Nguyen, S. N., Marquez, L. N., and Hudson, E. A. (1996). Determinations of uranium structures by EXAFS: Schoepite and other U(VI) oxide precipitates. *Radiochim. Acta*, 75:47–53. 127

[4] Amme, M., Renker, B., Schmid, B., Feth, M. P., Bertagnolli, H., and Dobelin, W. (2002). Raman microspectrometric identification of corrosion products formed on UO_2 nuclear fuel during leaching experiments. *J. Nucl. Mater.*, 306:202–212. 84, 127, 128, 196, 203

[5] Anisimov, V. I., Zaanen, J., and Andersen, O. K. (1991). Band theory and Mott insulators: Hubbard U instead of Stoner I. *Phys. Rev. B*, 44(3):943–954. 20

[6] Armstrong, D. P., Jarabek, R. J., and Fletcher, W. H. (1989). Micro-Raman Spectroscopy of Selected Solid $U_xO_yF_z$ Compounds. *Appl. Spectrosc.*, 43(3):461–468. 58

[7] Arnold, O., Bilheux, J. C., Borreguero, J. M., Buts, A., Campbell, S. I., Chapon, L., Doucet, M., Draper, N., Ferraz Leal, R., Gigg, M. A., Lynch, V. E., Markvardsen, A., Mikkelson, D. J., Mikkelson, R. L., Miller, R., Palmen, K., Parker, P., Passos, G., Perring, T. G., Peterson, P. F., Ren, S., Reuter, M. A., Savici, A. T., Taylor, J. W., Taylor, R. J., Tolchenov, R., Zhou, W., and Zikovsky, J. (2014). Mantid–Data analysis and visualization package for neutron scattering and μSR experiments. *Nucl. Instruments Methods Phys. Res. Sect. A*, 764:156–166. 7

[8] Arnold, P. L., Patel, D., Wilson, C., and Love, J. B. (2008). Reduction and selective oxo group silylation of the uranyl dication. *Nature*, 451:315–317. 3, 237, 238

[9] Arnold, P. L., Pécharman, A.-F., Hollis, E., Yahia, A., Maron, L., Parsons, S., and Love, J. B. (2010). Uranyl oxo activation and functionalization by metal cation coordination. *Nat. Chem.*, 2(12):1056–1061. 3, 237

[10] Arnold, P. L., Pécharman, A.-F., Lord, R. M., Jones, G. M., Hollis, E., Nichol, G. S., Maron, L., Fang, J., Davin, T., and Love, J. B. (2015). Control of oxo-group functionalization and reduction of the uranyl ion. *Inorg. Chem.*, 54(7):3702–3710. 3, 237

[11] Atoji, M. and McDermott, M. J. (1970). The crystal structure of anhydrous UO_2F_2. *Acta Crystallogr. Sect. B*, 26:1540–1544. 25, 27, 51

[12] Avrami, M. (1939). Kinetics of phase change. I General theory. *J. Chem. Phys.*, 7:1103–1112. 109

[13] Avrami, M. (1940). Kinetics of phase change. II Transformation-time relations for random distribution of nuclei. *J. Chem. Phys.*, 8:212–224. 109

[14] Baker, R. J. (2014). Uranium minerals and their relevance to long term storage of nuclear fuels. *Coord. Chem. Rev.*, 266-267:123–136. 196

[15] Baroni, S., De Gironcoli, S., Dal Corso, A., and Giannozzi, P. (2001). Phonons and related crystal properties from density-functional perturbation theory. *Rev. Mod. Phys.*, 73(2):515–562. 22

[16] Bartlett, J. R. and Cooney, R. P. (1989). On the determination of uranium–oxygen bond lengths in dioxouranium(VI) compounds by Raman spectroscopy. *J. Mol. Struct.*, 193:295–300. 2

[17] Bastians, S., Crump, G., Griffith, W. P., and Withnall, R. (2004). Raspite and studtite: Raman spectra of two unique minerals. *J. Raman Spectrosc.*, 35:726–731. 84, 196

[18] Berlizov, A., Ho, D. M. L., Nicholl, A., Fanghänel, T., and Mayer, K. (2016). Assessing hand-held Raman spectrometer FirstDefender RM for nuclear safeguards applications. *J. Radioanal. Nucl. Chem.*, 307(1):285–295. 84, 127, 128, 130, 196

[19] Billiet, V. and de Jong, W. F. (1935). Schoepiet en becquereliet. *Nat. Tijdschr. Ned.-Indie*, 17:157–162. 124, 126, 153, 160

[20] Bonales, L. J., Colmenero, F., Cobos, J., and Timón, V. (2016). Spectroscopic Raman characterization of rutherfordine: a combined DFT and experimental study. *Phys. Chem. Chem. Phys.*, 18(24):16575–16584. 20

[21] Boncella, J. M. (2008). Uranium gets a reaction. *Nature*, 451:250–252. 3, 237

[22] Brehm, M. and Kirchner, B. (2011). TRAVIS—A free analyzer and visualizer for Monte Carlo and molecular dynamics trajectories. *J. Chem. Inf. Model*, 51:2007–2023. 23

[23] Brooks, L. H., Garner, E. V., and Whitehead, E. (1956). Chemical and x-ray crystallographic studies on uranyl fluoride. Technical report, United Kingdom Atomic Energy Authority. 27, 74

[24] Brown, M. (1997). The Prout-Tompkins rate equation in solid-state kinetics. *Thermochim. Acta*, 300:93–106. 112

[25] Brugger, J., Meisser, N., Etschmann, B., Ansermet, S., and Pring, A. (2011). Paulscherrerite from the Number 2 Workings, Mount Painter Inlier, Northern Flinders Ranges, South Australia: "Dehydrated schoepite" is a mineral after all. *Am. Mineral.*, 96:229–240. 124, 126, 153, 160

[26] Buck, A. L. (1981). New equations for computing vapor pressure and enhancement factor. *J. Appl. Meteorol.*, 20(12):1527–1532. 75, 88

[27] Bullock, J. I. (1969). Raman and infrared spectroscopic studies of the uranyl ion: the symmetric stretching frequency, force constants, and bond lengths. *J. Chem. Soc. A*, pages 781–784. 10, 58

[28] Burns, P. C., Finck, R. J., Hawthorne, F. C., Miller, M. L., and Ewing, R. C. (1997). The crystal structure of ianthinite, a mixed-valence uranium oxide hydrate. *J. Nucl. Mater.*, 249:199–206. 127, 138

[29] Burns, P. C. and Hughes, K.-A. (2003). Studtite, $[(UO_2)(O_2)(H_2O)_2](H_2O)_2$: The first structure of a peroxide mineral. *Am. Mineral.*, 88(7):1165–1168. 84, 192, 193

[30] Burrows, H. D. (1976). A flash photolytic study of the photo-oxidation of some inorganic anions by the uranyl ion. *J. Photochem.*, 5(4):265–275. 232

[31] Canizares, A., Guimbretiere, G., Tobon, Y. A., Raimboux, N., Omnee, R., Perdicakis, M., Muzeau, B., Leoni, E., Alam, M. S., Mendes, E., Simon, D., Matzen, G., Corbel, C., Barthe, M. F., and Simon, P. (2012). In situ Raman monitoring of materials under irradiation: Study of uranium dioxide alteration by water radiolysis. *J. Raman Spectrosc.*, 43(10):1492–1497. 84, 127, 196, 203

[32] Charpin, P., Folcher, G., Lance, M., Nierlich, M., and Vigner, D. (1985). Structure d'un complexe binucléaire du nitrate d'uranyle et du N,N-diméthyl-formamide: μ-peroxo-bis[bis(N,N-diméthyl-formamide)nitratodioxouranium(VI)], $[(UO_2)_2(NO_3)_2O_2(C_3H_7NO)_4]$. *Acta Crystallogr. Sect. C*, 41(9):1302–1305. 207

[33] Christ, C. L. (1965). Phase transformations and crystal chemistry of schoepite. *Am. Mineral.*, 50:235–239. 122

[34] Christ, C. L. and Clark, J. R. (1960). Crystal chemical studies of some uranyl oxide hydrates. *Am. Mineral.*, 45:1026–1061. 122, 124, 126, 135, 137, 138, 153, 160

[35] Christensen, H. (1998). Calculations simulating spent-fuel leaching experiments. *Nucl. Technol.*, 124:165–174. 204

[36] Clarens, F., De Pablo, J., Díez-Perez, I., Casas, I., Gimenez, J., and Rovira, M. (2004). Formation of studtite during the oxidative dissolution of UO_2 by hydrogen peroxide: A SFM study. *Environ. Sci. Technol.*, 38(24):6656–6661. 203

[37] Clark, D. L. and Conradson, S. D. (1999). Chemical speciation of the uranyl ion under highly alkaline conditions. Synthesis, structures, and oxo ligand exchange dynamics. *Inorg. Chem.*, 38(7):1456–1466. 225

[38] Colmenero, F., Bonales, L. J., Cobos, J., and Timón, V. (2017a). Density functional theory study of the thermodynamic and raman vibrational properties of γ-UO3 polymorph. *J. Phys. Chem. C*, 121(27):14507–14516. 20

[39] Colmenero, F., Bonales, L. J., Cobos, J., and Timón, V. (2017b). Structural, mechanical and vibrational study of uranyl silicate mineral soddyite by DFT calculations. *J. Solid State Chem.*, 253(June):249–257. 20

[40] Colmenero, F., Bonales, L. J., Cobos, J., and Timón, V. (2017c). Study of the thermal stability of studtite by in situ Raman spectroscopy and DFT calculations. *Spectrochim. Acta Part A*, 174:245–253. 20, 84, 131, 195, 196, 221

[41] Colmenero, F., Cobos, J., and Timon, V. (2018). Periodic Density Functional Theory Study of the Structure, Raman Spectrum, and Mechanical Properties of Schoepite Mineral. *Inorg. Chem.*, 57:4470–4481. 20

[42] Corbel, C., Sattonnay, G., Guilbert, S., Garrido, F., Barthe, M. F., and Jegou, C. (2006). Addition versus radiolytic production effects of hydrogen peroxide on aqueous corrosion of UO_2. *J. Nucl. Mater.*, 348:1–17. 203

[43] Crandall, H. W. (1949). The formula of uranyl ion. *J. Chem. Phys.*, 17(7):602–606. 224

[44] de Burgh, J. M. and Foster, S. J. (2017). Influence of temperature on water vapour sorption isotherms and kinetics of hardened cement paste and concrete. *Cem. Concr. Res.*, 92:37–55. 114

[45] Debets, P. C. (1963). X-ray diffraction data on hydrated uranium peroxide. *J. Inorg. Nucl. Chem.*, 25(6):727–730. 122

[46] Deliens, M. and Piret, P. (1983). Metastudtite, a new mineral from Shikolobwe, Shaba, Zaire. *Am. Mineral.*, 68:456–458. 192

[47] Di Pietro, P. and Kerridge, A. (2016). U-Oyl stretching vibrations as a quantitative measure of the equatorial bond covalency in uranyl complexes: A quantum-chemical investigation. *Inorg. Chem.*, 55(2):573–583. 10, 58

[48] Doyle, G. A., Goodgame, D. M. L., Sinden, A., and Williams, D. J. (1993). Conversion of atmospheric dioxygen to a μ–η^2,η^2–peroxo bridge in a dinuclear uranium(VI) complex. *J. Chem. Soc., Chem. Commun.*, pages 1170–1172. 207

[49] Dudarev, S. L., Botton, G. A., Savrasov, S. Y., Humphreys, C. J., and Sutton, A. P. (1998). Electron-energy-loss spectra and the structural stability of nickel oxide: An LSDA+U study. *Phys. Rev. B*, 57(3):1505–1509. 20

[50] Dzaugis, M. E., Spivack, A. J., and D'Hondt, S. (2015). A quantitative model of water radiolysis and chemical production rates near radionuclide-containing solids. *Radiat. Phys. Chem.*, 115:127–134. 206

[51] Eilers, P. H. C. (2003). A perfect smoother. *Anal. Chem.*, 75(14):3631–3636. 14

[52] Eilers, P. H. C. (2004). Parametric time warping. *Anal. Chem.*, 76(2):404–411. 14

[53] Finch, R. J., Cooper, M. A., Hawthorne, F. C., and Ewing, R. C. (1996). The crystal structure of schoepite, $[(UO_2)_4O(OH)_6]\cdot 6\,H_2O$. *Can. Mineral.*, 34(5):1071–1088. 122, 123, 124, 126, 136, 137, 138, 153, 160

[54] Finch, R. J., Hawthorne, F. C., and Ewing, R. C. (1998). Structural relations among schoepite, metaschoepite and "dehydrated schoepite". *Can. Mineral.*, 36:831–845. 122, 127, 178

[55] Finch, R. J., Hawthorne, F. C., Miller, M. L., and Ewing, R. C. (1997). Distinguishing among schoepite, $[(UO_2)_8O_2(OH)_{12}](H_2O)_{12}$, and related minerals by x-ray powder diffraction. *Powder Diffr.*, 12(4):230–238. 122, 127

[56] Foley, S., Rotureau, P., Pin, S., Baldacchino, G., Renault, J. P., and Mialocq, J. C. (2005). Radiolysis of confined water: Production and reactivity of hydroxyl radicals. *Angew. Chemie – Int. Ed.*, 44(1):110–112. 206, 224

[57] Fortier, S. and Hayton, T. W. (2010). Oxo ligand functionalization in the uranyl ion (UO_2^{2+}). *Coord. Chem. Rev.*, 254(3-4):197–214. 3, 221, 224, 225, 228

[58] Frost, R. L. and Čejka, J. (2007). A Raman spectroscopic study of the uranyl carbonate rutherfordine. *J. Raman Spectrosc.*, 38(11):1488–1493. 151

[59] Frost, R. L., Čejka, J., Keeffe, E. C., and Dickfos, M. J. (2008). Raman spectroscopic study of the uranyl selenite mineral marthozite Cu[(UO2)3(SeO3)2O 2]·8H2O. *J. Raman Spectrosc.*, 39(10):1413–1418. 10

[60] Frost, R. L., Cejka, J., and Weier, M. L. (2007). Raman spectroscopic study of the uranyl oxyhydroxide hydrates: becquerelite, billietite, curite, schoepite and vandendriesscheite. *J. Raman Spectrosc.*, 38:460–466. 84, 127, 128

[61] Garcia-Hernández, M., Lauterbach, C., Krüger, S., Matveev, A., and Rösch, N. (2002). Comparative study of relativistic density functional methods applied to actinide species AcO_{22}^{+} and AcF_6 for Ac = U, Np. *J. Comput. Chem.*, 23(8):834–846. 34

[62] Greenspan, L. (1977). Humidity fixed points of binary saturated aqueous solutions. *J. Res. Natl. Bur. Stand. Sect. A*, 81(1):89–96. 88

[63] Guimbretiere, G., Canizares, A., Simon, P., Tobon-Correa, Y. A., Ammar, M. R., Corbel, C., and Barthe, M. F. (2011). In-situ raman observation of the first step of uranium dioxide weathering exposed to water radiolysis. *Spectrosc. Lett.*, 44(7–8):570–573. 203

[64] Guo, X., Ushakov, S. V., Labs, S., Curtius, H., Bosbach, D., and Navrotsky, A. (2014). Energetics of metastudtite and implications for nuclear waste alteration. *Proc. Natl. Acad. Sci.*, 111(50):17737–17742. 195, 203

[65] Hamada, I. (2014). van der Waals density functional made accurate. *Phys. Rev. B*, 89(12):121103. 162

[66] Hamada, I. and Yanagisawa, S. (2011). Pseudopotential approximation in van der Waals density functional calculations. *Phys. Rev. B*, 84(15):2–5. 162

[67] Hanson, B., McNamara, B., Buck, E., Friese, J., Jenson, E., Krupka, K., and Arey, B. (2005). Corrosion of commercial spent nuclear fuel. 1. Formation of studtite and metastudtite. *Radiochim. Acta*, 93(3):159–168. 196, 203

[68] Hiroki, A., Pimblott, S. M., and Laverne, J. A. (2002). Hydrogen peroxide production in the radiolysis of water with high radical scavenger concentrations. *J. Phys. Chem. A*, 106(40):9352–9358. 205

[69] Ho Mer Lin, D., Jones, A. E., Goulermas, J. Y., Turner, P., Varga, Z., Fongaro, L., Fanghänel, T., and Mayer, K. (2015). Raman spectroscopy of uranium compounds and the use of multivariate analysis for visualization and classification. *Forensic Sci. Int.*, 251:61–68. 84, 127, 128, 130

[70] Ho Mer Lin, D., Manara, D., Lindqvist-Reis, P., Fanghanel, T., and Mayer, K. (2014). The use of different dispersive Raman spectrometers for the analysis of uranium compounds. *Vib. Spectrosc.*, 73:102–110. 84, 127, 128, 130

[71] Hoekstra, H. R. and Siegel, S. (1973). The uranium trioxide-water system. *J. Inorg. Nucl. Chem.*, 35:761–779. 122, 127

[72] Hoover, W. G. (1985). Canonical dynamics: Equilibrium phase-space distributions. *Phys. Rev. A*, 31(3):1695–1697. 23

[73] Huq, A., Hodges, J. P., Gourdon, O., and Heroux, L. (2011). Powgen: A third-generation high-resolution high-throughput powder diffraction instrument at the Spallation Neutron Source. *Z. Krist. Proc.*, 1:127–135. 7, 9

[74] Icenhour, A. S. and Toth, L. M. (2003). Alpha radiolysis of sorbed water on uranium oxides and uranium oxyfluorides. Technical report, Oak Ridge National Laboratory. 204

[75] Ingram, K. I. M., Häller, L. J. L., and Kaltsoyannis, N. (2006). Density functional theory investigation of the geometric and electronic structures of $[UO_2(H_2O)_m(OH)_n]^{(2-n)}$ (n + m = 5). *Dalt. Trans.*, 2:2403–2414. 225

[76] Ishizuka, T., Watanabe, A., Kotani, H., Hong, D., Satonaka, K., Wada, T., Shiota, Y., Yoshizawa, K., Ohara, K., Yamaguchi, K., Kato, S., Fukuzumi, S., and Kojima, T. (2016). Homogeneous photocatalytic water oxidation with a dinuclear Co(III)-pyridylmethylamine complex. *Inorg. Chem.*, 55(3):1154–1164. 209

[77] Janik, D., Janik, I., and Bartels, D. M. (2007). Neutron and β/γ radiolysis of water up to supercritical conditions. 1. β/γ yields for H_2, $H^{\cdot}$ atom, and hydrated electron. *J. Phys. Chem. A*, 111(32):7777–7786. 206

[78] Jaumot, J., de Juan, A., and Tauler, R. (2015). MCR-ALS GUI 2.0: New features and applications. *Chemom. Intell. Lab. Syst.*, 140:1–12. 14

[79] Jaumot, J., Gargallo, R., de Juan, A., and Tauler, R. (2005). A graphical user-friendly interface for MCR-ALS: a new tool for multivariate curve resolution in MATLAB. *Chemom. Intell. Lab. Syst.*, 76(1):101–110. 14

[80] Jayasinghe, A. S., Applegate, L. C., Unruh, D. K., Hutton, J., and Forbes, T. Z. (2019). Utilizing autoxidation of solvents To promote the formation of uranyl peroxide materials. *Cryst. Growth Des.*, 19:1756–1766. 209, 212, 213

[81] John, G. H., May, I., Sarsfield, M. J., Steele, H. M., Collison, D., Helliwell, M., and McKinney, J. D. (2004). The structural and spectroscopic characterisation of three actinyl complexes with coordinated and uncoordinated perrhenate: $[UO_2(ReO_4)_2(TPPO)_3]$, $[[(UO_2)(TPPO)_3]_2(\mu_2{-}O_2)][ReO_4]_2$ and $[NpO_2(TPPO)_4][ReO_4]$. *Dalton Trans.*, 2(5):734–740. 207

[82] Johnson, T. J., Sweet, L. E., Meier, D. E., Mausolf, E. J., Kim, E., Weck, P. F., Buck, E. C., and McNamara, B. K. (2015). Time-resolved infrared reflectance studies of the dehydration-induced transformation of uranyl nitrate hexahydrate to the trihydrate form. *J. Phys. Chem. A*, 119(39):9996–10006. 10

[83] Jones, L. (1959). Determination of U–O bond distance in uranyl complexes from their infrared spectra. *Spectrochim. Acta*, 15:409–411. 2

[84] Jorgensen, W. L., Chandrasekhar, J., Madura, J. D., Impey, R. W., and Klein, M. L. (1983). Comparison of simple potential functions for simulating liquid water. *J. Chem. Phys.*, 79(2):926. 232

[85] Kailer, A., Nickel, K. G., and Gogotsi, Y. G. (1999). Raman microspectroscopy of nanocrystalline and amorphous phases in hardness indentations. *J. Raman Spectrosc.*, 30(10):939–946. 65

[86] Kips, R., Crowhurst, J., Kristo, M. J., Stefaniak, E., and Hutcheon, D. (2010). Micro-Raman spectroscopy of uranium oxyfluoride particulate material for nuclear safeguards. Technical report, Lawrence Livermore National Laboratory. 74

[87] Kips, R., Pidduck, A. J., Houlton, M. R., Leenaers, A., Mace, J. D., Marie, O., Pointurier, F., Stefaniak, E. A., Taylor, P. D. P., Van den Berghe, S., Van Espen, P., Van Grieken, R., and Wellum, R. (2009). Determination of fluorine in uranium oxyfluoride particles as an indicator of particle age. *Spectrochim. Acta Part B*, 64(3):199–207. 58, 75, 114, 120

[88] Kirkegaard, M., Miskowiec, A., Ambrogio, M., and Anderson, B. (2018). Evidence of a nonphotochemical mechanism for the solid-state formation of uranyl peroxide. *Inorg. Chem.*, 57:5711–5715. 20, 78, 80, 82, 84, 85, 87, 91, 101, 104, 131, 204, 209, 212

[89] Kirkegaard, M. C., Langford, J., Steill, J., Anderson, B., and Miskowiec, A. (2017). Vibrational properties of anhydrous and partially hydrated uranyl fluoride. *J. Chem. Phys.*, 146:024502. 20, 41, 51, 60, 77, 87

[90] Kirkegaard, M. C., Niedziela, J. L., Miskowiec, A., Shields, A. E., and Anderson, B. B. (2019). Elucidation of the structure and vibrational spectroscopy of synthetic metaschoepite and its dehydration product. *Inorg. Chem.* 14, 15, 23, 41, 124, 126, 127, 130, 137, 139, 140, 144, 147, 153, 160, 161, 162, 169, 177, 214, 222

[91] Klimeš, J., Bowler, D., and Michaelides, A. (2010). Chemical accuracy for the van der Waals density functional. *J. Phys. Condens. Matter*, 22(2):022201. 19, 21, 24, 34, 150, 231

[92] Klimeš, J., Bowler, D. R., and Michaelides, A. (2011). Van der Waals density functionals applied to solids. *Phys. Rev. B*, 83:195131. 19, 21, 24, 34, 150, 231

[93] Klingensmith, A. L., Deely, K. M., Kinman, W. S., Kelly, V., and Burns, P. C. (2007). Neptunium incorporation in sodium-substituted metaschoepite. *Am. Mineral.*, 92(4):662–669. 124, 126, 153, 160

[94] Kubatko, K.-A. H., Helean, K. B., Navrotsky, A., and Burns, P. C. (2003). Stability of peroxide-containing uranyl minerals. *Science*, 302(5648):1191–1193. 192, 203, 204, 233

[95] La Pierre, H. S. and Meyer, K. (2013). Uranium-ligand multiple bonding in uranyl analogues, $[L{=}U{=}L]^{n+}$, and the inverse trans influence. *Inorg. Chem.*, 52(2):529–539. 2

[96] Labs, S. (2015). *Secondary uranium phases of spent nuclear fuel - coffinite, $USiO_4$, and studtite, $UO_4 \cdot 4\,H_2O$—Synthesis, characterization, and investigations regarding phase stability*, volume 267 of *R. Energ. Umwelt / Energy Environ.* Forschungszentrum Jülich GmbH Zentralbibliothek. 84, 195, 196, 197, 198

[97] LaVerne, J. A. (2000). OH radicals and oxidizing products in the gamma radiolysis of water. *Radiat. Res.*, 153(2):196–200. 206

[98] Le Caër, S., Renault, J. P., and Mialocq, J. C. (2007). Hydrogen peroxide formation in the radiolysis of hydrated nanoporous glasses: A low and high dose rate study. *Chem. Phys. Lett.*, 450(1-3):91–95. 206, 224

[99] Liu, F., Sommer, F., Bos, C., and Mittemeijer, E. J. (2007). Analysis of solid state phase transformation kinetics: models and recipes. *Int. Mater. Rev.*, 52(4):193–212. 106, 109

[100] Lu, G., Haes, A. J., and Forbes, T. Z. (2018). Detection and identification of solids, surfaces, and solutions of uranium using vibrational spectroscopy. *Coord. Chem. Rev.*, 374:314–344. 10, 58

[101] Lutz, H. D. (1988). Bonding and structure of water molecules in solid hydrates. Correlation of spectroscopic and structural data. *Solid Mater. Struct. Bond.*, 69(8):97–125. 10

[102] Lychev, A. A., Mikhalev, V. A., and Sublobov, D. N. (1990). Crystalline hydrates of uranyl fluoride at 20°C. *Radiokhimiya*, 32(6):7–12. 27, 28, 30, 33, 60, 74

[103] Mao, Y. and Bakac, A. (1996). Photocatalytic oxidation of aromatic hydrocarbons. *Inorg. Chem.*, 35(13):3925–3930. 232

[104] Marshall, W. L., Gill, J. S., and Secoy, C. H. (1954). Phase equilibria of uranium trioxide and aqueous hydrofluoric acid in stoichiometric concentrations. *J. Am. Chem. Soc.*, 76(17):4279–4281. 28, 74

[105] Masci, B. and Thuéry, P. (2005). Uranyl complexes with the pyridine-2,6-dicarboxylato ligand: New dinuclear species with μ–η^2,η^2–peroxide, μ^2–hydroxide or μ^2–methoxide bridges. *Polyhedron*, 24(2):229–237. 207

[106] Matsushima, R. (1972). Mechanism of quenching of the uranyl fluorescence by organic compounds. *J. Am. Chem. Soc.*, 94(17):6010–6016. 232

[107] Maya, L. and Begun, G. M. (1981). A Raman spectroscopy study of hydroxo and carbonato species of the uranyl(VI) ion. *J. Inorg. Nucl. Chem.*, 43(11):2827–2832. 10, 128

[108] McCleskey, T. M., Burns, C. J., and Tumas, W. (1999). Uranyl photochemistry with alkenes: Distinguishing between H-atom abstraction and electron transfer. *Inorg. Chem.*, 38(25):5924–5925. 232

[109] McGlynn, S. P., Smith, J. K., and Neely, W. C. (1961). Electronic structure, spectra, and magnetic properties of oxycations. III. Ligation effects on the infrared spectrum of the uranyl ion. *J. Chem. Phys.*, 35(1):105–116. 2

[110] McGrail, B. T., Pianowski, L. S., and Burns, P. C. (2014). Photochemical water oxidation and origin of nonaqueous uranyl peroxide complexes. *J. Am. Chem. Soc.*, 136:4797–4800. 10, 207, 208

[111] Mikhailov, Yu. N., Gorbunova, Yu. E., Stolyarov, I. P., and Moiseev, I. I. (2001). A new modification of monoaquadifluorouranyl hydrate. *Dokl. Chem.*, 380:293–297. 28, 29, 30, 31, 33, 34, 36, 38, 52, 56, 74

[112] Miskowiec, A., Anderson, B. B., Huq, A., Mamontov, E., Herwig, K. W., Trowbridge, L., and Rondinone, A. (2016a). Time-dependent water dynamics in hydrated uranyl fluoride. *Mol. Phys.*, 114(1):61–71. 27, 34, 49, 51

[113] Miskowiec, A., Kirkegaard, M. C., Herwig, K. W., Trowbridge, L., Mamontov, E., and Anderson, B. (2016b). Quasielastic neutron scattering with in situ humidity control: Water dynamics in uranyl fluoride. *J. Appl. Phys.*, 119(9). 33, 34, 49, 112

[114] Miskowiec, A., Kirkegaard, M. C., Huq, A., Mamontov, E., Herwig, K. W., Trowbridge, L., Rondinone, A., and Anderson, B. (2015). Structural phase transitions and water dynamics in uranyl fluoride hydrates. *J. Phys. Chem. A*, 119(49):11900–11910. 28, 31, 32, 33, 34, 51, 58, 72

[115] Morato, F., Fulconis, J. M., Rouquerol, F., and Fourcade, R. (1998). Study of the dehydration process of uranyl difluoride hydrates stable under usual conditions of temperature, pressure, and atmospheric moisture. *J. Fluor. Chem.*, 91:69–73. 27, 33, 51

[116] Moriyasu, M. (1977). Quenching of uranyl luminescence by water molecule. *J. Inorg. Nucl. Chem.*, 39(12):2211–2214. 232

[117] Nagaishi, R., Katsumura, Y., Ishigure, K., Aoyagi, H., Yoshida, Z., Kimura, T., and Kato, Y. (2002). Photoreduction of the uranyl ion in aqueous solution II. Alcohols in acid solutions. *Photochem. Photobiol.*, 146:157–161. 232

[118] Nakashima, M. (1993). Radiolytic hydrogen gas formation for water adsorbed on type-A zeolites. *Radiat. Phys. Chem.*, 41(3):461–465. 206, 224

[119] Nakashima, M. and Masaki, N. M. (1996). Radiolytic hydrogen gas formation from water adsorbed on type-Y zeolites. *Radiat. Phys. Chem.*, 47(2):241–245. 206, 224

[120] Nakashima, M. and Tachikawa, E. (1983). Hydrogen evolution from tritiated water on silica gel by gamma-irradiation. *Radiochim. Acta*, 33(4):217–222. 206, 224

[121] Newville, M., Stensitski, T., Allen, D. B., and Ingargiola, A. (2014). LMFIT: Non-linear least-square minimization and curve-fitting for Python. 14

[122] Nguyen-Trung, C., Begun, G. M., and Palmer, D. A. (1992). Aqueous uranium complexes. 2. Raman spectroscopic study of the complex formation of the dioxouranium(VI) ion with a variety of inorganic and organic ligands. *Inorg. Chem.*, 31(25):5280–5287. 2, 10, 58

[123] Nipruk, O. V., Knyazev, A. V., Chernorukov, G. N., and Pykhova, Y. P. (2011). Synthesis and study of hydrated uranium(VI) oxides, $UO_3 \cdot nH_2O$. *Radiochemistry*, 53(2):146–150. 178

[124] Nosé, S. (1984a). A molecular dynamics method for simulations in the canonical ensemble. *Mol. Phys.*, 52(2):255–268. 23

[125] Nosé, S. (1984b). A unified formulation of the constant temperature molecular dynamics methods. *J. Chem. Phys.*, 81(1):511–519. 23

[126] Odoh, S. O., Shamblin, J., Colla, C. A., Hickam, S., Lobeck, H. L., Lopez, R. A. K., Olds, T., Szymanowski, J. E. S., Sigmon, G. E., Neuefeind, J., Casey, W. H., Lang, M., Gagliardi, L., and Burns, P. C. (2016). Structure and reactivity of X-ray amorphous uranyl peroxide, U_2O_7. *Inorg. Chem.*, 55:3541–3546. 195, 196, 203

[127] Ostanin, S. and Zeller, P. (2007). Ab initio study of uranyl peroxides: Electronic factors behind the phase stability. *Phys. Rev. B*, 75(7):2–5. 192, 196

[128] Perdew, J. P., Burke, K., and Ernzerhof, M. (1996). Generalized gradient approximation made simple. *Phys. Rev. Lett.*, 77:3865–3868. 19, 21, 24, 34, 150, 231

[129] Petrik, N. G., Alexandrov, A. B., and Vall, A. I. (2001). Interfacial energy transfer during gamma radiolysis of water on the surface of ZrO_2 and some other oxides. *J. Phys. Chem. B*, 105(25):5935–5944. 206, 224

[130] Plášil, J. (2017). Uranyl-oxide hydroxy-hydrate minerals: their structural complexity and evolution trends. *Eur. J. Mineral.*, 30(2):237–251. 122

[131] Plášil, J. (2018). The crystal structure of uranyl-oxide mineral schoepite, $[(UO_2)_4O(OH)_6](H_2O)_6$, revisited. *J. Geosci.*, 63:65–73. 124, 126, 153, 160

[132] Pointurier, F. and Marie, O. (2010). Identification of the chemical forms of uranium compounds in micrometer-size particles by means of micro-Raman spectrometry and scanning electron microscope. *Spectrochim. Acta Part B*, 65(9-10):797–804. 58, 84, 127, 196

[133] Protas, J. (1959). Contribution a l'etude des oxydes d'uranium hydrates. *Bull. Soc. Fr. Miner. Cristal.*, 82:239–272. 124, 126, 153, 160

[134] Prout, E. G. and Tompkins, F. C. (1944). The thermal decomposition of potassium permanganate. *Trans Faraday Soc.*, 40:488–498. 112

[135] Qiu, J. and Burns, P. C. (2013). Clusters of actinides with oxide, peroxide, or hydroxide bridges. *Chem. Rev.*, 113:1097–1120. 196

[136] Réal, F., Vallet, V., Wahlgren, U., and Grenthe, I. (2008). Ab initio study of the mechanism for photoinduced yl-oxygen exchange in uranyl(VI) in acidic aqueous solution. *J. Am. Chem. Soc.*, 130(35):11742–11751. 228, 229

[137] Rose, D., Chang, Y.-d., Chen, Q., and Zubieta, J. (1994). Reactions of uranyl thiolate complexes with molecular oxygen: synthesis and crystal and molecular structures of the uranyl thiolate peroxo species. *Inorg. Chem.*, 33(02):5167–5168. 207

[138] Rotureau, P., Renault, J. P., Lebeau, B., Patarin, J., and Mialocq, J. C. (2005). Radiolysis of confined water: Molecular hydrogen formation. *ChemPhysChem*, 6(7):1316–1323. 206, 224

[139] Sakuraba, S. and Matsushima, R. (1970). Photochemical reactions of uranyl ions with organic compounds. II. The mechanism of the photo-oxidation of alcohols by uranyl ions. *Bull. Chem. Soc. Jpn.*, 43:2359–2363. 232

[140] Sato, T. (1961). Thermal decomposition of uranium peroxide hydrate. *Sci. Nat.*, 48(22):693. 192

[141] Sattonnay, G., Ardois, C., Corbel, C., Lucchini, J. F., Barthe, M. F., Garrido, F., and Gosset, D. (2001). Alpha-radiolysis effects on UO_2 alteration in water. *J. Nucl. Mater.*, 288(1):11–19. 203

[142] Schoep, A. and Stradiot, S. (1947). Paraschoepite and epiianthinite, two new uranium minerals from Shinkolobwe (Belgian Congo). *Am. Mineral.*, 32:344–350. 124, 135

[143] Seleznev, V. P., Tsvetkov, A. A., Sudarikov, B. N., and Gromov, B. V. (1972). Uranyl fluoride hydrates. *Russ. J. Inorg. Chem.*, 17(9):1356–1357. 74

[144] Sigmon, G. E., Ling, J., Unruh, D. K., Moore-shay, L., Ward, M., Weaver, B., and Burns, P. C. (2009). Uranyl–peroxide interactions favor nanocluster self-assembly. *J. Am. Chem. Soc.*, 131:16648–16649. 196

[145] Skrdla, P. J. (2009). Crystallizations, solid-state phase transformations and dissolution behavior explained by dispersive kinetic models based on a maxwell-boltzmann distribution of activation energies: Theory, applications, and practical limitations. *J. Phys. Chem. A*, 113(33):9329–9336. 112

[146] Stefaniak, E. A., Darchuk, L., Sapundjiev, D., Kips, R., Aregbe, Y., and Van Grieken, R. (2013). New insight into UO_2F_2 particulate structure by micro-Raman spectroscopy. *J. Mol. Struct.*, 1040:206–212. 74

[147] Steiner, T. (2002). The hydrogen bond in the solid state. *Angew. Chem. Int. Ed.*, 41(1):49–76. 41

[148] Sunder, S., Shoesmith, D. W., Christensen, H., and Miller, N. H. (1992). Oxidation of UO_2 fuel by the products of gamma radiolysis of water. *J. Nucl. Mater.*, 190:78–86. 206

[149] Sweet, L. E., Blake, T. A., Henager, C. H., Hu, S., Johnson, T. J., Meier, D. E., Peper, S. M., and Schwantes, J. M. (2013). Investigation of the polymorphs and hydrolysis of uranium trioxide. *J. Radioanal. Nucl. Chem.*, 296(1):105–110. 128, 129, 130, 178

[150] Szabo, Z. and Grenthe, I. (2010). On the mechanism of oxygen exchange between uranyl(VI) oxygen and water in strongly alkaline solution as studied by ^{17}O NMR magnetization transfer. *Inorg. Chem.*, 49(11):4928–4933. 225

[151] Takao, K. and Ikeda, Y. (2010). μ-η^2:η^2-Peroxido-bis[nitratodioxidobis(pyrrolidin-2-one)uranium(VI)]. *Acta Crystallogr. Sect. E*, 66(5):m539–m540. 207

[152] Taylor, J. C. (1971). The structure of the α form of uranyl hydroxide. *Acta Crystallogr. Sect. B Struct. Crystallogr. Cryst. Chem.*, 27(6):1088–1091. 138, 170, 174, 175, 179, 180, 185

[153] Thangavelu, S. G. and Cahill, C. L. (2015). Uranyl-promoted peroxide generation: Synthesis and characterization of three uranyl peroxo $[(UO_2)_2(O_2)]$ complexes. *Inorg. Chem.*, 54:4208–4221. 207, 231, 232, 234

[154] Thomas, M., Brehm, M., Fligg, R., Vöhringer, P., and Kirchner, B. (2013). Computing vibrational spectra from ab initio molecular dynamics. *Phys. Chem. Chem. Phys.*, 15(18):6608–22. 23

[155] Thuéry, P. and Masci, B. (2003). Self-assembly of an octa-uranate cage complex with a rigid bis-catechol ligand. *Supramol. Chem.*, 15(2):95–99. 207

[156] Thuéry, P., Nierlich, M., Masci, B., Asfari, Z., and Vicens, J. (1999). An unprecedented trigonal coordination geometry for the uranyl ion in its complex with p-tert-butylhexahomotrioxacalix[3]arene. *J. Chem. Soc. Dalt. Trans.*, 186(18):3151–3152. 207

[157] Toby, B. H. and Von Dreele, R. B. (2013). GSAS-II: the genesis of a modern open-source all purpose crystallography software package. *J. Appl. Cryst.*, 46(2):544–549. 7

[158] Tsantis, S. T., Zagoraiou, E., Savvidou, A., Raptopoulou, C. P., Psycharis, V., Szyrwiel, L., Hołyńska, M., and Perlepes, S. P. (2016). Binding of oxime group to uranyl ion. *Dalt. Trans.*, 45(22):9307–9319. 209

[159] Tsushima, S. (2009). Photochemical reduction of UO_2^{2+} in the presence of alcohol studied by density functional theory calculations. *Inorg. Chem.*, 48(11):4856–4862. 232

[160] Tsvetkov, A. A., Seleznev, V. P., Sudarikov, B. N., and Gromov, B. V. (1972). Equilibrium diagram of the uranyl fluoride-water system. *Russ. J. Inorg. Chem.*, 17(7):1048–1050. 74

[161] Tsvetkov, A. A., Seleznev, V. P., Sudarikov, B. N., and Gromov, B. V. (1973). Infrared spectra of complexes of uranyl fluoride with water and hydrogen fluoride. *Russ. J. Inorg. Chem.*, 18(3):411–413. 75

[162] Urbanec, Z. and Cejka, J. (1979). Infrared spectra of liebigite, andersonite, voglite, and schroeckingerite. *Collect. Czechoslov. Chem. Commun.*, 44:10–23. 147, 151

[163] Walenta, K. (1974). On studtite and its composition. *Am. Miner.*, 59:166–171. 192

[164] Walker, T. L. (1923). Schoepite, a new mineral from Kasolo, Belgian Congo. *Am. Mineral.*, 8:67. 122

[165] Walshe, A., Spain, E., Keyes, T. E., Forster, R. J., and Baker, R. J. (2017). Redox processes in solid-state uranyl (oxy)hydroxide minerals. *ChemElectroChem.*, 4:1–7. 127, 128

[166] Wang, R. (1981). Spent fuel special studies progress report: probable mechanisms for oxidation and dissolution of single-crystal UO_2 surfaces. Technical report, Pacific Northwest Laboratory. 203

[167] Wang, W. D., Bakac, A., and Espenson, J. H. (1995). Uranium(VI)-catalyzed photooxidation of hydrocarbons with molecular oxygen. *Inorg. Chem.*, 34(24):6034–6039. 232

[168] Wang, Y., Gunten, K. V., Bartova, B., Meisser, N., Astner, M., Burger, M., and Bernier-latmani, R. (2016). Products of in situ corrosion of depleted uranium ammunition in Bosnia and Herzegovina soils. *Environ. Sci. Technol.*, 50:12266–12274. 212, 232

[169] Weck, P. F. and Kim, E. (2014). Layered uranium(VI) hydroxides: structural and thermodynamic properties of dehydrated schoepite $\alpha-UO_2(OH)_2$. *Dalt. Trans.*, 43(45):17191–9. 195

[170] Weck, P. F., Kim, E., Jové-Colón, C. F., and Sassani, D. C. (2012). Structures of uranyl peroxide hydrates: a first-principles study of studtite and metastudtite. *Dalt. Trans.*, 41(32):9748. 192, 194, 195

[171] Weller, M. T., Light, M. E., and Gelbrich, T. (2000). Structure of uranium(VI) oxide dihydrate, $UO_3 \cdot 2\,H_2O$; synthetic meta-schoepite $(UO_2)_4O(OH)_{65}H_2O$. *Acta Crystallogr. Sect. B*, 56(4):577–583. 124, 125, 126, 137, 138, 140, 141, 153, 156, 160, 170, 171

[172] Yusov, A. B. and Shilov, E. P. (2000a). Reduction of the photoexcited uranyl ion by water. *Russ. Chem. Bull.*, 40(2):285–290. 232

[173] Yusov, A. B. and Shilov, V. P. (2000b). Photochemistry of f-element ions. *Russ. Chem. Bull. Int. Ed.*, 49(12):1925–1953. 232

[174] Zachariasen, F. W. H. (1948). Crystal chemical studies of the 5f-series of elements. III. A study of the disorder in the crystal structure of anhydrous uranyl fluoride. *Acta Crystallogr.*, 1(6):277–281. 25, 26, 27, 51, 52, 56

[175] Zachariasen, W. H. (1944). CK-1367. Technical report. 192

Vita

Marie C. Kirkegaard is a PhD candidate in the Bredesen Center for Interdisciplinary Research and Graduate Education at the University of Tennessee–Knoxville and a member of the Nuclear Security Advanced Technologies Group at Oak Ridge National Laboratory. She is also a Nuclear Forensics Graduate Fellow with the US Department of Homeland Security.